Université PARIS-SUD
École Doctorale 517 - *Particules, Noyaux et Cosmos* -

THÈSE DE DOCTORAT

Discipline: Physique Nucléaire

présentée par

Claudio GEUNA

pour obtenir le grade de Docteur en Sciences de l'Université Paris-Sud, Orsay

Sujet:

J/ψ production in proton-proton collisions at $\sqrt{s}$ = 2.76 and 7 TeV in the ALICE Forward Muon Spectrometer at LHC

Soutenue publiquement le 12 Novembre 2012 devant le Jury composé de:

Achille STOCCHI	Président du Jury
Ginés MARTINEZ	Rapporteur
Frédéric FLEURET	Rapporteur
Jean-Philippe LANSBERG	Examinateur
Alberto BALDISSERI	Directeur de Thèse
Hervé BOREL	Co-Directeur de Thèse

Remerciements

Je souhaite d'abord remercier l'institution qui m'a accueilli et qui m'a permis matériellement de faire cette thèse : le SPhN de l'Irfu au CEA à Saclay sans qui je n'aurais pas pu assister au démarrage du LHC et participer aux premières prises de données et à leurs analyses, ni parcourir le monde comme j'en ai eu le droit. Je tiens à remercier tous le membres, en particulier le chef de Service Michel Garçon, pour m'avoir accueilli au sein du Service, ainsi que l'ensemble du groupe administratif.

J'aimerais aussi adresser un grand merci aux membres de mon jury pour avoir accepté d'en faire partie, en particulier : Achille Stocchi pour avoir accepté de présider le jury, mes rapporteurs Ginés Martinez et Frédéric Fleuret pour leur lecture critique du manuscrit, mon examinateur Jean-Philippe Lansberg pour les discussions instructives sur le contexte théorique de cette thèse.

Mes plus chaleureux remerciements vont à mon directeur de thèse, Alberto Baldisseri. Sa disponibilité, ses encouragements, ses qualités scientifiques et humaines m'ont permis de mener ce travail de thèse jusqu'à son terme.

Je voudrais aussi témoigner de ma reconnaissance pour mon co-directeur de thèse Hervé Borel et mon collègue Javier Castillo. Merci Hervé pour la lecture (et relecture) de mon manuscrit qui a beaucoup bénéficié de tes critiques. Merci Javier pour avoir toujours répondu à mes questions et d'avoir fait preuve d'une grande patience à mon égard. Merci Javier pour toutes les heures passées à me transmettre les connaissances et astuces nécessaires pour l'analyse de données.

C'est aussi avec grand plaisir que j'adresse mes remerciements à l'ensemble des membres du groupe ALICE du SPhN avec lesquelles j'ai travaillé quotidiennement : Andry, Hongyan, Hugo, Jean-Luc, Sanjoy. Merci pour l'expérience enrichissante et pleine d'intérêt que vous m'avez faite vivre pendant ces trois années de doctorat au sein du groupe.

J'ai eu la très grande chance durant cette thèse de rencontrer un grand nombre de personnes : professeurs, chercheurs, thésards, stagiaires, ... Merci surtout à tout ceux qui m'ont lancé une phrase d'amitié ou d'encouragement tout au long de ces 3 années.

Enfin, je voudrais terminer ces remerciements par une note plus personnelle pour ma famille et mes amis. Merci à ma famille de m'avoir toujours encouragée et soutenue pendant ces trois années de doctorat. Merci aux amis de rendre la vie toujours meilleur : Valentina, Piero, Michele, Astrid, Mafalda, Gian Michele, Alessandro, ... merci ! Et plus que tout merci à ma chère Martina !

Contents

Introduction

Quarkonia are meson states whose constituents are a *charm* or *bottom* quark and its corresponding antiquark ($Q\bar{Q}$). The study of the production of such $c\bar{c}$ and $b\bar{b}$ bound states, known also as *charmonia* and *bottomonia*, in high-energy hadron collisions represents an important testing ground for the Quantum Chromo-Dynamics (QCD), the theory of strong interactions.

Despite the fact that the quarkonium saga has already a 40-year history beginning with the discovery of the J/ψ meson in November 1974, the quarkonium production mechanism is still an open issue for which the interest of the current physics research is still lively.

Due to the large masses of the c and b quarks, the production of quarkonium states can be described as involving two different energy scales. The initial formation of the heavy quark-antiquark pair occurs via hard processes that can be reliably treated using a perturbative QCD approach. The heavy quark pair evolving towards the quarkonium bound state is, instead, a non-perturbative system which intrinsically involves soft energy scales. Therefore, the description of quarkonium production can be properly carried out by taking into account that such a process is governed by both perturbative and non-perturbative aspects of QCD. Several theoretical models have been developed in the last 40 years to describe the experimental data, such as the Color Singlet Model, the Color Evaporation Model, and the Non-Relativistic QCD approach. They mainly differ in the details of the non-perturbative evolution of the heavy quark pair towards the bound state.

Despite many improvements on the theoretical side, models are still not able to consistently reproduce, within the same calculation framework and at the same time, different physical observables like the quarkonium production cross section, the transverse momentum p_{T} distributions, and the polarization. Therefore, measurements at the new CERN Large Hadron Collider (LHC) energy regimes are clearly extremely interesting and represent a crucial step forward in understanding the physics involved in quarkonium hadroproduction processes. Furthermore, the range of Bjorken-x values accessible at LHC energies is unique: low-p_{T} charmonium measurements, in particular at forward rapidities, are sensitive to an unexplored region ($x < 10^{-5}$ at $Q^2 = m^2_{\mathrm{J}/\psi}$) of the gluon distribution function of the proton.

In this thesis, the study of inclusive J/ψ production in proton-proton (pp) collisions at center-of-mass energies of $\sqrt{s} = 2.76$ and 7 TeV, obtained with the ALICE experiment at the LHC, is presented. J/ψ mesons are measured at forward rapidity ($2.5 < y < 4$), down to zero transverse momentum p_{T}, via their decay into muon pairs ($\mu^+\mu^-$) which are detected by the ALICE Muon Spectrometer.

Quarkonium resonances also play an important role in probing the properties of the strongly interacting hadronic matter created, at high energy densities, in ultra-relativistic heavy-ion collisions. Under such extreme conditions, the created system, according to QCD, undergoes a phase transition from ordinary hadronic matter, constituted by uncolored bound states of quarks (i.e. baryons and

mesons), to a new state of deconfined quarks and gluons, called *Quark Gluon Plasma* (QGP). The ALICE experiment at CERN LHC has been specifically designed to study this state of matter in Pb-Pb collisions. Quarkonia, among other probes, represents one of the most promising tools to prove the QGP formation. In oder to correctly interpret the measurements of quarkonium production in heavy-ion collisions, a solid baseline is provided by the analogous results obtained in pp collisions.

Hence, the work discussed in this thesis, concerning the inclusive J/ψ production in pp collisions, also provides the necessary reference for the corresponding measurements performed in Pb-Pb collisions which were collected, by the ALICE experiment, at the very same center-of-mass energy per nucleon pair ($\sqrt{s_{NN}}$ = 2.76 TeV).

The structure of the manuscript is the following:

- **Chapter 1** is a general introduction on quarkonia in high-energy physics: after a short reminder of QCD, we present an overview of the present status of knowledge on quarkonium hadroproduction mechanisms as explained by different theoretical models. Then, an elementary introduction to the QGP physics is presented pointing out the role of quarkonia as probe of such deconfined nuclear matter;

- **Chapter 2** is an overview of the ALICE experiment, with a detailed description of the Muon Spectrometer and its muon tracking and trigger system;

- **Chapter 3** and **4** are dedicated to the description, in all its parts, of the analysis procedure adopted to measure the inclusive J/ψ production cross sections (integrated and differential) in pp collisions at $\sqrt{s}$ = 2.76 and 7 TeV, respectively;

- In **Chapter 5,** the measured differential J/ψ cross sections are compared to recent theoretical model predictions;

- Finally, the conclusions are drawn in **Chapter 6**.

Chapter 1

Heavy quarkonium in high-energy physics

High-energy physics has developed and validated, throughout the mid 20th century up to now, a detailed, though still incomplete, theory of elementary particles and their fundamental interactions. Such theory, called *Standard Model*, has been able to successfully explain, at a fundamental level, the phenomenology of interactions as obtained from several experimental measurements. Nevertheless, further investigations are necessary in order to answer to still unresolved questions about, for example, the origin of the mass, the nature of dark matter and dark energy and the origin of matter-antimatter asymmetry in the Universe. In addition, new developments, both theoretical and experimental, are required to apply and extend the *Standard Model* to complex and dynamically evolving systems of finite size, as the ones produced in high-energy nucleus-nucleus collisions.

The Large Hadron Collider (LHC) [1], with its high center-of-mass energies[1] and its possibility to accelerate and collide both proton and nucleus (lead (Pb) nuclei up to now) beams, has been providing, since the beginning of the LHC activities at the end of 2009, a deep understanding and insight into such topics.

Among the four experiments at LHC, namely ALICE [2], ATLAS [3], CMS [4] and LHCb [5], ALICE is the only detector specifically designed to study ultra-relativistic heavy-ion collisions. The aim is to explain how collective phenomena and macroscopic properties of the finite-size system produced in nucleus-nucleus collisions and involving many degrees of freedom, rise from the microscopic laws of elementary particle physics. Specifically, heavy-ion physics addresses these questions to the theory of strong interaction, the Quantum Chromodynamics (QCD), by analyzing nuclear matter under conditions of extreme density and temperature.

QCD predicts the occurrence of a phase transition from ordinary hadronic matter, constituted by uncolored bound states of quarks, to a new state of deconfined quarks and gluons, called *Quark Gluon Plasma* (QGP). This phase transition is supposed to take place for an energy density $\varepsilon \approx 1$ GeV/fm^3 and/or a temperature $T \approx 200$ MeV [6].

Understanding the phase transition is of great interest not only in particle physics, but also in cosmology. In fact, according to the Big Bang model, the Universe evolved from an initial state of extremely high density to its present state through a rapid expansion and cooling, thereby traversing

[1] For what concerns the proton-proton program, the LHC machine delivered, in the period 2009 - 2012, collisions at $\sqrt{s} = 0.9$, 2.76, 7 and 8 TeV. The Pb-Pb collisions, instead, were delivered, at the end of 2010 and 2011, at a center-of-mass energy per nucleon-nucleon collision, $\sqrt{s_{NN}}$, equal to 2.76 TeV.

a series of phase transitions predicted by the *Standard Model* (including the ones previously mentioned). Global features of our Universe, like baryon-antibaryon asymmetry or large scale structures (galaxy distribution), are believed to be linked to characteristic properties of such transitions.

In order to recreate and study, in the laboratory, the QGP, the only way is to collide two heavy nuclei which provide a unique opportunity to produce droplets of strongly interacting hadronic matter at extreme temperatures and energy densities. The system formed undergoes a fast dynamical evolution from the initial extreme conditions to final ordinary hadronic matter, making direct measurements impossible. In order to test the properties of the new state of matter and answer the question whether the matter reaches a deconfined phase, several signatures have been proposed. Among them, the production of quarkonium states, such as J/ψ and Υ belonging, respectively, to the charmonium and bottomonium family, plays an important role as a test of deconfinement.

In this Chapter, after a short introduction to the Quantum Chromodynamics theory, we present an overview of the present status of knowledge of the quarkonium production in high-energy hadron collisions. Several quarkonium production models are discussed explaining their key features and showing how they can describe the most recent experimental measurements of quarkonia (differential production cross section, polarization, etc.). Finally, in the last section, an elementary introduction to the physics of QGP is given pointing out the role of heavy quarkonia as probe of such deconfined nuclear matter.

1.1 A short introduction to Quantum Chromodynamics

Quantum Chromodynamics (QCD) is the sector of the *Standard Model* that is relevant for the strong interaction which is responsible for binding together protons and neutrons within the atomic nucleus and for several hadronic reactions [7, 8, 9]. The strong force is described as the interaction between fundamental objects called *quarks* and *gluons* which build up the *hadron*s, by definition, strongly interacting particles such as protons, neutron, pions, etc [2]. Quarks are fermions (spin $\frac{1}{2}$) and come in several varieties or flavours (see Table 1.1 for a summary of the properties of the known quarks[3]) while gluons are massless bosons (spin 1) with zero electric charge.

The dynamic of the interactions described by QCD presents several analogies with the Quantum Electrodynamics (QED) theory which explains the interactions between electrically charged particles in term of exchange of massless bosons called *photons.* The QCD charge responsible for the strong interaction is the so-called *color charge.* Each quark can exist in one of three different color states, designed as red, blue and green. Gluons, which also carry a color charge, act as the exchange particles for the strong force (called also colored force) between quarks.

However, despite the analogies, the strong and electromagnetic interactions present some fundamental differences leading to qualitatively different phenomena. First of all, it should be mentioned the fact that, in QED, there is only one type of electric charge while in QCD the color charge, for quarks, can appear in three states. Furthermore, unlike photons, mediators of the electromagnetic force carrying zero electric charge, gluons are colored and can therefore interact among each others (self-interaction). Finally, unlike the electric charge, the color charge doesn't appear as a physical degree of freedom for systems at macroscopic scale. Indeed, observable objects are always colorless hadrons.

[2] In QCD, nucleons (i.e. protons and neutrons) are treated not as fundamental objects in their own right, but as composite states of size roughly 1 fm (1 fm = 10^{-15} m) made by more elementary particles (quarks and gluons).

[3] The u-, d-, and s-quark masses are estimates of so-called *current-quark masses* in a mass-independent subtraction scheme ($\overline{MS}$) at a scale $\mu \approx 2$ GeV. The c- and b-quark masses are the *running* masses in the $\overline{MS}$ scheme. The t-quark mass is based on direct measurements of top events (see *[10]*).

Quark flavour	Mass	Electric charge
up (u)	$2.3^{+0.7}_{-0.5}$ MeV	+ $^2/_3$
down (d)	$4.8^{+0.7}_{-0.3}$ MeV	- $^1/_3$
strange (s)	95 ± 5 MeV	- $^1/_3$
charm (c)	1.275 ± 0.025 GeV	+ $^2/_3$
bottom (b)	4.18 ± 0.03 GeV	- $^1/_3$
top (t)	$173.5 \pm 0.6 \pm 0.8$ GeV	+ $^2/_3$

Table 1.1. *Summary of properties of the known quarks [10].*

As a matter of fact, the phenomenological dissimilarities between QED and QCD are the consequence of their deeply different mathematical structure.

1.1.1 QCD Lagrangian

Mathematically, Quantum Chromodynamics is a Yang-Mills theory with local gauge group $SU(3)$[4] vectorially coupled to six Dirac fields of different masses, corresponding to the six quark flavours [11]. In order to derive the QCD Lagrangian density which summarizes the dynamics of systems subject to strong interaction, the starting point is the Dirac Lagrangian density for the free quark fields:

$$\mathscr{L}_{Dirac} = \sum_{\alpha=1}^{3} \sum_{j=1}^{N_f} \overline{\Psi_j^\alpha} (i\gamma^\mu \partial_\mu - m_j) \Psi_j^\alpha, \tag{1.1}$$

where Ψ_j^α is the Dirac spinor representing the field of a quark of mass m_j, flavour j (j = u, d, s, c, b, t) and color α (α = 1, 2, 3). The Dirac matrices (4×4) γ^μ (μ= 0, ..., 3) generalize the Pauli spin matrices. The Dirac Lagrangian, required to be invariant under the $SU(3)$ local gauge transformation, is consequently modified by replacing the partial derivative ∂_μ with the covariant derivative D_μ defined as

$$D_\mu = \partial_\mu - ig \sum_{a=1}^{8} T_a A_\mu^a, \tag{1.2}$$

where g is the QCD coupling constant which determines the strength of the strong interaction. T_a (a = 1, .., 8) are the generators of the gauge group $SU(3)_{color}$ while A_μ^a (a = 1, .., 8) are the so-called gauge fields. These eight vector fields can be identified as the vector gauge bosons that mediate strong interactions of quarks in QCD, the gluons.

The kinetic energy term of the QCD Lagrangian for gluons, $SU(3)_{color}$ gauge-invariant too, can be expressed as

$$\mathscr{L}_{gauge} = -\frac{1}{4} G_{\mu\nu}^a G_a^{\mu\nu}, \tag{1.3}$$

where $G_{\mu\nu}^a$ is the gluon field strength tensor defined as

[4]The number of quark color states, n = 3, is the degree of the QCD symmetry group $SU(3)_{color}$.

$$G^a_{\mu\nu} = \partial_\mu A^a_\nu - \partial_\nu A^a_\mu + g \sum_{b,=1}^{8} f^a_{bc} A^b_\mu A^c_\nu, \tag{1.4}$$

with f^a_{bc} structure constants of the $SU(3)_{color}$ group.

Finally, the QCD Lagrangian density, obtained as $\mathscr{L}_{QCD} = \mathscr{L}_{Dirac} + \mathscr{L}_{gauge}$, reads

$$\mathscr{L}_{QCD} = \sum_{\alpha=1}^{3} \sum_{j=1}^{N_f} \overline{\Psi^\alpha_j} (i\gamma^\mu D_\mu - m_j) \Psi^\alpha_j - \frac{1}{4} G^a_{\mu\nu} G^{\mu\nu}_a. \tag{1.5}$$

The interaction terms of $\mathscr{L}_{QCD}$ permits both quark-gluon and gluon-gluon interactions. In particular, the gluon self-interactions, shown schematically in Fig. 1.1, emerge from the non-Abelian structure of the $SU(3)_{color}$ gauge theory. Actually, as shown in Eq. 1.4, the definition of the tensor $G^a_{\mu\nu}$ contains, apart from the standard partial derivate terms, a non-linear component in term of the gauge potential A^a_μ.

Figure 1.1. *Possible self-interactions of gluons in QCD.*

Therefore, the eight QCD gluons do not come in as a simple repetition of the QED photon since they can interact among each others with three- and four-gluon self-interactions. Such peculiar QCD feature, consequence of gluons carrying color charge, is the source of the key differences between QCD and QED. In fact, these interactions are responsible for many of the unique and salient features of QCD, such as asymptotic freedom and color confinement. In the following two sections, we briefly discuss these important properties of the QCD dynamics.

1.1.2 Asymptotic freedom

One of the most striking features of QCD is asymptotic freedom which states that the interaction strength between quarks and gluons becomes smaller as the distance between them gets shorter or the energy reaction gets higher [12]. In other words, the strong coupling constant α_s, defined as $\alpha_s = \frac{g^2}{4\pi}$, is a running coupling constant decreasing as a function of the momentum transfer Q of the process. For this discovery, Gross, Politzer and Wilczek won the 2004 Nobel prize in physics [13, 14, 15].

A first intuitive explanation of the asymptotic freedom can be given by recalling that, in electromagnetism, the electric force between two charges q_1 and q_2 in vacuum can be expressed by Coulomb's law as

$$F = \frac{1}{4\pi} \frac{q_1 q_2}{r^2}. \tag{1.6}$$

On the other hand, if the two electric charges are placed inside a medium with dielectric constant ε ($\varepsilon > 1$), the force becomes

$$F = \frac{1}{4\pi\varepsilon}\frac{q_1 q_2}{r^2}, \tag{1.7}$$

which can be also expressed in the above vacuum form, Eq. 1.6, by introducing the effective charge $\tilde{q}_i = q_i/\sqrt{\varepsilon}$. Therefore, the presence of the dielectric medium may be regarded as modifying the electric charges producing a charge screening effect.

In quantum field theory, the vacuum state is not simply an empty space but it is the ground state (lowest energy state) of a system. It can be depicted as a sea of continuously appearing and disappearing virtual particle–antiparticle pairs, called vacuum fluctuations, which are created out of the vacuum and then annihilate each other. In QED, such electron-positron pairs virtually created out of the vacuum (see left diagram of Fig. 1.2), in the presence of an electromagnetic field, act as an electric dipole. In analogy to what happens in classical electromagnetism, these electron-positron pairs reposition themselves, thus partially counteracting the electromagnetic field with a screening effect (similar to the one produced by a dielectric medium). Therefore the field is weaker than would be expected in the case of a classical vacuum completely empty. The phenomenon, relative to the particle–antiparticle pairs virtually created, is referred to as vacuum polarization.

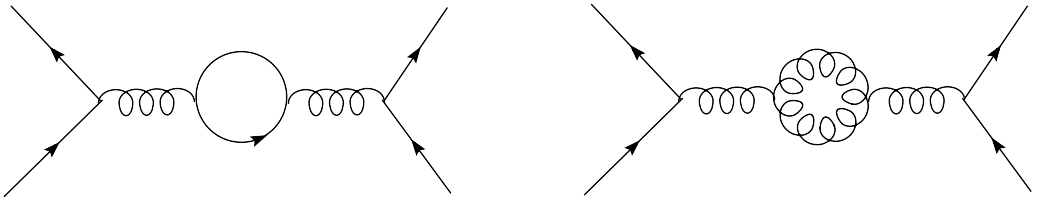

Figure 1.2. *Quantum vacuum polarization diagrams affecting the interaction strength. The first diagram, shared by QED and QCD (the wavy line represents a photon in QED and a gluon in QCD), makes interactions weaker at large distances (screening effect). The second diagram, arising from the non-linear interaction between gluons in QCD, makes interactions weaker at short distances (anti-screening effect).*

As a consequence of this vacuum property, the interaction between two electrons in vacuum becomes

$$F = \frac{e_{eff}^2}{4\pi r^2} = \frac{\alpha_{em}(r)}{r^2}, \tag{1.8}$$

where e_{eff} is the effective electron charge and $\alpha_{em}(r)$ is the electromagnetic running coupling constant, depending on the distance r or the momentum transfer of the process $Q \sim 1/r$. As $r \to 0$ or equivalently, $Q \to \infty$, the QED interaction strength gets stronger. Therefore, QED becomes a strongly-coupled theory at very short distance scale (or at high momentum transfer)[5].

The considerations, based on the existence of the vacuum polarization, can be also applied in the case of QCD. As a consequence of the non-Abelian structure of the $SU(3)_{color}$ gauge theory, QCD allows two different types of vacuum fluctuations. The first one, which is shared by QCD and QED (shown in the left diagram of Fig. 1.2), is a fermion fluctuation producing a screening effect. Therefore it contributes to make the interaction strength weaker at very large distances. On the contrary, the

[5]The measurement of the electromagnetic running coupling constant in low-energy reactions gives $\alpha_{em}(Q^2 = 0) = 1/137.035$. At $Q^2 \approx M_W^2 (= 80.399 \pm 0.023\ GeV)$ the value is $\sim 1/128$ [10].

second type of fluctuation (shown in the right diagram of Fig. 1.2) is a gluon fluctuation which produces an anti-screening effect with stronger interaction at larger distances. Finally, the contribution relative to gluon fluctuations results to be more important than the fermion one and, consequently, the strong interaction strength can be shown to have a specific scale-dependence decreasing as the momentum transfer of the reaction $Q \to \infty$ or the distance $r \to 0$.

The dependence of the strong coupling constant on the momentum transfer scale Q^2 can be formally determined, in QCD, through the renormalization group equation

$$Q^2 \frac{\partial \alpha_s(Q^2)}{\partial Q^2} = \beta(\alpha(Q^2)). \tag{1.9}$$

The perturbative expansion of the β function, calculated in 1-loop approximation, gives

$$\beta(\alpha_s(Q^2)) = -\beta_0 \alpha_s^2(Q^2) + \mathscr{O}(\alpha_s^3), \tag{1.10}$$

with $\beta_0 = \frac{11N_c - 2N_f}{12\pi}$, where N_c is the number of QCD color states and N_f is the number of active quark flavors at the energy scale Q^2. A solution of Eq. 1.9, in 1-loop approximation, i.e. neglecting β_1 and higher order terms, is

$$\alpha_s(Q^2) = \frac{\alpha_s(\mu^2)}{1 + \alpha_s(\mu^2)\beta_0 ln\frac{Q^2}{\mu^2}}, \tag{1.11}$$

where μ is the renormalization scale adopted in the calculation. Eq. 1.11, giving a relation between the values of α_s at two different energy scales Q^2 and μ^2, describes the property of asymptotic freedom: if Q^2 becomes large and β_0 is positive, i.e. if $N_f < 17$, $\alpha_s(Q^2)$ will asymptotically decrease to zero. Likewise, Eq. 1.11 indicates that $\alpha_s(Q^2)$ grows to large values and, in this perturbative form, actually diverges to infinity at small Q^2 (large distance): for example, with $\alpha_s(\mu^2 \equiv M_{Z^0}^2) \approx 0.12$ and for typical values of N_f = 2 ... 5, $\alpha_s(Q^2)$ exceeds unity for $Q^2 \leq \mathscr{O}$(100 MeV ... 1 GeV). This is the region where perturbative expansions in α_s, like Eq. 1.19, are not meaningful anymore and therefore energy scales below 1 GeV have to be regarded as the non-perturbative region where confinement, an important QCD property described in Section 1.1.3, sets in.

The parametrization of the running coupling constant $\alpha_s(Q^2)$ can be, alternatively, expressed introducing a dimensional parameter Λ_{QCD}. Setting

$$\Lambda_{QCD}^2 = \frac{\mu^2}{e^{1/(\beta_0 \alpha_s(\mu^2))}}, \tag{1.12}$$

Eq. 1.11, calculated in 1-loop approximation, transforms into

$$\alpha_s(Q^2) = \frac{1}{\beta_0 ln\frac{Q^2}{\Lambda_{QCD}^2}}. \tag{1.13}$$

Hence, $\alpha_s(\mu^2)$ is replaced by a suitable choice of the Λ_{QCD} parameter which is technically identical to the energy scale Q where $\alpha_s(Q^2)$ diverges to infinity, i.e. $\alpha_s(Q^2) \to \infty$ for $Q^2 \to \Lambda_{QCD}^2$.

In quantum field theories, like QCD and QED, physical observables, O, can be expressed by a perturbation series in powers of the coupling parameter α_s or α_{em}, respectively ($O = O_0 + \alpha 0_1 + \alpha^2 0_2 + ...$). If these couplings are sufficiently small, i.e. $\alpha \ll 1$, the series may converges providing a realistic prediction of O, even if only a limited number of perturbative orders can be calculated.

The scale parameter Λ_{QCD} represents therefore the limit of validity of the perturbative approach. For large momentum transfer $Q^2 \gg \Lambda_{QCD}^2$ (hard processes), the application of perturbative QCD

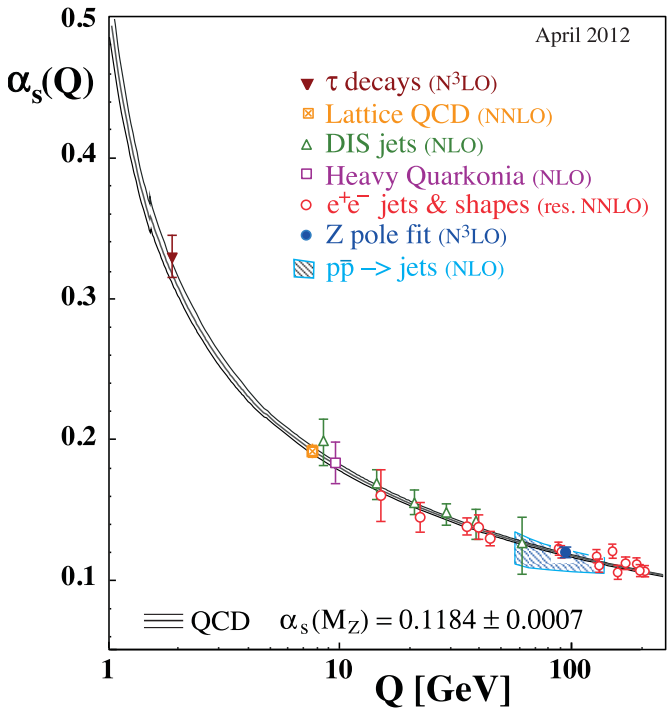

Figure 1.3. *The running of the QCD coupling constant as a function of the momentum transfer Q. Experimental data (points) are compared to QCD prediction (curves) [10].*

(pQCD) theory is allowed and provides quantitative predictions of physical observables. On the contrary, for soft processes having $Q^2 \lesssim \Lambda^2_{QCD}$, the perturbative approach becomes inappropriate and therefore non-perturbative methods have been developed like hadronization models, describing the transition of quarks and gluons into hadrons, or the Lattice QCD technique [16].

Experimentally [10], the actual world-average value of $\alpha_s(Q^2)$, measured at the energy scale of $M_{Z^0} = 91.1876 \pm 0.0021$ GeV, is

$$\alpha_s(M_{Z^0}) = 0.1184 \pm 0.0007 \tag{1.14}$$

which corresponds to a Λ_{QCD} value, in the standard renormalization scheme ($\overline{MS}$) and for a number of active quark flavours $N_f = 5$, $\Lambda_{QCD} \equiv \Lambda^{N_f=5}_{\overline{MS}} = (213 \pm 8)$ MeV.

1.1.3 Confinement

One of the prominent features of QCD is the quark confinement which is a necessary requirement to explain the apparent absence of free quarks in Nature. Although the quark model of hadrons[6] establishes quarks, with an electric charge $\pm\frac{1}{3}e$ and $\pm\frac{2}{3}e$ and with a quantum property called *color charge*, as the basic constituents of hadrons, no isolated quarks have ever been observed in any experiment.

An intuitive argument, displayed in Fig. 1.4, can be introduced to explain this property. Let us suppose, for example, we have a meson system which contains a quark-antiquark pair tied together by a color string. One may try to break the system by separating the quark from the antiquark pulling

[6]The quark model of hadrons was first introduced by Gell-Mann and Zweig in 1964.

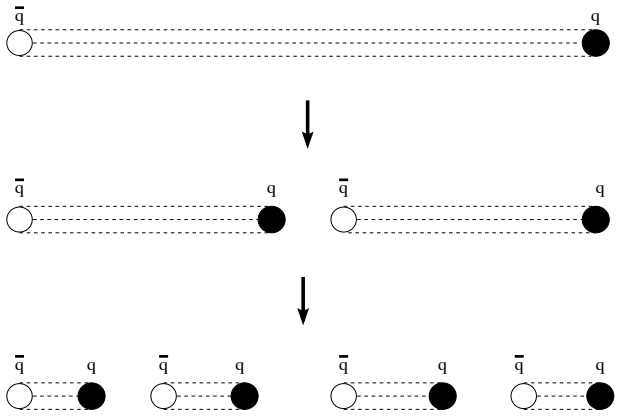

Figure 1.4. *String breaking by quark-antiquark pair production.*

them apart. As described in Section 1.1.2, the strong interaction gets stronger at large distances, or - equivalently - at low momentum transfer $Q^2 \lesssim \Lambda^2_{QCD} \sim (1\text{ fm})^{-2}$, and, similarly, the system's stretching energy increases when the quark-antiquark separation grows. Finally, beyond a certain distance, a new quark-antiquark pair will be created out of the vacuum: part of the stretching energy goes therefore into the creation of the new pair, and as a consequence of it, the breaking down of the string does not result in quarks as free particles. In other words, the strong interaction favors quark confinement because, at a certain quark-antiquark separation range, it is more energetically favorable to create a new pair than to continue to elongate the color string.

The explanation above discussed is, in some sense, a sort of self-consistent speculation which is not the same thing as a deep understanding from first QCD principles. It is important to mention, for instance, that quark confinement has to be reformulated with the more general concept of color confinement, which means that there are no isolated particles in Nature with non-vanishing color charge, i.e. all asymptotic particles states are color singlet. This property, based on the experimental fact that the hadron spectroscopy fits nicely into a scheme in which the constituent quarks combine in color-singlet states, is still a theoretical conjecture consistent with a large numbers of experimental results.

Despite several efforts, the confinement proof in QCD is a challenge that has not been met. Nevertheless, there have been some very interesting developments over the last years coming from lattice QCD investigations [17, 18]. Some results for the potential $V(r)$ and the force $F(r)$, describing a static quark-antiquark pair separated by a distance r, are plotted in Fig. 1.5.

They show that the static potential $V(r)$ is monotonically rising and eventually grows linearly for large separations. The force $F(r)$ is fairly strong, at least 1 GeV / fm in the whole range of distances, and if this continues to be so at larger values of r it will evidently not be possible to separate the quark-antiquark pair. On the other hand, at short distances, the data points of the potential $V(r)$ rapidly approach the curves that can be obtained in perturbation theory since the effective gauge coupling is small in this regime.

1.2 Quarkonia production in pp collisions

The quarkonia saga began in November 1974 with the simultaneous discovery of the J/ψ meson by two different research teams: Ting *et al.* at the Brookhaven National Laboratory (BNL) [21] and

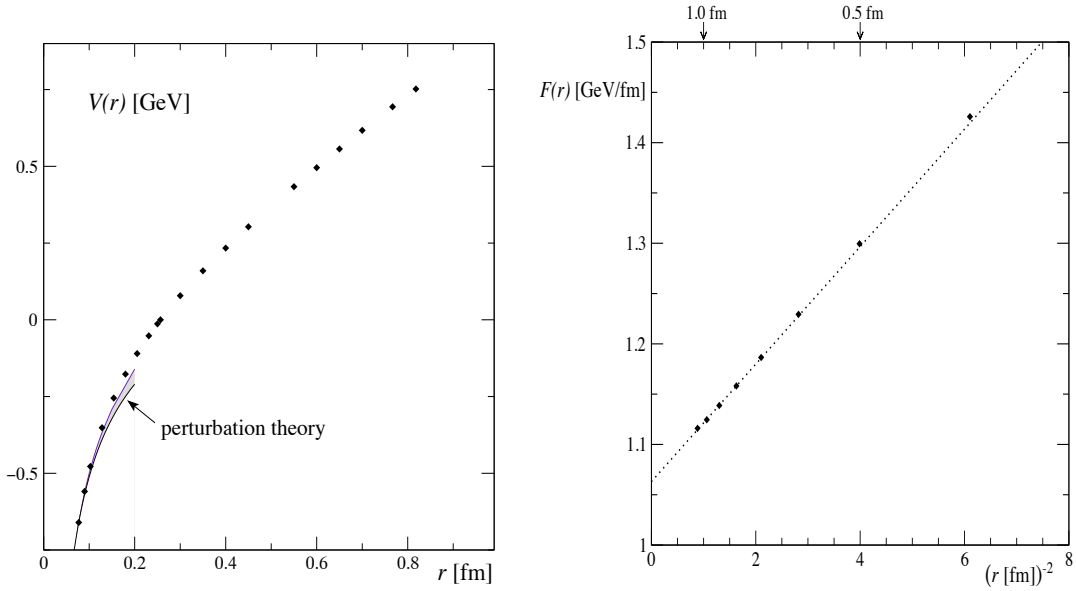

(a) *Potential V(r).* (b) *Force F(r).*

Figure 1.5. *Lattice QCD calculations for the static potential V(r) [19] (a) and the force F(r) [20] (b) relative to a static quark-antiquark pair .*

Richter *et al.* at the Stanford Linear Accelerator Center (SLAC) [22] [7].

Ting's observation was performed from the reaction $p + Be \rightarrow e^+ + e^- + x$ by measuring the e^+e^- invariant mass spectrum with a pair spectrometer. The experiment used the high-intensity proton beams of the Alternating Gradient Synchrotron (AGS) working at the energy of 30 GeV, which bombarded a Be fixed target. On the contrary, Richter's experiment measured the cross section for $e^+e^- \rightarrow$ hadrons, e^+e^-, and possibly $\mu^+\mu^-$ with Mark I detector at the SLAC electron-positron storage ring SPEAR [8].

It became clear that the new J/ψ resonance[9] was the first observed state of a system containing previously unknown (but anticipated[10]) charmed quark and its antiquark: $c\bar{c}$. The new system, called *charmonium* in analogy with positronium (e^+e^- system), was then verified to contain a spectrum of resonances[11], corresponding to various excitations of the $c\bar{c}$ quark-antiquark pair. The properties of charmonium, and of its heavier sibling bottomonium[12], are determined by the strong interaction, therefore they played an important role for understanding hadronic dynamics, as the study of the hydrogen atom allowed to explain the atomic physics.

[7] The Nobel Prize in Physics 1976 was awarded jointly to Burton Richter and Samuel Chao Chung Ting "for their pioneering work in the discovery of a heavy elementary particle of a new kind".

[8] The name chosen for the new resonance was *J* at BNL and ψ at SLAC.

[9] Few weeks after the discovery of the J/ψ, the Frascati group [23] confirmed the presence of the new particle.

[10] The existence of the charm quark was required, among others, by the mechanism of Glashow, Iliopoulos and Maiani (GIM) [24]

[11] The first radial excited state of charmonia, called ψ' or $\psi(2S)$, was directly found just ten days after the J/ψ [25].

[12] In 1977, the elementary particle physics was further enriched by the discovery of a new resonance, the Υ, which was identified as a bound state of the beauty (or bottom) quark with its antiquark ($b\bar{b}$). The discovery was possible thank to the proton synchrotron accelerator at Fermilab [26]. As for charmonia, the first radial excited state ($\Upsilon(2S)$) was directly found thereafter [27].

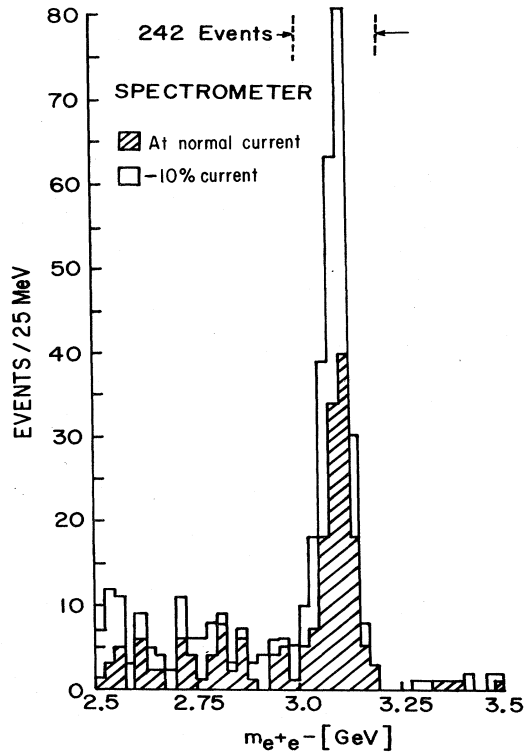

(a) *Invariant mass spectrum for opposite-sign electron pairs (e^+e^-).*

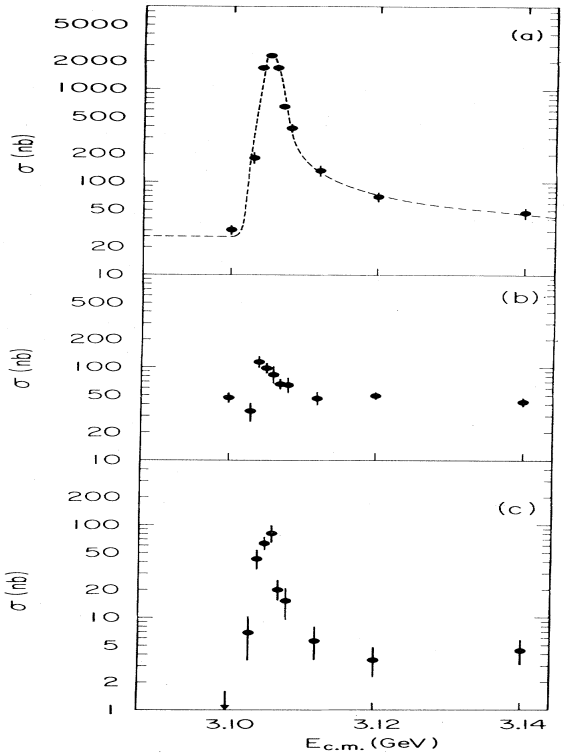

(b) *Cross section versus center-of-mass energy for (a) multihadron final states, (b) e^+e^- final states, and (c) $\mu^+\mu^-$, $\pi^+\pi^-$ and K^+K^- final states.*

Figure 1.6. *First published results of the discovery of the J/ψ meson at BNL [21] (a) and at SLAC [22] (b).*

The basis of the charmonium spectroscopy are provided in Section 1.2.1, while the Section 1.2.3 is devoted to the problem of the charmonium production mechanism.

1.2.1 The Charmonium Spectroscopy

The quantum numbers and basic properties of the majority of states in the charmonium family can be, partially, explained by a non-relativistic description of the quark-antiquark pair $c\bar{c}$ [28]. The applicability, in a certain extent, of such a description requires the estimation of the significance of the relativistic effects for charmonia. This can be approximately performed from the masses of the resonances, e.g. the mass difference ΔM between the charmonium ground state (J/ψ) and its first radial excitation (ψ') in units of either of the masses provides an estimate of the relativistic parameter v^2/c^2

$$\frac{v^2}{c^2} \sim \frac{\Delta M}{M} \sim 0.2. \tag{1.15}$$

Such moderate, but not very small magnitude of the relativistic effects, allows to treat the charmonium dynamics in the non-relativistic limit including the relativistic effects as perturbations in powers of v/c.

In a non-relativistic picture, the charmonium states are characterized by three physical variables: the orbital angular momentum L, the total spin S of the quark pair, and finally the total angular momentum J. As usual, the total angular momentum, which defines the particle spin, is given by the vector sum of the orbital and the spin momenta: $\overrightarrow{J} = \overrightarrow{L} + \overrightarrow{S}$. Similarly, the total spin S is the vector sum of the quark and antiquark spins: $\overrightarrow{S} = \overrightarrow{s_c} + \overrightarrow{s_{\bar{c}}}$. S can take the values 0 or 1 and consequently the four possible spin states of the $c\bar{c}$ pair can be splitted into a singlet and a triplet. In addition, due to the excitation of the radial motion of the $c\bar{c}$ pair, the spectrum contains levels, with same L, S and J, differing by the radial quantum excitation number n_r (n_r = 0 corresponds to the lowest state in the spectrum). It has become a common standard to express the values of these quantum numbers for each charmonium state in the form:

$$(n_r + 1)^{(2S+1)}L_J. \tag{1.16}$$

The combination $2S+1$ allows to indicate the spin multiplicity, while the value of L, L = 0, 1, 2, 3, . . . are written, following the standard atomic physics notation, as S, P, D, F, ... The lowest state, corresponding to L = 0, S = 0 and, consequently, J = 0 is represented as 1^1S_0 (η_c resonance) while the first radial excited state (n_r = 1) with the same quantum numbers is 2^1S_0 (η_c' resonance).

Finally, the L value determines the parity (P) for each of the states: $P = (-1)^{L+1}$, while L and S combined together fix the charge conjugation parity: $C = (-1)^{L+S}$.

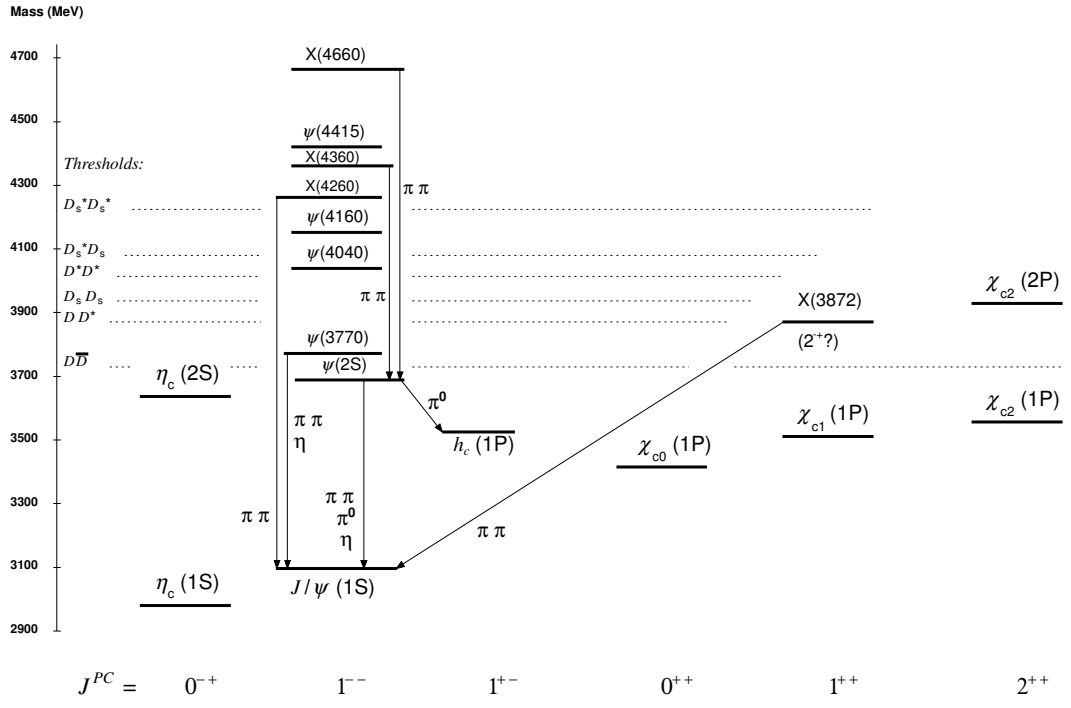

Figure 1.7. *Spectrum and transitions of the known charmonium and charmonium-related family. (from ref. [10]).*

Therefore, the previously mentioned $^1S_0$ states have quantum numbers $J^{PC} = 0^{-+}$ while $^3S_1$ states (J/ψ, ψ', . . .) have $J^{PC} = 1^{--}$, the same quantum numbers as the electromagnetic current (photon). So these charmonium states can be produced in e^+e^- annihilations.

The diagram of the spectrum of the known charmonium and charmonium-related states and their transitions, as of today, is presented in Fig. 1.7. Table 1.2 presents instead a summary of the main characteristics of the observed charmonium states.

Meson	$n\,^{2S+1}L_J$	J^{PC}	**Mass (MeV)**	**Full width** Γ
η_c	1^1S_0	0^{-+}	2981.0 ± 1.1	29.7 ± 1.0 MeV
J/ψ	1^3S_1	1^{--}	3096.916 ± 0.011	92.9 ± 2.8 keV
χ_{c0}	1^3P_0	0^{++}	3414.75 ± 0.31	10.4 ± 0.6 MeV
χ_{c1}	1^3P_1	1^{++}	3510.66 ± 0.07	0.86 ± 0.05 MeV
χ_{c2}	1^3P_2	2^{++}	3556.20 ± 0.09	1.98 ± 0.11 MeV
h_c	1^1P_0	1^{+-}	3525.41 ± 0.16	< 1 MeV
$\eta_c(2S)$	2^1S_0	0^{-+}	3638.9 ± 1.3	10 ± 4 MeV
ψ'	2^3S_1	1^{--}	$3686.109^{+0.012}_{-0.0014}$	304 ± 9 keV

Table 1.2. *Summary of properties of charmonia [10].*

1.2.2 Different types of J/ψ production: prompt, non-prompt and direct

The detection of quarkonia requires the identification of their various hadronic- and leptonic-decay products. Concerning the J/ψ resonance, whose production in proton-proton collisions at $\sqrt{s}$ = 2.76 and 7 TeV is discussed in this manuscript (see Chapter 3 and 4), Table 1.3 shows the possible J/ψ decay modes with the corresponding branching ratios.

Decay Mode	**Fraction** (Γ_i / Γ)
hadrons	(87.7 ± 0.5) %
e^+e^-	(5.94 ± 0.06) %
$\mu^+\mu^-$	(5.93 ± 0.06) %

Table 1.3. *J/ψ(1S) decay modes [10].*

The production of the J/ψ meson can occur in four ways:

- the direct production, i.e. J/ψ produced directly in the initial collision as result of the $c\bar{c}$ pair hadronization through the process (for proton-proton collisions): $pp \to c\bar{c} + X$ where $c\bar{c} \to$ J/ψ.
- the prompt production by decay of χ_c, i.e. J/ψ produced indirectly via radiative decay of χ_c through the process (for proton-proton collisions): $pp \to c\bar{c} + X$ where $c\bar{c} \to \chi_c \to$ J/$\psi + \gamma$;
- the prompt production by decay of ψ', i.e. J/ψ produced indirectly via decay of ψ' ($\psi(2S)$) through the process (for proton-proton collisions): $pp \to c\bar{c} + X$ where $c\bar{c} \to \psi' \to$ J/$\psi + X$;
- the non-prompt production, i.e. J/ψ produced from the decay of b-hadrons through the process (for proton-proton collisions): $pp \to B + X \to$ J/$\psi + X'$;

The total J/ψ production, called *inclusive* production, can therefore be divided into two main components: the *prompt* production, J/ψ produced directly in the initial collisions or from decays of heavier charmonium states, and a *non-prompt* production, J/ψ produced from b-hadron decays.

Figure 1.8 shows recent LHC measurements of f_b, the fraction of J/ψ coming from b-hadron decays as a function of the J/ψ p_{T}. These measurements, performed on proton-proton data at $\sqrt{s}$ = 7 TeV, cover two rapidity domains: mid-rapidity (ALICE [29], ATLAS [30] and CMS [31] results) (a) and forward rapidity (LHCb [32] result) (b).

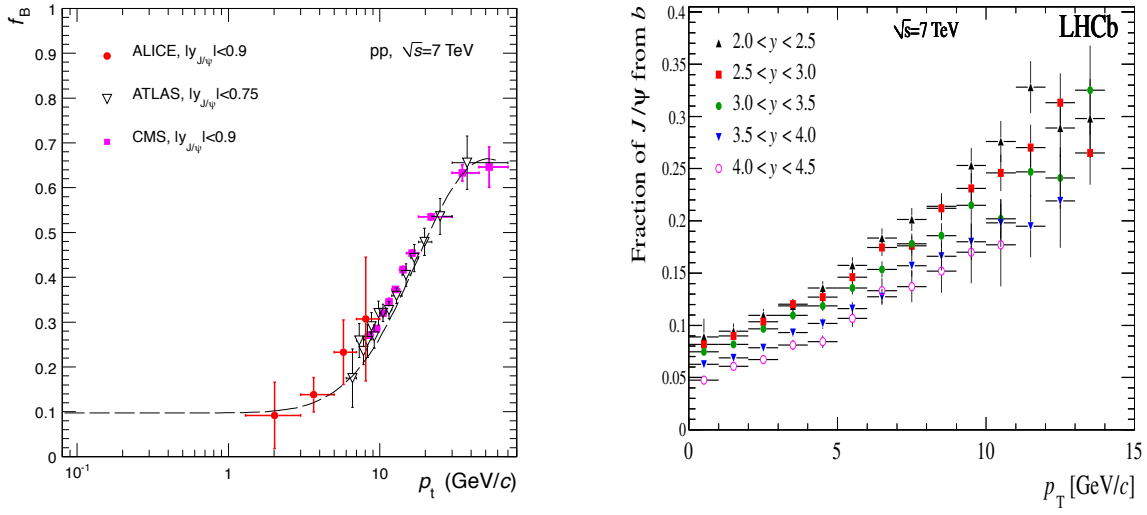

(a) *Mid-rapidity.* (b) *Forward rapidity.*

Figure 1.8. *The fraction f_b of J/ψ from the decay of b-hadrons as a function of p_T of J/ψ in proton-proton collisions at $\sqrt{s}$ = 7 TeV. ALICE [29], ATLAS [30] and CMS [31] results are compared at mid-rapidity (a). LHCb [32] result is plotted in y bins at forward rapidity (b).*

Integrating over the transverse momentum p_{T} and rapidity y, the f_b fraction can be calculated in a specific kinematical region. The ALICE measurement, performed for $p_{\mathrm{T}} > 1.3$ GeV at mid-rapidity ($|y| < 0.9$), gives $f_b = 0.149 \pm 0.037(stat.)^{+0.018}_{-0.027}(syst.)$. The LHCb collaboration obtains in the fiducial region $0 < p_{\mathrm{T}} < 14$ GeV/c and $2 < y < 4.5$, the value[13] f_b = 0.098 $\pm$ 0.001 (stat.) $\pm$ 0.018 (syst.).

For what concerns the prompt J/ψ production, Fig. 1.9 shows the three fractions of J/ψ, with the contribution from the decay of B mesons removed (i. e. direct J/ψ and J/ψ from the decay of χ_c or ψ'), as a function of the J/ψ p_{T}. The data presented were measured by the CDF collaboration at the Tevatron (Fermilab) with proton-antiproton collisions at $\sqrt{s}$ = 1.8 TeV. The analysis was performed on a J/ψ sample with $|\eta_{J/\psi}| < 0.6$ [33].

It was found that the fraction of direct produced J/ψ is $F^{J/\psi}_{direct}$ = (64 $\pm$ 6) % and, as shown in Fig. 1.9, is almost constant from 5 to 18 GeV in p_{T} [34].

[13] In [32], the LHCb collaboration has released the prompt and the non-prompt J/ψ production cross sections. Taking into account that $\sigma^{prompt}_{J/\psi} = (1-f_b)\cdot\sigma_{J/\psi}$ and $\sigma^{non-prompt}_{J/\psi} = f_b\cdot\sigma_{J/\psi}$ being $\sigma_{J/\psi}$ the inclusive J/ψ production cross section, the fraction f_b can be derived as $f_b = \frac{\sigma^{non-prompt}_{J/\psi}}{\sigma^{prompt}_{J/\psi}+\sigma^{non-prompt}_{J/\psi}}$.

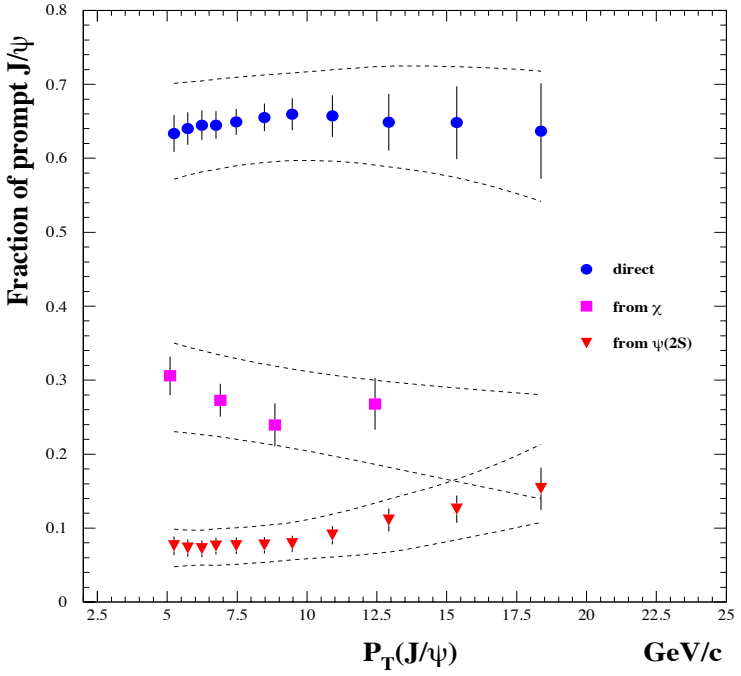

Figure 1.9. *Fractions of J/ψ with the contribution from the decay of B mesons removed. The error bars correspond to the statistical uncertainty. The dashed lines show the upper and lower bounds corresponding to the statistical and systematic uncertainties combined [33].*

1.2.3 Charmonium Production models

From the CDF analysis presented in Fig. 1.9 , we may conclude that the direct production is the principal contribution to the *inclusive* J/ψ production. This section is therefore devoted to various theoretical models describing the direct J/ψ production mechanisms in proton-proton collisions.[14]

Firstly, the so-called factorization theorem has to be discussed being a theoretical concept common to all models which describe the quarkonium production mechanisms. Secondly, for what concerns the identification of the partons within the proton involved in the initial $c\bar{c}$ pair production, we should consider the parton distributions of the proton. Finally, we review various theoretical models which provide an explanation of how the initial partons can form the $c\bar{c}$ pair system which gives the charmonium resonance via hadronization processes.

1.2.3.1 The factorization theorem

The production of heavy quark pairs $c\bar{c}$ (or $b\bar{b}$) in proton-proton collisions, occurring through the interaction of two partons, is a 3-stage process [35].

The first part, before the pp collision takes place, is characterized by non-perturbative conditions relative to the nucleon (proton) structure in term of parton distributions. Then, during the collision, the heavy quark $c\bar{c}$ pairs is created via a hard process that can be treated using a perturbative approach. Actually, the energy scale Q^2 involved in the process is at least $Q^2 \sim (2m_c)^2$ where $m_c = 1.275 \pm 0.025$ GeV is the mass of the charm quark [10]. Therefore the energy scale is much larger than the QCD scale parameter, i. e. $Q^2 \gg \Lambda_{QCD}$, and, consequently, $\alpha_s(Q^2) \ll 1$ allowing a pQCD approach.

[14] Of course, also direct χ_c and ψ' production mechanisms have to be taken into account.

Finally, the last stage consists in the non-perturbative evolution of the $c\bar{c}$ pair into a charmonium resonance (ψ).

The creation of the $c\bar{c}$ pair, in the initial partonic interaction, and the successive hadronization into a charmonium resonance are governed by the following parton-parton cross section:

$$\hat{\sigma}(a+b \to c\bar{c}(^{2S+1}L_J^c) + X \to \psi; \hat{s}, m_c^2, Q^2, \alpha_s(Q^2)), \tag{1.17}$$

where

1. a and b are the two partons involved in the initial proton-proton collision;
2. $\hat{s}$ is the squared center-of-mass energy of the partonic interaction;
3. $^{2S+1}L_J^c$ are the quantum numbers of the produced $c\bar{c}$ pair. c indicates the $c\bar{c}$ color state (singlet or octet);
4. X indicates the other products that might be created in the initial partonic interaction;
5. ψ is the generic charmonium resonance with mass M_ψ produced via hadronization of the $c\bar{c}$ pair. The $c\bar{c}$ pair, evolving through a non-perturbative process into ψ, is referred to as pre-resonance;
6. Q^2 is the transfer momentum of the reaction i. e. the energy scale of the parton-parton scattering;

Actually, the existence of such a 3-stage process is intimately connected to the unique quarkonium properties. A general heavy quarkonium state $Q\bar{Q}$ has mainly three intrinsic momentum (or energy) scales: the heavy quark mass m_Q, the momentum of the heavy quark or antiquark in the quarkonium rest reference frame ($\sim m_Q v$) and the binding energy of the heavy quark-antiquark system which is of order $\sim m_Q v^2$. The quantity v indicates the typical velocity of the heavy quark or antiquark in the quarkonium rest frame ($v^2 \sim 0.3$ for the J/ψ and $v^2 \sim 0.1$ for the Υ). In addition to the intrinsic quarkonium scales, a new energy scale, the already mentioned energy scale $Q^2 \sim (2m_Q)^2$, has to be introduced in the description of the hard-scattering production process of quarkonia.

The initial production of the $Q\bar{Q}$ pair, which would occur at scale $Q^2 \gg \Lambda_{QCD}^2$, can be therefore treated as a perturbative process and involves short distances or, equivalently, time scales of order $1/Q$. On the contrary, the subsequent evolution of the $Q\bar{Q}$ pair into a quarkonium resonance, which would involve smaller dynamical scales ($m_Q v$ and $m_Q v^2$) of order $\sim \Lambda_{QCD}$ and larger distances / time scales $\sim 1/\Lambda_{QCD}$, is a typical non-perturbative QCD process. On the basis of the above considerations, one might expect intuitively that the short-distance, perturbative process at the energy scale Q^2 can be separated from the long-distance, non-perturbative dynamics. Such a property would allow to re-express the parton-parton cross section, shown in Eq. 1.17, as follows

$$\begin{aligned}\hat{\sigma}(a+b \to \psi + X; \hat{s}, m_c^2, Q^2, \alpha_s(Q^2)) = \\ \hat{\sigma}_{pQCD}(a+b \to c\bar{c}(^{2S+1}L_J^c) + X;\ \hat{s}, m_c^2, Q^2, \alpha_s(Q^2)) \times \hat{\sigma}_{npQCD}(c\bar{c}(^{2S+1}L_J^c) \to \psi).\end{aligned} \tag{1.18}$$

The validity of this approach can be proven by demonstrating the so-called *factorization theorem*, where Q^2 defines the factorization scale at which the theorem is applied [36, 37, 38].

This crucial QCD property allows therefore to calculate $\hat{\sigma}_{pQCD}$ as a perturbative expansion in powers of $\alpha_s(Q^2)$ using the standard pQCD approach. The final result is then obtained at a certain

order - leading order (LO), next to leading order (NLO), etc. - by truncating the perturbative series as shown in Eq. 1.19

$$\hat{\sigma}_{pQCD} = \underbrace{\underbrace{\hat{\sigma}_i \cdot \alpha_s^i}_{LO} + \hat{\sigma}_{i+1} \cdot \alpha_s^{i+1}}_{NLO} + ... \tag{1.19}$$

The non-perturbative component of the cross section, $\hat{\sigma}_{npQCD}$, is generally parametrized using a phenomenological approach which can vary from model to model.

1.2.3.2 Proton PDFs (parton distribution function)

The total cross section to produce the charmonium resonance ψ in a proton-proton collision at the center-of-mass energy $\sqrt{s}$, σ_ψ^{pp}, is then obtained by convoluting the partonic cross section, shown in Eq. 1.17, with the parton distribution functions (PDFs) of the interacting protons as follows

$$\sigma_\psi^{pp} = \sum_{a,b} \int\int dx_1 dx_2 \; f_a^p(x_{1,Q^2}) \, f_b^p(x_2, Q^2) \; \hat{\sigma}(a+b \to \psi + X;\, \hat{s}, m_c^2, Q^2, \alpha_s(Q^2)). \tag{1.20}$$

Here, x_1 and x_2 are the fractions of the proton momenta p carried by each parton (a and b respectively) i. e. $x_{1,2} = p_{parton}^{1,2} / p_{proton}^{1,2}$ where 1 and 2 stand for each of the two colliding protons. The total cross section depends on the functions $f_{a,b}^p$, the so-called PDFs[15], which represent the distributions of the fractional momenta $x_{1,2}$ of the partons a and b inside the proton at momentum transfer Q^2.

The total production cross section, expressed using Eq. 1.20, has been obtained within the standard formulation of the parton model called *standard collinear approach*. This approach does not include transverse momenta for the interacting partons[16], i. e. the intrinsic transverse momentum k_T carried by partons is assumed to be negligible being $k_T \ll M_\psi$, and consequently PDFs only depend on one energy scale, the momentum transfer Q^2.

The parton kinematics, under this hypothesis on k_T, can therefore be expressed, in case of proton-proton colliding along the z-axis at the center-of-mass energy $\sqrt{s}$, as follows

$$p_1^{parton} = \frac{1}{2}\sqrt{s}\,(x_1, 0, 0, x_1) \qquad\qquad p_2^{parton} = \frac{1}{2}\sqrt{s}\,(x_2, 0, 0, -x_2), \tag{1.21}$$

where $p_{1,2}^{parton}$ are the parton quadri-momenta in the laboratory reference frame.

At the leading order (LO) , the only two pQCD[17] processes responsible for heavy-quark pair ($Q\bar{Q}$) hadroproduction are quark-antiquark annihilation and gluon fusion, as shown in Fig. 1.10.

[15]The parton distribution function $f^p(x, Q^2)$ is defined as the probability density of finding the parton with a certain fraction x of the proton momentum at the energy scale Q^2. The p label, explicitly shown in the expression $f^p(x, Q^2)$, indicates that the PDF refers to free protons, i. e. protons outside nuclei. On the contrary, if the protons are inside nuclei, their partons have modified distribution functions by the nuclear environment.

[16]Approaches, which include parton transverse momenta, have been developed and are known as k_T-factorization approaches [39]. Within these models, the PDFs depend explicitly on two energy scales: Q^2 and k_T. For this reason they are more generally called *unintegrated parton distribution function* (UPDF), in opposition to the *collinear approach* where PDFs are k_T-independent or - equivalently - integrated over k_T.

[17]In principle, one should also consider the hypothesis of electromagnetic heavy-quark pair production via $q\bar{q}$ annihilation. If this process was the dominant production channel, the J/ψ production rate should be suppressed in $\pi^+ - N$ collisions by a factor ~ 4 with respect to the $\pi^- - N$ collisions due to the different valence quark content for $\pi^+(u\bar{d})$ and $\pi^-(d\bar{u})$. Different experiments obtained that the J/ψ production rate is identical in $\pi^{+/-} - N$ collisions proving that the electromagnetic J/ψ production channel is negligible. The strong interaction is indeed stronger than the electromagnetic one.

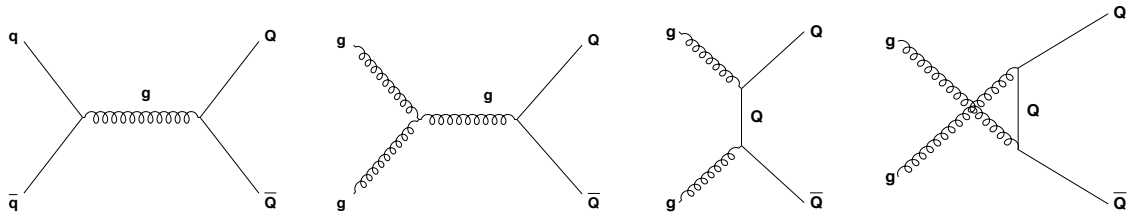

Figure 1.10. *Four leading-order diagrams responsible for heavy-quark pair production in perturbative QCD.*

The process $q\overline{q} \to Q\bar{Q}$ is similar to QED processes, like $e^+e^- \to \mu^+\mu^-$, where the only difference is an overall color factor, while the gluon-gluon fusion $g\overline{g} \to Q\bar{Q}$ is a typical process of pure QCD. Furthermore, it should be mentioned that in $q\overline{q} \to Q\bar{Q}$, the $Q\bar{Q}$ pair is always created in a color-octet state, while in $g\overline{g} \to Q\bar{Q}$ both color-singlet and color-octet are allowed [40].

For LO processes $2 \to 1$, the squared heavy-quark pair invariant mass $M^2_{Q\bar{Q}}$ is equal to the square of the center-of-mass energy, $\hat{s}$, of the initial partons (massless quarks / gluons) and can be re-expressed in term of the fractional momenta as

$$M^2_{Q\bar{Q}} = \hat{s} = x_1 x_2 s, \tag{1.22}$$

where s is the squared proton-proton center-of-mass energy ($\sqrt{s}$ = 2.76, 7 and 8 TeV at LHC). The rapidity y for the $Q\bar{Q}$ system is given by

$$y = \frac{1}{2} ln \left(\frac{E + p_z}{E - p_z} \right) = \frac{1}{2} ln \left(\frac{x_1}{x_2} \right). \tag{1.23}$$

Hence, using Eq. 1.22, we obtain (for $2 \to 1$ processes)

$$x_1 = \frac{M_{Q\bar{Q}}}{\sqrt{s}} e^y \qquad\qquad x_2 = \frac{M_{Q\bar{Q}}}{\sqrt{s}} e^{-y}. \tag{1.24}$$

Therefore, different values of $M_{Q\bar{Q}}$, $\sqrt{s}$ and y allow to probe different values of x_1 and x_2 of the colliding protons. In general, for any value of $M_{Q\bar{Q}}$ and y, in the plot shown in Fig. 1.11 (a) at $\sqrt{s} = 7$ TeV, there will be two (dashed) lines that give the x values at which the protons are probed.

As the x momentum fraction is proportional to the heavy-quark pair invariant mass, it is clear that charmonia probe smaller x than bottomonia[18]. For instance, we can consider the ALICE Muon Spectrometer rapidity acceptance for quarkonia, $2.5 < y < 4$. The explored x-ranges can therefore be roughly calculated using Eq. 1.24[19]. For J/ψ resonances produced (at threshold) in LHC pp collisions at $\sqrt{s}$ = 7 TeV, we obtained the following x-ranges: $5.4{\cdot}10^{-3} < x_1 < 2.4{\cdot}10^{-2}$ and $8.1{\cdot}10^{-6} < x_2 < 3.6{\cdot}10^{-5}$.

The value of proton PDFs in the above mentioned x-range should be taken into account in order to estimate which of the two channels, $q\overline{q} \to Q\bar{Q}$ or $g\overline{g} \to Q\bar{Q}$, dominates the $Q\bar{Q}$ production. In Fig. 1.11 (b), the parton distribution functions inside a proton are plotted showing the different parton contributions: *up* quark (valence + sea), *down* quark (valence + sea), $\overline{up}$ antiquark (sea), $\overline{down}$ antiquark (sea), *strange* quark (sea), *charm* quark (sea) and *gluon* (sea). The quantity $x \cdot f^p(x, Q^2)$,

[18] Due to the proportionality between x and $1/\sqrt{s}$, the x-values that can be explored get smaller when $\sqrt{s}$ increases.

[19] For NLO processes, Eq. 1.24 is not valid.

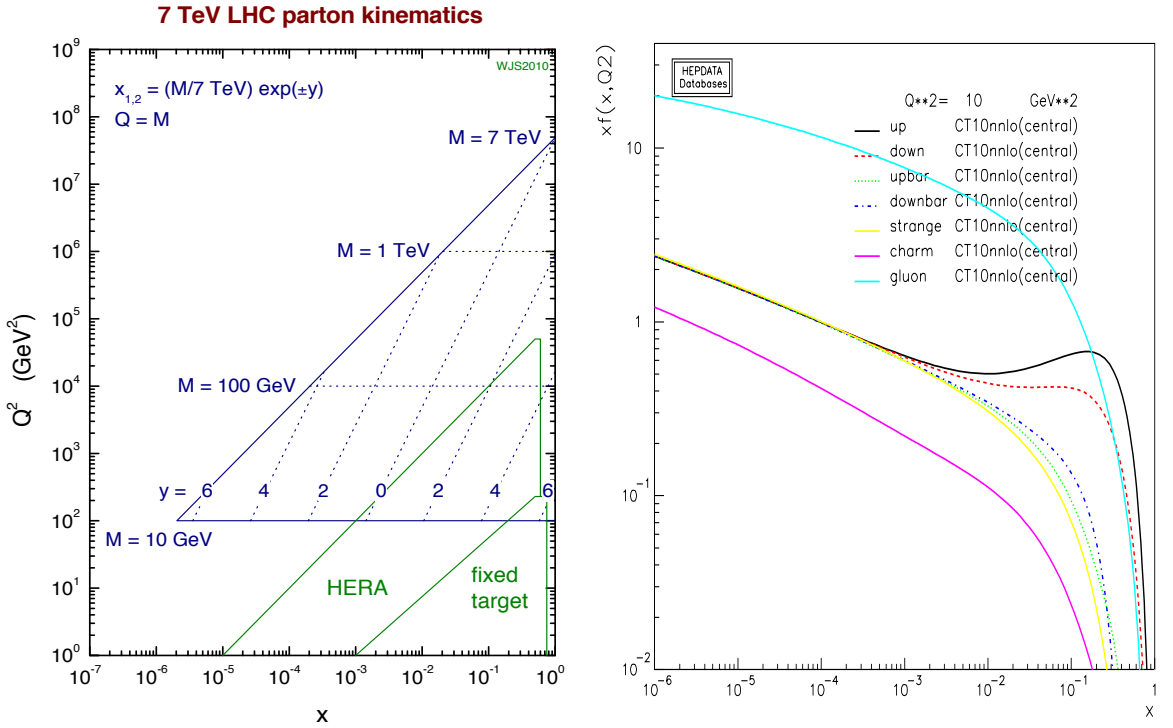

(a) *(Q^2, x) plane showing, in blue color, the area that can be accessible at the LHC center-of-mass energy $\sqrt{s}$ = 7 TeV and for produced resonances with a mass M above 100 GeV (from http://www.hep.phy.cam.ac.uk/~wjs/plots/plots.html).*

(b) *Parton distribution functions inside a proton. The colored curves represent the different partonic contributions (u, d, $\bar{u}$, $\bar{d}$, s, c and g) at energy scale $Q^2 = 10$ GeV. The NNLO CT1O(central) parametrization is used for the PDFs (from http://hepdata.cedar.ac.uk).*

Figure 1.11

plotted as a function of x, has been evaluated at energy scale $Q^2 = 10$ GeV^2, a value relevant for $c\bar{c}$ production, according to the NNLO CT1O(central) parametrization.

It can be immediately verified that, in the x-ranges we can access, the dominant partonic contribution is the gluon distribution, i.e. at low x-values we mostly find gluons. As a consequence, we can state that quarkonium production at LHC energies mainly proceeds via gluon-gluon interaction ($g\overline{g} \to Q\bar{Q}$ at LO).

It is instructive, in relation to the previous statement, to see Fig. 1.12. It shows the relative contribution of gluon fusion to the total $c\bar{c}$ production cross section, as a function of $\sqrt{s}$, as calculated for proton-proton collisions.

The remainder of the total cross section is, at leading order, due to $q\bar{q}$ annihilation. In Fig. 1.12 three different parametrizations (CTEQ6L (2002), GRV98 LO and MRST LO (2001) have been used to describe the parton distributions inside the protons. The contribution from gluon fusion is, already for $\sqrt{s} > 70$ GeV, larger than 90 %.

Once the dominant pQCD process responsible for heavy-quark pair ($Q\bar{Q}$) hadroproduction at LHC energies is known, two points have to be discussed and developed. First of all, concerning the initial perturbative QCD process, we should investigate the main channels (in term of Feynman diagrams) involved in the initial $Q\overline{Q}$ pair creation. Then, the non-perturbative evolution of the $Q\overline{Q}$ pair into a quarkonium state has to be treated in terms of the language of QCD effective theories.

Different hypothesis on the perturbative and non-perturbative components lead therefore to var-

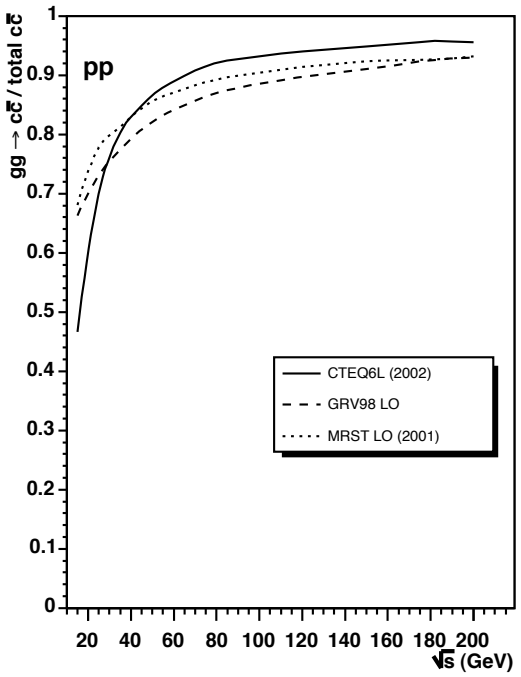

Figure 1.12. *Relative contribution of gluon fusion to the total $c\bar{c}$ production cross section, as a function of $\sqrt{s}$, in pp collisions [41].*

ious theoretical models for quarkonium production. Most notable among these are the color-singlet model (CSM), the color-evaporation model (CEM) and the non-relativistic QCD (NRQCD) approach, explained in their main features in the following sections.

1.2.3.3 Color-singlet Model (CSM)

The color-singlet model was first proposed shortly after the J/ψ discovery. The central hypothesis of the CSM consists in the assumption that the non-perturbative $Q\bar{Q}$ pair evolution into the quarkonium resonance occurs without any modification of its quantum numbers (spin S, angular-momentum L and color c). Therefore, in order to produce a quarkonium state, the $Q\bar{Q}$ pair must be generated with the quarkonium quantum numbers, and, in particular, the pair has to be created in a color-singlet state (c=1). This explains the name Color-single Model (CSM).

The non-perturbative evolution of the $Q\bar{Q}$ pair, which involves the non-perturbative transition

$$|\,Q\bar{Q}\,(^{2S+1}L_J^{c=1})\,> \rightarrow\ |\,\psi\,(^{2S+1}L_J^{c=1})\,>, \tag{1.25}$$

occurs via emission of low energy (soft) gluons.

The total cross section of the partonic process $a+b \rightarrow \psi + X$ can be derived under two important approximations. The first one concerns the so-called *factorization theorem*. As already mentioned in Section 1.2.3.1, if one assumes that the quarkonium production can be decomposed in two steps clearly separated in time, first the creation of the heavy-quark $Q\bar{Q}$ pair and then their binding to make the meson, the total cross section can, consequently, be factored into two components. In the second approximation, the velocity of the heavy-quarks (charm and bottom quarks) in the meson is assumed to be negligible. We can therefore suppose that the quarkonium resonances are created with their two constituent quarks at rest in the meson reference frame. This is known as *static approximation*.

In the end, the total cross section of the process $a+b \to \psi + X$ can be expressed as

$$\hat{\sigma}(a+b \to |\psi(^{2S+1}L_J^{c=1}) > +X) = \hat{\sigma}_{pQCD}(a+b \to |c\bar{c}(^{2S+1}L_J^{c=1}) > +X) \times \left| \frac{d^l}{dr^l} R_{nl}^{\psi}(0) \right|^2, \quad (1.26)$$

where $\hat{\sigma}_{pQCD}(a+b \to |c\bar{c}(^{2S+1}L_J^{c=1}) > +X)$ is the term calculable in pQCD, while $\left| \frac{d^l}{dr^l} R_{nl}^{\psi}(0) \right|^2$ parametrizes the non-perturbative component. The last term contains the function $R_{nl}^{\psi}(\overrightarrow{r})$ which is the color-singlet $c\bar{c}$ wave-function in coordinate space for ψ. The production cross section for each quarkonium resonance ψ is therefore related to the absolute values of the $c\bar{c}$ wave-function and its derivatives (the degree depends on the L value[20]) evaluated at the origin ($\overrightarrow{r} = 0$), i.e. zero $c\bar{c}$ separation.

The $c\bar{c}$ wave-function[21] is connected to the amplitude of the transition shown in Eq. 1.25 which cannot be calculated in pQCD being a non-perturbative process. This quantity is therefore extracted from experimental measurements of quarkonium decay rates. Once this extraction has been carried out, the CSM has no other free parameters: for each charmonium state, $R_{nl}^{\psi}(0)$ is actually the only phenomenological parameter.

For what concerns the perturbative term $\hat{\sigma}_{pQCD}(a+b \to |c\bar{c}(^{2S+1}L_J^{c=1}) > +X)$, it can be calculated as a perturbative expansion in powers of α_s using the standard pQCD methods. The final result is then obtained at a certain order - leading order (LO), next-to-leading order (NLO), next-to-next-to-leading order (NNLO), etc. - by truncating the perturbative series. In the original formulation of CSM, the dominant process is the gluon fusion [22]. Figure 1.13 and 1.14 show representative Feynman diagrams that contribute to the $c\bar{c}$ hadroproduction, via gluon fusion, at order α_s^2 and α_s^3, respectively.

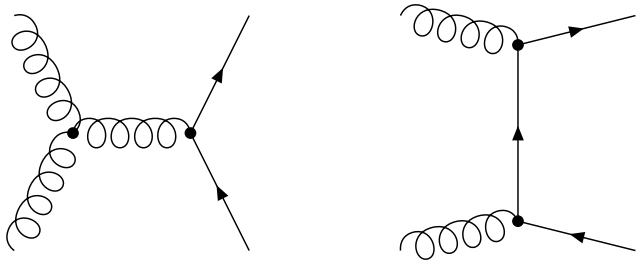

Figure 1.13. *Representative diagrams that contribute to the $c\bar{c}$ hadroproduction, via gluon fusion, at order α_s^2.*

In more detail, both diagrams shown in Fig. 1.13 can produce pre-resonance $c\bar{c}$ states in only two quantum number configurations $^{2S+1}L_J$: $^1S_0$ and ^3P_J. As for the color state, both color-singlet and

[20] For example, $l = 0$ for S-wave, $l = 1$ for P-wave, etc. .

[21] Due to the heavy masses of the constituent quarks (charm and bottom), quarkonium spectroscopy can be studied reasonably well in non-relativistic potential theories. The color potential of the $Q\bar{Q}$ system can be represented phenomenologically (at temperature T = 0 K) by the sum $V(\overrightarrow{r}) = \sigma|\overrightarrow{r}| - \frac{\alpha}{|\overrightarrow{r}|}$ where the second term is the coulombian contribution, induced by gluon exchange between the quark and the antiquark, while the first term is the confinement one. The color-singlet $Q\bar{Q}$ wave function can be derived within these non-relativistic static potential theories.

[22] Actually, for charmonia produced at high transverse momentum, $p_T \gg M_\psi$, the gluon fragmentation results to be the dominant process.

color-octet are allowed by the two diagrams. Furthermore, within the *standard collinear approach,* which assumes the initial parton momenta collinear to the proton ones, these diagrams imply that the $c\bar{c}$ system is created with a transverse momentum $p_T = 0$, due to the 4-momenta conservation.

On the contrary, for what concerns the three diagrams shown in Fig. 1.14, only the following quantum number configurations $^{2S+1}L_J$ are allowed for the pre-resonance $c\bar{c}$ states : $^1S_0$, $^3S_1$,^3P_J (a), $^1S_0$, ^3P_J (b) and $^1S_0$, ^3P_J (c). As previously mentioned, both color-singlet and color-octet states can be produced by the three diagrams. Finally, within the *standard collinear approach*, the three diagrams at order α_s^3 allow a non-zero transverse momentum p_T for the $c\bar{c}$ system. In fact, the transverse momentum carried by the gluon in the final state counterbalances the p_T of the $c\bar{c}$ pair.

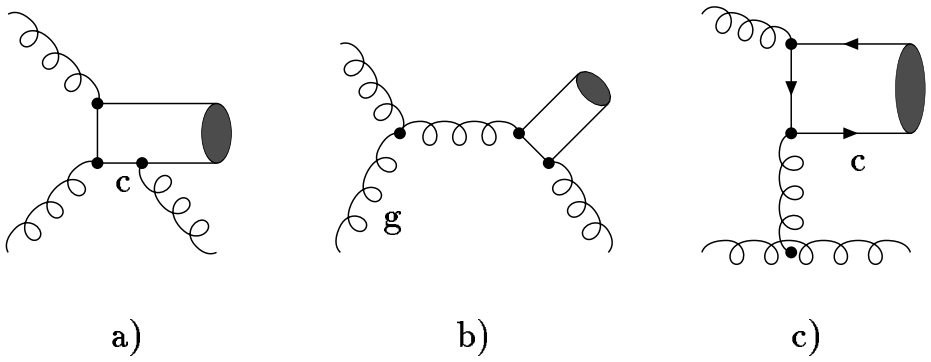

Figure 1.14. *Representative diagrams that contribute to the $c\bar{c}$ hadroproduction, via gluon fusion, at order α_s^3.*

In conclusion, remembering the quantum number configuration for J/ψ (and ψ') $^{2S+1}L_J = {}^3S_1$, we obtain that, in the color-singlet model at leading order (CSM LO), the only diagram which contributes to the direct J/ψ (and ψ') production is the diagram, at order α_s^3, shown in Fig. 1.14 (a).

1.2.3.4 Color-evaporation model (CEM)

The color-evaporation model was first introduced at the end of the 70s. Contrary to the CSM, the heavy-quark pair $c\bar{c}$ is not necessary produced in a color-singlet state. Actually, the CEM does not specify the quantum numbers (spin S, angular-momentum L and color c) of the pre-resonance $c\bar{c}$ state that can be produced without any constraints on the color or spin of the final state. Therefore, both color-singlet and color-octet states are allowed in the CEM which does not provide the fraction of $c\bar{c}$ pairs produced in the two color states. In case of $c\bar{c}$ pairs produced in color-octet state, the CEM assumes that the neutralization of the color occurs via interaction with the collision-induced color field: the exchange of gluons determines a color evaporation which explains the model's name.

The final asymptotic $c\bar{c}$ state (resonance), in term of spin and color, is therefore randomized by numerous soft interactions occurring during the non-perturbative process of hadronization, and, as a consequence, it is not correlated with the quantum numbers of the $c\bar{c}$ pair initially produced. As an example of the CEM features, the production of a $^3S_1$ state (J/ψ, ψ', ...) by one gluon is possible, whereas in the CSM it was forbidden by color conservation.

The first hypothesis of the color-evaporation model is that the probability for the initial $c\bar{c}$ pair to evolve into a charmonium state ψ is given by a constant $f_{c\bar{c}\to\psi}$ that is energy-momentum and process independent. Within the CEM, the $f_{c\bar{c}\to\psi}$ probability is therefore an universal constant in any kinematic region ($\sqrt{s}$, y, p_T) and for any process ($p+p$, $p+A$, $\pi+A$, $e+p$, ...). In addition, the

$f_{c\bar{c}\to\psi}$ probability, being determined by non-perturbative processes, is non calculable in pQCD and requires an estimation from experimental data.

Once the $f_{c\bar{c}\to\psi}$ probability is known for each state ψ_i of the charmonium family, it can be written

$$\sum_i f_{c\bar{c}\to\psi_i} = 1. \tag{1.27}$$

These probabilities can also be interpreted as the fractions of the total $c\bar{c}$ production cross section responsible for the production of the different charmonium states. In case of J/ψ production in proton-proton collisions at center-of-mass energy $\sqrt{s}$, we have

$$\sigma^{pp}_{\mathrm{J}/\psi}(s) = f_{c\bar{c}\to\mathrm{J}/\psi} \cdot \sigma^{pp}_{c\bar{c}}(s). \tag{1.28}$$

Hence, the most basic prediction of the CEM is that the ratio of the production cross sections for any charmonium state is a constant, independently from the process and the kinematic region. Considering two general reactions, $A+B$ and $A'+B'$, we obtain

$$\frac{\sigma^{A+B}_{\psi_i}(s)}{\sigma^{A'+B'}_{\psi_j}(s)} = \frac{f_{c\bar{c}\to\psi_i}}{f_{c\bar{c}\to\psi_j}} = const. \tag{1.29}$$

Despite some experimental confirmations[23], variations in these ratios have been observed: for example, the ratio between the production cross sections of χ_c and J/ψ varies consistently in photoproduction and hadroproduction. Such variations present a serious challenge to the applicability of the CEM as a quantitative model for quarkonium production. Nevertheless, the model is still widely used as benchmark.

In order to obtain the total production cross section for the charmonium state ψ in pp collisions, $\sigma^{pp}_{\psi}(s)$, one should evaluate, as follows from Eq. 1.28, the total $c\bar{c}$ production cross section $\sigma^{pp}_{c\bar{c}}(s)$. The CEM assumes that every produced $c\bar{c}$ pair evolves into a charmonium resonance if it has an invariant mass below the threshold for producing the pair $D\bar{D}$, where D is the lowest mass meson containing heavy quark c and $\bar{c}$. In other words, every $c\bar{c}$ pair is supposed to evolve into a meson pair $D\bar{D}$ when the $c\bar{c}$ invariant mass is larger than $2m_D$, with m_D being the D meson mass[24].

The total production cross section for the charmonium state ψ in pp collisions can be therefore expressed as

$$\sigma^{pp}_{\psi}(s) = f_{c\bar{c}\to\psi} \cdot \sum_{a,b} \int_{(2m)^2_c}^{(2m_D)^2} d\hat{s} \int\int dx_1 dx_2 \, f^p_a(x_1, Q^2) \cdot f^p_b(x_2, Q^2) \cdot \frac{d}{d\hat{s}} \hat{\sigma}_{pQCD}(a+b \to c\bar{c}+X; \hat{s}, Q^2), \tag{1.30}$$

where $\hat{s} = x_1 x_2 s$. The quantity $\hat{\sigma}_{pQCD}(a+b \to c\bar{c}+X; \hat{s}, Q^2)$ represents the partonic cross section for the inclusive $c\bar{c}$ production in a general state with quantum numbers $^{2S+1}L^{(c)}_J$. Since CEM does

[23] The validity of the CEM prediction is confirmed, up to a certain extent, for J/ψ and ψ' production in several hadronic collisions $p+A$.

[24] Actually, it is possible to produce a meson pair $D\bar{D}$ even if the $c\bar{c}$ invariant mass is less than the $D\bar{D}$ threshold, $2m_D$. In this case, the additional energy, required to create the heavy-flavour meson pair, can be obtained from the non-perturbative color field. Thus, the sum of the fractions $\sum_i f_{c\bar{c}\to\psi_i}$ can be less than unity.

not specify these quantum numbers, the sum over all the possible values for the spin S, the angular-momentum L and the color c is required to get $\hat{\sigma}_{pQCD}(a+b \to c\bar{c}+X;\hat{s},Q^2)$[25].

1.2.3.5 Non-Relativistic QCD (NRQCD) factorization approach

As briefly discussed in Section 1.2.3.1, the quarkonium system involves several different energy scales that are separated by the velocity v of the two heavy-quarks forming the $Q\bar{Q}$ bound state as a consequence of the small v value. The first scale is set by the heavy quark mass m_Q which fixes the energy scale ($Q^2 \sim (2m_Q)^2$) and the typical distance range ($\sim 1/m_Q$) for $Q\bar{Q}$ pair creation. The heavy constituent's typical momentum $m_Q v$, which is inversely proportional to the $Q\bar{Q}$ state's spatial size, represent the second scale. Finally, the third scale is given by the kinetic energy $m_Q v^2$ which determines the constituent's interaction time (typical hadronization time of order $\sim 1/m_Q v^2$).

As $m_Q \to \infty$, the heavy quark velocity v tends towards zero[26]. Thus, if m_Q is sufficiently large, the heavy quark and antiquark can be considered non-relativistic and, being $v \ll 1$, the three energy scales become well-separated:

$$(\Lambda_{QCD})^2 \sim (m_Q v^2)^2 \ll (m_Q v)^2 \ll m_Q^2. \tag{1.31}$$

This hierarchy is well realized for bottomonia ($v_b^2 \sim 0.1$) and reasonably good for charmonia ($v_c^2 \sim 0.3$). As shown in Eq. 1.31, the QCD scale Λ_{QCD}, associated with non-perturbative effects involving gluon and light quarks, and $m_Q v^2$ are comparable for both charmonia and bottomonia.

The presence of these different (space / energy / time) scales allows to interpret the quarkonium production in terms of two distinct stages: the initial $c\bar{c}$ production, involving a short-distance / high-energy scale, and the $c\bar{c}$ hadronization into the final ψ resonance characterized by a long-distance / low-energy scale. This features can be formally demonstrated in the so-called *factorization theorem*. It states that the two stages, involved in the quarkonium production, can be treated separately, using perturbative QCD methods for the initial partonic hard process and a non-perturbative QCD approach for the final hadronization.

A convenient way to carry out this separation, keeping track of the scale hierarchy, can be represented by the QCD effective field theory formalism called non-relativistic Quantum Chromodynamics (NRQCD). NRQCD consists of a non-relativistic Schrödinger field theory for the heavy quark and antiquark (charm and bottom) that is coupled to the usual relativistic field theory for light quarks and gluon. The theory reproduces full QCD accurately at momentum scales of order $m_Q v$ and smaller.

NRQCD, as discussed in the following, is based upon a double power series expansion in the strong interaction coupling constant α_s and the velocity parameter v. Short distance processes which involve energy scale comparable to or greater than the heavy quark mass m_q can be treated with a perturbative computation within the effective theory. On the contrary, long distance effects are described in term of matrix elements, scaling with the heavy-quark velocity v, of NRQCD operators. The matrix element values are not calculable within the NRQCD theory and must be determined from experiment or lattice QCD calculations. In NRQCD, interactions involving the two energy scales can therefore be separated and power counting rules allow to determine the dominant contributions to various processes .

Due to the large masses of the charm and bottom quarks, quarkonium states can be approximately described as non-relativistic bound states of a heavy quark and antiquark $Q\bar{Q}$ in a static gluon field that

[25] Due to the absence of any correlation, in term of quantum numbers, between the initial $c\bar{c}$ pair and the final ψ charmonium resonance, the CEM is not able to give any predictions on the degree of polarization of the resonance.

[26] The typical velocity v of the two heavy-quarks forming the $Q\bar{Q}$ bound state decreases as the heavy quark mass m_Q increases. For large enough m_Q, v results to be proportional to the running coupling $\alpha_s(m_q^2)$, and it therefore decreases asymptotically $\sim 1/log(m_Q)$.

sets up a static confining potential (e. g. $V(\overrightarrow{r}) = \sigma|\overrightarrow{r}| - \frac{\alpha}{|\overrightarrow{r}|}$, where $\sigma|\overrightarrow{r}|$ is the confinement term). Although this simple picture had many phenomenological success, it fails to take into account gluons inside a quarkonium resonance with wavelengths much greater than the bound state's characteristic size ($1/m_Q v$). The presence of such low energy gluons, which is included in NRQCD approach, implies that the quarkonium state cannot always be regarded as residing in a color-singlet configuration. Actually, within NRQCD, the physical quarkonium state results to be a superposition of different states (both color-single and color-octet states are allowed) in a velocity v expansion.

For instance, the Fock state decomposition of the $J/\psi(^3S_1)$ wave function, at order $\mathcal{O}(v^2)$, can be written as

$$\begin{aligned}|J/\psi\rangle = {} & \mathcal{O}(1)\left|c\bar{c}\left[^3S_1^{(1)}\right]\right\rangle + \mathcal{O}(v)\left|c\bar{c}\left[^3P_J^{(8)}\right]g\right\rangle + \\ & \mathcal{O}(v^2)\left|c\bar{c}\left[^1S_0^{(8)}\right]g\right\rangle + \mathcal{O}(v^2)\left|c\bar{c}\left[^3S_1^{(1)}\right]gg\right\rangle + \mathcal{O}(v^2)\left|c\bar{c}\left[^3S_1^{(8)}\right]gg\right\rangle + \ldots\end{aligned} \tag{1.32}$$

The quantum numbers $^{2S+1}L_J^{(c)}$ of the J/ψ state within the various Fock components are indicated inside the square brackets where the superscripts (1) and (8) indicate the color state of the $c\bar{c}$ pair. The $\mathcal{O}(v^n)$ factors give the order in the velocity expansion at which the corresponding Fock state participates to the quarkonium production. As shown in Eq. 1.32, the $c\bar{c}$ pair in its first Fock component, at order $\mathcal{O}(1)$, has precisely the same angular momentum and color quantum numbers as the full physical J/ψ state.

Within the NRQCD framework, the inclusive cross section for the direct production of a charmonium state H can therefore be written in the following factorized form

$$\sigma(H) = \sum_n \sigma_{c\bar{c}[n]}(\Lambda)\left\langle \mathcal{O}_n^H(\Lambda)\right\rangle, \tag{1.33}$$

where

- Λ is the ultraviolet cutoff of the effective theory;
- $\sigma_{c\bar{c}[n]}$ are the short-distance coefficients and are expressed as expansions in powers of v. They represent the perturbatively calculated partonic cross sections $\sigma(a+b \to c\bar{c}[n]+X)$ describing the production of a $c\bar{c}$ pair in an intermediate Fock state n (S, L and c) convoluted with the parton distribution functions which are quantities depending on the non-perturbative dynamics of the initial colliding hadrons;
- $\left\langle \mathcal{O}_n^H(\Lambda)\right\rangle$ are the matrix elements of the NRQCD four-fermion operators $\mathcal{O}_n^H(\Lambda)$, i. e. the vacuum-expectation values $\left\langle \mathcal{O}_n^H(\Lambda)\right\rangle = \left\langle 0\left|\mathcal{O}_n^H(\Lambda)\right|0\right\rangle$ of the NRQCD operators. Those non-perturbative quantities, called Long Distance Matrix Elements (LDMEs), describe the transition of the intermediate $c\bar{c}$ state (Fock state n) into the physical charmonium resonance H, occurring via soft gluon radiation emission. NRQCD predicts each of the LDMEs to scale with a power of the velocity v.
- n runs over all the possible color and angular momentum states of the $c\bar{c}$ pair.

Unlike the CSM and the CEM which depend on few free parameters, the NRQCD quarkonium production cross section depends on an infinite number of unknown matrix elements. However, when Eq. 1.33, which is a double expansion in powers of v and α_s, is truncated at a fixed order in v only few matrix elements enter in the calculation. The validity of the NRQCD approach requires the validity

of such a truncation and also the perturbative calculability of the quarkonium cross section, conditions verified in the limit $\Lambda_{QCD}/m_Q \to 0$. Moreover, the NRQCD matrix elements have the important property of being universal, i.e. process independent, which greatly increases the prediction power of the theory.

In case of $H = J/\psi$, the leading order contribution in the v expansion (see Eq. 1.32) is $n = {}^3S_1^{[1]}$ which correspond to the color-singlet model[27] contribution at LO (α_s^3). The leading relativistic corrections, instead, are made by $n = {}^1S_0^{[8]}$, ${}^3S_1^{[8]}$, ${}^3P_J^{[8]}$. They are the so-called color-octet (CO) contributions.

1.3 Quarkonia as a probe of the Quark-Gluon Plasma

The study of quarkonium production in pp collisions is an important test of QCD calculations provided by several theoretical models which have been discussed in Section 1.2. In particular, the measurements in the new energy regime of the LHC are crucial for a deeper insight into the physics involved in quarkonium hadroproduction processes and for a more general understanding of elementary particle interactions.

In addition to this, quarkonia represents also one of the most powerful tools to probe the nature of the medium produced in heavy-ion collisions. Such strongly interacting hadronic matter, created at extreme temperatures and energy densities, is supposed to undergo a transition from an ordinary color-confined hadronic phase to a plasma of deconfined colored quarks and gluons (QGP). In this section, after a brief explanation of what is QGP and of why it is studied in heavy-ions collisions, the importance of quarkonia for this study is discussed showing the most relevant experimental results.

1.3.1 Quark-Gluon Plasma

The existence of a deconfined phase of hadronic matter at extreme temperatures and energy densities has been conjectured long ago on the basis of the key features of the strong interaction, asymptotic freedom and confinement [42]. Afterward, such hypothesis has also received ample support from QCD simulations on the lattice [43, 44].

Theoretical results from lattice QCD theory indicate that when the distance scale is comparable to the size of the hadron, the quarks interact with an effective strength which goes approximately linearly with the spatial separation. Since the interaction strength increases with the distance, it becomes impossible to isolate a quark by separating it from its partner inside the hadron: this is the origin of quarks confinement. However, for systems with sufficiently high energy densities (of the order of 1 GeV/fm^3), the hadrons overlap and are compressed so much that their constituents can freely move inside the system without being confined inside hadrons. Furthermore, due to the asymptotic freedom, if the energy density becomes very large, the interaction strength between quarks and gluons becomes weak and the formed system, called Quark-Gluon Plasma, can be described as made of deconfined quarks and gluons.

Some of the lattice QCD results are displayed in Fig. 1.15. On the left, it is displayed the potential between two static quarks as a function of the distance r between them. The solid black line is the potential predicted at zero temperature which shows a linear rise at large distance, i.e. a sign of quark confinement. The dotted colored lines show instead the same potential at increasing temperatures. The main property is that, while the short distance behavior is not much affected, the linearly increasing tail eventually disappears. This allows to state that above a certain temperature, it costs only a finite amount of energy to separate the two quarks.

[27] Color-singlet model is obtained by dropping all color octet contributions in Eq. 1.33.

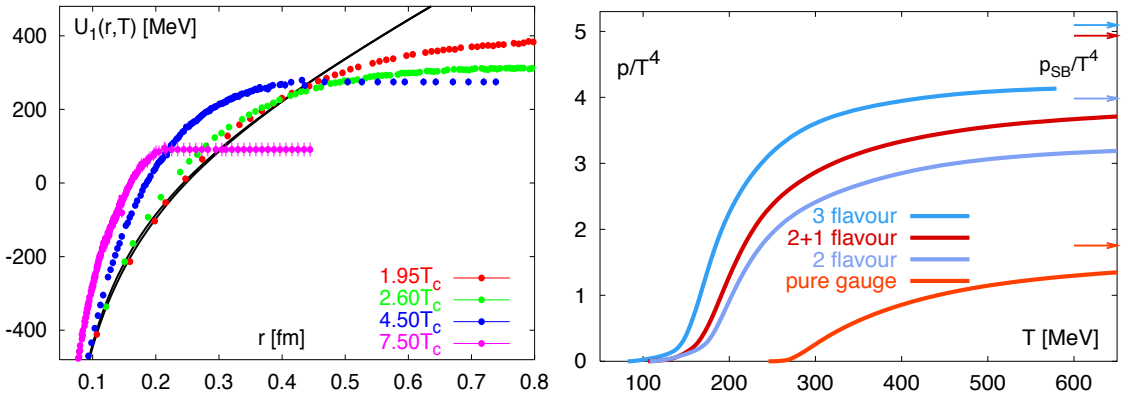

Figure 1.15. *Lattice QCD results. Left: quark potential as a function of the separation r at various temperatures. Right: pressure as a function of temperature (from [45]).*

Another hint for the occurrence of a phase transition, above a certain temperature, is shown in the right plot of Fig. 1.15. It shows, for a given system, the pressure as a function of temperature. It can be noticed that the pressure rises very rapidly at a certain temperature (the value of which depends on the quark content of the theory and it is of the order of 200 MeV), indicating a sudden increase in the number of degrees of freedom of the system. This is interpreted as a transition from hadronic bound states to a plasma of deconfined quarks and gluons.

The energy density and temperature conditions leading to the QGP formation are expected to have taken place in the first phases of the early universe, few micro-seconds after the Big-Bang. This explains why the study of the QGP is of great interest not only in particle physics, but also in astrophysics and cosmology.

1.3.2 Phenomenology of heavy-ion collisions

The formation of a plasma of deconfined quarks and gluons requires extreme conditions of energy density. They can be recreated in laboratory in high-energy heavy ion collisions [46]. The multiple collisions between the constituent nucleons (protons and neutrons) allow to deposit a large amount of energy in a small region, that is the fundamental requirement for the occurrence of the phase transition.

The new state of matter, created in ultra-relativistic heavy-ion collisions, can be described in terms of a thermodynamic-based formulation. Two fundamental properties are satisfied in such collisions. Firstly, the number of constituents of the system is large enough, so that the system can be described by means of macroscopic variables. Secondly, the system's lifetime is longer compared to the typical time-scales of the strong interactions ($\sim$ 1 fm/c) in order to eventually reach a thermodynamic equilibrium.

During the nucleus-nucleus collisions, the nucleons loose a substantial fraction of their energy and are therefore slowed-down. The energy lost by the nucleons is deposited in an extended volume, i.e. large compared to the typical hadronic size, so that thermodynamical concepts can be applied. If the created energy density is larger than the critical one, the formation of a Quark-Gluon Plasma is allowed. As schematically shown in Fig. 1.16, the standard evolution of a high-energy nucleus-nucleus collision involves several stages [45]:

- **pre-equilibrium:** hard and soft processes occur during the initial parton scatterings. The hard processes, that account for the hard particles in the final state (jets, heavy quarks, ...), take place

at extremely short time scales ($\tau \sim 0$ fm/c) and can be calculated using the standard tools of perturbative QCD. The soft processes instead, which give origin to the majority of the particles in the final state (99% of the multiplicity in a collision at RHIC[28] is made of particles with $p_{\mathrm{T}} \leq 2$ GeV/c) take place slightly later ($\tau \sim 0.2$ fm/c);

- **equilibrium:** at sufficiently high energy densities the medium, a deconfined phase of quarks and gluons (QGP), eventually reaches a state of local thermal equilibrium which can be described by hydrodynamics;
- **hadronization:** the expanding medium cools down and reaches a critical temperature T_c where hadrons are formed. Below T_c, the quarks and gluons becomes again confined into hadrons;
- **freeze-out:** the expansion of the medium and the consequent temperature fall lead first to a reduction of the inelastic interactions among hadrons, until the relative abundance of hadron species is fixed (chemical freeze-out), and finally to the turn-off of any elastic interaction fixing the kinematic spectra (kinetic freeze-out).

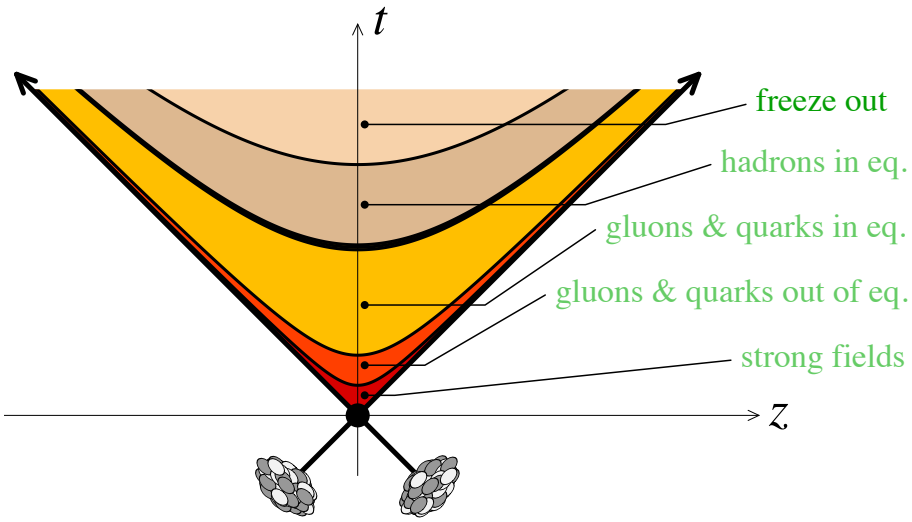

Figure 1.16. *Successive stages of the collision of two nuclei (from [45]).*

In order to characterize the hot and dense medium created in the early stages of the collision, different experimental probes have to be considered. They can be classified into two classes: early and late signatures. The abundances and spectra of hadrons made of light quarks (u and d), for example, belong to the latter category and can provide useful information on the hadronization and freeze-out stages of the collision. On the other hand, thermal photons produced in the plasma and heavy flavors and quarkonia constitute early probes of the medium.

1.3.3 Quarkonium suppression

The Quark-Gluon plasma is, by definition, a medium made of deconfined and hence colored gluons, quarks and anti-quarks. One of the peculiar features of an electromagnetic plasma is the *Debye*

[28] The Relativistic Heavy Ion Collider (RHIC, http://www.bnl.gov/rhic/) at BNL (Brookhaven National Laboratory) delivered Au-Au collisions at $\sqrt{s_{NN}} = 200$ GeV.

charge-screening, which reduces the long-range Coulomb potential in vacuum to a much shorter-range screened in-medium form. The electric fields are therefore screened by the presence of mobile charge carriers. In a plasma of color-charged constituents, a similar property is expected.

The study of quarkonium production in heavy-ion collisions represents one of the most powerful tools to probe such property of the medium. Quarkonia are a special kind of hadrons: they are bound states of a heavy (c or b) quark and its antiquark. Due to the heavy masses of the constituent quarks ($m_c \approx 1.275$ GeV and $m_b \approx 4.18$ GeV [10]), quarkonium spectroscopy (see Section 1.2.1) can be studied in non-relativistic potential theories. Within this approach, the color potential of the $Q\bar{Q}$ pair can be described phenomenologically (at temperature $T = 0$ K) by the sum of a confining linear potential and a Coulomb potential [47]:

$$V(\vec{r}) = \sigma|\vec{r}| - \frac{\alpha}{|\vec{r}|}. \tag{1.34}$$

When quarkonia are created inside the Quark-Gluon Plasma, the $Q\bar{Q}$ system is affected by the presence of the deconfined medium. On the one hand, the QGP alters the confinement contribution which vanishes at the onset of deconfinement. On the other hand, the presence of deconfined color charges leads to the screening of the coulombian term of the potential $V(\vec{r})$. The long-range Coulomb type interaction is therefore modified into a short-range Yukawa type one as shown in Eq. 1.35:

$$V(\vec{r}) = -\frac{\alpha}{|\vec{r}|} \cdot e^{-|\vec{r}|/r_D}, \tag{1.35}$$

where r_D is the Debye or screening radius which decreases with increasing medium temperature T. The fate of the quarkonium states in the deconfined medium depends therefore on the relative size of the color screening radius: if $r_D \gg r_Q$ (radius of the $Q\bar{Q}$ system), the medium does not affect the binding of the two heavy quarks. Once $r_D \ll r_Q$, however, the color charge between the two heavy quarks is screened by the presence of the surrounding deconfined quarks and gluons and hence the bound state will melt [48]. Quarkonia are therefore expected to survive in the QGP for temperatures $T \lesssim T_c$ while, for $T \gg T_c$, the $Q\bar{Q}$ pair dissociates into a separate Q and $\bar{Q}$ in the plasma, which subsequently can hadronize by combining with light quarks.

Since the different quarkonium states have different radii and binding energies, quarkonia will follow a sequential suppression pattern for increasing medium temperature. First, the larger and more loosely bound excited states are dissolved, finally the small and tightly bound ground states. Figure 1.17 illustrates the sequential suppression for the charmonium family.

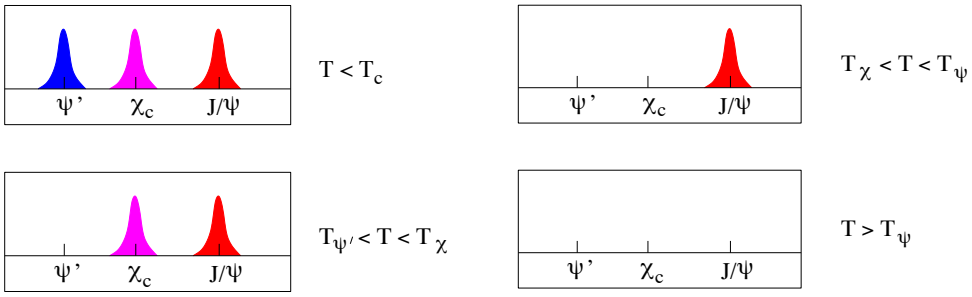

Figure 1.17. *Charmonia as thermometer (from [42]).*

The binding energies of the $\psi(2S)$, $\chi_c(1P)$ and J/ψ(1S) are, respectively, $\triangle E = 0.05, 0.20, 0.64$ GeV corresponding to decreasing radii $r_Q = 0.9, 0.72, 0.5$ fm [47]. The different charmonium states

are then expected to have different melting temperatures in a QGP. Hence the analysis of in-medium quarkonium dissociation can provide a QGP thermometer.

Such behavior has been recently confirmed by finite temperature lattice QCD studies which allow a direct spectral analysis of quarkonia. In Fig. 1.18, the spectral functions $\sigma(M,T)$, describing the distribution in mass M at temperature T, are shown for the J/ψ and the χ_c resonances. The resulting functions, plotted at different temperatures, prove that the spectrum for the ground state J/ψ remains essentially unchanged even at $1.5T_c$, while at $3T_c$ it has completely disappeared. The remaining spectrum is that of the $c\bar{c}$ continuum of J/ψ quantum numbers at that temperature. On the contrary, the χ_c signal is already suppressed at $1.1T_c$, with only the corresponding continuum present [47]. These results clearly support the sequential suppression scenario.

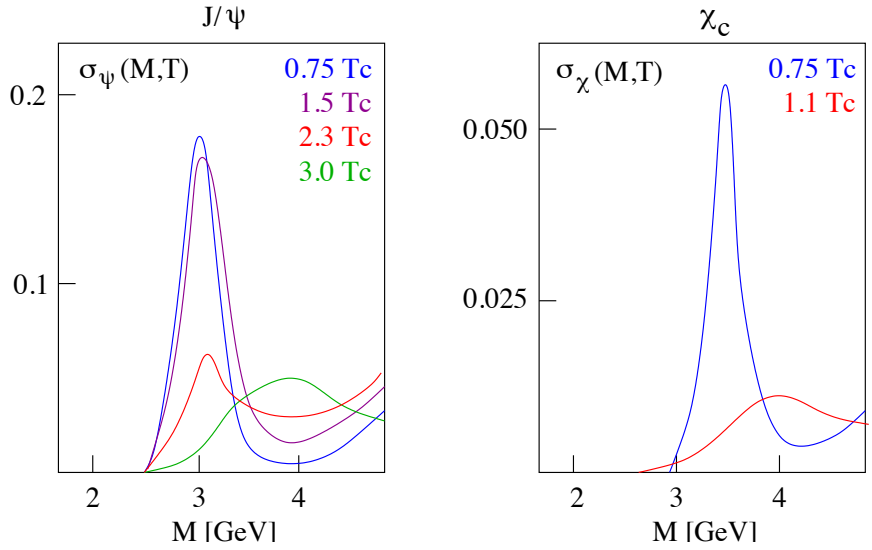

Figure 1.18. *J/ψ and χ_c spectral functions at different temperatures (from [47]).*

1.3.4 Experimental results

The study of the quarkonium suppression mechanism in a hot and dense medium can be experimentally conducted by extracting the distribution of quarkonium yields as a function of the nucleus-nucleus collision centrality. The yields are in fact expected to be suppressed in central collisions (w.r.t peripheral collisions) when the number of interacting nucleons (N_{part}) is high enough to reach energy densities above the threshold for deconfinement.

The interpretation of experimental data is actually complicated by the presence of several concurring mechanisms which can modify the simple picture of the quarkonium yield suppression as probe of the creation of a QGP. Besides the quarkonium dissociation, other mechanisms can change the yields in nucleus-nucleus collisions such as:

- **cold nuclear matter effects:** these effects, involving properties of the ordinary nuclear matter, affect the quarkonia production in both the initial state (e.g. shadowing of the Parton Distribution Functions in the nucleus [29]) and the final state (nuclear absorption of quarkonia). These

[29]The Parton Distribution Functions (PDFs) of nucleons inside nuclei are modified by the nuclear environment. They are not the superposition of PDFs of free nucleons (outside nuclei).

effects can be studied in nucleon-nucleus collisions where the deconfined phase is not expected to be formed;

- **quarkonium regeneration:** quarkonia ($Q\bar{Q}$) can be recreated during (or at the term of) the hot deconfined phase from initially uncorrelated Q and $\bar{Q}$ quarks through statistical recombination. This effect is expected to be more important when the center of mass energy of the collision increases since more heavy quarks are produced in the collision.

The status of the studies on charmonium suppression, before the beginning of the LHC activities, can be summarized by the two plots shown in Fig. 1.19.

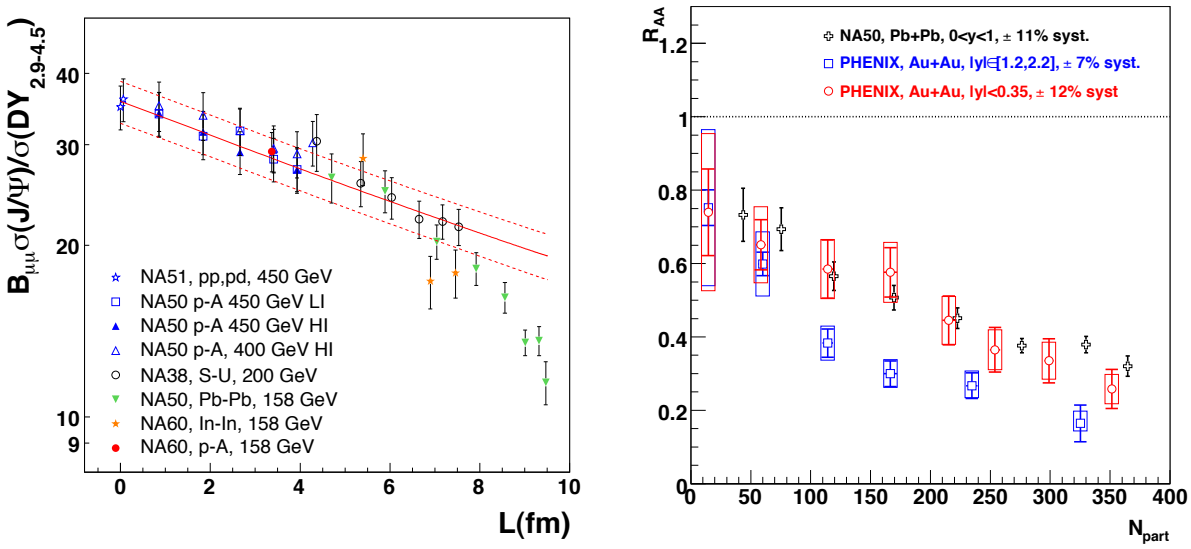

Figure 1.19. *(Left): Compilation of the $\sigma_{J/\psi}/\sigma_{DY}$ values in p-A and nucleus-nucleus collisions as a function of the nuclear thickness L as measured at the CERN SPS (from [49]). (Right): J/ψ nuclear modification factor R_{AA} for the hottest SPS (Pb-Pb) and RHIC (Au-Au) collisions, as a function of the number of participants N_{part} (from [50]).*

The left part of Fig. 1.19 shows a compilation of J/ψ cross sections normalized by Drell-Yan[30] cross sections measured at the CERN SPS in p-A and nucleus-nucleus collisions as a function of the nuclear thickness L[31] [49]. The pp, p-A, S-U and peripheral In-In or Pb-Pb collisions can be described by a simple model (red solid line with the dotted lines indicating the size of the error) in which the produced J/ψ is absorbed by the nuclear matter (characterized through the L parameter).

Instead, both the In-In and Pb-Pb more central collisions (corresponding to large L values) exhibit further anomalous suppression with a clear deviation with respect to the predicted red line. One can therefore think that, at SPS energies $\sqrt{s_{NN}} \approx 20$ GeV, charmonium resonances behave exactly like the predicted QGP signature: dissociation of quarkonia associated with nuclear absorption. The suppression observed for In-In and Pb-Pb collisions is in fact not compatible with a pure nuclear absorption scenario.

[30] The Drell-Yan process ($q + \bar{q} \rightarrow l^+ l^-$) is known and observed to scale with binary collisions. It can therefore be used to normalized the quarkonium cross section.

[31] The nuclear thickness L is the mean thickness of nuclear matter crossed by the produced J/ψ. It increases on passing from p-A collisions to central nucleus-nucleus collisions.

At the Relativistic Heavy Ion Collider (RHIC), J/ψ suppression was instead measured in Au-Au collisions at $\sqrt{s_{NN}}$ = 200 GeV by the PHENIX experiment at mid ($|y| < 0.35$) and forward ($1.2 < |y| < 2.2$) rapidities [51]. The results obtained brought up two striking features, as shown on the right part of Fig. 1.19 where the nuclear modification factor R_{AA}[32] is plotted as a function of the number of participants N_{part}. First, at mid-rapidity (red circles), the amount of suppression is surprisingly similar to the one observed at SPS (black crosses) as a function of N_{part}. Since the energy density should be higher at RHIC and the cold nuclear matter effects should be drastically different[33], there is no evident reason for this to happen. Even more surprising is the second feature: at forward rapidity (blue squares), J/ψ are further suppressed (by approximately 40%) than at mid-rapidity, where the energy density is expected to be higher.

A possible explanation of the RHIC J/ψ data involves the so-called coalescence or recombination models. Due to the high number of $c\bar{c}$ pairs (> 10) initially produced in a nucleus-nucleus central collision at RHIC, the uncorrelated c and $\bar{c}$ quarks can combine during (or at the term of) the hot partonic phase recreating a J/ψ. They could therefore be indeed more suppressed at RHIC than at SPS but then recreated via recombination. This argument could also explain the lower suppression at mid-rapidity where the number of $c\bar{c}$ pairs is higher (higher energy density). On the contrary, the higher suppression at forward rapidity could be due to cold nuclear matter effects: gluon shadowing parameterizations are in fact poorly constrained by data and further saturation effects are not excluded.

Charmonium production has been recently studied at the Large Hadron Collider (LHC) in Pb-Pb collisions at $\sqrt{s_{NN}}$= 2.76 TeV [52, 53, 54] allowing new investigations on quarkonium suppression. The LHC heavy ions program started at the end of 2010 when the first Pb-Pb collisions were delivered to the three experiments participating to the data taking: ALICE, ATLAS and CMS. Then, a new period of data taking was performed one year later at the same energy, but with higher luminosity.

In Fig. 1.20 (Top) and 1.21, the new results on J/ψ R_{AA} as a function of the number of participants N_{part}, released by the ALICE and CMS collaborations, are shown. The comparison between the LHC points and the RHIC ones is shown as well and leads to the following general considerations. First, the magnitude of the J/ψ suppression at forward rapidity and low p_{T} is less important at LHC with respect to RHIC: this is evident by looking at Fig. 1.20 (Top) and could be explained by a larger regeneration contribution (due to the high LHC energy) which is expected to be more important at low p_{T}. This could also explain why J/ψ R_{AA} as a function of the p_{T}, as shown in Fig. 1.20 (Bottom), decreases for increasing p_{T}. The behavior at mid-rapidity can, instead, be inferred from Fig. 1.21, where the ALICE (Top) and the CMS (Bottom) results are compared to the RHIC ones. At low p_{T} (J/ψ measured down to zero p_{T}), ALICE data are less suppressed than in PHENIX, while for the CMS high-p_{T} data (J/ψ transverse momentum higher than 6.5 GeV/c) the situation seems to be the opposite if compared to STAR points ($p_{\mathrm{T}} > 5$ GeV/c). According to the current interpretation, the lower suppression at low p_{T} can be explained by regeneration which contributes, at LHC, mainly in such p_{T} range. The higher suppression at higher p_{T} is supposed to come from a stronger color screening effect.

More data are needed to achieve better measurements and improve our current understanding of the quarkonium suppression mechanism. In addition, a deeper understanding of this process requires

[32]The quarkonium suppression in nucleus-nucleus collisions can be quantified through the estimation of the so-called nuclear modification factor (R_{AA}) which is defined as $R_{AA} = \frac{Y_{AA}^{J/\psi}}{N_{coll} \times Y_{pp}^{J/\psi}}$. It is the ratio of the J/ψ yield collected in nucleus-nucleus collisions normalized with a reference J/ψ yield obtained in no-QGP conditions (pp collisions) multiplied by the number of binary collisions N_{coll}. R_{AA} is expected to be equal to 1 if the nucleus-nucleus collision is simply a superimposition of many pp collisions.

[33]For example, the gluon PDFs should be further shadowed since at RHIC energies smaller Bjorken x values can be explored.

a precise knowledge of cold nuclear matter effects that could be achieved analyzing p-Pb collisions which are expected to be delivered by LHC machine in 2013.

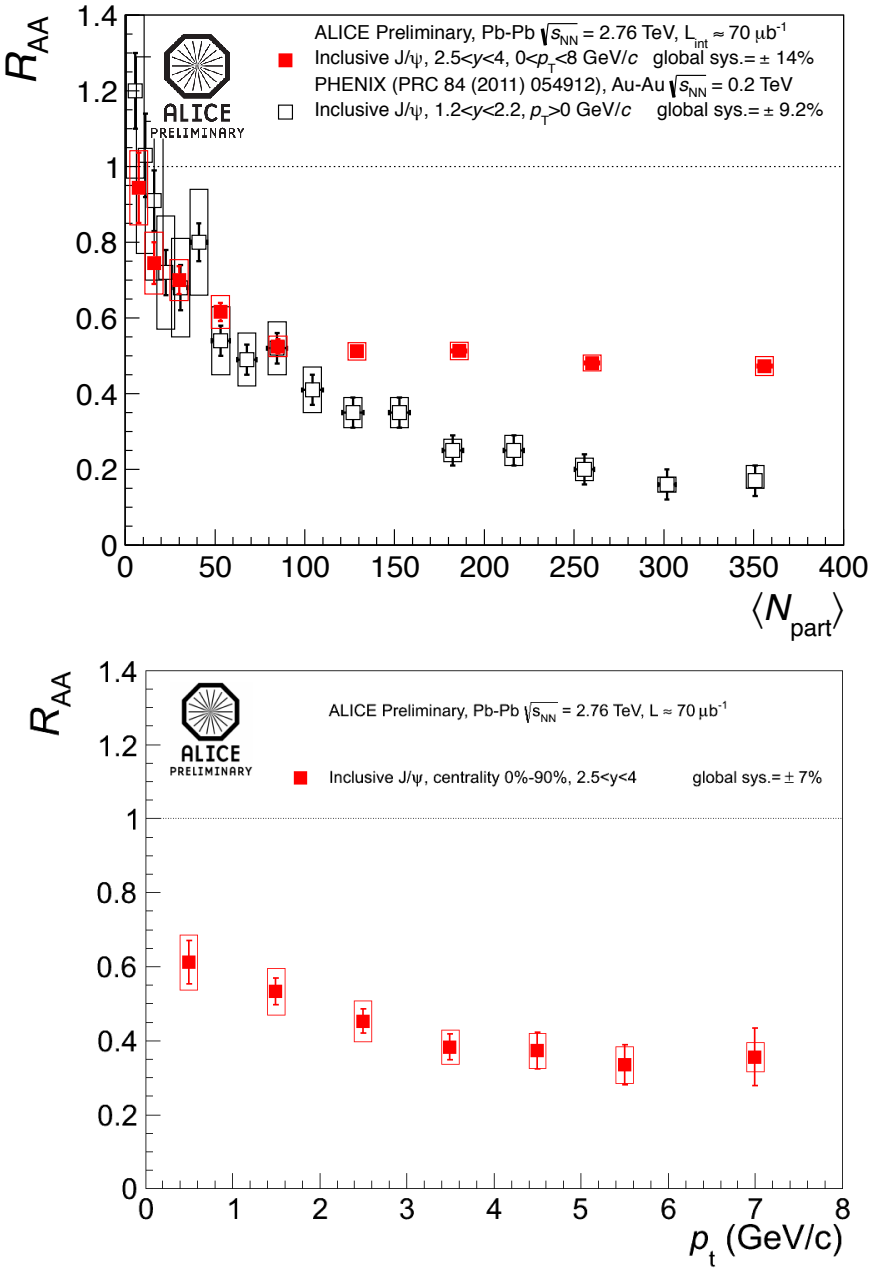

Figure 1.20. *(Top) J/ψ R_{AA} as a function of N_{part} at forward rapidity and low p_T as measured by ALICE (red points) [55]. A comparison to PHENIX measurements (black points) at forward rapidity is shown as well. (Bottom) J/ψ R_{AA} as a function of p_T as measured by ALICE [55].*

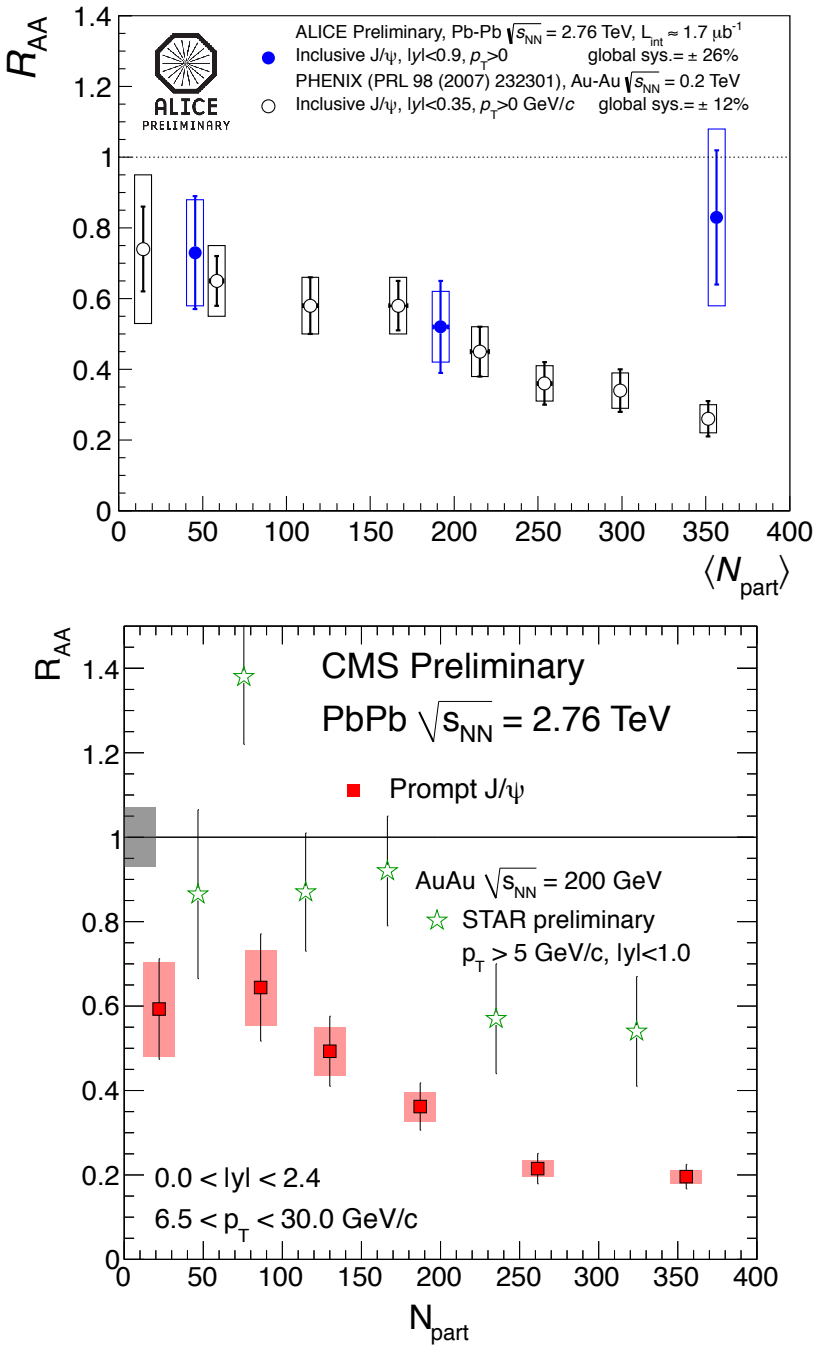

Figure 1.21. *(Top): J/ψ R_{AA} as a function of N_{part} at mid-rapidity and low p_T as measured by ALICE (blue points) [55]. A comparison to PHENIX measurements (black points) at mid-rapidity is shown as well. (Bottom): J/ψ R_{AA} as a function of N_{part} at mid-rapidity and high p_T as measured by CMS (red points) [56]. The CMS points are compared to the STAR (RHIC) ones (green points) [57] measured at mid-rapidity and high p_T too.*

Chapter 2

The ALICE experiment

ALICE (A Large Ion Collider Experiment) is the experiment at the CERN Large Hadron Collider (LHC) specifically designed to study the physics of strongly interacting matter at extreme energy densities and temperatures. Under these extreme conditions, that can be reached on the Earth only in ultra-relativistic nucleus-nucleus collisions (Pb-Pb at LHC), the ordinary color-confined hadronic matter is expected to undergo a phase transition to a colored plasma of deconfined quarks and gluons, called *Quark Gluon Plasma*. The study of the properties of such state of QCD matter is the main goal of the ALICE collaboration. Nevertheless, proton-proton collisions play also an important role in the ALICE physics program by providing a crucial reference for the QGP-related measurements and a fundamental testing ground of QCD predictions. The ALICE detector design is therefore driven by both (Pb-Pb and pp) physics programs.

This chapter, after a very short introduction on the LHC hadron accelerator (Section 2.1), is devoted to the description of the ALICE detector layout. Section 2.2 gives a brief overview of the main ALICE detector systems, while, in Section 2.3, the ALICE Forward Muon Spectrometer, which is the relevant detector for the analysis presented in this manuscript, is described in more details.

2.1 The Large Hadron Collider

The Large Hadron Collider (LHC) [1] is, at present, the biggest and most powerful hadronic accelerating facility in the world. It is designed to accelerate and collide protons and lead ions at the center-of-mass energy $\sqrt{s}$ of 14 TeV for pp collisions and 5.5 TeV per nucleon pair for *Pb-Pb* collisions, the highest center-of-mass energies ever achieved in high-energy physics. The nominal peak instantaneous luminosity that can be reached is, respectively, $\mathscr{L} = 10^{34} cm^{-2} s^{-1}$ and $\mathscr{L} = 10^{27} cm^{-2} s^{-1}$.

The LHC accelerator system is installed inside a 27 km circumference circular tunnel originally built to host the Large Electron Positron Collider (LEP). The tunnel is located between 45 and 170 meters underground across the swiss-french border not far from Geneva (Switzerland) (see Fig. 2.1). The LHC can accelerate two counter-rotating beams circulating in two separate beam pipes and colliding in eight different points. The high center-of-mass energies, that can be reached, require the use, among other things, of superconducting dipole magnets: they are cooled down at the temperature of 1.9 K using super-fluid Helium at atmospheric pressure and can produce magnetic fields of the order of 8.4 T.

The proton acceleration is performed in many steps (see Fig. 2.2): initially protons are injected from a linear accelerator (LINAC2) into the Proton Synchrotron Booster and then to the Proton Syn-

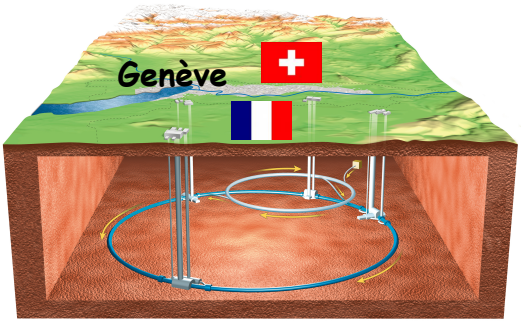

(a) *Scheme of the underground position of the LHC tunnel.*

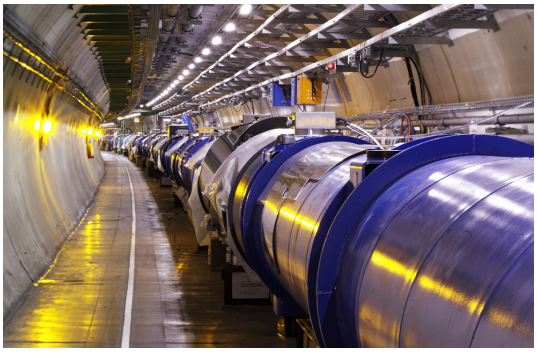

(b) *View of the hadron accelerator (blue modules) inside the underground tunnel.*

Figure 2.1. *Large Hadron Collider (LHC) at CERN.*

chrotron (PS), where they are accelerated up to a momentum of 25 GeV/c. Afterwards, the proton beams are transferred to the Super Proton Synchrotron (SPS), where they reach a momentum of 450 GeV/c, and finally are injected in the LHC ring. The ion acceleration is more complicated due to the additional stripping and accumulation phases at the beginning of the acceleration chain.

Large experiments are installed in four of the eight interaction points and allow the detection of the scattering products of the colliding beams:

- ALICE (A Large Ion Collider Experiment), experiment specifically dedicated to heavy-ion collisions;
- ATLAS (A Toroidal LHC ApparatuS), general purpose experiment focused on the search of the Higgs boson, as well as on physics beyond the Standard Model;
- CMS (Compact Muon Solenoid), experiment with similar purposes as ATLAS;
- LHCb (Large Hadron Collider beauty), experiment focusing on beauty (bottom) detection for precise measurements of CP violation and rare decays;
- LHCf (Large Hadron Collider forward), experiment sharing the interaction point with ATLAS and focusing on forward particles created at the LHC as a source to simulate cosmic rays in laboratory conditions;
- TOTEM (TOTal and Elastic Measurement), experiment, sharing the interaction point with CMS, dedicated to total cross sections, elastic scattering and diffractive dissociation measurements.

On the 10th September 2008, after the injection operations, a first proton beam circulated inside the LHC ring. Unfortunately, due to a serious accident occurred at the very beginning of the LHC commissioning phase, the machine had to be stopped for an entire year allowing the necessary reparations. In November 2009, operations were resumed and the LHC era officially began.

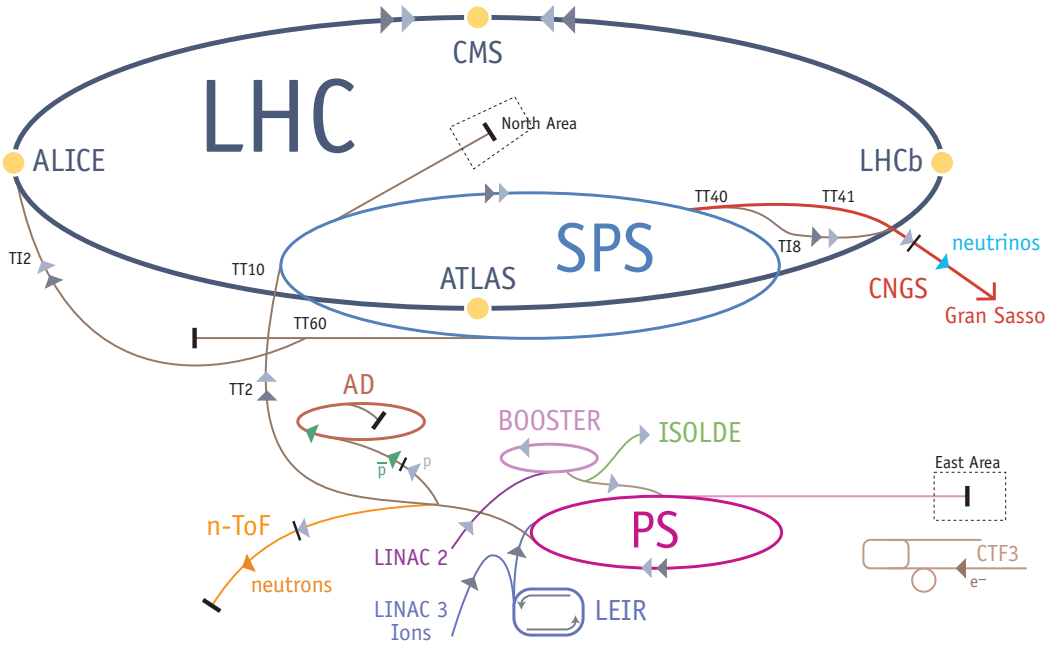

Figure 2.2. *The accelerator complex at CERN .*

In the period 2009 - 2012, the machine delivered proton-proton collisions at $\sqrt{s}$ = 0.9, 2.76, 7 and 8 TeV and, for what concerns the ion program, Pb-Pb collisions were delivered, at the end of 2010 and 2011, at a center-of-mass energy per nucleon $\sqrt{s_{NN}}$ = 2.76 TeV. In its first three years the machine was conservatively kept at lower energy with respect to the nominal one which is expected to be achieved in the next years.

2.2 Overview of the ALICE experiment

The ALICE experiment [2], built by a collaboration of more than 1000 physicists and engineers from about 33 countries, is a general-purpose heavy-ion experiment which is sensitive to the majority of known physics observables and able to detect photons, hadrons, electrons and muons. Its experimental design is driven by several requirements: tracking and identifying particles in a wide transverse momentum range (from about 100 MeV/c up to about 100 GeV/c), reconstructing short-lived particles such as D and B mesons and detecting quarkonia. In addition, these tasks should be performed in an environment with large charged-particle multiplicities. These features are required to achieve a complete and detailed description of the system produced in heavy-ion collisions, from the initial hard scattering processes to the collective phenomena arising in a complex system.

The ALICE detector (see Fig. 2.3) has the typical aspect of detectors at colliders, with a cylindrical shape around the beam axis, with in addition a Forward Muon Spectrometer which is able to detect muons at forward pseudorapidity[1]. Moreover, the central barrel angular acceptance is completed by detectors located at large pseudorapidities, thus allowing measurements of low-p_{T} particles and of global event structure.

ALICE can be divided in three parts:

[1] In particle physics, the pseudorapidity is defined as $\eta = -ln\left[tan(\frac{\theta}{2})\right]$, where θ is the polar angle with respect to the beam line. It has a pure geometrical meaning, being related only to the angle that the particle makes with the beam axis.

1. the central part covers the angular domain $\pm 45^\circ$ (corresponding to the pseudorapidity interval $|\eta| < 0.9$) over the full azimuth and is embedded in a large magnet (L3) with a weak solenoidal field (maximum field of 0.5 T). It consists of (from inside to outside)

   - an Inner Tracking System (ITS);
   - a cylindrical Time Projection Chamber (TPC);
   - a Transition-Radiation Detector (TRD);
   - a Time-Of-Flight (TOF) detector;
   - a High-Momentum Particle Identification Detector (HMPID);
   - a PHOton Spectrometer (PHOS);
   - an ElectroMagnetic Calorimeter (EMCal);

2. the forward detectors are

   - a Forward Multiplicity Detector (FMD);
   - a Photon Multiplicity Detector (PMD);
   - VZERO scintillators (V0)
   - T0 Cherenkov counters;
   - Zero Degree Calorimeters (ZDCs);

3. the Forward Muon Spectrometer (FMS) which covers, in the ALICE official reference frame, an angular acceptance of $171^\circ < \theta < 178^\circ$ corresponding to a negative η range (-4 < η < -2.5). (See Section 2.3 for more details).

The detector of the central barrel are now considered.

Inner Tracking System (ITS). The ITS consists of six cylindrical layers of silicon detectors, with a radius varying from 4 to 44 cm. Pixel, drift and strip detectors have been chosen for the two innermost (SPD), the two intermediate (SDD) and the two outer layers (SSD), respectively. The high resolution pixel detectors have an extended pseudorapidity coverage ($|\eta| < 1.98$) to provide, together with the forward detectors, a large coverage in rapidity for charged particles multiplicity. The six layers operate, together with the central detectors, at low frequency ($\sim$ 100 Hz), while the Silicon Pixel Detector (SPD) can run at higher rate ($\sim$ 1 kHz) providing vertex information required for events triggered by the Forward Muon Spectrometer. The ITS design allows to localize the primary vertex with a resolution better than 100 μm, reconstruct the secondary vertexes from the decay of hyperons, D and B mesons, track and identify low momentum particles (p < 100 MeV/c) and, finally, complete and improve the information provided by the TPC.

Time Projection Chamber (TPC). The TPC is the main tracking detector of the ALICE central barrel. The TPC design provides charged-particle momentum measurements up to p_{T} = 100 GeV/c, vertex determination in the high-multiplicity environment expected in Pb-Pb collisions and good particle identification. The simultaneous detection of high and low momentum particles can be achieved with a low magnetic field ($\leq$ 0.5 T) and a large detector volume which allows to measure a large section of the track, thus increasing the sensitivity for the sagitta determination. The TPC has an inner radius of about 85 cm and an outer one of about 250 cm, with a total length of about 500 cm. This leads to a 88 μs drift time which is the limiting factor for the luminosity delivered to ALICE in proton-proton collisions [2]. The study of soft hadronic observables requires a resolution of 1% for momenta between 100 MeV/c and 1 GeV/c, while the detection of hard probes requires a 10% resolution for tracks with p_{T} = 100 GeV/c. The latter can be achieved by using the TPC in combination with ITS and TRD. The resolution on the relative momentum between two particles, necessary to measure two-particle correlations, has to be better than 5 MeV/c. Finally, the TPC can provide particle identification by $\mathrm{d}E/\mathrm{d}x$ measurement in certain momentum ranges from the low-momentum region up to few tens of GeV/c, in combination with TOF, TRD and ITS.

Transition Radiation Detector (TRD). The TRD provides electron identification for momenta greater than 1 GeV/c, where the pion rejection capability through energy loss measurement in the TPC is no longer sufficient. Its use, in conjunction with TPC and ITS, allows to measure the production of light and heavy vector meson resonances and, thanks to the determination of the impact parameter, of open charm and beauty. A similar technique can be used to separate the promptly produced J/ψ mesons from those produced via B-decays. The TRD consists of 18 sectors of 6 layers each with a 5-fold segmentation along the beam direction, for a total of $18 \times 6 \times 5 = 540$ detector modules. Each module consists of a radiator of 4.8 cm thickness, a multi-wire proportional readout chamber and its front-end electronic. The TRD increases the ALICE pion rejection capabilities by a factor of 100 for electron momenta above 3 GeV/c and allows a mass resolution of 100 MeV/c^2 for the $\Upsilon(b\bar{b})$ resonance.

Time-Of-Flight (TOF). The TOF detector is a large-area detector used for particle identification in the intermediate momentum range, from 0.2 to 2.5 GeV/c. Combined with the ITS and TPC it provides an event-by-event identification of large samples of pions, kaons and protons. The large coverage requires the use of a gaseous detector: Multi-gap Resistive Plate Chambers were chosen, providing an intrinsic time resolution of better than 40 ps and an efficiency close to 100%. The detector is segmented in 18 sectors in ϕ and 5 segments in z. The whole device is located in a cylindrical cell with an internal radius of 370 cm and an external one of 399 cm.

High Momentum Particle Identification Detector (HMPID). Dedicated to the inclusive measurement of identified hadrons with $p_{\mathrm{T}} > 1$ GeV/c, the HMPID is designed as a single-arm array with a pseudorapidity acceptance of $|\eta| < 0.6$ and an azimuthal coverage of about 58° which corresponds to 5% of the central barrel phase space. The detector is based on proximity-focusing Ring Imaging Cherenkov counters and consists of seven modules of about 1.5×1.5 m^2 each. The HMPID enhances the PID capability of ALICE by enabling the identification of particles beyond the momentum interval attainable through energy loss (in ITS and TPC) and time-of-flight measurements (in TOF). The detector is optimized to extend the range for π/K and K/p discrimination, on a track-by-track basis,

[2] As a consequence of the high TPC drift time, ALICE cannot cope with high interaction rates and, therefore, the luminosity in proton-proton collisions must be reduced, by displacing the proton beams, with respect to the other LHC experiments.

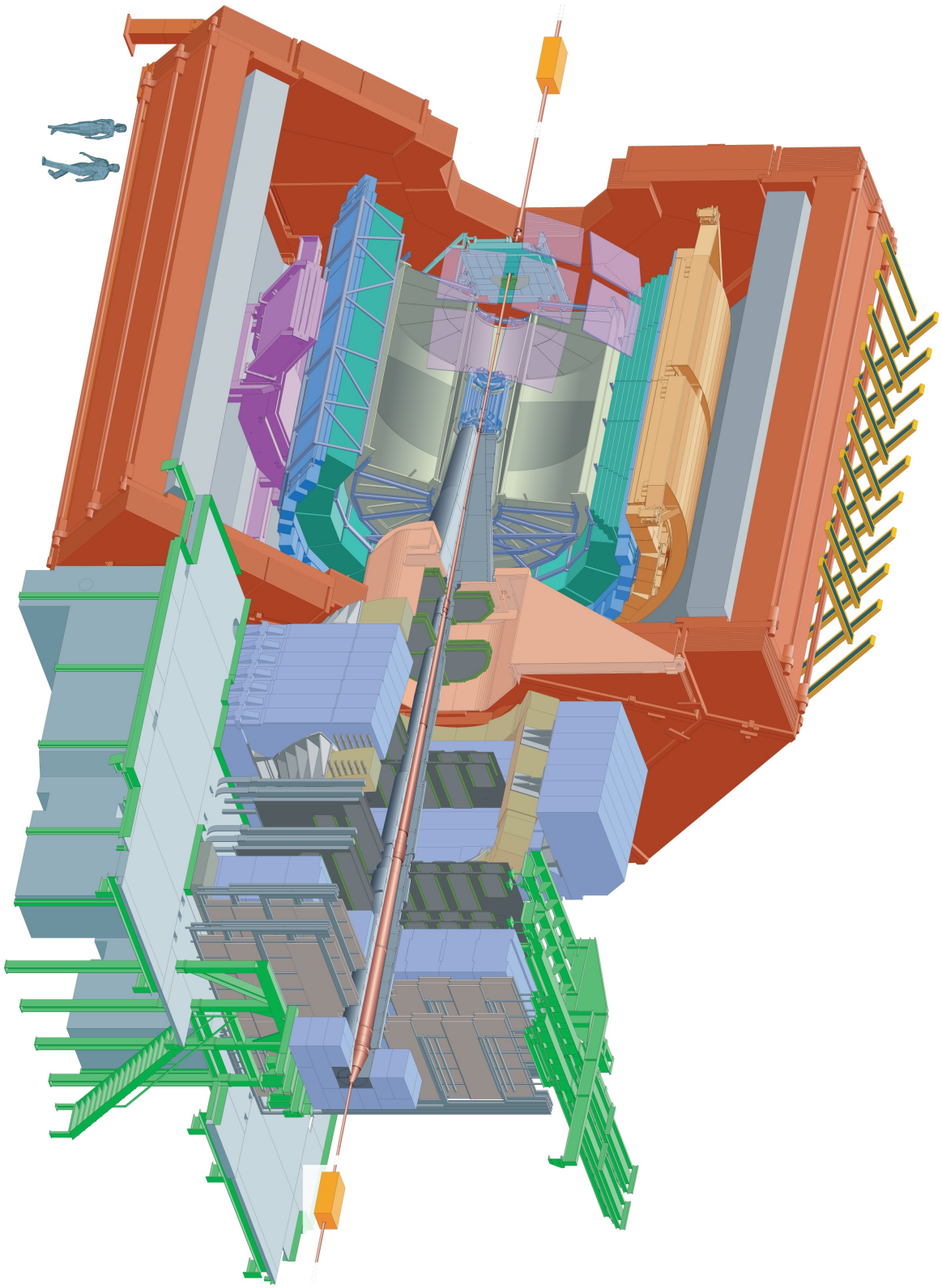

Figure 2.3. *Layout of the ALICE experiments.*

up to 3 GeV/c and 5 GeV/c, respectively.

PHOton Spectrometer (PHOS). The PHOS is a single-arm spectrometer including a highly segmented electromagnetic calorimeter made of lead-tungstenate crystals and a charged particle veto detector consisting of a Multi-Wire Proportional Chamber with cathode-pad readout. The spectrometer, positioned at the bottom of the ALICE setup at a distance of 460 cm from the interaction point, covers a pseudorapidity range of $|\eta| < 0.12$ and 100° in the azimuthal angle. The PHOS is designed to provide photon identification, as well as neutral meson identification, through the two-photons decay channel.

ElectroMagnetic Calorimeter (EMCal). The EMCal, the last detector added to the ALICE layout, enhances the ALICE capabilities for high-energy jet measurements by improving jet energy resolution. It also augments the capabilities to measure high momentum photons and electrons. The EMCal is located at 4.5 m from the beam line with an azimuthal acceptance coverage of 110°, limited by the PHOS and the HMPID. The chosen technology is a layered Pb-scintillator sampling calorimeter with alternating layers of 1.44 mm of lead and 1.76 mm of scintillator.

The forward detectors are now considered.

Forward Multiplicity Detector (FMD). The FMD provides charged particle multiplicity informations in the pseudorapidity range $-3.4 < \eta < -1.7$ (Muon Spectrometer side) and $1.7 < \eta < 5.1$ (PMD side). The FMD consists of silicon strip detectors divided in seven disks perpendicular to the beam pipe and placed at distances between 42 and 225 cm from the interaction point (IP).

Photon Multiplicity Detector (PMD). It is a pre-shower detector measuring the multiplicity and spatial (η - ϕ) distribution of photons, on an event-by-event basis, in the forward region ($2.3 < \eta < 3.7$). Placed at about 360 cm from the interaction point, in the side opposite to the Forward Muon Spectrometer, the PMD estimates the transverse electromagnetic energy and the reaction plane on an event-by-event basis for Pb-Pb collisions analysis. It consists of two identical planes of detectors, made of gas proportional counters with honeycomb structure and wire readout, with a $3X_0$ thick lead converter in between.

VZERO Detector (V0). The V0 detector is made of two arrays of scintillator material, located at 90 cm (Muon Spectrometer side) and 340 cm (PMD side) from the interaction point. The detectors are segmented into 64 elementary counters distributed in 8 rings, covering two pseudorapidity ranges: $-3.8 < \eta < -1.7$ and $2.8 < \eta < 5.1$. The measurement of the time-of-flight difference between the two detectors allows to identify and reject the beam-gas events, thus providing a minimum bias (MB) trigger for the central barrel detectors and a validation signal for the muon (μ-MB) trigger. The V0 can also measure the charged particle multiplicity, thus resulting in a centrality indicator for Pb-Pb collisions analysis.

T0 Detector. The T0 consists of two arrays of Cherenkov counters, with a time resolution better than 50 ps, asymmetrically placed at 72.7 cm (Muon Spectrometer side) and 375 cm (PMD side) from the interaction vertex, with a pseudorapidity coverage of $-3.28 < \eta < -2.97$ and $4.61 < \eta < 4.92$, respectively. It is designed to provide a signal for the TOF detector, to measure the vertex position along the beam axis with a precision of $\pm$ 1.5 cm and to measure the particle multiplicity, generating a centrality trigger.

Zero Degree Calorimeters (ZDCs). The ZDC provides a centrality estimation and trigger in Pb-Pb collisions by measuring the energy carried in the forward direction (at zero degrees relative to the beam direction) by non-interacting (spectator) nucleons. The detector consists of two pairs of quartz-fibers hadronic calorimeters (for neutron and protons), placed on both sides of the interaction point, at 116 m from it. Being placed between the beam pipes, the neutron calorimeter (ZN) has the most severe geometrical constraints: the transverse dimensions have to be smaller than 7 cm, requiring a very dense "passive" material (tungsten). The stringent space constraints do not hold for the proton calorimeter (ZP), which is made with a less dense material (lead). The ZN, segmented in four regions, can also provide an estimation of the reaction plane. The ZDC system also presents two electromagnetic calorimeters (ZEM), both placed at about 7 m from the IP (PMD side), which allow to resolve ambiguities in the determination of the centrality. The electromagnetic calorimeter (ZEM), made of lead and quartz fibres, is designed to measure the energy of particles, mostly photons generated from π^0 decays, at forward rapidities ($4.8 < \eta < 5.7$). Differently from the ZN and ZP, the ZEM fibres are oriented at 45°, a choice that maximizes the detector response.

2.3 Forward Muon Spectrometer

The Forward Muon Spectrometer is primarily designed to measure the production of heavy quarkonia, both charmonium (J/ψ, ψ') and bottomonium (Υ, Υ', Υ") families, as well as the low mass mesons (ρ, ω, ϕ), in the muon pair $\mu^+\mu^-$ decay channel. In addition to vector mesons, the study of open heavy flavour (charm and bottom) and weak boson production can also be performed via their muonic decay channels.

The spectrometer has angular acceptance between $171° < \theta < 178°$[3] corresponding to a pseudo-rapidity range -4 < η < -2.5 which provides good acceptance down to zero transverse momentum and a manageable background from hadron decays. The layout of the muon spectrometer, shown in Fig. 2.4, consists of a composite front absorber of $\sim 10\lambda_{int}$ (interaction length) starting about 90 cm from the vertex, a large dipole magnet with a 3 Tm field integral placed outside the L3 magnet, and ten planes of very thin high-granularity cathode-pad tracking stations. The picture is completed by a second absorber, made of iron ($\sim$ 7.2 λ_{int}) and acting as a muon filter, and, at the end of the spectrometer, four planes of Resistive Plate Chambers used for muon identification and triggering.

The spectrometer is shielded, throughout its length, by a dense conical absorber tube which protects the tracking chambers from secondary particles created in the beam pipe.

The main design criteria of the muon spectrometer are driven by several requirements. First of all, as the accuracy of quarkonium measurements is statistics limited (in particular for the Υ family), the spectrometer's geometrical acceptance was chosen as large as possible. In addition, measuring the direct J/ψ production requires a large acceptance down to zero p_{T}, where the J/ψ contribution coming from B hadron decays is lower. In order to separate all resonance states, a resolution of 100 MeV/c^2 is needed in the bottomonium mass range. This last feature is determined by several components: the multiple scattering in the front absorber, intrinsic spatial resolution of the muon tracking system and the bending strength of the spectrometer magnet.

Finally, the tracking and trigger detectors of the spectrometer have to cope with the high particle multiplicity expected in heavy-ion collision at LHC energies and have therefore a very high granularity read-out.

[3]The ALICE official coordinate system is a right-handed orthogonal Cartesian system with the z-axis parallel to the beam line and pointing in the direction opposite to the MUON Spectrometer, the x-axis aligned to the local horizon and pointing to the accelerator center and the y-axis perpendicular to the other two and pointing upward. In this reference frame, the angular acceptance of the spectrometer, in term of polar angle θ, results to be $171° < \theta < 178°$.

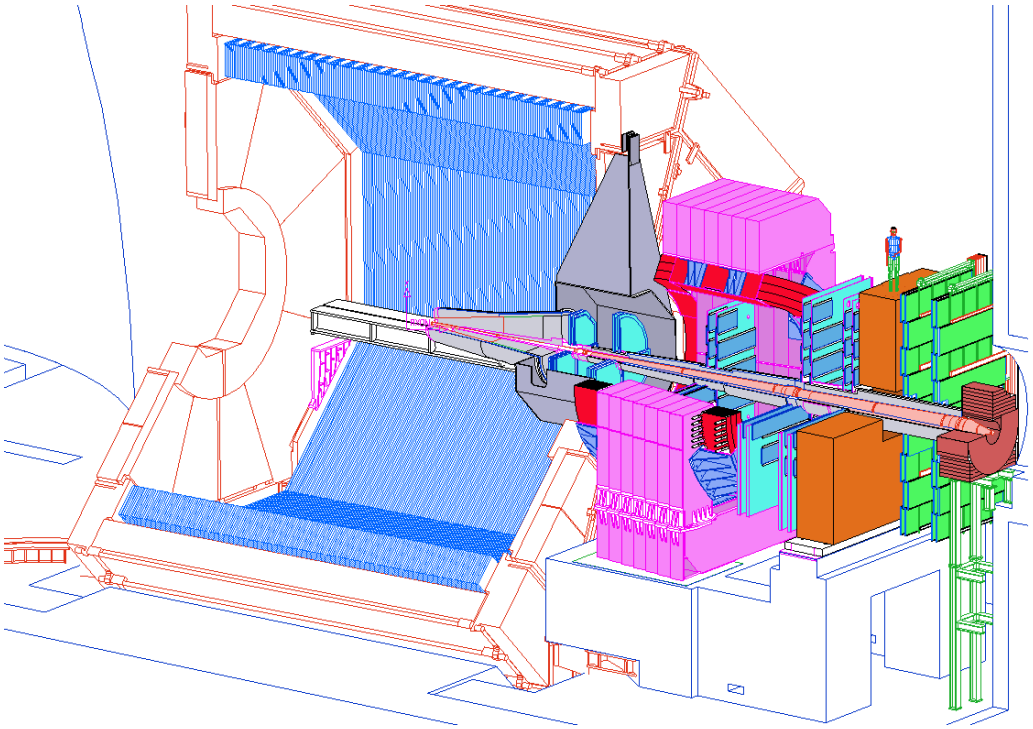

(a) *3D view.*

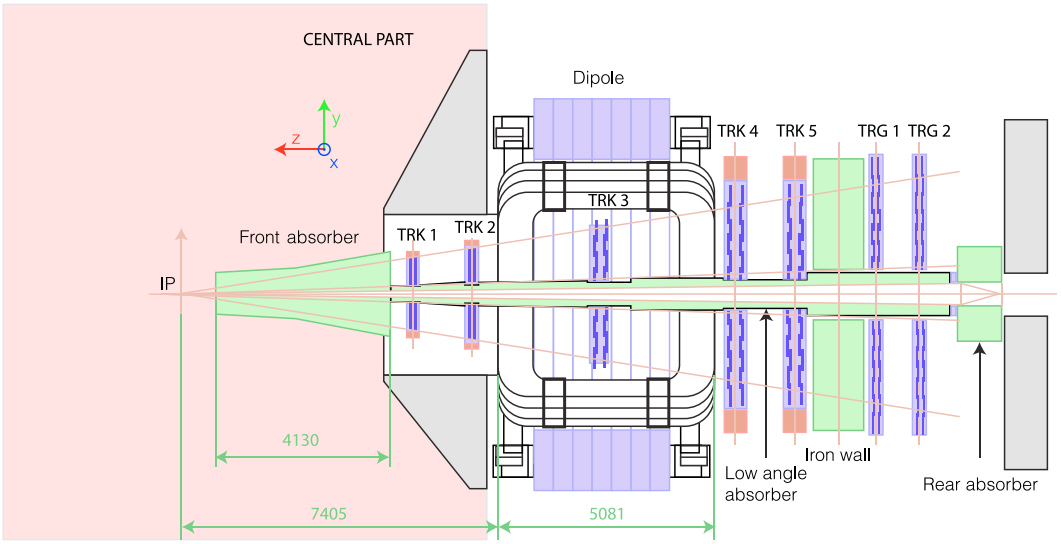

(b) *Longitudinal section.*

Figure 2.4. *Schematic view of the ALICE Forward Muon Spectrometer.*

2.3.1 Absorber and shielding

The Muon Spectrometer contains three absorber sections: a front absorber in the acceptance region, a beam shield surrounding the beam pipe and a muon filter between the tracking and the trigger chambers.

The front absorber, shown in Fig. 2.5, is located inside the ALICE solenoid magnet L3 and has a total length of 4.13 m (corresponding to $\sim 10\ \lambda_{int}$ and ~ 60 radiation lengths X_0).

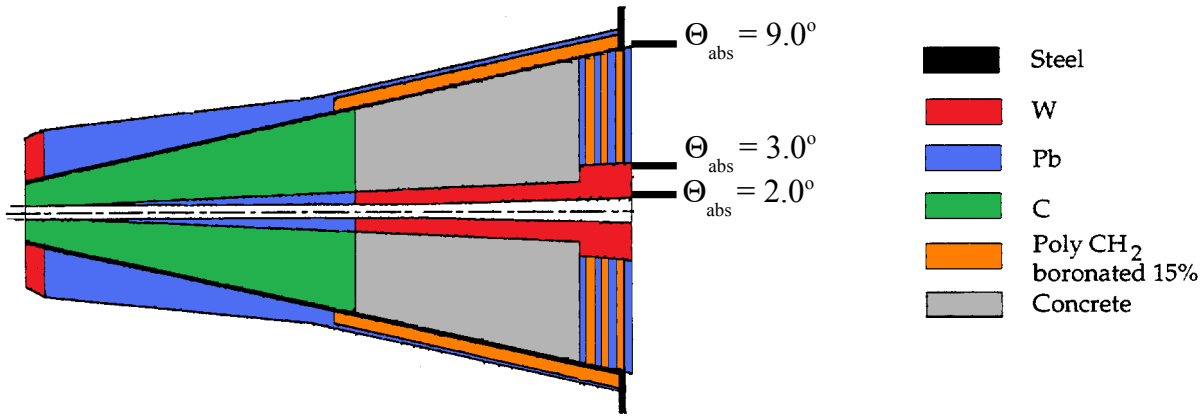

Figure 2.5. *Schematic view of the Front Absorber.*

It has the double task of attenuating the particle flux into the spectrometer by at least two orders of magnitude and of decreasing the muon background by limiting the free path for primary π, K $\rightarrow \mu$ decays. The minimal distance to the interaction point ($\sim$ 90 cm) is imposed by the dimensions of the Inner Tracking System and the position of the multiplicity counters. The front absorber design and composition are optimized to provide good shielding capabilities on the one hand, and a limited multiple scattering which should not compromise the spectrometer mass resolution on the other. This can be achieved by using low-Z material in the absorber layers close to the IP and high-Z shielding materials at the rear end, as shown in Fig. 2.5. The fiducial volume of the absorber is made predominantly by a combination of concrete and carbon. It is worth noting that the use of very dense material at the end of the absorber has an important consequence for the tracking. Since the multiple scattering in this layer is large whereas the distance to the first tracking chamber is small (30 cm), the muon production angle is best defined when the position measurement in the first chamber is combined with the position of the interaction vertex, determined by the ITS.

The small-angle beam shield protects the tracking chambers by reducing background particle produced in the beam pipe. It is made of dense materials (pure tungsten in the most critical region, tungsten-lead mixture elsewhere) and encased in a 4 cm thick stainless steel tube. Its outer envelope is "pencil-shaped": it follows the 178° acceptance line up to a maximum radius of 30 cm and then stays constant up to the end of the spectrometer.

While the front absorber and the beam shield are sufficient to protect the tracking chambers, the trigger chambers require additional protection. For this reason the muon filter, an iron wall 1.2 m thick ($\sim 7.2\ \lambda_{int}$), is placed after the last tracking chamber, in front of the first trigger chamber. Due to the presence of the front absorber and muon filter, muons with momenta less than 4 GeV/c are stopped.

2.3.2 Dipole Magnet

The Muon Spectrometer is equipped with a dipole magnet. The size, 5 m length $\times$ 7.1 m width $\times$ 9 m height with a total weight of about 890 tons, is defined by the requirement on the angular acceptance of the spectrometer $171^\circ < \theta < 178^\circ$. The magnetic field ($B_{nominal}$ = 0.67 T and 3 Tm field integral between IP and muon filter) is instead determined by the requirements on the quarkonium mass resolution (resolution of 100 MeV/c^2 is required in the bottomonium mass range). With such dipole magnet characteristics, it is not necessary to use a superconducting magnet. It was therefore chosen a window-frame warm magnet equipped with resistive coils and arranged to produce a magnetic field in the horizontal direction, along the x-axis, whose polarity can be reverted. The magnet is placed 7 m from the interaction vertex.

2.3.3 Tracking Chamber System

The main challenge for the tracking chambers is the muon detection in a complex environment characterized by very large particle multiplicities as the ones produced in Pb-Pb collisions. When the detector conception started, the Au-Au RHIC data [58, 59] were not yet available and therefore the Monte Carlo calculations were performed with a very conservative estimation of the charged particle multiplicity $|\mathrm{d}N_{ch}/\mathrm{d}\eta|_{\eta=0}$ = 8000. Moreover, a safety factor 2 was introduced leading to a maximum hit density of about 5×10^{-2} cm^{-2} (in Pb-Pb central collisions) where a few hundred particles are expected to pass simultaneously through the first muon chamber with a rapidly increasing hit density near the beam pipe. Detectors are therefore requested to have a very fine granularity keeping the occupancy below 5 % (the occupancy is defined as the number of hit pads divided by the overall number of pads).

Other important challenge concerns the mass resolution which has to be of the order of 100 MeV/c^2 at the bottomonium mass range to correctly separate all the resonances. As a consequence of it, the tracking chambers had to achieve a spatial resolution of about 100 μm in the spectrometer bending plane and 1 mm in the non-bending one. In addition, to limit the multiple scattering on the trajectories, the chamber thickness had to be as small as a few percent of radiation length per plane. In the end, Multiwire Proportional Chambers (MWPC) with segmented cathode planes and filled with a 80%Ar / 20%CO_2 gas mixture were chosen. Such chambers, called *Cathode Pad Chambers* (CPC), are able to fulfill all the constraints described above. In particular, the two segmented cathode planes provide two-dimensional hit informations needed to reconstruct the muon candidate track.

The measurement of the muon momenta requires the determination of, at least, two points of the muon candidate track before the magnetic field and two after. Although not mandatory, a fifth point, measured in the center of the magnet, would increase the precision on the sagitta. Hence, the use of five tracking chambers is strongly recommended. In order to have an even more robust tracking system against possible breakdown of wires and also to increase the detection efficiency, these five chambers were doubled and associated by pairs in stations. The detector system is therefore arranged in five stations each made of two chamber planes: two stations are placed before, one inside and two after the dipole magnet.

Because of the different size of the stations, ranging from few square meters for station 1 to more than 30 m^2 for station 5, two different designs have been adopted, as shown in Fig. 2.6. The first two stations are based on a quadrant structure with the read-out electronics distributed on their surface (see Fig. 2.6 (a)). For the other stations, a slat architecture was chosen (see Fig. 2.6 (b)). The maximum size of a slat is 40×240 cm^2 and the electronics is implemented on the top and bottom part of the slat, as schematically shown in Fig. 2.7. The slats and the quadrants overlap to avoid dead zones on the detector. The tracking system covers a total area of about 100 m^2.

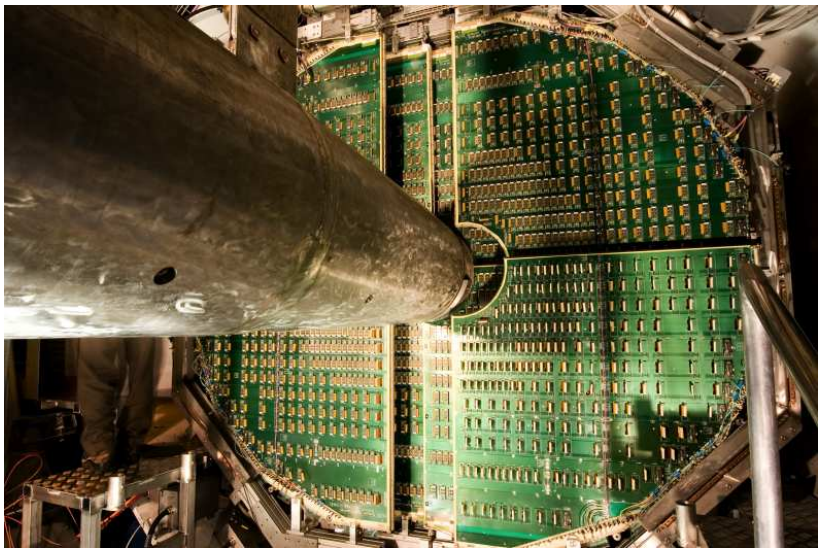

(a) *Layout of station 2 (quadrant architecture) of the tracking system. Read-out electronics is distributed on the surface.*

(b) *Layout of stations 4 and 5 (slat architecture) of the tracking system. Read-out electronics is implemented on the top and bottom part of the slat.*

Figure 2.6. *Muon Tracking Chambers installed in the ALICE cavern.*

Multiple scattering of the muons in the chamber is minimized by using composite material, such as carbon fibres which gives chamber thickness corresponding to about $0.03X_0$.

Electronics and read-out. The design of the read-out electronics of the muon tracking system is driven by two main requirements. Firstly, the electronics and readout system must perform the pulse shaping of the charges collected by ~ 1.08 millions pads of the tracking chambers at a maximum rate of 1 kHz. Then, to achieve a mass resolution of ~ 100 MeV/c^2 (~ 70 MeV/c^2) in the Υ (J/ψ) region,

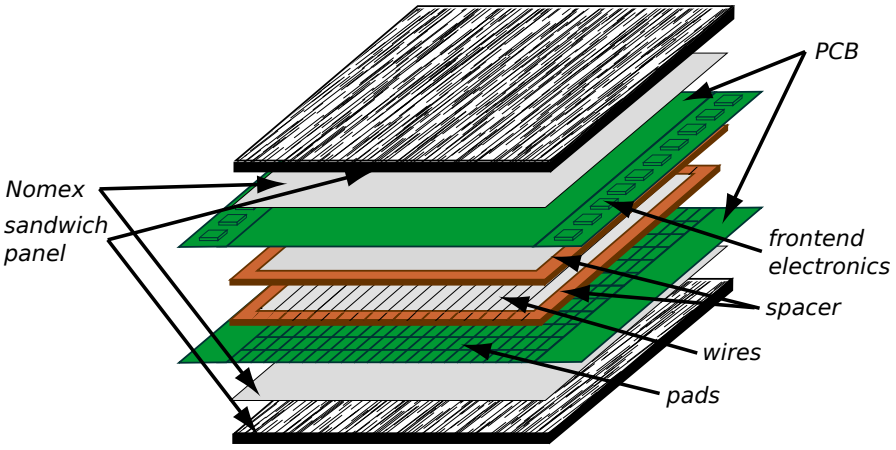

Figure 2.7. *Schematic view of the structure of a slat type cathode pad chamber.*

the spatial resolution, in the bending plane, has to be $\sim 100\ \mu$m. In order to satisfy this requirement, the Front-End Electronics (FEE) must have low noise and small gain dispersion.

The muon tracking electronics architecture can be divided in three parts (see Fig. 2.8): the front-end electronics called MANU (MAnas NUmérique), the read-out system called CROCUS (Cluster Read Out Concentrator Unit System) and the interface with the ALICE Central Trigger Processor (CTP) called TCI (Trigger Crocus Interface).

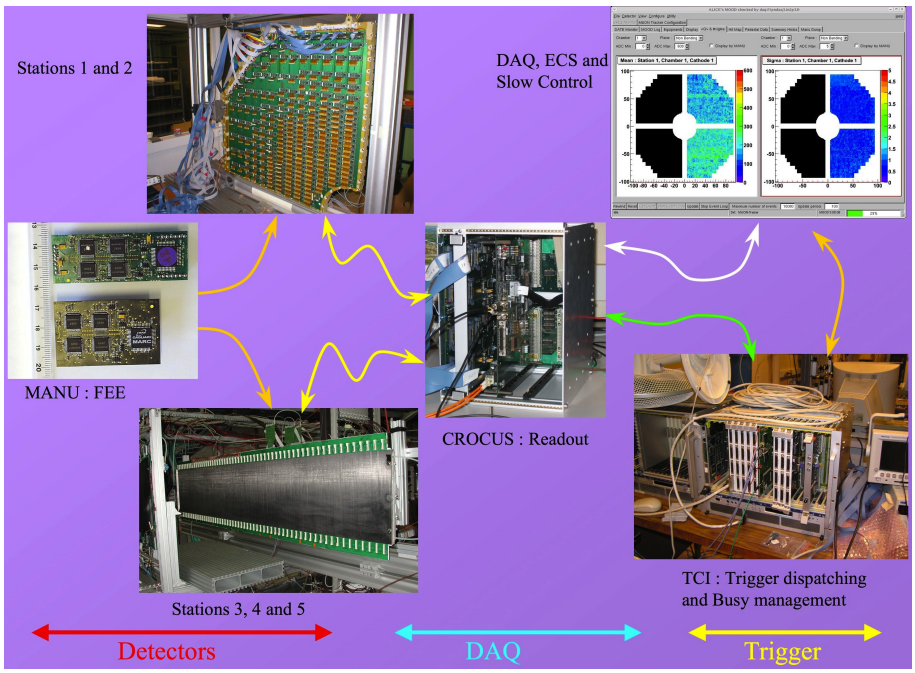

Figure 2.8. *General overview of the muon tracking electronics architecture.*

For all five stations, the front-end electronics is based on a 16-channel chip called MANAS (Multiplexed ANAlogic Signal processor) which includes several functionalities like charge amplifier, filter, shaper and track & hold. The signal digitization is performed directly on board. The channels of

four of these chips are fed into two 12-bits ADC, read out by the Muon Arm Readout Chip (MARC), whose functionalities include zero suppression.

The entire chain is mounted on the MANU: the $\sim$ 1.08 millions channels of the tracking system are treated by about 17000 MANU cards. The Protocol for the ALICE Tracking CHamber (PATCH) buses provide the connection between the MANUs and the Cluster Read Out Concentrator Unit System (CROCUS) crate, i.e. PATCH buses allow data transmission between the detector and the read-out system. Each chamber is readout by two CROCUS, which concentrate and format the data, transfer them to the ALICE DAQ (Data Acquisition) and dispatch the trigger signals, coming from the Central Trigger Processor (CTP). These crates allow also the control of the FEE and of the calibration processes.

Alignment. The requirements on the mass resolution δM [4], needed to separate the different states of the charmonium and bottomonium families, puts strict constraints on the alignment of the tracking chambers [60]. During the installation phase, the muon chambers were positioned according to theodolite measurements and with photogrammetry, with a spatial accuracy of few tenths of a millimeter. Of course, such a precision is not sufficient for our analysis purpose. Therefore, at the beginning of each data taking period, dedicated runs without dipole magnetic field ($B = 0$ T) are carried out in order to align the ten tracking chambers. The collected straight muon tracks can be processed using the so-called Millepede algorithm[5]which permits to estimate, through an iterative procedure, the deviations from the nominal position (residual misalignment) for each detection element of the tracking system.

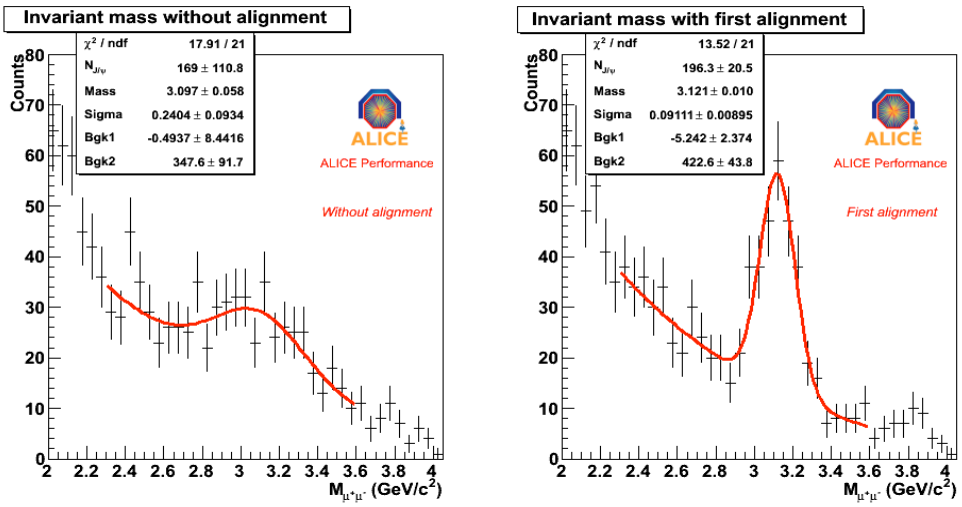

Figure 2.9. *Invariant mass spectra for OS muon pairs in the J/ψ mass region before (Left) and after (Right) the alignment of the Muon Tracking System.*

These corrections are then implemented in the muon track reconstruction phase [61, 62]. Figure 2.9 shows the invariant mass spectra for opposite sign muon pairs in the J/ψ mass region before (Left)

[4]Nominally, $\delta M \sim 100$ MeV/c^2 (~ 70 MeV/c^2) at the mass of the Υ (J/ψ) resonance.

[5]See [60] and http://www.desy.de/ blobel/wwwmille.html for more details.

and after (Right) the alignment of the Muon Tracking System. A clear improvement in the resonance mass resolution is observed: the J/ψ resonance width decreases from 230 MeV to 90 MeV.

However, after switching on the magnet and electronic power supplies, the chamber positioning, obtained applying the alignment procedure, can be disturbed by the forces of the L3 and dipole magnetic fields. These displacements and deformations are measured and recorded during data taking by the Geometry Monitoring System (GMS), with a resolution $\sim$ 20 μm. The GMS is an array of about 460 optical sensors which are placed on platforms located at each corner of the tracking chambers. Using the GMS's information, all the displacements and deformations can be corrected and the nominal spatial resolution (< 100 μm in the bending plane) can be achieved.

2.3.4 Trigger Chamber System

The main goal of the Muon Trigger System is to properly select muon tracks (unlike-sign muon pairs and single muons) in order to study the decays of quarkonium resonances and the open heavy flavour production.

In central Pb-Pb collisions, about eight low-p_{T} muons from π and K decays are emitted per event in the muon spectrometer acceptance. The distribution of these background muons is peaked at low transverse momenta, as shown in Fig. 2.10. To minimize the probability of triggering on background muons, a p_{T} cut has to be applied at the trigger level on each individual muon. The selection of high-p_{T} muons emitted in the decay of quarkonia (or in the semi-leptonic decay of open charm and beauty) can therefore be maximize. Two programmable cuts (low-p_{T} and high-p_{T} cuts), are performed in parallel by the trigger electronics and the values of the p_{T} thresholds can range from $\sim$ 0.5 to $\sim$ 4 GeV/c.

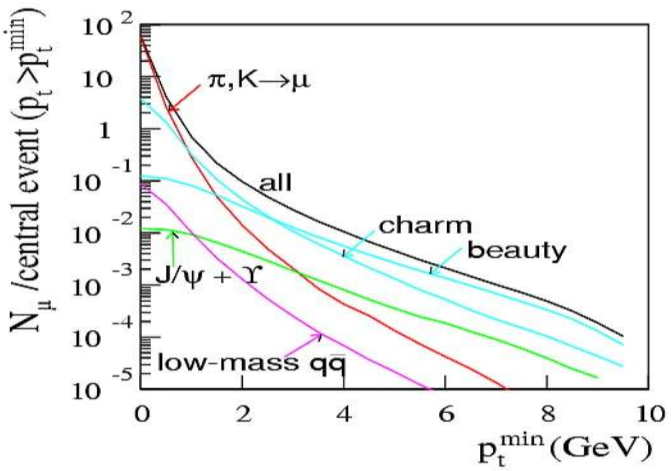

Figure 2.10. *Average number of muons per central Pb-Pb collision with $p_T \geq p_T^{min}$ as a function of p_T^{min} in the pseudorapidity range -4 < η < -2.5 [63].*

The p_{T} thresholds therefore represent a compromise between background rejection and signal detection efficiency. To attain these requirements, a large-area trigger system based on position sensitive detectors with a resolution of the order of the mm is needed: this is realized by means of Resistive Plate Chambers (RPC) [64].

RPCs are gaseous detector designed to measure the time and position of charged particles crossing its active area, that is the gas volume. The typical structure of the ALICE single-gap RPCs is presented

in Fig. 2.11: the 2 mm thick gas[6] gap (active volume) is enclosed between two parallel electrode plates (2 mm thick) treated with linseed oil to smooth the surface. The electrodes, made of low-resistivity Bakelite ($\rho \sim 3{\times}10^9$ Ω·cm), are separated by a frame and by spacers of insulating material. The spacers, 10 mm diameter cylinders with a 2 mm height, are placed on a $10{\times}10$ cm^2 grid. The external side of the electrodes are covered with a thin graphite layer to ensure a uniform electric field all over the active volume. One electrode is connected to the HV and the other one to the ground.

The trigger system of the ALICE Muon Spectrometer consists of two trigger stations (MT1 and MT2) located at about 16 m from the interaction point and 1 m apart from each other, placed behind an iron muon filter, as shown in Fig. 2.4. The filter has a thickness of 120 cm and performs muon selection by stopping the low-energy background muons and hadrons escaped from (or produced in) the front absorber. Each station consists of two planes of 18 Resistive Plate Chambers for a total active area of about 140 m^2.

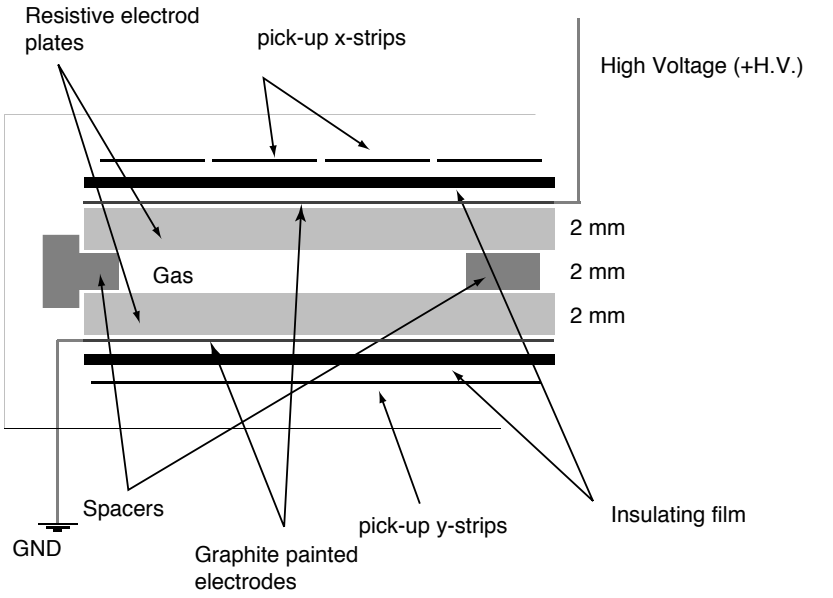

Figure 2.11. *Structure of a single-gap Resistive Plate Chamber.*

The signal produced in the gap by a charged particle is picked-up by two orthogonal strip planes placed on the external side of the electrodes. Such read-out strips are connected with the Front-End Electronics (FEE), which basically consists of a leading-edge discriminator stage followed by a shaper. The strips, placed on both sides of the chambers, provide a bi-dimensional information. In particular, the horizontal strips measure the bending deviation due to the dipole magnetic field, while the vertical strips measure the non-bending direction. The two layers of read-out strips are therefore called "bending" and "non-bending" plane respectively.

In order to ensure a flat occupancy throughout the four trigger planes, the pitch and length of the strips increase with the distance from the beam pipe, approximately in the same proportion as the hit-rate per surface unit decreases. The pitch of the strips is also conditioned by the momentum resolution required for the p_{T} cut: the horizontal strips (bending plane) have widths ranging from about 1 cm (near to the beam pipe) to about 4 cm (in the most peripheral regions), while the vertical

[6]Two different gas mixtures are used depending on the RPC operation mode (streamer or avalanche mode). See [65] for more details.

strips have only widths of 2 and 4 cm since the resolution requirements in the non-bending plane are less stringent. The strips are arranged according to a projective geometry, i.e. the strips pitches in the four detection planes scale with the distance of the plane from the interaction point.

Trigger principle. The p_T cut, required to select the high-p_T muons emitted for instance in the decay of heavy quarkonia, is implemented in the muon trigger system according to a method [65] illustrated in Fig. 2.12.

A muon μ^+ (blue line) created at the interaction point is bent by the dipole magnetic field and fires the two trigger stations MT1 and MT2 in two points whose coordinates, in the bending plane $y-z$, are (y_1, z_1) and (y_2, z_2), respectively. The deviation induced along the y direction by the dipole magnet is defined as

$$\delta y_2 = y_2 - y_{2,\infty} \tag{2.1}$$

where $y_{2,\infty}$ is the y-coordinate of the point in which a muon with infinite momentum crossing MT1 at y_1 would fire MT2. For small deviations (less than 10°), δy_2 can be written in term of the muon p_T with reasonable approximation as

$$\delta y_2 = (z_2 - z_1) \cdot \frac{eBL}{z_1} \cdot (\frac{R_f}{p_T}) \tag{2.2}$$

where B is the dipole magnetic field, L is the dipole length and R_f is the estimated radial position of the muon in the dipole mid-plane. It is therefore clear that a cut on δy_2[7] corresponds to a cut on p_T.

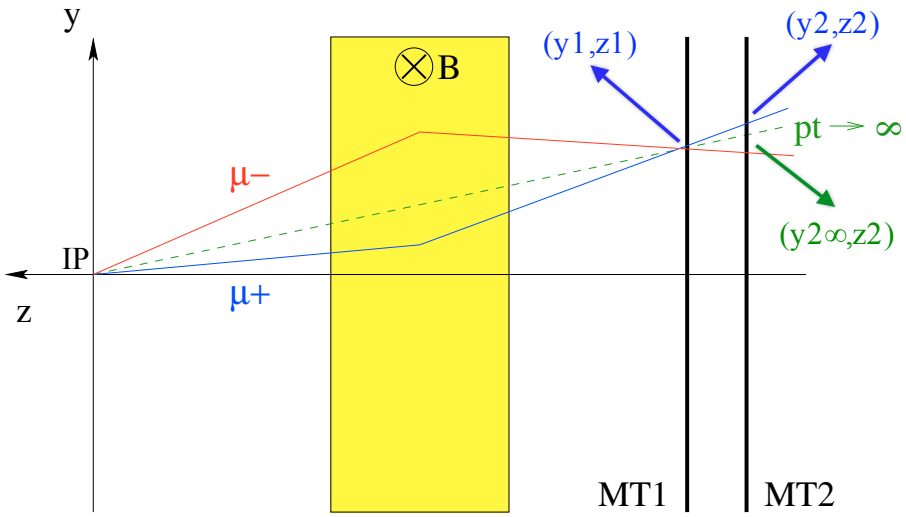

Figure 2.12. *The muon spectrometer trigger principle.*

The δy_2 values, corresponding to a certain p_T cut, have been computed in unit of strips and stored in dedicated tables to be compared with the measured deviations. When one of the two planes in the first trigger station is fired, the trigger algorithm open a road, i.e. a set of strips that should be fired in the other three planes if the track is coming from the IP. If three out of the four planes have

[7] Positive and negative muons (blue and red lines in Fig. 2.12) can be distinguished according to the sign of the deviation.

hits belonging to that road, the track is processed ad its p_{T} is estimated. Depending on the trigger configuration, the trigger signal is issued if there are two unlike-sign tracks or two like-sign tracks or a single track, with transverse momentum above the p_{T} threshold. The choice of a 3/4 condition accounts for possible detector inefficiencies or dead channels.

Trigger electronics

The signals produced in the RPC by a charged particle are picked-up by two orthogonal strip planes and then processed by the Front- End Electronics (FEE), which basically consists of a discriminator. The RPCs are equipped with the ADULT [66] FEE which employs an original dual threshold technique to improve the time resolution of RPC (in streamer mode). A 1-2 ns time resolution, needed for the identification of the bunch crossing (each 25 *ns* in nominal pp collisions), is achieved.

The trigger electronics is organized in three levels: local, regional and global.

First, the digital signals from the FEE are sent to the local trigger electronics: the whole system is divided in 234 detection areas, each of them associated with a local trigger board. The algorithm of the local trigger boards, which are hosted in 16 crates placed close to the trigger stations, searches for a single track pointing approximately back to the IP, using the informations coming from the four RPC detector planes according to a 3/4 trigger condition. In case of single tracks above the (low/high) p_{T} threshold, a trigger signal is delivered.

The local trigger information is then sent to the regional trigger boards (one for each of the above mentioned crates), then to the global trigger electronics which gather the signals of all local boards. The single muon, like-sign and unlike-sign dimuon triggers of the whole detector are finally delivered and enter the general ALICE trigger.

Chapter 3

Data analysis: $J/\psi \to \mu^+\mu^-$ in proton-proton collisions at $\sqrt{s} = 2.76$ TeV

The ALICE experiment at the LHC has recorded, in March 2011, proton-proton (pp) collisions at a center-of-mass energy of $\sqrt{s}$ = 2.76 TeV. The main goal of this short 3-day run was to provide a reference for the Pb-Pb data which were taken at the same $\sqrt{s}$ per nucleon pair at the end of 2010 and end of 2011.

In this chapter, we present the details of the analysis on inclusive J/ψ production in pp collision at $\sqrt{s}$ = 2.76 TeV as obtained by the ALICE Muon Spectrometer. J/ψ mesons are measured, down to zero transverse momentum $p_{\rm T}$, through their dimuon decay channel into $\mu^+\mu^-$ pairs at forward rapidity[1] ($2.5 < y < 4$). We describe the different steps required to obtain the *integrated* and *differential cross-section* for inclusive J/ψ production, the latter one as a function of the J/ψ transverse momentum $p_{\rm T}$ and rapidity y.

First, details are provided concerning the criteria adopted to select runs and events used for the analysis. The different techniques for the extraction of the J/ψ signal are discussed as well as the method followed to determine the acceptance and efficiency corrections. Finally, after describing the procedure for the evaluation of the luminosity and of the sources of systematic errors, the values of the integrated, $p_{\rm T}$-differential and y-differential J/ψ cross-section are presented.

These results also offer the possibility to study J/ψ production at an intermediate energy between the one reached at the Fermilab Tevatron hadron collider (proton-antiproton collisions at $\sqrt{s}$ = 1.8 and 1.96 TeV) and the present (2012) LHC top energy (proton beams at 3.5 and 4 TeV). It represents therefore an interesting test for the available theoretical models.

3.1 Data sample

At the end of March 2011, the LHC accelerator at CERN delivered pp collisions at a center-of-mass energy of $\sqrt{s}$ = 2.76 TeV for a short 3-day run (34 hours of stable beam). The integrated luminosity

[1] In particle physics, the rapidity is defined as $y = \frac{1}{2} ln(\frac{E+p_z}{E-p_z})$ where E and p_z are, respectively, the particle energy and the component of particle momentum along the beam axis. This quantity depends both on the geometry and the kinematics. In the limit of high momentum ($p \gg M$), one obtains $y \simeq \eta$, where η is the pseudorapidity.

$\mathscr{L}_{\rm INT}$, delivered by LHC to the ALICE experiment, correspond to 52.9 nb^{-1}. In Fig. 3.1, we show the time dependence of the instantaneous luminosity for a specific LHC proton beam fill (Fill 1650, $E_{\rm Beam}$ = 1380 GeV) delivered to the four LHC experiments [2].

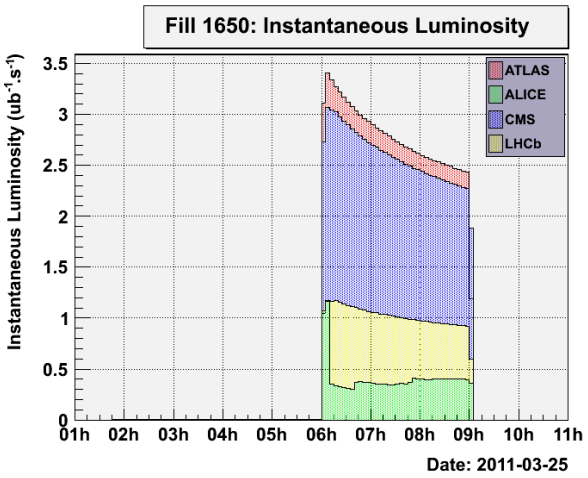

Figure 3.1. *Time dependance of the instantaneous luminosity for the LHC proton beam fill 1650 (E_{Beam} = 1380 GeV). The four colors correspond to the four LHC experiments.*

For the analysis described in this Chapter, the relevant ALICE detector system for muon identification and tracking is the Forward Muon Spectrometer. The details on the detectors used for this analysis can be found in Chapter 2.

The event sample used in this analysis corresponds to two different trigger conditions: the Minimum Bias (MB) and the Muon (μ-MB) trigger conditions. The ALICE data acquisition system (DAQ) has collected MB events with a trigger based on the Silicon Pixel Detector (SPD) and the VZERO counters. The MB trigger is defined as the logical OR between the requirement of at least one fired read-out chip in the SPD, and a signal in at least one of the two VZERO detectors. It also requires a coincidence with signals from two beam pick-up counters, one on each side of the interaction region, indicating the presence of two passing proton bunches. Finally, the μ-MB trigger condition consists in a more restrictive definition by requiring at least one track (above a $p_{\rm T}$ threshold equal to 0.5 GeV/c) in the muon trigger system in addition to the MB trigger condition.

The analysis of the data sample is performed using the official ALICE software framework, called AliROOT[3]. In particular, it takes profits from the ALICE Environment AliEn [67]. AliEn is a Grid framework which provides a virtual file catalogue, allowing access to huge distributed datasets, and a certain number of cooperating computer resources. AliEn enables users to submit, inspect and manipulate a large number of task jobs running concurrently at many sites.

The Event Summary Data (ESD) root files, produced at the end of the reconstruction chain of raw data[4], are the starting input of the analysis process. They contain the full lists of reconstructed tracks/particles and global event properties for each ALICE detector on event basis.

[2] ALICE cannot cope with the high LHC interaction rates and, therefore, the luminosity in pp collisions must be reduced, by displacing the proton beams, with respect to the other LHC experiments. This explains the lower ALICE instantaneous luminosity value shown in Fig. 3.1.

[3] http://aliweb.cern.ch/Offline/AliRoot/Manual.html.

[4] http://aliweb.cern.ch/Offline/Activities/Reconstruction/index.html.

3.1.1 Data Quality Assurance (QA)

The starting point of the analysis is the selection, among all pp collisions data sets at $\sqrt{s}$ = 2.76 TeV recorded by ALICE, of the run list[5] suitable for physics analysis. This list is built up according to quality checks on the detector performances and on beam status.

The first rough selection is performed using the ALICE Electronic Logbook. It is a web interface containing the basic informations, in a run by run format, about different fields such as run duration, beam condition, list of detectors involved in the data taking and number of events collected.

A specific set of cuts was applied following a standard procedure. The main ones are listed thereafter:

- run duration and number of events (MB) recorded greater than, respectively, 10 minutes and 5000 events;
- muon trigger system, VZERO, SPD present in the run, all at once, as Trigger Detectors;
- muon tracking and trigger system, VZERO, SPD present in the run, all at once, as Readout Detectors;

After this selection, we can extract a first list of 20 runs fulfilling the necessary requirements.

Additional informations on the status of the detectors and the proton beam during the whole data-taking period are mandatory to complete the selection and obtain a robust run list for the analysis. For instance, all the runs dedicated to luminosity measurements (Van Der Meer scan) are rejected in the analysis because of the instability of the proton beams.

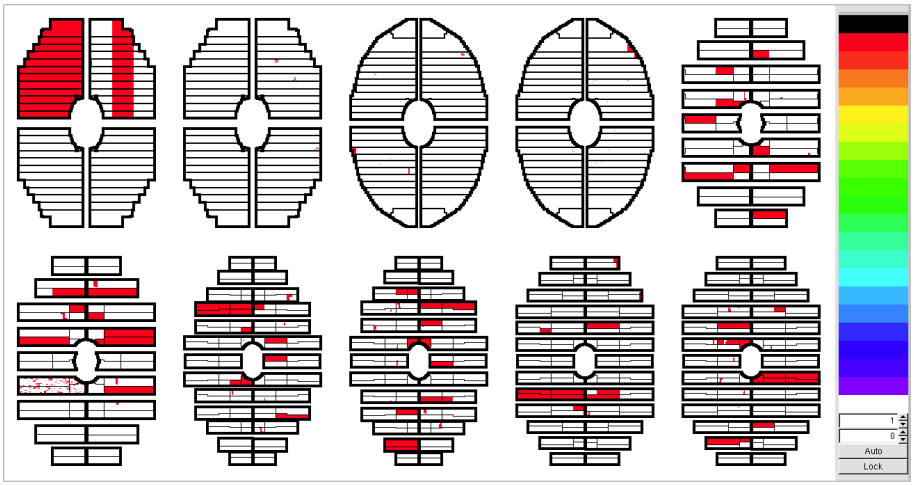

Figure 3.2. *Bending plane status map of the ten tracking chambers during run 146748. Red pads are removed from the configuration.*

In Fig. 3.2 we show, as an example, the status of the ten muon tracking chambers during one of the pp runs at $\sqrt{s}$ = 2.76 TeV taken in March 2011. Each part of the detector which does not fulfill the requirements (red zones) in term of stability of the high voltage, pedestal, noise level or maximum occupancy over the run duration was either removed from the data taking or excluded afterward during the reconstruction.

[5]The ALICE data acquisition system records pp collisions data during various periods of operation called *runs*.

Other relevant variable that should be monitored to check the data quality is the number of tracks, reconstructed in the Forward Muon Spectrometer, per MB or μ-MB trigger event as a function of the different runs. The results are presented in Fig. 3.3.

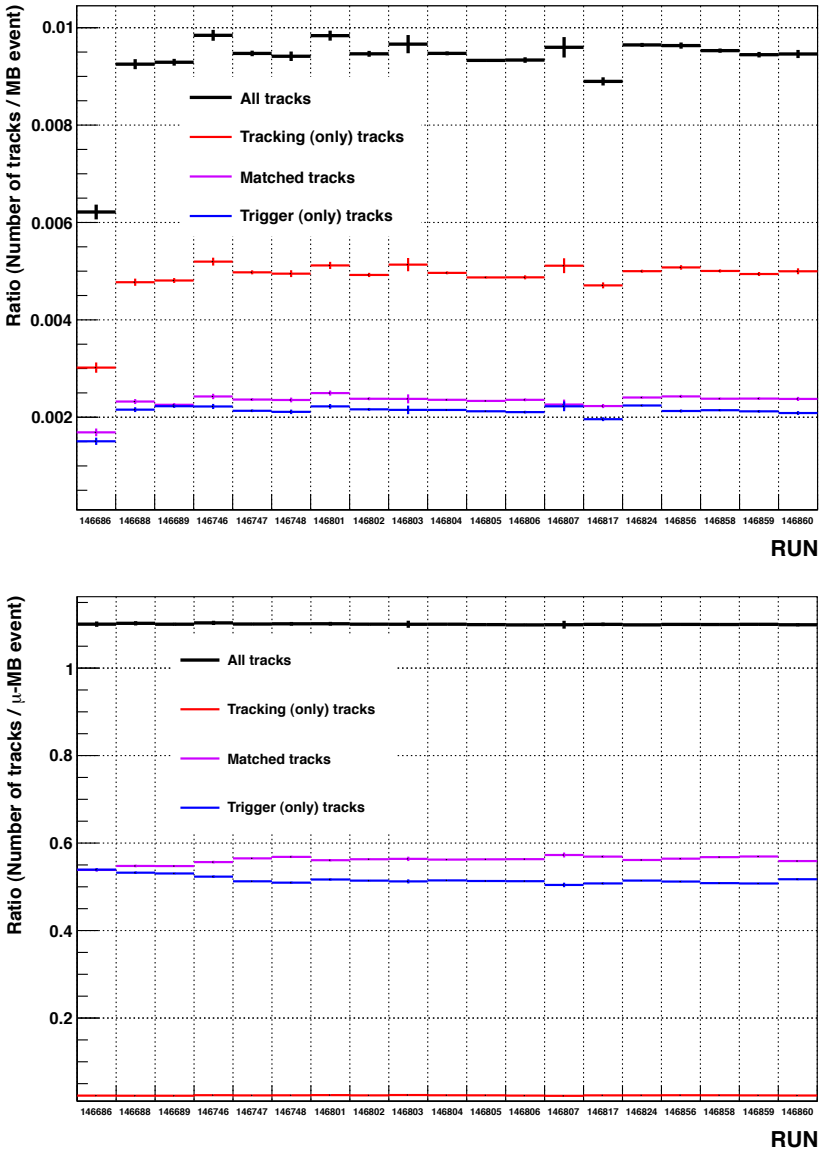

Figure 3.3. *Number of tracks (reconstructed in the Forward Muon Spectrometer) per MB (Top) and μ-MB (Bottom) trigger event as a function of the different runs considered in this analysis.*

This quantity allows us to investigate the status of the Muon Spectrometer in term of efficiency losses which mainly affect the track reconstruction in the detector.

Tracks can be divided into three categories:

- matched tracks are reconstructed tracks containing informations in both the tracking and the trigger detectors of the muon spectrometer;

- tracking-only tracks are tracks reconstructed only in the tracking chambers without any informations from the trigger chambers;

- trigger-only tracks are tracks reconstructed only in the trigger chambers. They cannot be matched to any tracking-only track;

We can observe a quite good stability of these ratios (for both triggers, MB and μ-MB) over the full data-taking period with some fluctuations mostly explicable by the misbehavior of a few detection elements. This is absolutely not an issue since the simulations, used to calculate the acceptance and efficiency corrections (see Section 3.3), are performed on a run-per-run basis taking into account the realistic conditions of the detector in each run.

As we can see in Fig. 3.3 (Top), the ratios in the first column (corresponding to run 146686) present an evident discrepancy with respect to the other runs. Looking at it more in detail, problems with the Silicon Pixel Detector were discovered as a consequence of noisy electronic channels. Therefore, this run was excluded.

In addition, it is interesting to notice the absolute value of the ratios in the two plots (Fig. 3.3 Top and Bottom). The values related to muon trigger events (μ-MB) are higher with respect to minimum bias trigger event (from 0.002 to 0.55 for matched tracks). This can be explained by remembering the μ-MB trigger definition which requires the presence of one muon in the Muon Trigger chambers in coincidence with a MB trigger.

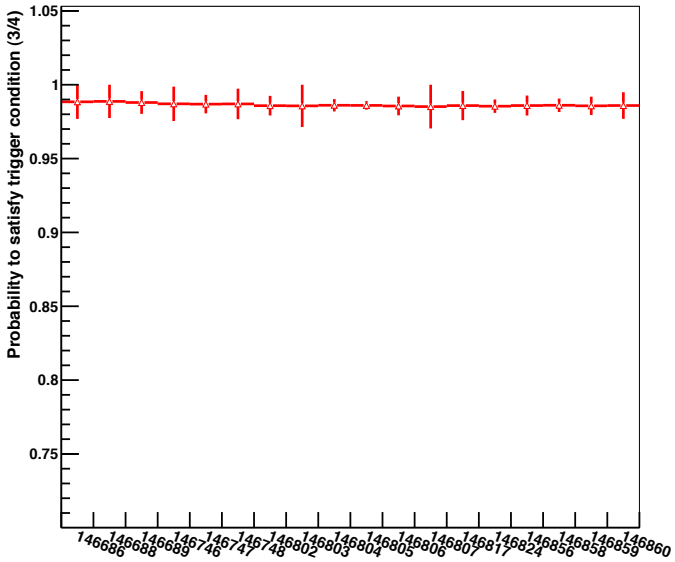

Figure 3.4. *Trigger efficiency of muon trigger system for the analyzed period.*

The status of the Muon Spectrometer trigger system was also monitored by measuring the trigger efficiency (i.e. probability to satisfy the trigger condition, see Appendix D for details) as a function of the different runs. The results, shown in Fig. 3.4, present a good stability with time (~ 99%).

As explained in Appendix D, the trigger efficiency can be inferred, according to the trigger definitions, from the status of the efficiencies of the chambers (i.e. probability of having a signal in the chamber) which are shown in Fig. 3.5. The plot confirms the stability of the chamber efficiency for the 4 planes over the full analyzed period.

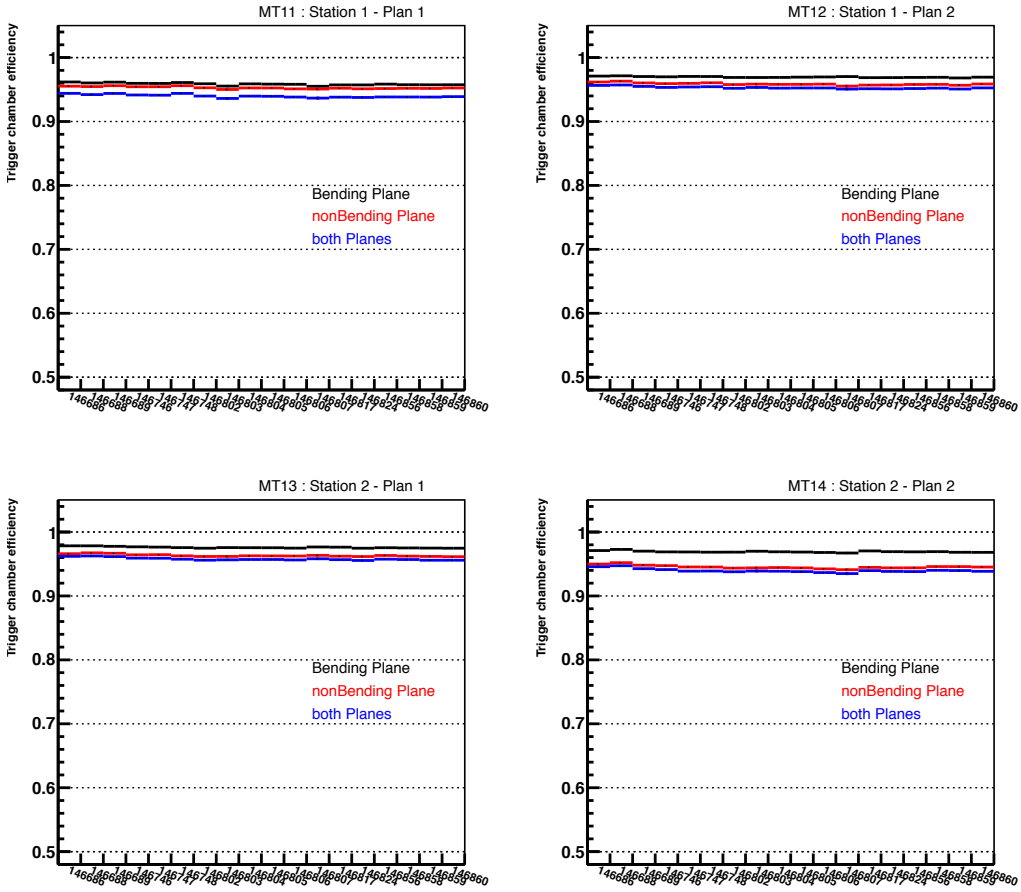

Figure 3.5. *Efficiencies of the trigger chambers as a function of the runs analyzed. The value shown takes into account the intrinsic efficiency of the detection elements and the presence of dead electronic channels. Since the electronic is placed on both sides of the chamber (bending and non-bending plane) in order to provide a bi-dimensional information, the probability of having a signal in each plane separately as well as the probability of having a signal in both planes is shown.*

It should be remarked that the presence of dead areas located in front of each other within the same station (correlated dead areas) can lead to an overestimation of the efficiency. The method (described in Appendix D), used to measure the trigger chamber efficiencies and consequently the trigger efficiency, is blind to these correlated inefficiencies of the detector.

In order to study the impact of the correlated component of the efficiency on the data quality, we can check the number of trigger tracks (matched and trigger-only tracks) per minimum bias event for the analyzed period. The results, shown in Fig. 3.6, present a good stability with time except for the first run which presents a clear drop and was therefore rejected.

In Table 3.1, we show a summary of the chamber efficiencies for the 4 planes of the Muon Trigger system. It shows a good efficiency overall with a slightly better performance in the bending plane than in the non-bending plane.

Finally, after the different selections previously described, 18 runs are qualified as good runs for physics analysis summing up a total of 36 millions MB events and 9 millions μ-MB events (see

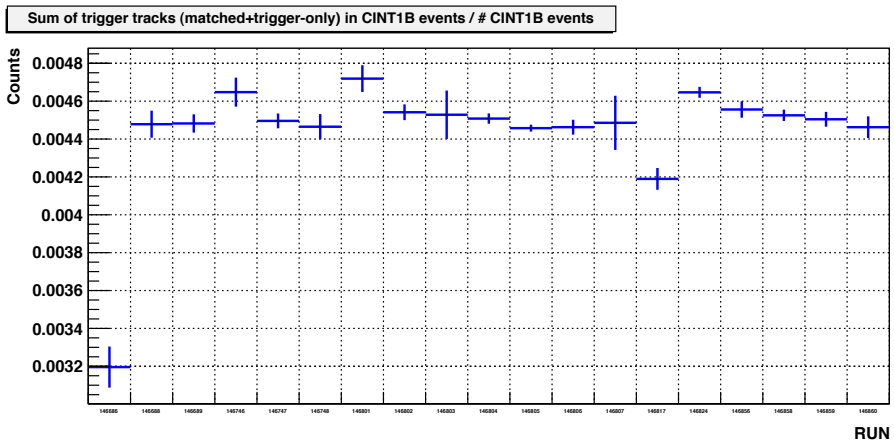

Figure 3.6. *Number of trigger tracks (matched and trigger-only tracks) per minimum bias event for all runs analyzed.*

Global efficiencies (%)

Muon Trigger	MT 11	MT 12	MT 13	MT 14
bending	95.83	96.92	97.53	96.90
non-bending	95.23	95.81	96.26	94.49

Table 3.1. *Summary of the chamber efficiencies for the 4 planes of the Muon Trigger system.*

Appendix A for details).

3.1.2 Event selection

Further selections, at the event level, are mandatory to improve the purity of the total data sample available. In this paragraph we present the physics selection and the vertex selection.

The physics selection is an ALICE framework tool (implemented in a specific class of AliROOT) used to properly select the interesting physics events, i.e. pp collision candidates, in all the data samples. It allows to reject electromagnetic interactions (beam halo) and beam-gas events. These spurious events can be identified with time measurements, performed by the VZERO scintillators. In Fig. 3.7 an example of this measurement is shown.

The total data sample used for our physics studies, after the analysis of all the available ESD files corresponding to the 18-run list, amounts to $3.49 \cdot 10^7$ MB events and $8.8 \cdot 10^6$ events satisfying the μ-MB condition. Once the physics selection is applied, we finally obtain $3.46 \cdot 10^7$ MB events and $8.65 \cdot 10^6$ μ-MB events with a reduction of the statistics of, respectively, 0.9% and 1.8%.

In Fig. 3.8, the percentage reduction of the statistics due to the physics selection is shown as function of the runs analyzed. This allows us to monitor the performances of the rejection over the full period. The trend is quite stable for both trigger events, except for few runs with proton beam instabilities creating higher background events.

As explained in the introduction of this chapter, J/ψ mesons are measured via their dimuon decay channel into $\mu^+\mu^-$ pairs. All tracks reconstructed by the Muon spectrometer are therefore considered

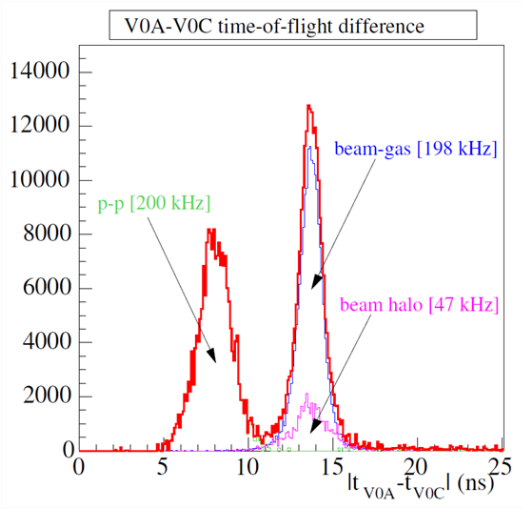

Figure 3.7. *Event identification with time-of-flight difference measurement performed by the VZERO scintillator (VOA and VOC).*

in order to extract the muon pair candidates coming from J/ψ decay process.

Looking at minimum bias events passing the physics selection, 462143 tracks (tracking-only or matched) are found in the pseudorapidity range -4 < η < -2.5 covered by the forward muon spectrometer. While for muon trigger events passing the physics selection, $4.66 \cdot 10^6$ tracks, under the same conditions, are reconstructed.

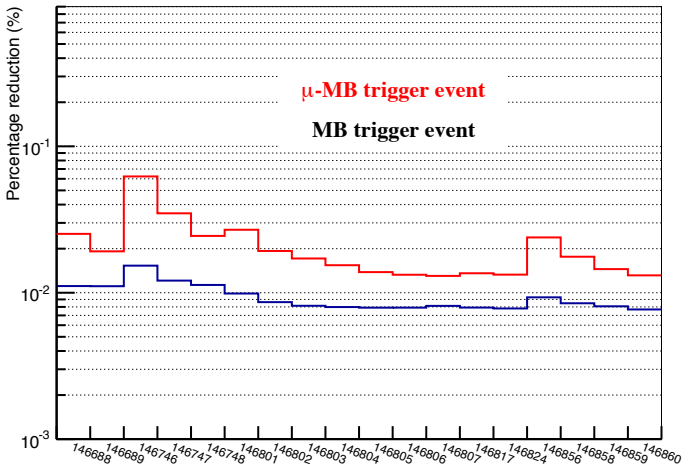

Figure 3.8. *Percentage reduction of the statistics after the application of the physics selection for the full analyzed period (18 runs).*

As we can notice from the previously quoted two numbers, the trigger condition for muon events enables us to enrich considerably our muon sample with respect to minimum bias events. Hence, only muon trigger events are retained in the following steps of the analysis presented.

Another event selection is finally applied taking into account the interaction vertex of the pp

collisions. Events are required to have at least one primary interaction vertex reconstructed by the SPD. Practically, the number of SPD tracklets (called number of contributors) used for primary vertex determination has to be greater than zero. Knowing the primary vertex position allows to improve the reconstruction of the kinematics of the event, in particular in term of track momentum.

This cut rejects 3.76% of the muon event statistics leaving a total of $8.32 \cdot 10^6$ μ-MB events for further analysis.

3.1.3 Muon track selection

The extraction of the J/ψ signal requires the study of the invariant mass distribution for opposite-sign (OS) muon pairs in a mass region around the mass value of the J/ψ resonance ($m_{J/\psi}$= 3096.916 $\pm$ 0.011 MeV from PDG group [10]). From the muon candidate list for each event, we can obtain the muon pairs by considering all the possible combinations of the tracks which are required to have hits at least in the muon tracking chambers.

In Fig. 3.9, the plot shows the invariant mass distributions for opposite-sign muon pairs before and after the application of the event selections (physics and vertex selection). The two distributions, plotted in the mass region $1 < M_{\mu^+\mu^-} < 5$ GeV/c^2, refer only to μ-MB trigger events.

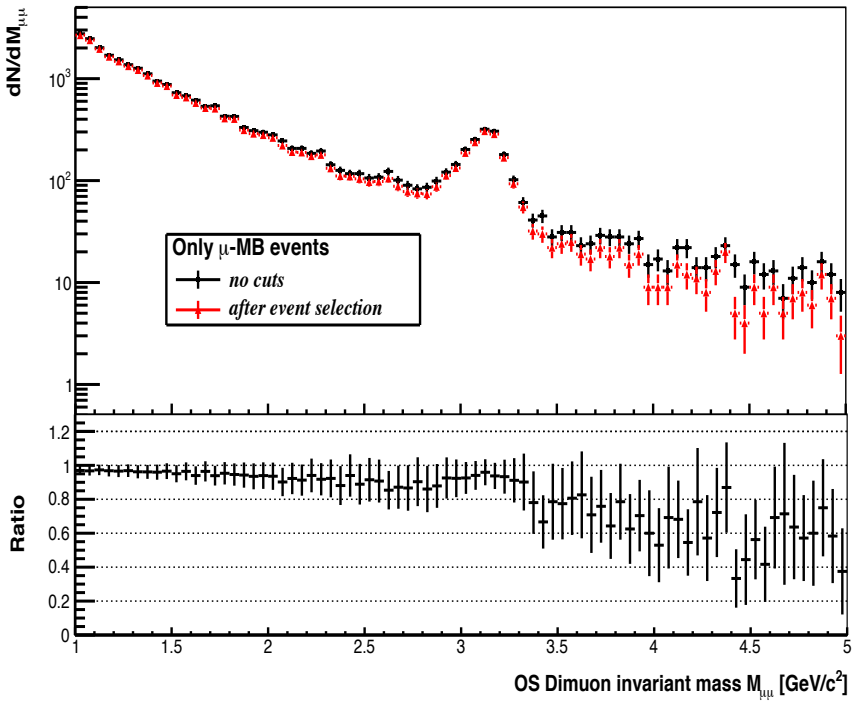

Figure 3.9. *(Top) Invariant mass distribution for opposite-sign muon pairs in the mass region 1 < $M_{\mu^+\mu^-}$ < 5 GeV/c^2. The black and red points correspond, respectively to the distributions before and after the event selection. Only μ-MB trigger events are retained in the analysis. (Bottom) Ratio of the two distributions.*

Initially, the opposite-sign dimuon sample, in the mass region $1 < M_{\mu^+\mu^-} < 5$ GeV/c^2, consists of 25897 OS muon pairs. The event selection reduces this number to 24562 with a decrease of the statistics of 5.16%. Although the distributions shown in Fig. 4.9 are still quite raw and more cuts

are needed to extract the resonance signal, a peak corresponding to the J/$\psi \to \mu^+\mu^-$ decay is clearly visible in the spectrum on top of a continuum.

In order to increase the purity of the muon sample, two track selection criteria are introduced. First, it is required that at least one of the two muon candidates, forming the OS pair, is a matched track. This track, reconstructed in the muon tracking chambers, has therefore to match the corresponding hits in the muon trigger chambers. This cut rejects ~1.5% of the OS muon pairs in the mass region $1 < M_{\mu^+\mu^-} < 5$ GeV/c^2.

With this requirement, hadrons (π, K), produced in the front absorber and stopped by the iron wall positioned upstream of the trigger chambers, can be efficiently rejected. Furthermore, as explained in Chapter 2, the logic of the trigger system allows to select muon candidate tracks having a transverse momentum p_{T} larger than a predefined value. Such a p_{T}^{trig} cut, equal to $\sim$ 0.5 GeV/c for the data sample under analysis, is used to reject soft muons which come mainly from pion and kaon decays.

In Fig. 3.10, the transverse momentum p_{T} distribution for muons coming from J/ψ decay (black points) is shown. It is obtained by a Monte Carlo simulation of 50000 J/ψ produced in proton-proton collision at $\sqrt{s}$ = 2.76 TeV at forward rapidity.

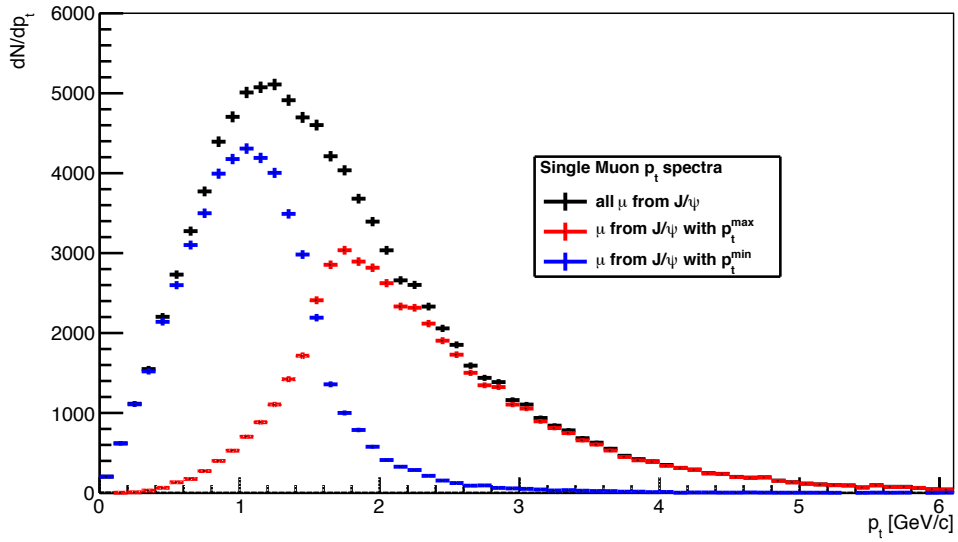

Figure 3.10. *(Black points) Transverse momentum distribution for muons coming from J/ψ decay obtained by a Monte Carlo simulation of 50000 J/ψ in pp collision at $\sqrt{s}$ = 2.76 TeV at forward rapidity. (Red/Blue points) Transverse momentum distribution for the muon carrying the higher/lower p_T of the OS muon pair.*

For each unlike-sign muon pair of the simulated J/ψ sample, it is possible to identify the muon carrying the higher/lower transverse momentum p_{T}. The corresponding p_{T} distribution is plotted with red/blue points in Fig. 3.10.

The J/ψ signal loss induced by the muon trigger cut introduced, as can be verified by analyzing the previous distributions, is negligible. In fact, in the 99.8% of the cases at least one of the two J/ψ decay muons has a transverse momentum larger than the trigger p_{T} threshold (p_{T}^{trig} = 0.5 GeV/c).

In principle, it would be possible to increase even more the purity of the muon sample requiring both candidate muon tracks to be matched tracks. This strict selection would lead to an increase

of the signal to background ratio (S/B), at the J/ψ invariant mass, from 3.8 to 4.9 while the signal significance[6] would remain quite stable (passing from 30.7 to 28.4).

On the other hand, it was checked that this cut would lead to a loss of ~20% of the J/ψ event statistics. Finally, the requirement of having both candidate muon tracks as matched tracks has not been applied since the loss of signal is not justified by the modest increase of the signal to background ratio at the J/ψ invariant mass.

A second track selection concerning R_{abs}, the radial coordinate of the track at the end of the front absorber (Fig. 3.11), is introduced in the analysis. For each track, we require the following condition, $17.6 < R_{abs} < 89.5$ cm, to be respected. This cut allows to retain only unlike-sign muon pairs whose tracks are in the angular window $2° < \theta_{abs} < 10°$, where θ_{abs} is the angle corresponding to the track position at the end of the front absorber.

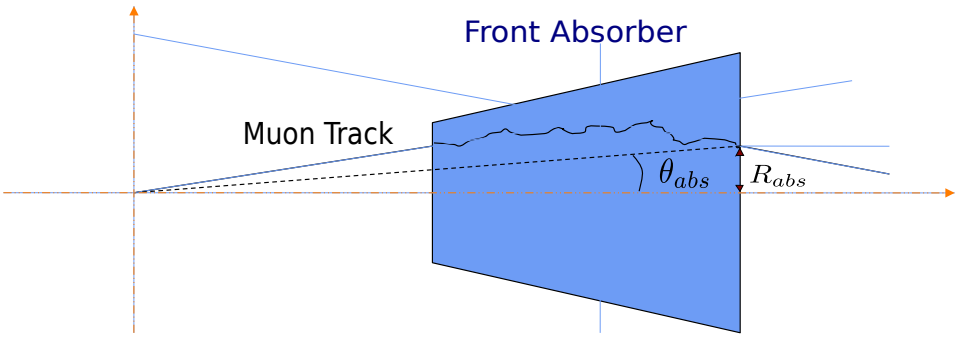

Figure 3.11. *Schematic view of R_{abs} and θ_{abs} in the front absorber.*

With this quality cut, muons emitted at small angles, that have crossed a significant fraction of the thick beam shield (see Chapter 2 for details on the composition of the front absorber) and, consequently, have experienced many multiple Coulomb scatterings in the absorber, can be rejected. Muons emitted at the edge of the front absorber ($\theta_{abs} > 10°$) are rejected as well. This selection discards ~9% of the OS muon pairs in the mass region $1 < M_{\mu^+\mu^-} < 5$ GeV/c^2.

Finally, to define a precise acceptance window where to make the measurement, a cut on the unlike-sign muon pair rapidity[7] ($2.5 < y_{Dimuon} < 4$) is applied.

After the application of the event and muon track selection, the OS muon pair sample available for analysis purpose consists of 21858 dimuon pairs. In Table 3.2, we show a summary of all selection cuts introduced pointing out the effect on the number of OS muon pairs in the mass region $1 < M_{\mu^+\mu^-} < 5$ GeV/c^2.

3.2 Signal extraction

In Fig. 3.12 (red points) we present the OS invariant mass spectrum for the mass region $1 < M_{\mu^+\mu^-} < 5$ GeV/c^2 after the application of the event and muon track selection. A peak corresponding to to the J/$\psi \to \mu^+\mu^-$ decay is clearly visible in the spectrum on top of a continuum while the signal corresponding to the $\psi(2S)$ decay is too weak to be visible.

[6] Definition of signal significance: $\frac{S}{\sqrt{S+B}}$.

[7] The muon spectrometer covers, in the ALICE official reference frame, a negative η range and, consequently, a negative y range. However, since in proton-proton collisions the physics is symmetric with respect to y = 0, the negative sign, when quoting the rapidity values, has been dropped.

Summary of the selection cuts

Selection cuts	Number of OS muon pairs
only μ-MB events	25897
+ event selection	24562
+ 1 muon matching MTR	24198
+ 17.6 < R_{abs} < 89.5 cm	21992
+ 2.5 < y_{Dimuon} < 4	21858

Table 3.2. *Summary of the selection cuts introduced in the analysis. The second column shows the number of OS muon pairs in the mass region 1 < $M_{\mu^+\mu^-}$ < 5 GeV/c^2, after the application of the different selection cuts.*

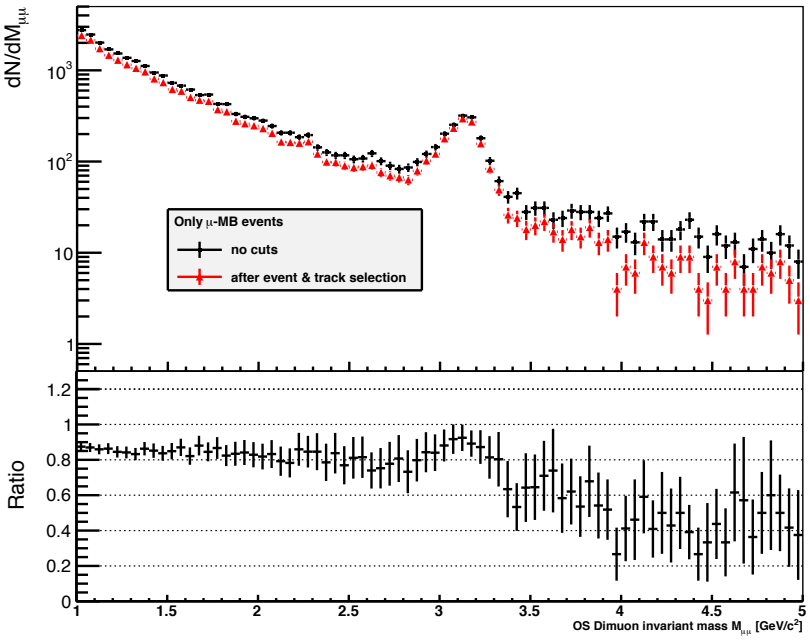

Figure 3.12. *(Top) Invariant mass distribution for opposite-sign muon pairs in the mass region 1 < $M_{\mu^+\mu^-}$ < 5 GeV/c^2. The black and red points correspond, respectively, to the distributions before and after the selections (event and track). Only μ-MB trigger events are retained in the analysis. (Bottom) Ratio of the two distributions.*

The integrated J/ψ raw yield (total number of J/ψ, $N_{J/\psi}$, under the conditions 2.5 < $y_{J/\psi}$ < 4 and $p_T{}^{J/\psi}$> 0) is extracted by fitting the invariant mass spectrum (red distribution in Fig. 3.12) in the mass region 1 < $M_{\mu^+\mu^-}$ < 5 GeV/c^2.

The fitting function contains two components: the underlying continuum (background) and the J/ψ signal (the ψ(2S) signal is not included in the fitting procedure). In order to correctly subtract the background, it is important to reproduce it very well knowing its origin.

The source of the background can be divided into two different contributions. The first one, which

is dominant before the J/ψ peak at low $M_{\mu^+\mu^-}$, consists of muons (μ^+ and μ^-) coming from the decays of pions and kaons (π, K). While the second one, which is dominant at high $M_{\mu^+\mu^-}$ after the J/ψ peak, is composed of muons produced in semi-leptonic decays of heavy quarks (c and b).

The two sources of the background allow to explain its different shape before and after the J/ψ peak. As we can see in Fig. 3.12 (Top), where a logarithmic scale is used on the y-axis, the underlying continuum presents a practically linear behavior with two different slopes away from the J/ψ resonance region. A sum of two exponentials $B(x)$ (Eq. 3.1) has been consequently assumed as fitting function for the background:

$$B(x) = A \cdot e^{B \cdot x} + C \cdot e^{D \cdot x}. \tag{3.1}$$

The four parameters A, B, C and D are all kept as free parameters in the fit procedure.

Concerning the J/ψ signal, different functions have been tested in the fit to describe the resonance line shape: the Gaussian function, the Crystal Ball functions [68] (in the standard and extended form) and the so-called NA50 / NA60 function [69] (definitions in Appendix B).

As shown in Fig. 3.13, showing the invariant mass distribution for opposite-sign muon pairs of a pure Monte Carlo J/ψ signal sample, the J/ψ line shape is clearly asymmetric due to non-gaussian fluctuations around the J/ψ mass pole. They are the result of the energy-loss processes involving every muon track crossing the front absorber, and of the radiative J/ψ decay.

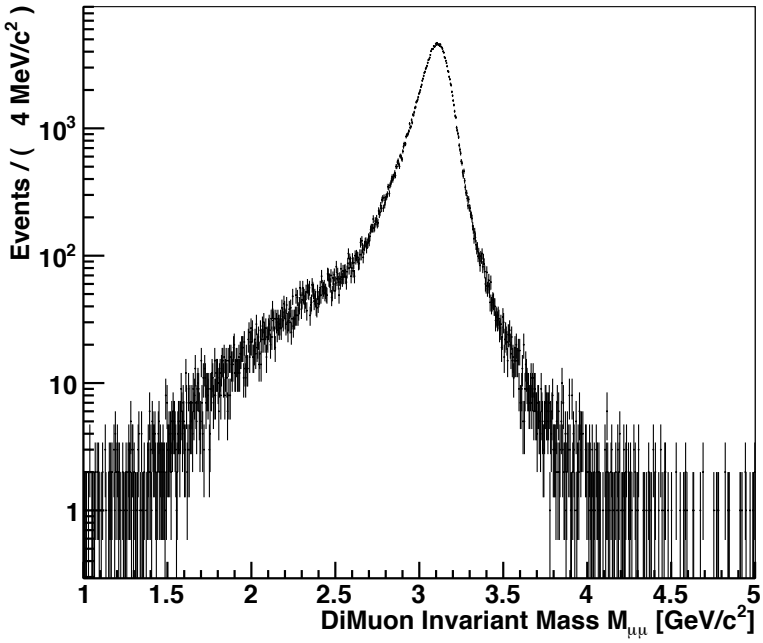

Figure 3.13. *Invariant mass distribution for opposite-sign muon pairs in the mass region 1 < $M_{\mu^+\mu^-}$ < 5 GeV/c^2 of a pure Monte Carlo J/ψ signal sample (~ 2.5· 10^5 J/ψ). The simulation of the sample of J/ψ signal events, according to a specific p_T and y distribution (see details in Section 3.3), is performed taking into account the realistic conditions of the Forward Muon Spectrometer.*

For that reason, the Gaussian function appears to be unsuitable to describe correctly the J/ψ line shape in the fit procedure and, consequently, has been discarded.

Although all the other fitting functions (CBs and NA50/NA60) can reproduce, in a satisfactory way, the J/ψ resonance with the ultimately collected statistics, the standard Crystal Ball function

has been finally selected for the J/ψ signal extraction. It minimizes the number of free parameters involved in the fit procedure with respect to the other functions and, in addition, it is widely adopted by different LHC experiments as standard fit function for charmonia resonances.

The comparison of the J/ψ yields coming from different extraction methods will be important afterward, as described in Section 3.5.1, since it allows to estimate the systematic uncertainties on the signal extraction procedure.

As explained in Appendix B, the Crystal Ball function consists of a Gaussian core portion and a power-law low-end tail defined by two parameters: α and n. In the fit process, the two parameters can be left completely free, within a certain interval, or they can be fixed using the values obtained by fitting the expected mass distribution of a pure Monte Carlo J/ψ signal sample (Fig. 3.13).

Finally, the second conservative approach has been followed since, with the available statistics and signal to background ratio, the tail's parameters can not be reliably fixed through the fitting procedure. The fit to the invariant mass distribution of the pure Monte Carlo J/ψ signal sample, performed by a Crystal Ball function, is shown in Fig. 3.14.

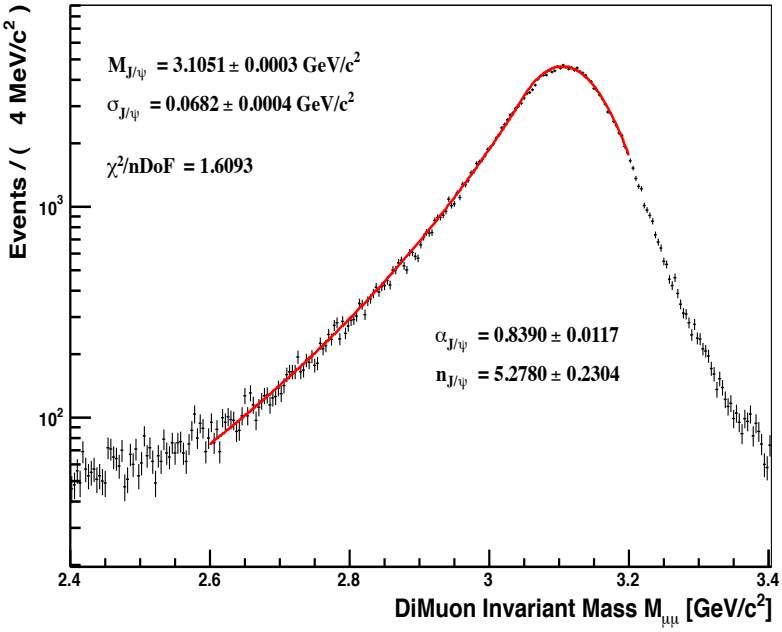

Figure 3.14. *Invariant mass distribution for opposite-sign muon pairs of a pure Monte Carlo J/ψ signal sample in the mass region 2.4 < $M_{\mu^+\mu^-}$ < 3.4 GeV/c^2 . The invariant mass spectrum is fitted by a Crystal Ball function in the mass range 2.6 < $M_{\mu^+\mu^-}$ < 3.2 GeV/c^2 and the result of the fit is shown in red.*

The low-end tail's parameters, extracted from the previous fit (χ^2/nDoF = 1.61), are: α = 0.84 ± 0.01 and n = 5.28 ± 0.23. With this choice of parameters, we can finally extract the integrated J/ψ yield $N_{J/\psi}$. In order to account for small uncertainties in the Monte Carlo description of the experimental set-up, the position of the J/ψ mass pole $m_{J/\psi}$, as well as the width of the Crystal Ball function $\sigma_{J/\psi}$, is kept as free parameters in the final fit. This consists of two different steps.

Firstly, an initial estimation of the background is obtained by fitting the underlying continuum, away from the J/ψ resonance (1.5 < $M_{\mu^+\mu^-}$ < 2.2 GeV/c^2 and 3.8 < $M_{\mu^+\mu^-}$ < 5 GeV/c^2), with the exponential function $B(x)$ (Eq. 3.1). We can, therefore, roughly determine an estimate for the

parameters A, B, C and D that can be used as initial values in the next fitting step. Finally, we perform the global fit, signal and background together, to get the best estimation of all the parameters.

This fit procedure leads to a satisfactory fit (χ^2/nDoF = 1.42) of the integrated invariant mass distribution in the mass range $1.5 < M_{\mu^+\mu^-} < 5$ GeV/c^2, as shown in Fig. 3.15.

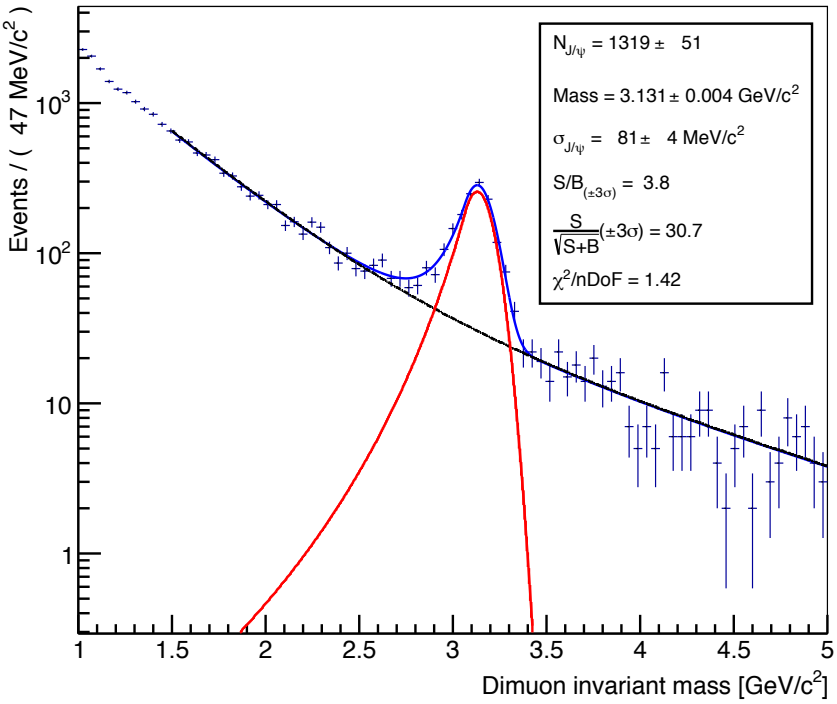

Figure 3.15. *Invariant mass distribution for opposite-sign muon pairs ($2.5 < y_{J/\psi} < 4$, $p_T^{J/\psi} > 0$ GeV/c) in the mass region $1 < M_{\mu^+\mu^-} < 5$ GeV/c^2 with the result of the fit performed in the mass range $1.5 < M_{\mu^+\mu^-} < 5$ GeV/c^2. Three different functions are plotted. The blue line represents the global fit. The J/ψ signal contribution is shown in red line. The dashed black line shows the background contribution.*

The standard Crystal Ball function, describing the J/ψ line shape, is peaked at $m_{J/\psi} = 3.131 \pm 0.004$ GeV/c^2. Such a value is larger than the one quoted by the Particle Data Group [10] (PDG value: $m_{J/\psi} = 3096.916 \pm 0.011$ MeV/c^2) by ~ 1%, showing that the accuracy of the magnetic field mapping, of the energy loss correction and of the tracking chamber alignment is reasonably under control.

The measured width of the Crystal Ball function, $\sigma_{J/\psi} = 81 \pm 4$ MeV/c^2, presents a discrepancy with respect to the value, $\sigma_{J/\psi} = 68.2 \pm 0.4$ MeV/c^2, obtained fitting the pure Monte Carlo J/ψ signal sample (Fig. 3.14). This can be explained by considering the details of the simulation procedure. Although the Monte Carlo simulation takes into account the realistic conditions of the detector, the generation of the J/ψ particles and the successive reconstruction of the unlike-sign muon pairs are not fully realistic. Actually, all the J/ψ particles are generated, for simplicity reasons, exactly in the nominal interaction point (nominal IP {0.,0.,0.}). The same approximation is used at the reconstruction stage of the OS muon pairs. This results in an overestimated resolution (lower $\sigma_{J/\psi}$) of the Forward Muon Spectrometer. Once a realistic vertex distribution is implemented in the Monte Carlo

simulation code, the measured J/ψ width is in fair agreement with MC value[8].

Finally, the total number of J/ψ signal events, obtained by integrating the Crystal Ball function over the mass range $1 < M_{\mu^+\mu^-} < 5$ GeV/c^2, is $N_{J/\psi} = 1319 \pm 51$ (stat.). The signal to background ratio, at three standard deviations, $S/B_{(\pm 3\sigma)}$ is equal to 3.8 while, for the signal significance, one gets $S/\sqrt{S+B}_{(\pm 3\sigma)} = 30.7$.

The J/ψ statistics, collected in the dimuon channel, also allow us to study the resonance production as a function of two kinematic variables: the transverse momentum p_T and the rapidity y (see Fig. 3.16 and 3.17). The p_T-dependance has been studied in seven bins {0-1, 1-2, 2-3, 3-4, 4-5, 5-6, 6-8 GeV/c} while six bins ($2.5 < y < 4$, $\Delta y = 0.25$) have been considered for the y-dependence.

The fitting technique is the same as the one used for the integrated invariant mass spectrum (Fig. 3.15). The underlying continuum is described with the sum of two exponential functions, $B(x)$ (Eq. 3.1), and the J/ψ line shape is fitted using the standard Crystal Ball function.

The tails of the CB function are fixed, bin by bin, to the Monte Carlo since the available J/ψ statistics cannot permit to reliably extract the α and n parameters from the fitting procedure. The α and n values, used to fix the CB's tails in each p_T and y bin, are listed in Appendix B.

Unlike the integrated case, the value of the CB width has been fixed for each bin i to the value $\sigma^i_{J/\psi} = \sigma_{J/\psi} \cdot (\sigma^{i,MC}_{J/\psi} / \sigma^{MC}_{J/\psi})$, i.e. by scaling the measured width for the integrated spectrum ($\sigma_{J/\psi}$) with the MC ratio between the widths for the bin i and for the integrated spectrum. This conservative approach follows as a consequence of the limited available J/ψ statistics which prevent us to be fully confident in the extraction of the resonance's width directly from the measured distributions. Finally the position of the J/ψ mass pole $m_{J/\psi}$ is kept as free parameter in the final fit.

In Fig. 3.16 and 3.17 the invariant mass spectra corresponding to the various p_T and y bins are shown, together with the results of the fits. As we can clearly see in the various plots, the J/ψ signal is well visible also in the bins with lower statistics and the quality of the fits is similar to the one obtained for the integrated mass spectrum (in details: $0.81 < \chi^2/\text{nDoF} < 2.43$ for p_T and $0.66 < \chi^2/\text{nDoF} < 1.55$ for y). The sum of the J/ψ signal events for both p_T and y bins agrees well (within 0.24% and 0.53% respectively) with the result of the fit to the integrated mass spectrum (Fig. 3.15).

3.3 Acceptance and efficiency corrections

In order to calculate the integrated and the differential (p_T and y) J/ψ production cross sections, the J/ψ yields extracted from the previous fits must be properly corrected. The corrections take into account the acceptance of the apparatus and the realistic conditions of the detectors during the data taking, in term of reconstruction and triggering efficiencies.

The numerical values of the acceptance and efficiency corrections can be obtained with a Monte Carlo simulation based on the generation of a large sample of signal events (~ $1 \cdot 10^6$ J/ψ generated in total). The J/ψ resonances are generated using realistic p_T and y distributions, tuned for proton-proton collisions at $\sqrt{s}$ = 2.76 TeV, by interpolating existing measurements at different energies (Tevatron, RHIC and LHC).

In more details, the transverse momentum and rapidity distributions used as input for the Monte Carlo simulations are based on the phenomenological interpolations discussed in [70]. In this article, a procedure to evaluate the energy dependence of the inclusive J/ψ integrated and differential cross sections in pp collisions is presented following different approaches.

In Fig. 3.18 we show the two distributions used, in our analysis, as input for Monte Carlo simulations. A model independent approach to the extrapolation of the p_T and y distribution has been finally

[8] A realistic vertex distribution has been implemented in the Monte Carlo simulation code tuned for Pb-Pb collisions. The MC and real J/ψ widths are, in this case, compatible (75 *vs* 78 MeV/c^2).

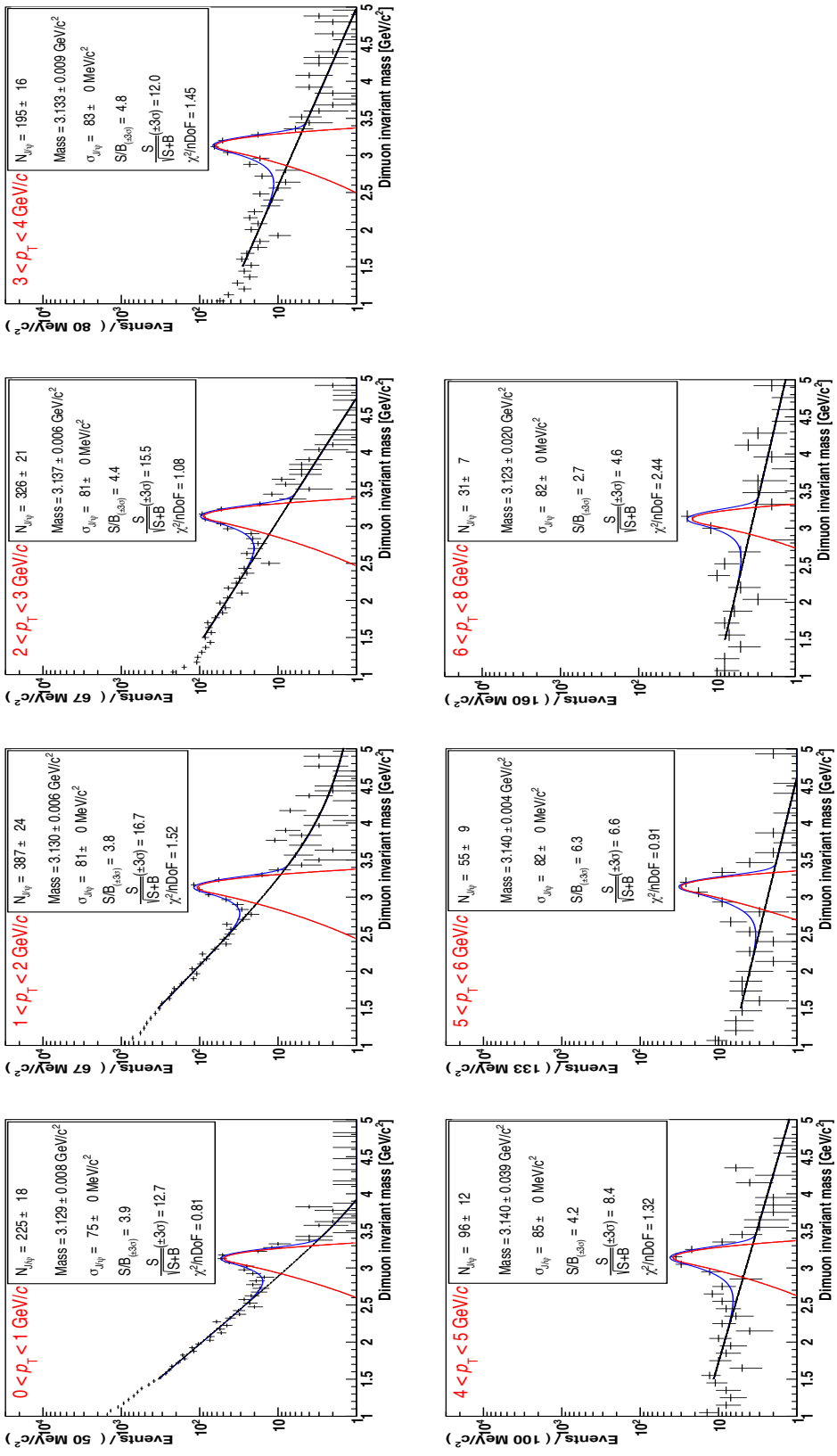

Figure 3.16. *Invariant mass spectra for OS muon pairs ($2.5 < y < 4$) in 7 bins of p_T in the range 0-8 GeV/c. The results of the fits are also shown. Three different functions are plotted for each p_T bin. The blue line represents the global fit. The J/ψ signal contribution is shown in red line. The dashed black line shows the background contribution.*

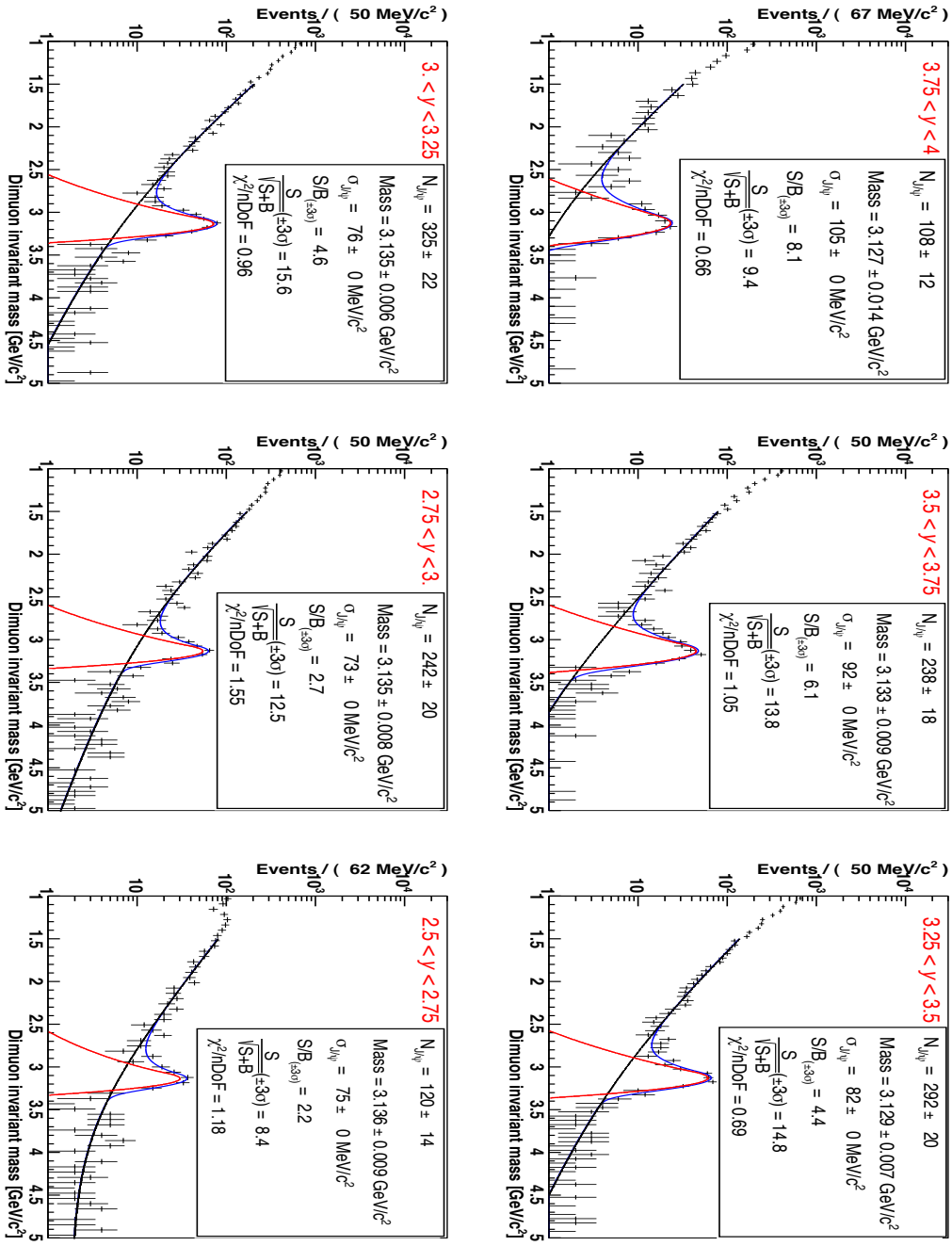

Figure 3.17. *Invariant mass spectra for OS muon pairs ($p_T > 0$ GeV/c) in 6 bins of rapidity in the range $2.5 < y < 4$. The results of the fits are also shown. Three different functions are plotted for each y bin. The blue line represents the global fit. The J/ψ signal contribution is shown in red line. The dashed black line shows the background contribution.*

adopted looking for an universal energy scaling behavior in the two distributions measured at different energies. With this approach there is no need for *a priori* assumptions and the results only depend on the function form (gaussian for the rapidity distribution) used to fit the existing measurements with their uncertainties at different energies. In Appendix C the exact definition of the two functions is shown.

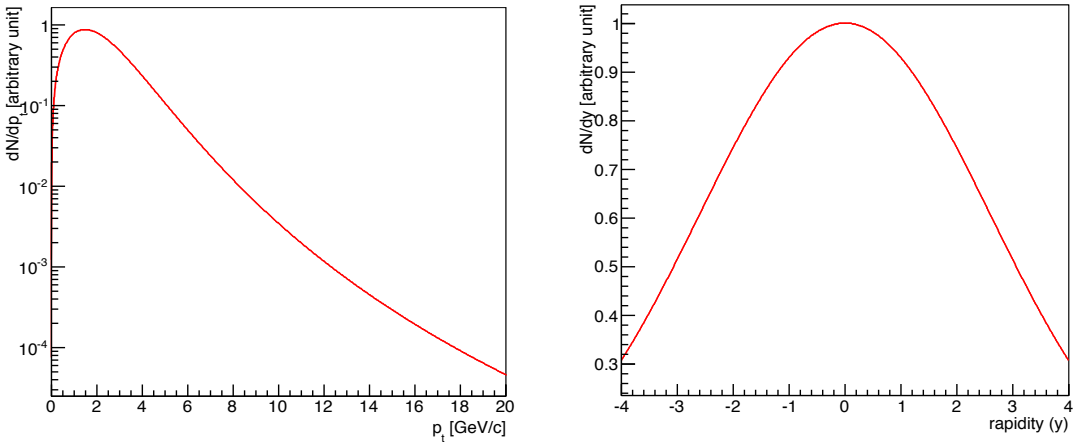

(a) *Transverse momentum p_T distribution.* (b) *Rapidity y distribution.*

Figure 3.18. *p_T and y dependence used as input in the Monte Carlo simulations required for the determination of the acceptance and efficiency corrections.*

As implemented in the Monte Carlo simulation code (based on AliROOT)[9], each generated event contains one single J/ψ which is forced to decay into an opposite-sign muon pairs ($\mu^+\mu^-$). In order to take into account the loss of J/ψ events due to smearing effects at the edge of the rapidity acceptance ($2.5 < y < 4$), the J/ψ generation was performed over a y range ($2.3 < y < 4.2$) wider than that covered by the forward muon spectrometer. Furthermore, the J/ψ production was assumed completely unpolarized in our simulations.

Although the status of the forward muon spectrometer was rather stable all over the full period of data taking, small run by run variations of the tracking and trigger systems, like readout-masked regions or high-voltage-tripped regions, may have occurred. These effects must be included within the simulations to correctly reproduce the realistic conditions of the detector. This can be achieved by performing a Monte Carlo generation separately for the 18 runs of the data sample under analysis. For each run the number of J/ψ signal events generated should be proportional to the integrated luminosity collected in that specific run. This condition allows to properly take into account the different run statistics in the calculation of the acceptance and efficiency corrections.

To take into consideration, within the Monte Carlo simulation code, the real conditions of the detector during the data taking, for both tracking and trigger systems, the following procedure has been adopted. The starting point is a database, the so-called Offline Conditions Database (OCDB[10]), the place where detailed run-dependent informations on the detector status are stored during the data taking. For what concern the muon tracking system, different informations can be found in the OCDB

[9] See http://aliweb.cern.ch/Offline/Activities/Simulation/index.html.

[10] The Offline Conditions Database (OCDB) is not a "database" in the literal sense of the word (like Oracle, MySQL, etc) Actually, it is a set of entries in the AliEn file catalog [67] that points to physical entities (ROOT files stored in the various storage elements of the Grid).

like the status of each electronic channel with respect to the Front-end readout, the high voltage (HV) status of the ten tracking planes or the residual misalignment of the detection elements.

During the reconstruction of the raw data, the objets stored in the OCDB allow to calibrate the detectors and then to properly reconstruct the recorded data by applying quality cuts defined in the reconstruction parameters. The same calibration objects and reconstruction parameters can also be used during the reconstruction of the Monte Carlo simulated data, thus making sure the same selections are applied with respect to the real raw data reconstruction.

Thank to these informations, the detector response (after the muon passage in the detector) can therefore be tuned in the simulations according to the realistic detector behavior. For example, the cluster charge/size measured for the tracking chambers can be reproduced including a realistic channel-dependent electronic noise corresponding to the pedestal fluctuations measured during the data taking.

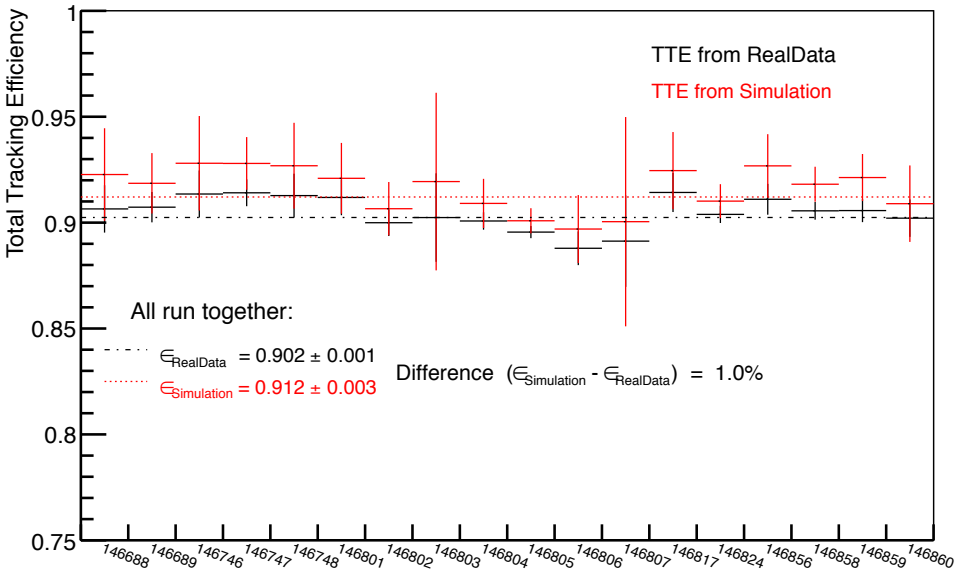

Figure 3.19. *Total Tracking Efficiency as a function of the run number. The black and red points correspond, respectively, to the tracking efficiency evaluated from the real data and simulated data.*

In order to verify the validity of this procedure, it can be useful to consider the total tracking efficiency of the muon spectrometer (the method for its evaluation is presented in Appendix D). In Fig. 3.19, the total tracking efficiency is shown for the 18 runs analyzed, comparing the result obtained from the real data (black points) to the simulated data (red points). The total tracking efficiencies are, respectively, $(90.2 \pm 0.1)\%$ and $(91.2 \pm 0.3)\%$. With a 1% difference, we can be confident about the validity of procedure used to reproduce the realistic status of the muon spectrometer.

Finally, for what concern the trigger system, a realistic description of the trigger response is achieved by directly using in the simulations the efficiency of the detection elements measured with the real data and averaged over the full period of data taking. The obtained efficiencies (see in Appendix D the method used to calculate the trigger efficiency) are simply plugged, through the OCDB database, in Monte Carlo simulation.

3.3.1 Integrated acceptance and efficiency correction

For each run, the ratio between the total number of reconstructed J/ψ events, satisfying the analysis cuts presented in Section 3.1.3, and the total number of generated events in the kinematical ranges p_{T} > 0 GeV/c and 2.5 < y < 4 gives the integrated correction, A×ε, for acceptance and efficiency. They are shown in Fig. 3.20.

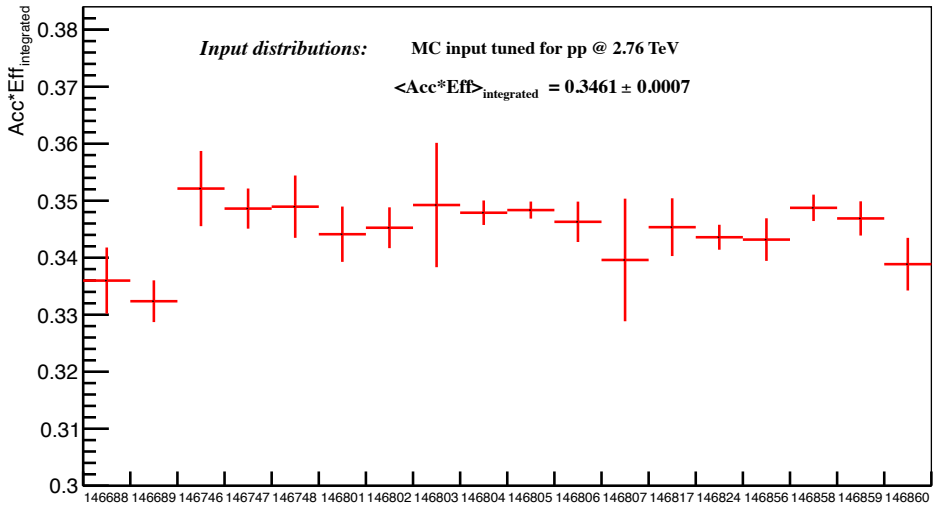

Figure 3.20. *The integrated acceptance and efficiency corrections, A×ε_i, as a function of the 18 runs analyzed.*

The differences between the A×ε_i for the various runs do not exceed 4% with respect to their average value which is equal to <A×ε> = 0.3461 ± 0.0007.

3.3.2 p_{T} and y dependence of the acceptance and efficiency corrections

The study of the differential J/ψ production as a function of the transverse momentum and the rapidity requires the evaluation of the p_{T} and y dependence of the A×ε corrections. Due to the limited collected statistics which prevent us from doing an analysis of the J/ψ production in bin of p_{T} and y together, a one-dimension approach has been used. Hence, the acceptance and efficiency corrections are calculated separately for p_{T} and y.

The same binning, introduced in Section 3.2 to extract the differential J/ψ yield, is used here. In Fig. 3.21 the A×ε corrections are plotted as a function of the two kinematical variables for the 18 runs under analysis. The p_{T} and y dependence of the A×ε corrections, averaged over the full period of data taking, are instead plotted in Fig. 3.22 and 3.23.

It is worth noting that the A×ε corrections exhibit, at forward rapidity in the muon spectrometer, a rather small variation as a function of the J/ψ p_{T} varying in the range 0.326 - 0.507. This corresponds to, respectively, - 6% and + 47% with respect to the integrated A×ε value, <A×ε> = 0.3461 ± 0.0007. Furthermore, the p_{T} dependence of A×ε, which shows an increase with the J/ψ p_{T}, presents a non-zero correction down to low p_{T}. As a consequence, the study of the J/ψ production is feasible down to zero p_{T} and represents an unique feature of ALICE at the LHC.

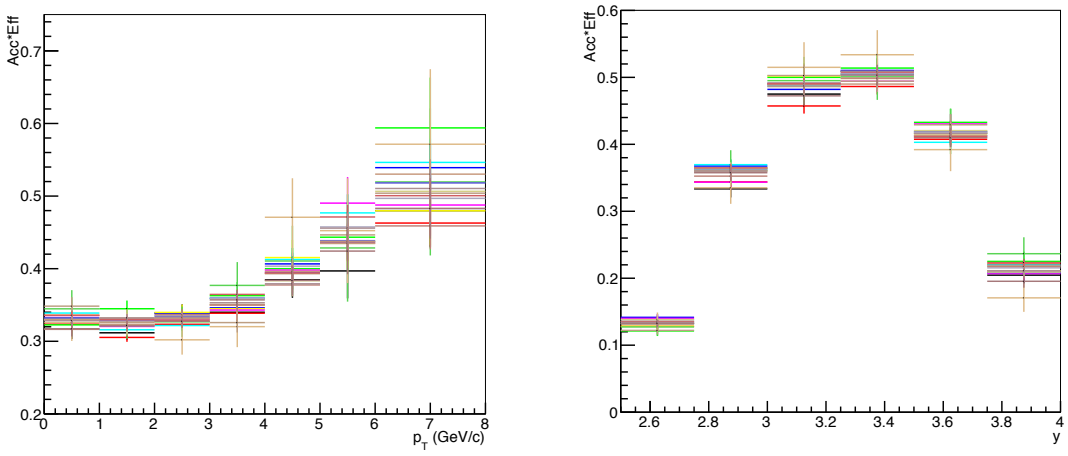

(a) p_T *dependence.* (b) *y dependence.*

Figure 3.21. *Acceptance and efficiency corrections as a function of the kinematical variables, p_T (a) and y (b), for the 18 runs analyzed(plotted with different colors).*

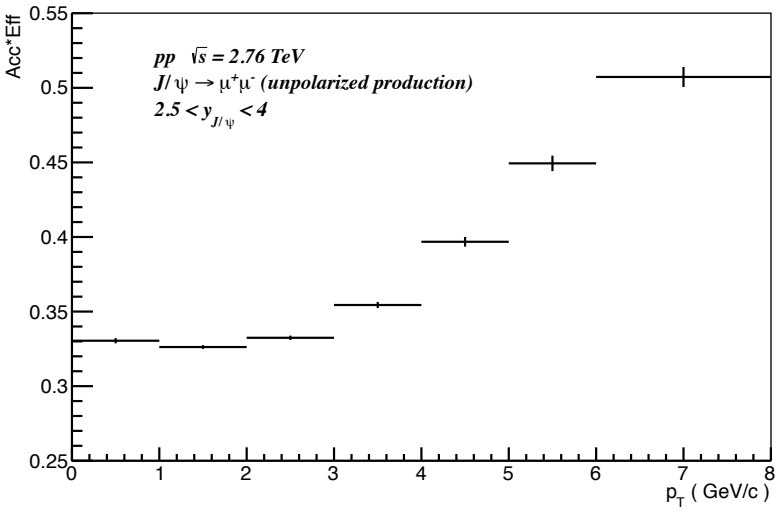

Figure 3.22. *(Top) Transverse momentum dependence of the A×ε corrections averaged over the full period of data taking.*

3.3.3 The effect of the J/ψ polarization

The A×ε corrections, shown in Fig. 3.22 and 3.23, are calculated by performing a Monte Carlo simulation of fully unpolarized J/ψ meson. However, since the degree of J/ψ polarization is unknown, it is important to study and quantify the effect of a J/ψ non-zero polarization on the corrections.

Experimentally, the J/ψ polarization can be measured through the angular analysis of the its decay products. The angular distribution of the decay muons can be expressed in the general form [71]

$$W(\theta,\phi) \propto \frac{1}{3+\lambda_\theta}(1+\lambda_\theta cos^2\theta + \lambda_\phi sin^2\theta cos2\phi + \lambda_{\theta\phi} sin2\theta cos\phi), \tag{3.2}$$

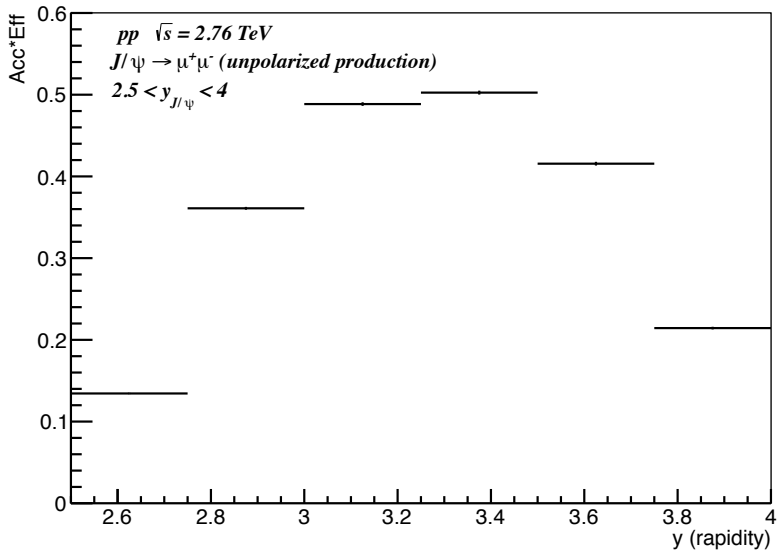

Figure 3.23. *Rapidity dependence of the A×ε corrections averaged over the full period of data taking.*

where θ (ϕ) are the polar (azimuthal) muon angles in a given reference frame[11]. The two reference frames relevant in our analysis are: the Collins-Soper (CS) and helicity (HE) frames [72], schematically displayed in Fig. 3.24.

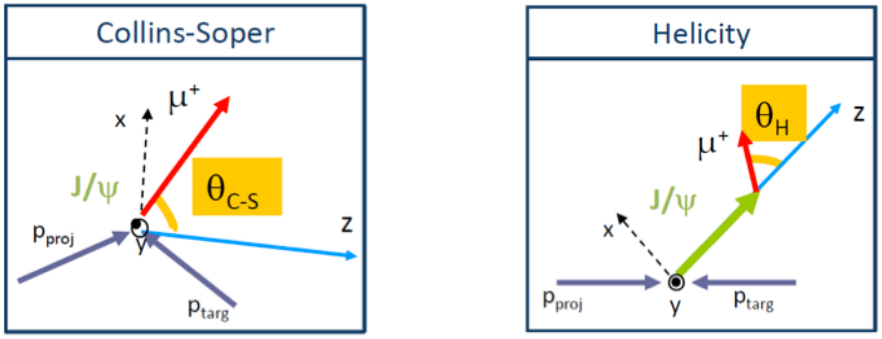

(a) *Collins-Soper reference frame.* (b) *Helicity reference frame.*

Figure 3.24. *Schematic view of the two reference frames used to perform the J/ψ polarization studies.*

In the CS frame, the z axis is defined as the bisector of the angle between the direction of one beam and the opposite of the direction of the other one, in the rest frame of the decaying J/ψ meson. In the HE reference frame, the z axis is given by the direction of the decaying particle in the center of mass frame of the collision.

[11] The θ variable is defined as the angle between the direction of the μ^+ momentum and the direction of the defined z axis, while ϕ is the angle measured with respect to the production plane formed by the momenta of the colliding protons in the J/ψ rest frame.

Equation 3.2 contains the three parameters λ_θ, λ_ϕ and $\lambda_{\theta\phi}$ which quantify the degree of the J/ψ polarization. In particular, when $\lambda_\phi = 0$ and $\lambda_{\theta\phi} = 0$, the values λ_θ = +1, -1, 0 correspond to fully transverse, fully longitudinal, and no polarization, respectively. These three extreme J/ψ polarization scenarios are considered in the analysis.

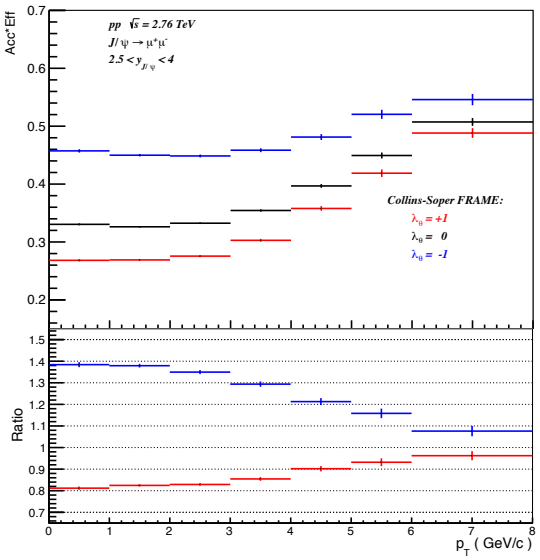

(a) *Collins-Soper frame.*

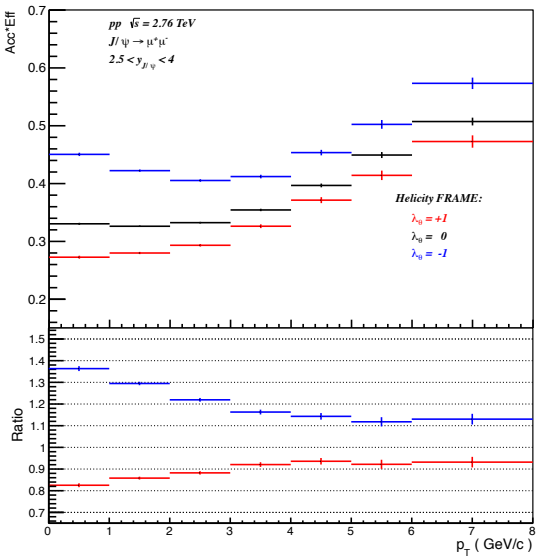

(b) *Helicity frame.*

Figure 3.25. *(Top) Transverse momentum dependence of the $A \times \varepsilon$ corrections averaged over the full period of data taking. Three different data series are plotted. The black, red and blue points correspond, respectively, to the three extreme J/ψ polarization scenario: completely unpolarized, completely transversally polarized and completely longitudinally polarized. (Bottom) Ratio of the red and blue distribution with respect to the black one.*

As shown in Fig. 3.25, the J/ψ polarization significantly affects the acceptance and efficiency corrections in particular at low p_{T}. The relative A$\times\varepsilon$ correction with respect to the unpolarized scenario varies in a range, depending on p_{T}, between 0.83 - 1.36 in HE frame and 0.81 - 1.38 in CS frame.

The unknown degree of J/ψ polarization introduces therefore large uncertainties on the J/ψ production cross sections. Their measurement will be given for the default polarization scenario (J/ψ unpolarized) and a separate uncertainty, due to the unknown polarization, will be assigned. Future measurements of the J/ψ polarization will allow to remove the uncertainties.

Recently, the ALICE Collaboration, studying the inclusive J/ψ production in pp collisions at $\sqrt{s}$ = 7 TeV, has measured the polarization parameters λ_θ and λ_ϕ. According to the measurement, carried out in the kinematical region $2.5 < y < 4$ and $2 < p_{\mathrm{T}} < 8$ GeV/c, the parameters are consistent with zero, in both the Helicity and Collins-Soper reference frame [71]. Due to the limited statistics, this results has not yet been implemented in the analysis to remove the uncertainties. This will be done as soon as the collected statistics will permit it.

3.3.4 $A \times \varepsilon$ corrected p_{T} and y spectra

Finally, the A$\times\varepsilon$ corrections, shown in Fig. 3.22 and 3.23, can be applied to J/ψ yields extracted from the fits performed in Fig. 3.16 and 3.17. The effect of the correction is shown, in Fig. 3.26, for the p_{T} (a) and y (b) dependence. The two data series, red and blue points, correspond respectively to the distributions before and after the A$\times\varepsilon$ correction.

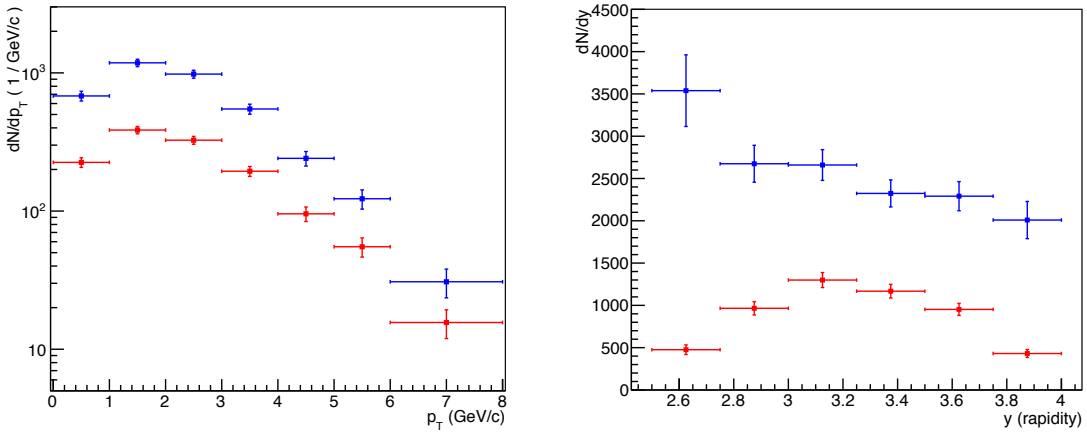

(a) p_T *dependence.* (b) y *dependence.*

Figure 3.26. *Transverse momentum and rapidity dependence of the J/ψ yield. The red and blue points correspond, respectively, to the distributions before and after the A$\times\varepsilon$ correction.*

For what concern the p_{T}- and y-integrated J/ψ yield, we obtain $N^{corr}_{\mathrm{J}/\psi} = N_{\mathrm{J}/\psi} / < A \times \varepsilon > = 3811 \pm 148$ (stat.) in the kinematical region $2.5 < y < 4$ and $p_{\mathrm{T}} > 0$ GeV/c.

An important check on the p_{T} and y input distributions, used to perform the Monte Carlo simulations (Fig. 3.18), must be done at this stage. The Monte Carlo inputs should be compared to the A$\times\varepsilon$ corrected spectra for the two kinematical variables. As shown in Fig. 3.27, real data and Monte Carlo inputs, for both p_{T} and y dependence, are compatible within one sigma.

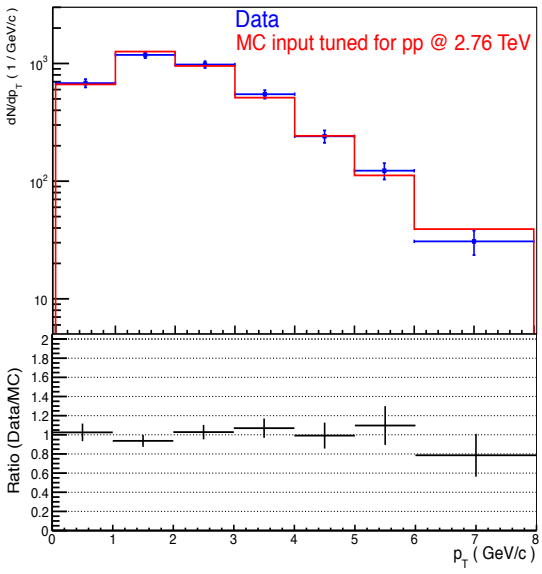

(a) p_T *dependence.*

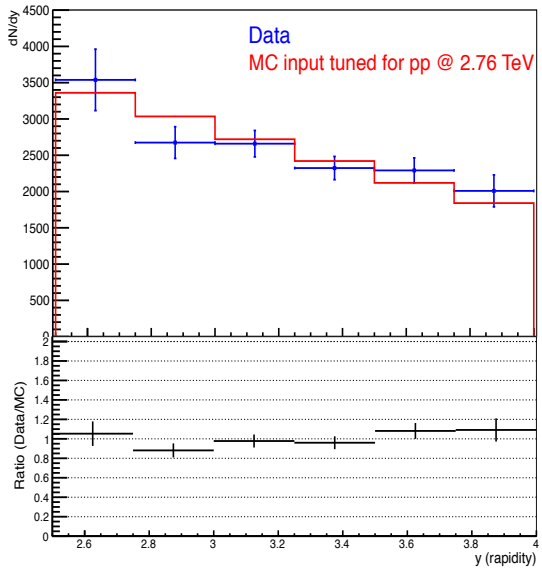

(b) *y dependence.*

Figure 3.27. *(Top) A×ε corrected spectra compared to the Monte Carlo inputs for the two kinematical variables (p_T and y). (Bottom) Ratio of the two distributions.*

3.4 Luminosity normalization

To calculate the integrated J/ψ production cross section, the A×ε corrected J/ψ yields $N^{corr}_{J/\psi}$ must be normalized to the integrated luminosity $\mathscr{L}_{\rm INT}$ corresponding to the analyzed data sample ($\mathscr{L}_{\rm INT} = \int \mathscr{L}(t)\, {\rm d}t$ where $\mathscr{L}(t)$ is the instantaneous luminosity). The integrated cross section is calculated as

$$\sigma_{J/\psi}(2.5 < y < 4) = \frac{N^{corr}_{J/\psi}}{BR(J/\psi \to \mu^+\mu^-)} \cdot \frac{1}{\mathscr{L}_{INT}} \tag{3.3}$$

where BR ($J/\psi \to \mu^+\mu^-$) = (5.94 $\pm$ 0.06) % is the branching ratio for the J/ψ decay into a muon pair [10].

The integrated luminosity $\mathscr{L}_{INT}$ can be calculated using σ_{MB}, the absolute cross section for minimum bias (MB) trigger events which have been chosen as reference process in our analysis [73]. Adopting as a reference the occurrence of the MB condition, the integrated luminosity would be simply $\mathscr{L}_{INT} = N_{MB}/\sigma_{MB}$ where N_{MB} is the total number of MB-triggered events, passing the physics selection introduced in Section 3.1.2, collected. In Section 3.4.1 the procedure followed to measure the σ_{MB} cross section is described.

3.4.1 σ_{MB} measurement *via* van der Meer scan

The measurement of the cross section σ_p for a chosen reference process p is a prerequisite for the luminosity normalization required for various cross section measurements. Actually, for a given data sample, the corresponding integrated luminosity can be simply obtained from the number of reference process events N_p collected in the sample as $\mathscr{L}_{INT} = N_p/\sigma_p$.

At present, ALICE uses the van der Meer scan method [74] to measure the reference cross section σ_p. During the scans [75][76], performed in dedicated runs, the instantaneous luminosity is varied by changing the distance between the two proton beams in the horizontal (x) and vertical (y) directions (x-y being the plane transverse to the beam axis). The reference trigger rate R_p follows the luminosity and its dependence on the beam displacement in x-y is measured during the van der Meer scan.

A bell-shaped curve is obtained for the counting rate R_p of the reference trigger as a function of the beam separation (Δx and Δy) with its peak at zero displacement. The analysis of such curves, $R_p(\Delta x, 0)$ and $R_p(0, \Delta y)$, allows us to determine the head-on luminosity[12] $\mathscr{L}$ as

$$\mathscr{L} = nN_1N_2f_{rev}Q_xQ_y, \tag{3.4}$$

where n is the number of colliding bunches in the orbit, f_{rev} is the orbital frequency, $N_{1,2}$ is the number of protons per bunch in the two beams and $Q_{x,y}$ is the beam shape factor in the x (y) direction. The beam shape factor is defined as $Q_{x,y} = R_p(0, 0) / S_{x,y}$, ratio between the head-on rate and S_x (S_y) which is the scan area defined as the area below the $R_p(\Delta x, 0)$ ($R_p(0, \Delta y)$) curve. Once the scan areas are obtained (via a fit or numerical integration), the cross section σ_p for the reference process can be derived as $\sigma_p = R_p(0,0)/\mathscr{L}$.

The reference process p, chosen by the ALICE experiment for luminosity measurements, is the coincidence of hits in the VZERO detector which consists of two forward scintillators V0A and V0C (see Chapter 2). The V0AND trigger input is therefore defined as V0AND = (V0A *AND* V0C), with the logical operator *AND* applied to the two VZERO signals. The V0AND contamination from beam-gas interactions during the scan was measured and found to be relatively small (much less than a few Hertz)[13].

During the pp collision data taking at $\sqrt{s}$ = 2.76 TeV (March 2011), a van der Meer scan was performed with 48 bunch pairs colliding in ALICE. The σ_{VOAND} cross section was so measured separately for all bunch pairs and the 48 values were averaged. The final result is σ_{VOAND} = (47.7 $\pm$ 0.9) mb, with 0.9 mb (1.9%) total uncertainty (stat. + syst.).

[12] Instantaneous luminosity at zero beam displacement (Δx and Δy =0).

[13] The measurement of a relatively small V0AND contamination from beam-gas interactions is an important check of the applicability of the van der Meer scan method at the LHC.

As mentioned above, the reference process chosen in the present analysis is actually the occurrence of the minimum bias condition (MB). Therefore, it is required to calculate the relative factor $r = \sigma_{\mathrm{VOAND}}/\sigma_{\mathrm{MB}}$ which is obtained as the fraction of MB events where the L0 trigger input corresponding to the V0AND conditions has fired. The r value is equal to 0.87 and it is quite stable, within 0.5%, over the analyzed data sample (see Fig. 3.40).

Finally, the σ_{MB} cross section can be derived as $\sigma_{\mathrm{MB}} = \sigma_{\mathrm{VOAND}}/r$ and it is equal to 55.4 $\pm$ 1.0 (total) mb.

3.4.2 *R* factor and pile-up correction

As explained in 3.1.2, the analysis of the J/ψ signal in the muon channel is performed considering only the events satisfying the μ-MB trigger condition. Therefore, the $\mathscr{L}_{\mathrm{INT}}$ expression has to include an additional multiplicative factor R which takes into account the enhancement of the muon sample in muon trigger events with respect to minimum bias events. Practically, the R factor is obtained by linking the occurrence of a reference process in the μ-MB and MB event samples.

The process used as reference for the R factor estimation is the yield N_μ of single muons (μ^+ and $\mu-$) detected in the pseudorapidity region -4 < η^μ < -2.5. The single muon tracks are required to satisfy different selection cuts: the radial coordinate of the track at the end of the front absorber (Fig. 3.11), R_{abs}, has to be in the range 17.6 < R_{abs} < 89.5 cm, the transverse momentum p_{T}^{μ} has to be larger than 1 GeV/c and, finally, only matched tracks are retained.

The R factor is then defined in Eq. 3.5 as the ratio

$$R = \frac{N_\mu^{\mu-MB}}{N_\mu^{MB}} \tag{3.5}$$

of the single muon yields for the two event samples (physics selection is active). In Fig. 3.28 the R factor is plotted as a function of the runs under analysis.

The numerical values of the R factor strongly depend on the relative bandwidth assigned by the ALICE data acquisition to the two trigger samples (MB and μ-MB) over time. For the period of data taking under analysis, one gets, considering the runs all together, R = 29.7 $\pm$ 0.2 with small variations run by run (<10% with respect to the R mean value).

It is important to notice that the choice of the single muon p_{T}^{μ} cut has no significant influence on the R value, as can be inferred from the numerical values shown in the summary Table 3.3. The use of three different p_{T}^{μ} cut values (1, 2 and 3 GeV/c) results in compatible R values within the uncertainties. This is due to the fact that both the μ-MB and MB muon samples are subject to the same set of cuts, including the requirement of the matching between the tracking track and the corresponding trigger track.

R factor: summary

p_{T}^{μ} ***cut***	$\boldsymbol{N_\mu^{\mu-MB}}$	$\boldsymbol{N_\mu^{MB}}$	***R***
p_{T}^{μ} > 1 GeV/c	686132	23136	29.7 $\pm$ 0.2
p_{T}^{μ} > 2 GeV/c	81368	2744	29.7 $\pm$ 0.6
p_{T}^{μ} > 3 GeV/c	22820	767	29.8 $\pm$ 1.1

Table 3.3. *Summary of the numerical data needed for the R factor calculation.*

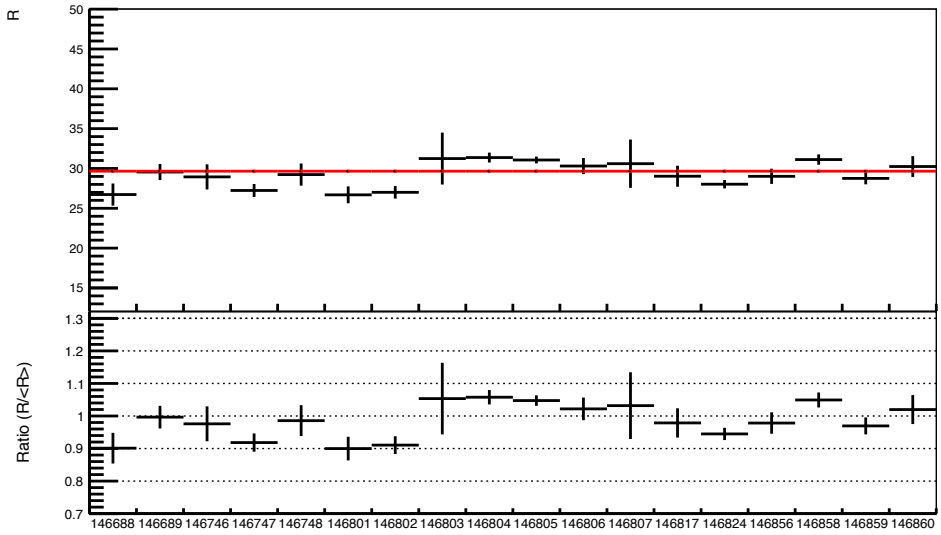

Figure 3.28. *(Top) R factor plotted as a function of the different analyzed runs (black points). The red line represents the R mean value obtained considering the runs all together. (Bottom) Ratio of the black data set with respect to the R mean value.*

The integrated luminosity $\mathscr{L}_{\rm INT}$ can be finally calculated using the relation shown in Eq. 3.6:

$$\mathscr{L}_{\rm INT} = \int \mathscr{L}(t)\,dt = \frac{\sum_i (N_{\rm MB}^{{\rm run}_i} \cdot f_\mu^{{\rm run}_i})}{\sigma_{\rm MB}} \cdot R = \frac{N_{\rm MB}^{\text{pile-up}}}{\sigma_{\rm MB}} \cdot R, \tag{3.6}$$

where $f_\mu^{run_i}$ is the factor that allows to correct, run by run, $N_{\rm MB}^{{\rm run}_i}$ (number of MB trigger events in run$_i$) for the probability of having multiple interactions in a single bunch crossing. The pile-up correction factor f_μ, which can vary from run to run, can be expressed as

$$f_\mu = \frac{\mu(t)}{1 - e^{-\mu(t)}}, \tag{3.7}$$

where μ is the expected value of the Poisson distribution which is used to describe the above mentioned probability [75]. In Fig. 3.29 the pile-up correction factor f_μ is plotted as a function of the runs under analysis.

The analysis performed on the 18-run list (see Section 3.1.2) gives a total data sample which amounts to $3.46{\cdot}10^7$ MB events. After the run-by-run pile-up correction, we obtain $\sum_i (N_{\rm MB}^{{\rm run}_i} \cdot f_\mu^{{\rm run}_i})$ = $3.54{\cdot}10^7$ MB events which corresponds to an average correction factor $<f_\mu>$ = 1.023 (blue dotted line in Fig. 3.29).

We have now all the ingredients to calculate, according to Eq. 3.6 , the integrated luminosity $\mathscr{L}_{\rm INT}$. Being $\sigma_{\rm MB}$ equal to 55.4 $\pm$ 1.0 (total) mb, we finally obtain $\mathscr{L}_{\rm INT}$ = 18.96 $\pm$ 0.13 (stat.) nb^{-1} (systematic uncertainties on luminosity are discussed in Section 3.5.5).

3.5 Systematic uncertainties

In this Section the estimation of the systematic uncertainties on the inclusive J/ψ cross sections (both integrated and differential) is discussed considering the possible sources of error.

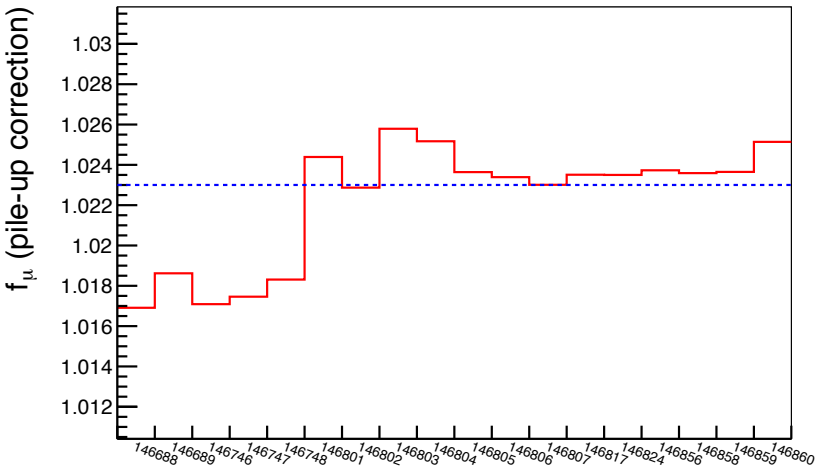

Figure 3.29. *Pile-up correction factor f_μ plotted as a function of the different analyzed runs (red line). The blue dotted line represents the f_μ mean value obtained considering the runs all together.*

3.5.1 Signal extraction

As explained in Section 3.2 for the integrated case, the default fitting function consists of a background component described with the sum of two exponentials (Eq. 3.1) and a J/ψ signal reproduced by a standard Crystal Ball function (CB) [68]. The CB low-end tail is fixed to the Monte Carlo while the J/ψ mass pole and width are free parameters in the fit. In addition, the $\psi(2S)$ signal, which is too weak to be detected, is not included in the calculation. This fit is shown in Fig. 3.30 (a).

The systematic uncertainty on the signal extraction method is estimated by testing alternative shapes for the signal and the background with respect to the default fitting choice.

Firstly, we can try to release, in the fit, the values of the two parameters (α and n) which characterize the asymmetric left tail of the Crystal Ball function, as done in Fig. 3.30 (c). Secondly, the J/ψ line shape can be fitted using a different function called Double Crystal Ball (CB2) which is an extended form of the standard Crystal Ball function (see Appendix B). Unlike the CB shape, the CB2 has two asymmetric power-law tails governed by four parameters (α_L, n_L, α_R and n_R). Due to the limited statistics, the CB2's tails have to be fixed to Monte Carlo while the J/ψ mass pole and width are free in the fit (Fig. 3.30 (e)).

Finally, the fits performed using these three different shapes for the J/ψ signal (CB with tail fixed, CB with tail free and CB2 with tails fixed) can be repeated adding, in the global fitting function, the ψ(2S) contribution. This is done in Fig. 3.30 (b), (d) and (f). Due to the small statistics, the $\psi(2S)$ parameters are tied to those of the J/ψ resonance. The $\psi(2S)$ power-law tail(s) are parametrized by the same J/ψ tail parameters (α and n) while the $\psi(2S)$ mass and width are expressed as a function of the corresponding J/ψ values under the following hypothesis.

For what concerns the mass, we know that the measured J/ψ mass value, $m_{J/\psi}$, is shifted with respect to the Particle Data Group [10] value by a quantity $\Delta m_{J/\psi} = m_{J/\psi} - m^{PDG}_{J/\psi}$ (with $\Delta m_{J/\psi}/m^{PDG}_{J/\psi}$ ~ 1%). A similar behavior is expected for the experimental $\psi(2S)$ mass, $m_{\psi(2S)}$, which is shifted by a quantity $\Delta m_{\psi(2S)} = m_{\psi(2S)} - m^{PDG}_{\psi(2S)}$. Under the hypothesis that $\Delta m_{J/\psi}/m^{PDG}_{J/\psi} = \Delta m_{\psi(2S)}/m^{PDG}_{\psi(2S)}$, $m_{\psi(2S)}$ can be expressed as a function of the experimental J/ψ mass:

$$m_{\psi(2S)} = m^{\rm PDG}_{\psi(2S)} + \Delta m_{\rm J/\psi} \cdot \frac{m^{\rm PDG}_{\psi(2S)}}{m^{\rm PDG}_{\rm J/\psi}}. \tag{3.8}$$

For the $\psi(2S)$ resonance width, a different approach is adopted to derive its expression as a function of the measured J/ψ width. According to the detector design, the ALICE Forward Spectrometer can measure the J/ψ and $\Upsilon(1S)$ resonances with a nominal invariant mass resolution of 70 MeV/c^2 and 100 MeV/c^2, respectively (intrinsic detector resolution without any misalignment effects).

Under the hypothesis that the resonance resolution σ has an approximately linear dependence with the resonance mass, the slope, s, of this line can be calculated[14]. Actually, due to a not perfect alignment of the muon chambers, the J/ψ resonance is measured with a larger width ($\sigma_{\rm J/\psi}$ = 81 $\pm$ 4 MeV/c^2) with respect to the nominal one. Applying the linear approximation, with slope s, for the mass dependence of the resonance resolution, one gets, from the measured point ($m_{\rm J/\psi}$, $\sigma_{\rm J/\psi}$), the following relation:

$$\sigma_{\psi(2S)} = \sigma_{\rm J/\psi} + s \cdot (m_{\psi(2S)} - m_{\rm J/\psi}), \tag{3.9}$$

where $\sigma_{\psi(2S)}$ is function of $m_{\rm J/\psi}$ and $\sigma_{\rm J/\psi}$. The summary of the J/ψ parameters obtained with the different fitting techniques is listed in Table 3.4. To calculate, in the integrated case, the systematic uncertainty on the signal extraction, we can consider the absolute deviations $\Delta = |N_{\rm J/\psi} - N_{ref}|$ of the J/ψ yields with respect to the reference value. In Fig. 3.31, the absolute deviations are shown (blue points) with the result of the fit (horizontal black line) which allows us to estimate the average absolute deviation <Δ>. This quantity gives a systematic uncertainty of 3%.

Integrated J/ψ yields vs fit methods

J/ψ line shape	***J/ψ yield***	$\sigma_{\rm J/\psi}$ **(MeV/c^2)**	$\chi^2/nDoF$
CB tail fixed w/o ψ(2S)	1319 $\pm$ 51 (stat.)	81 $\pm$ 4	1.42
CB tail free w/o ψ(2S)	1302 $\pm$ 53 (stat.)	82 $\pm$ 4	1.46
CB2 tails fixed w/o ψ(2S)	1353 $\pm$ 55 (stat.)	77 $\pm$ 4	1.41
CB tail fixed w/ ψ(2S)	1356 $\pm$ 59 (stat.)	83 $\pm$ 4	1.34
CB tail free w/ ψ(2S)	1345 $\pm$ 57 (stat.)	83 $\pm$ 5	1.38
CB2 tails fixed w/ ψ(2S)	1398 $\pm$ 58 (stat.)	81 $\pm$ 4	1.32

Table 3.4. *Summary of the J/ψ parameters obtained performing the J/ψ signal extraction using six different fitting techniques. The first line corresponds to the default fitting technique.*

[14] $s = (100 MeV/c^2 - 70 MeV/c^2)/(m^{\rm PDG}_{\Upsilon(1S)} - m^{\rm PDG}_{\rm J/\psi})$.

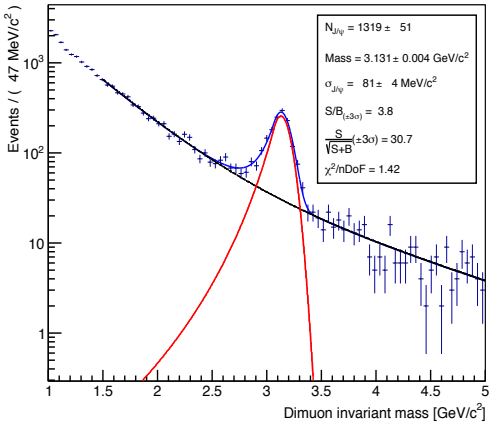

(a) *J/ψ : CB tail fixed*

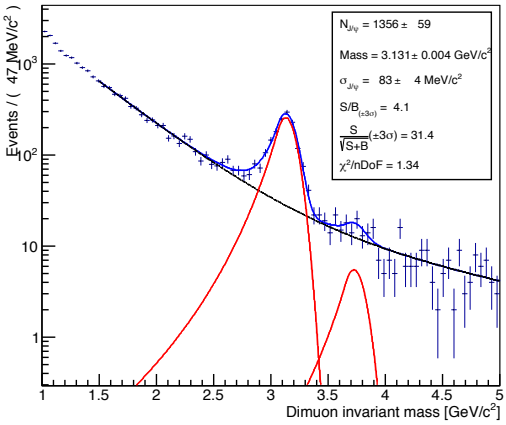

(b) *J/ψ and ψ(2S) : CB tail fixed*

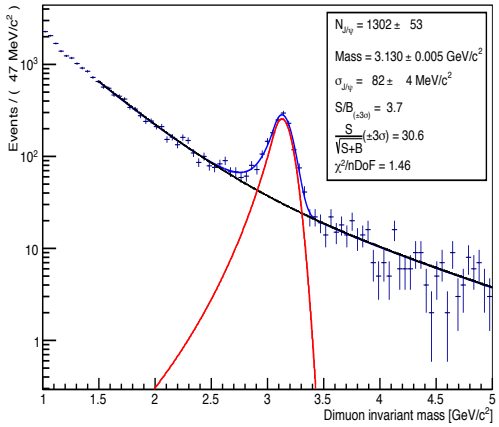

(c) *J/ψ : CB tail free*

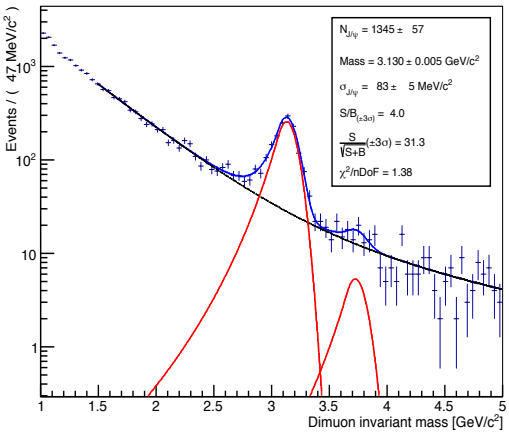

(d) *J/ψ and ψ(2S) : CB tail free*

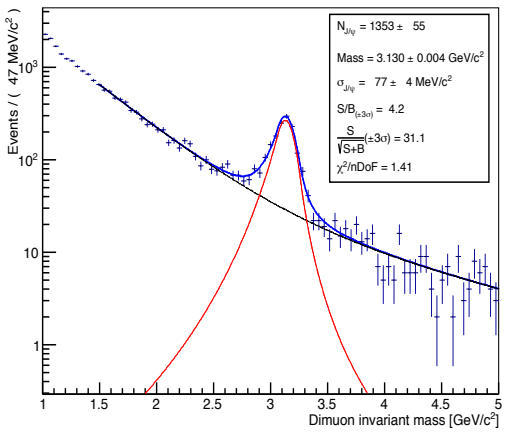

(e) *J/ψ : CB2 tails fixed*

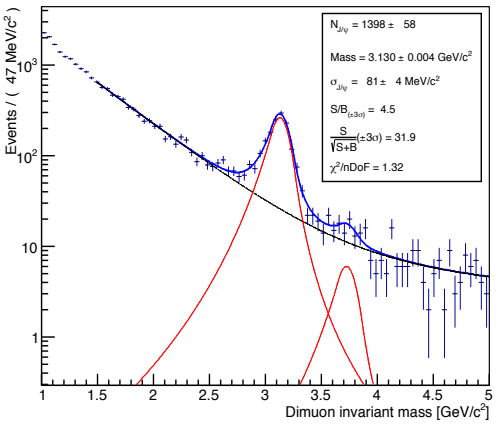

(f) *J/ψ and ψ(2S) : CB2 tails fixed*

Figure 3.30. *Extraction of the integrated J/ψ yield with different fitting techniques.*

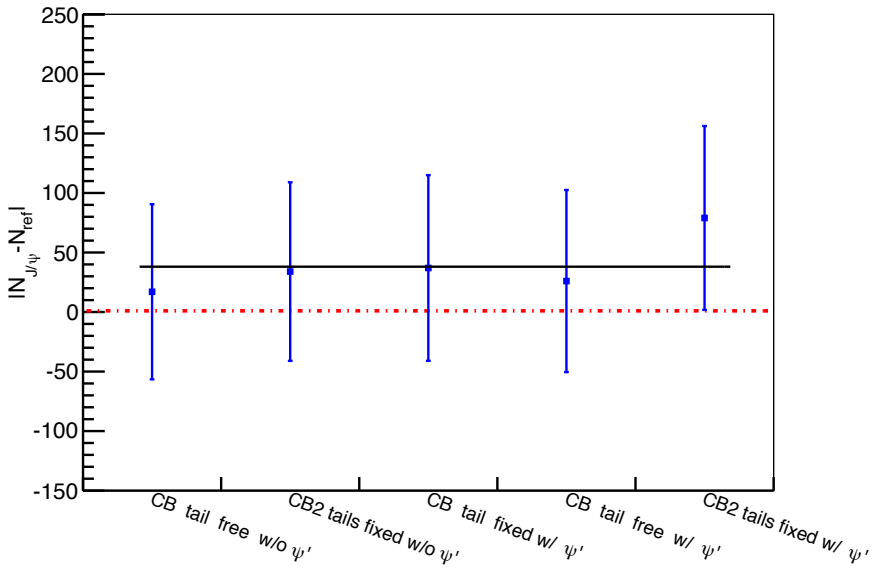

Figure 3.31. *Absolute deviation of the J/ψ yields with respect to the reference value (blue points). The horizontal black line represents the fit of the data points with a constant function.*

There is another way to determine the systematic uncertainty by considering the root mean square (RMS) and the mean value of the data points shown in Fig. 3.32 (Top).

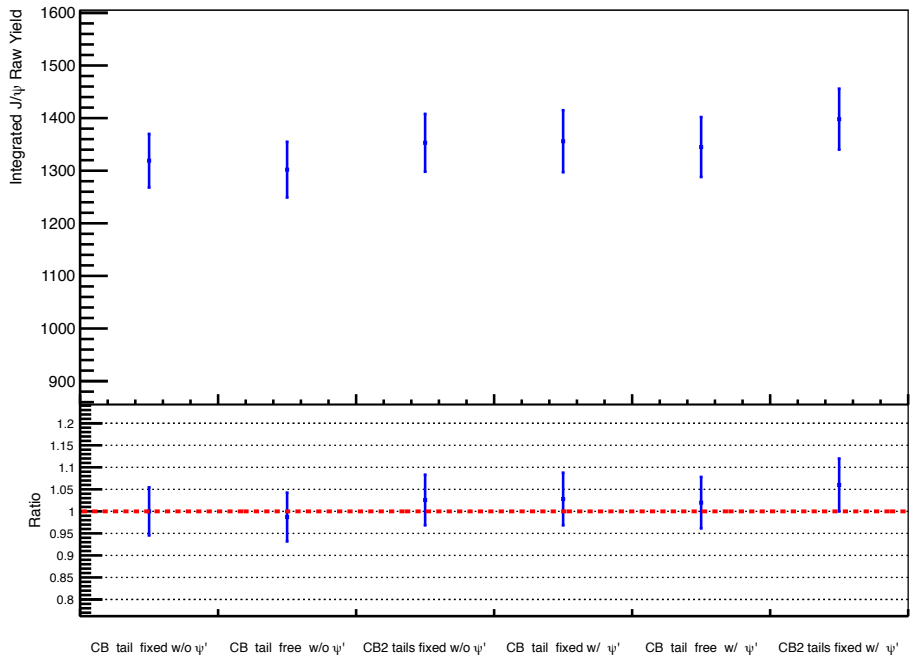

Figure 3.32. *(Top) Integrated J/ψ yield for the six different fitting techniques. (Bottom) Ratio with respect to the reference integrated J/ψ yield, the one plotted in the first bin on the left (CB tail fixed w/o $\psi(2S)$).*

The ratio between the RMS and mean gives an estimation of the systematic uncertainty on the signal extraction which is equal to 2.3%. Other alternative functions for the description of the J/ψ resonance and background shapes have been tested. In particular, for the J/ψ resonance, a variable-width Gaussian function, adopted in the past by the NA50 and NA60 Collaboration (CERN) [69] (definitions in Appendix B), has been used.

Finally, the overall systematic uncertainty on the signal extraction, in the integrated case, can be estimated with the conservative value of 4%.

In principle the systematic uncertainty on the signal extraction may present a dependence with respect to the p_T and y bins. In order to check the stability of the signal extraction, bin by bin, several tests have been done using alternative functions for the J/ψ signal line shape. The following checks have been performed:

- J/ψ signal described by a CB with tail fixed, bin by bin, to Monte Carlo and width fixed, for each bin i, to the value $\sigma^i_{J/\psi} = \sigma_{J/\psi} \cdot (\sigma^{i,MC}_{J/\psi} / \sigma^{MC}_{J/\psi})$[15] (reference choice);
- J/ψ signal described by a CB with tail fixed, bin by bin, to Monte Carlo and width free parameter in the fit;
- J/ψ signal described by a CB with tail fixed to the Monte Carlo p_T- and y-integrated value and width fixed, for each bin i, to the value $\sigma^i_{J/\psi} = \sigma_{J/\psi} \cdot (\sigma^{i,MC}_{J/\psi} / \sigma^{MC}_{J/\psi})$;
- J/ψ signal described by a CB with tail fixed to the Monte Carlo p_T- and y-integrated value and width free parameter in the fit;
- J/ψ signal described by a CB2 with tail fixed to the Monte Carlo p_T- and y-integrated value and width fixed, for each bin i, to the value $\sigma^i_{J/\psi} = \sigma_{J/\psi} \cdot (\sigma^{i,MC}_{J/\psi} / \sigma^{MC}_{J/\psi})$;

For each test, the background is always described with the sum of two exponentials (Eq. 3.1). For what concerns the $\psi(2S)$ contribution, it has been both excluded and included in the fit process, in the latter case by tying the ψ(2S) parameters to those of the J/ψ resonance, as explained above. Figure 3.33 (Top) and 3.34 (Top) show, respectively, the transverse momentum and the rapidity dependence of the J/ψ yield for several tests performed. The corresponding ratios, calculated with respect to the reference J/ψ yield (red points), are shown on the bottom.

From the different tests performed, no clear trend as a function of the two kinematic variables, p_T and y, is observed. So, the systematic uncertainty on the signal extraction calculated for the integrated case (4%) is assigned to each bin and considered uncorrelated between the bins.

3.5.2 Acceptance inputs

To estimate the systematic uncertainties relative to the choice of the Monte Carlo inputs, p_T and y (see Figure 3.18),the following procedure has been adopted. Both transverse momentum and rapidity distribution have been varied using several alternative shapes (see Appendix C for the exact definition of the functions).

First of all, we have considered two different parametrizations, for both p_T and y, tuned for proton-proton collisions at $\sqrt{s}$ = 1.96 and 3.94 TeV. These two energies are, respectively, slightly lower and higher than the one presently under analysis ($\sqrt{s}$ = 2.76 TeV). More in details, at $\sqrt{s}$ = 1.96 TeV, the J/ψ transverse momentum spectrum is obtained by fitting the p_T distribution of the

[15] The CB width has been fixed to a value obtained by scaling the measured width for the integrated spectrum ($\sigma_{J/\psi}$) with the ratio between the MC widths for the bin$i$ and for the integrated spectrum.

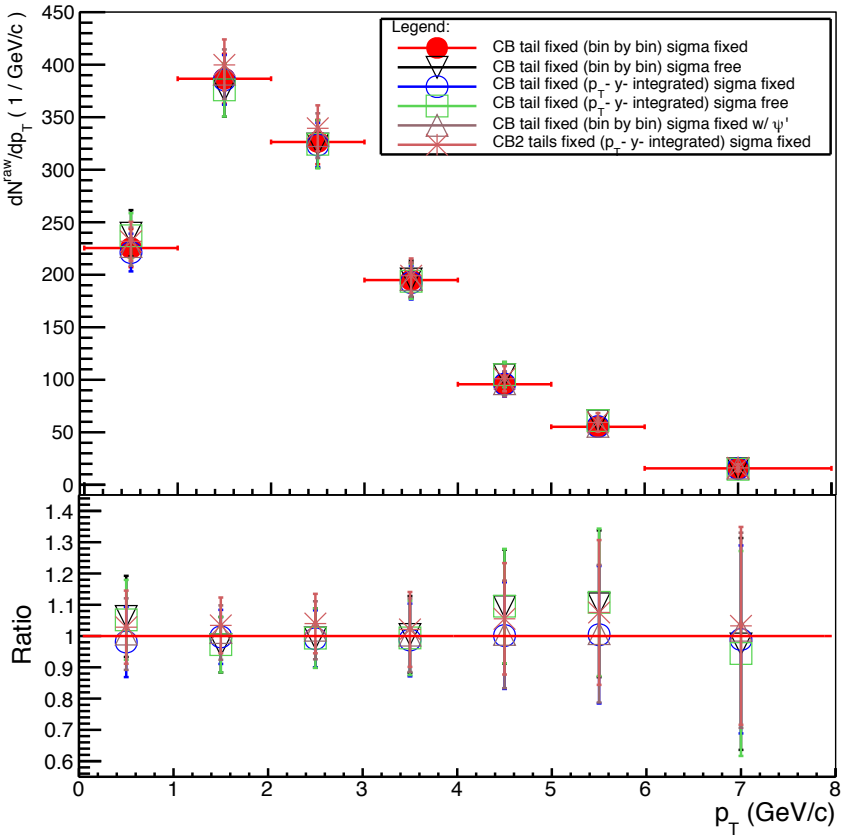

Figure 3.33. *(Top) Transverse momentum dependence of the J/ψ yield calculated using alternative functions for the J/ψ signal line shape. (Bottom) Ratios calculated with respect to the reference J/ψ yield (plotted in red).*

inclusive J/ψ production measured in pp̄ collisions at $\sqrt{s}$ = 1.96 TeV (Run II) by the CDF experiment at the Tevatron collider [77]. This CDF measurement is performed over a rapidity of $|y| < 0.6$ for all transverse momentum from 0 to 20 GeV/c. For the J/ψ rapidity spectrum, instead, following the phenomenological interpolations discussed in [70], a gaussian shape, tuned at $\sqrt{s}$ = 1.96 TeV, is used.

On the contrary, at $\sqrt{s}$ = 3.94 TeV, the J/ψ transverse momentum spectrum is obtained by extrapolating to that energy the previously mentioned CDF J/ψ results at mid-rapidity. The y distribution is then computed as a parametrization of the Color Evaporation Model (CEM) predictions at $\sqrt{s} = 3.94$ TeV (details in [78]).

As explained in Section 4.3, the acceptance and efficiency corrections, shown in Figure 3.20, 3.22, 3.23, are calculated using, as Monte Carlo inputs, realistic p_{T} and y distributions tuned for proton-proton collisions at $\sqrt{s}$ = 2.76 TeV. The two parametrizations are obtained with a phenomenological interpolations of existing measurements at different energies based on a model independent approach [70]. In particular, the rapidity dependence is described by a gaussian shape.

The p_{T} and y shapes tuned for proton-proton collisions at $\sqrt{s}$ = 2.76 TeV and used as reference, have also been modified by considering alternatives parametrizations. The p_{T} dependence was obtained by scaling, as explained in [78], the CDF J/ψ results at mid-rapidity [77] at $\sqrt{s}$ = 2.76 TeV. For the rapidity dependence, instead, a polynomial functional form (with n = 4), was adopted on the base

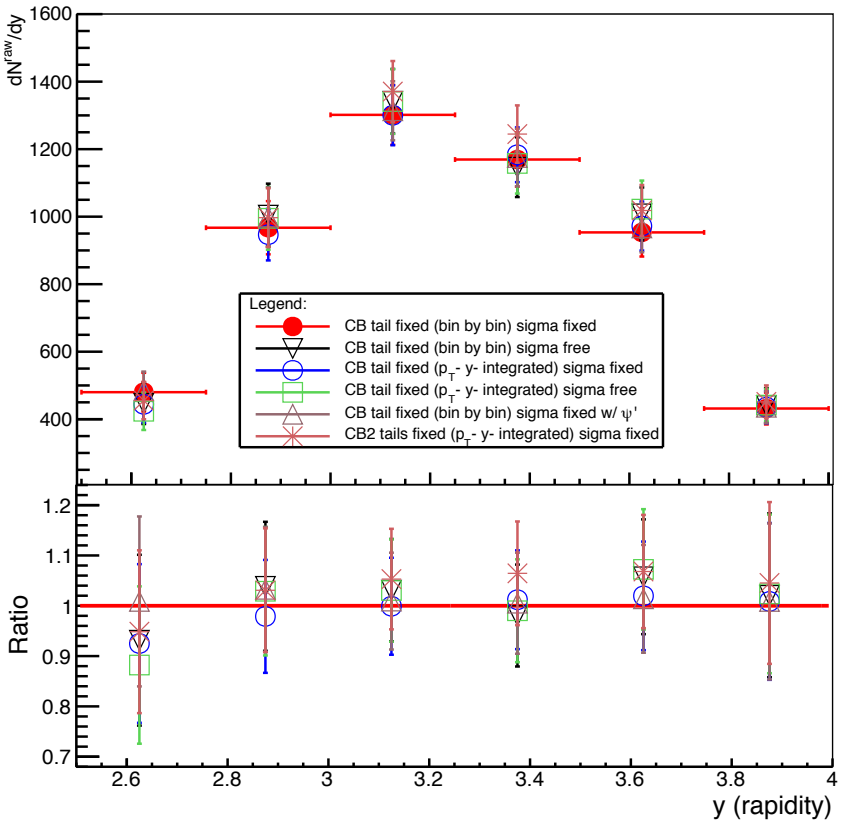

Figure 3.34. *(Top) Rapidity dependence of the J/ψ yield calculated using alternative functions for the J/ψ signal line shape. (Bottom) Ratios calculated with respect to the reference J/ψ yield (plotted in red).*

of the model independent approach presented in [70] .

Figure 3.35 shows the integrated acceptance and efficiency corrections, $A\times\varepsilon_i$, as a function of the 18 runs analyzed for the several Monte Carlo inputs tested. In Table 3.5, the $A\times\varepsilon$ corrections, averaged over the full period of data taking, are listed quoting, in last column, the percentage differences respect to the reference integrated $A\times\varepsilon$ correction. From these percentage differences, the overall systematic uncertainty on the choice of the Monte Carlo inputs, in the integrated case, can be estimated with value of 4%.

For the systematic uncertainties relative to the choice of the MC inputs, their values may in principle vary with either rapidity or transverse momentum. Therefore, a differential study of these effects has been performed as shown in Figure 3.36 3.37. They show, for each p_T and y bin, the ratios between the $A\times\varepsilon$ correction value, obtained with a certain MC input, and the reference value. The study observes no clear dependence as a function of the two kinematic variables. So, the systematic uncertainty calculated for the integrated case (4%) is assigned to each p_T and y bin and considered uncorrelated between the bins.

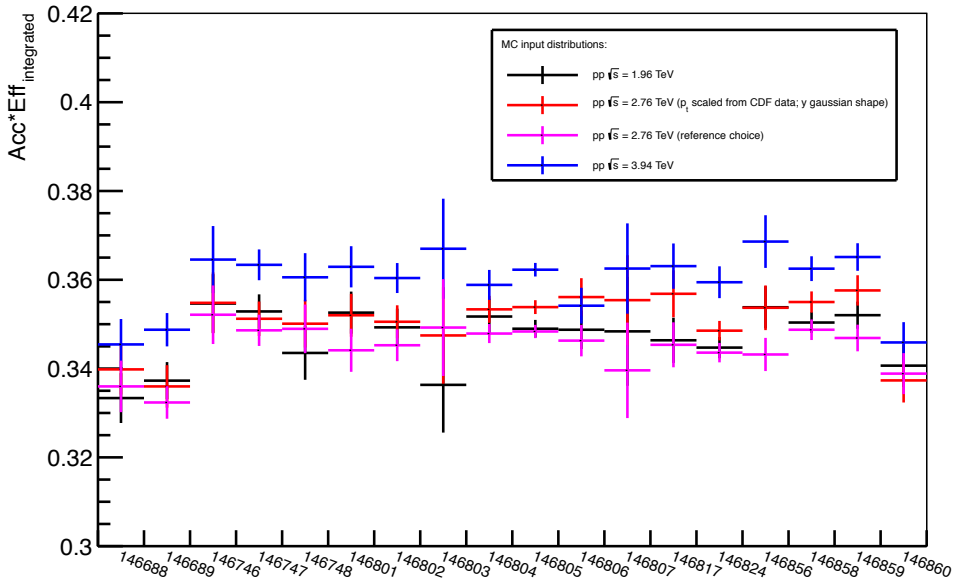

Figure 3.35. *The integrated acceptance and efficiency corrections, $A\times\varepsilon_i$, as a function of the 18 runs analyzed for four Monte Carlo inputs tested.*

Summary of the Monte Carlo inputs

Energy	p_T MC input	y MC input	Integrated A$\times\varepsilon$	Difference
pp $\sqrt{s}$ = 1.96 TeV	fit of CDF data	gaussian shape	0.3485 $\pm$ 0.0008	4.2%
pp $\sqrt{s}$ = 2.76 TeV	scaled from CDF data	gaussian shape	0.3520 $\pm$ 0.0008	1.7%
pp $\sqrt{s}$ = 2.76 TeV	universal fit	gaussian shape	**0.3461 $\pm$ 0.0007**	-
pp $\sqrt{s}$ = 2.76 TeV	universal fit	polynomial shape (n = 4)	0.353 $\pm$ 0.002	2.0%
pp $\sqrt{s}$ = 3.94 TeV	scaled from CDF data	parametrization from CEM	0.3604 $\pm$ 0.0008	0.7%

Table 3.5. *Summary of the Monte Carlo inputs tested with the corresponding integrated acceptance and efficiency corrections, averaged over the full period of data taking. The last column shows the percentage differences with respect to the reference value (in red color).*

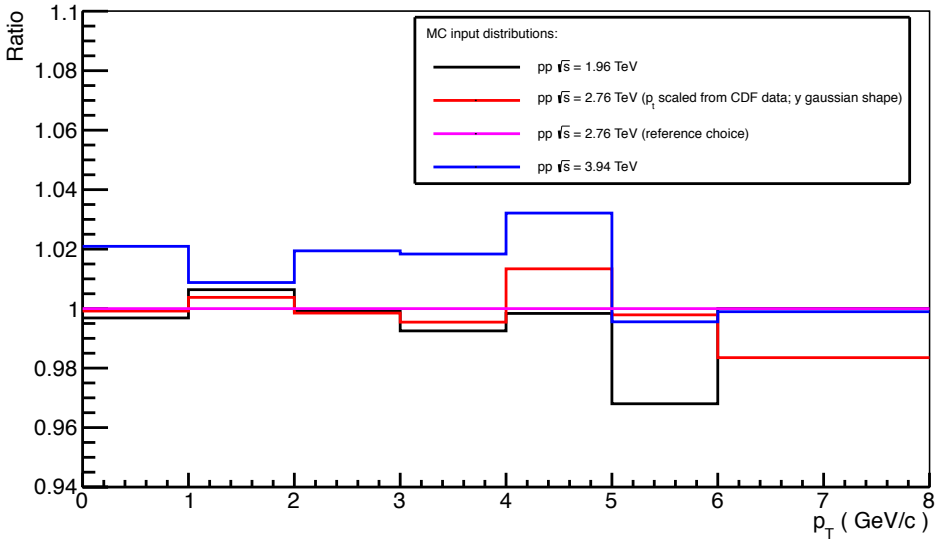

Figure 3.36. *Ratios between the A×ε correction values, obtained with a certain MC input, and the reference values for each p_T bin.*

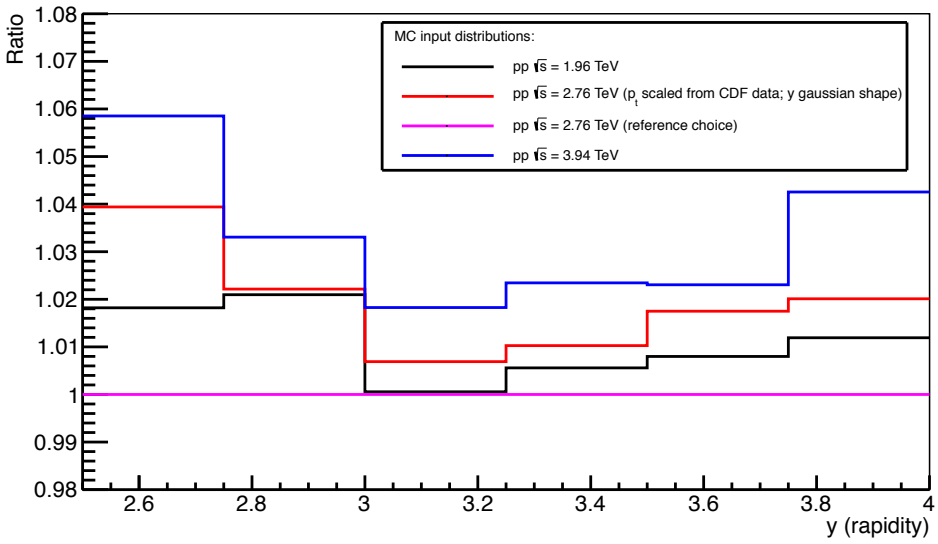

Figure 3.37. *Ratios between the A×ε correction values, obtained with a certain MC input, and the reference values for each rapidity bin.*

3.5.3 Trigger efficiency

The systematic uncertainty on the muon trigger efficiency calculation was estimated following two alternative approaches. In the first one, we compare the A×ε corrected J/ψ yield $N^{corr}_{J/\psi}$ for the sample where only one of the two decay muons is required to match the trigger condition (reference choice),

with the same quantity for the sample where both muons are required to satisfy that condition. For the data sample under analysis, we obtain, respectively,

$$N_{J/\psi}^{corr} = \frac{N_{J/\psi}}{< A \cdot \varepsilon >} = \frac{1319 \pm 51}{0.3461 \pm 0.0007} = 3811 \pm 148 \tag{3.10}$$

$$N_{J/\psi}^{corr} = \frac{N_{J/\psi}}{< A \cdot \varepsilon >} = \frac{1072 \pm 42}{0.2711 \pm 0.0006} = 3954 \pm 153 \tag{3.11}$$

The 3.6% discrepancy between the two quantities can be taken as first estimation of the systematic uncertainty.

In principle, such an approach may be influenced by statistical effects. Another method has therefore been tested on the base of the following procedure. The efficiency of the trigger boards[16] is varied by a certain amount (-2%, -5% and -10%) and, implementing this new conditions in the Monte Carlo simulation code, the A$\times\varepsilon$ correction is recalculated as shown in Fig. 3.38.

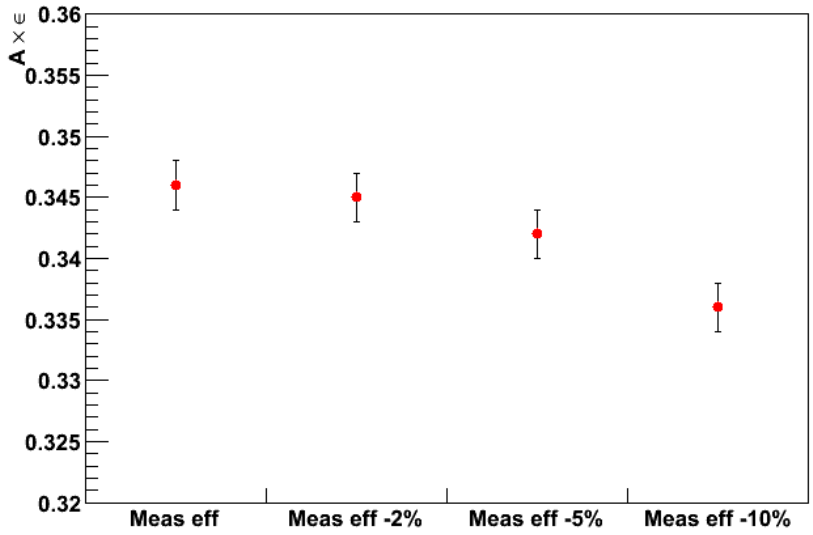

Figure 3.38. *Ratios between the A$\times\varepsilon$ correction values, obtained with a certain MC input, and the reference values for each rapidity bin.*

Finally, if a 5% variation in the trigger board efficiency is conservatively assumed, we obtain a 1% effect on the A$\times\varepsilon$ correction. Combining the results obtained with the two alternative approaches, a 2% systematic uncertainty on the evaluation of the trigger efficiency has been adopted. The same value is also assigned to each bin and considered as correlated between the bins.

3.5.4 Reconstruction efficiency

In order to study the systematic uncertainty on the reconstruction efficiency, we have developed a method to measure the total tracking efficiency of the tracker system. This measurement was performed both on real data and realistic Monte Carlo simulations and the difference between the two quantities gives an estimate of the systematic uncertainty mentioned above.

[16]The trigger local boards allow to read the informations of the front-end electronics (FEE) of the Muon trigger system (more details in Chapter 2).

The total tracking efficiency, ε_{TTE} can be evaluated starting from the determination of the efficiency per chamber. This is computed using the redundancy of the tracking informations in each station, i. e. the fact that the two tracking chambers, contained in a station, do not need to be fired together for a track to be reconstructed (details in Appendix D). Figure 3.39 shows the efficiencies for the ten chambers of the muon spectrometer comparing the results obtained with real data (black points) and MC simulations (red points).

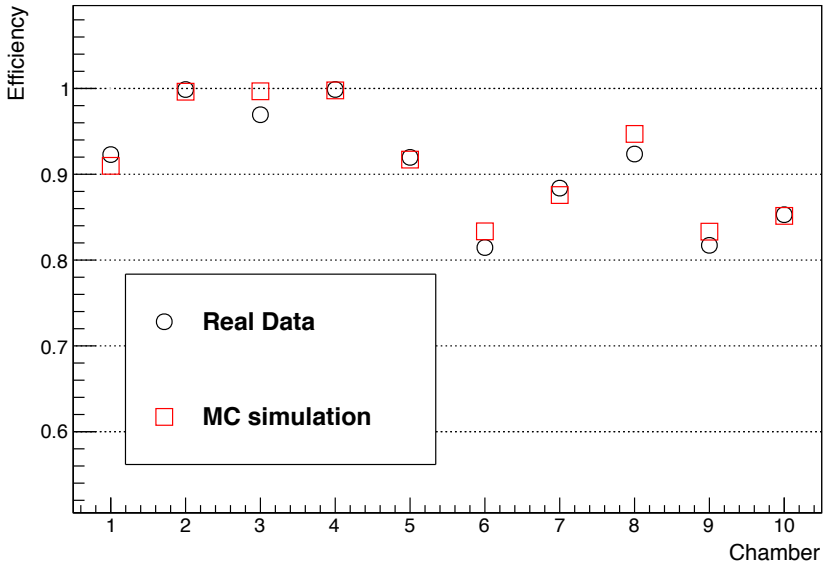

Figure 3.39. *Comparison of the measured efficiencies for the ten tracking chambers in real data (black points) and in realistic Monte Carlo simulations (red points) .*

The values thus obtained are in the range from 81.5 to 99.9% for real data and from 83.3 to 99.8% for MC simulated data. By combining the individual chamber efficiencies according to the reconstruction criteria, the overall reconstruction efficiency ε_{TTE} can be finally determined. As explained in Appendix D, the tracking algorithm requires at least one cluster in each of the first three stations and at least three clusters in three different chambers in the last two stations to validate the track reconstruction.

The total tracking efficiencies evaluated for real data and for Monte Carlo simulations are, respectively, $(90.2 \pm 0.1)\%$ and $(91.2 \pm 0.3)\%$. These two quantities differ by 1%, which is taken as a first estimate of the systematic uncertainty on the reconstruction efficiency.

However, this procedure of measuring the reconstruction efficiency is blind to the correlated inefficiencies of the detection elements (DE), i. e. dead areas located in front of each other within the same station. This effect leads to an overestimation of the efficiency. Such correlated dead areas were studied, on real data, by developing a dedicated method able to spot and to correct these inefficiencies. The corresponding loss of efficiency on ε_{TTE}, in real data, was estimated to be equal to $(0.83 \pm 0.2)\%$.

Taking into account this effect, the resulting systematic uncertainty on the reconstruction efficiency increases reaching a larger value of 1.8%. Nevertheless, a 1% additional systematic error was assumed to allow for small-area correlations that could be missed in the present method. Finally, combining this contribution with the error previously mentioned, the overall systematic uncertainty

on the muon tracking efficiency is 2% which gives a 4% for muon pair detection.

The 4% value is assigned to each p_{T} and y bin as a correlated systematic uncertainty.

3.5.5 Luminosity

The systematic uncertainty on the luminosity (L_{INT}) measurement, calculated using Eq. 3.6, consists of different sources. The dominant component is the systematic uncertainty on the determination of σ_{VOAND} which is required to obtain σ_{MB}. This source of systematic uncertainty, assumed to be equal to 1.8%, is due to the uncertainties on the proton beam intensities [79] and on the procedure followed to analyze the van der Meer scans of the V0AND signal [75].

The second component, which contributes to the systematic uncertainty on L_{INT}, is related to the relative factor r needed to derive the cross section of the reference process, σ_{MB}, from the measured cross section σ_{VOAND} . The factor r, obtained as the fraction of MB events where the L0 trigger input corresponding to the V0AND condition has fired, presents a run-to-run oscillation within 0.5% over the analyzed data sample (see Fig. 3.40 (a)) . The amplitude of the oscillation is therefore taken as an estimate of the r contribution to the systematic uncertainty on L_{INT}.

Finally, the last contribution is related to the choice of the reference process used to calculate the integrated luminosity L_{INT} corresponding to the data sample under analysis. In Section 3.4, the occurrence of the MB condition was adopted as reference. An alternative process has been therefore taken into account by measuring the cross section $\sigma_{\mu-MB}$, relative to the occurrence of the μ-MB trigger condition. It was calculated, like σ_{MB}, starting from the measured σ_{VOAND} and the ratio σ_{VOAND} / $\sigma_{\mu-MB}$. The procedure followed gives $\sigma_{\mu-MB}$ = (447 $\pm$ 16) μb. Figure 3.40 (b) shows, as a function of the analyzed runs, the ratio between L_{INT}^{MB} and $\mathrm{L}_{INT}^{\mu-MB}$, the integrated luminosities calculated using as reference, respectively, the MB and the μ-MB trigger condition. The discrepancy related to the choice of the two reference processes can be estimated to be equal to 0.2%.

At the end, the three contributions to the systematic uncertainty on L_{INT} (1.8%, 0.5% and 0.2%) have been quadratically added giving as final value 1.9%.

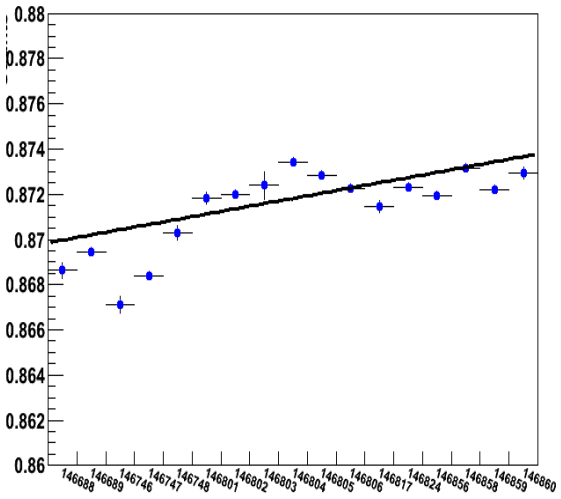

(a) *r factor*

/Users/claudio/Desktop/good.pdf

(b) $\mathscr{L}_{INT}^{MB}/\mathscr{L}_{INT}^{\mu-MB}$ *ratio.*

Figure 3.40. *(Left) r factor ($r = \sigma_{VOAND}/\sigma_{MB}$) as a function of the runs under analysis. (Right) $\mathscr{L}_{INT}^{MB}/\mathscr{L}_{INT}^{\mu-MB}$ ratio as a function of the runs under analysis.*

In addition, as shown in Eq. 3.6, the calculation of the integrated luminosity requires the estimate of the R factor. This multiplicative factor allows to take into account the enhancement of the muon sample in muon trigger events, used in the present analysis, with respect to minimum bias events. This quantity was evaluated by linking the occurrence of a reference process, the yield of single muons (μ^+ and μ^-), in the two trigger event samples. Eq. 3.5 shows the definition of the R factor that has been used.

An alternative way to calculate the R factor was therefore adopted using the information of the trigger scalers and taking into account the dead-time of the triggers [73]. In order to calculate the trigger rate for a given process, the trigger scalers must be counted. There are 3 trigger levels (L0, L1 and L2) and each of them presents two sub-levels identified by b and a, where b and a stand for, respectively, $before$ and $after$ vetoes. In particular, L0b gives directly the number of times a given trigger class is fired while L2a gives the number of times the same trigger class passes the CTP (Central Trigger Processor) and the detector dead-time, as well as any other possible vetoes. These counters are measured online and can be retrieved off-line for each run[17]. According to the trigger selection programmed in the CTP for the proton-proton data taking under analysis, the R factor is given by

$$R = \frac{N_{L2a}^{MB}}{N_{L0b}^{MB}} \cdot \frac{N_{L0b}^{\mu-MB}}{N_{L2a}^{\mu-MB}} \tag{3.12}$$

where N_{L0b}^{MB} and N_{L2a}^{MB} are the CTP scalers for the MB trigger type recorded at L0b and L2a, respectively, and $N_{L0b}^{\mu-MB}$ and $N_{L2a}^{\mu-MB}$ are the CTP scalers for the μ-MB trigger type recorded at L0b and L2a, respectively. It can also be noticed that $N_{L2a}^{MB}/N_{L0b}^{MB}$ and $N_{L2a}^{\mu-MB}/N_{L0b}^{\mu-MB}$ are, respectively, the relative live-times of the two trigger classes, MB and μ-MB.

By comparing the R factors obtained with the two different methods, using Eq. 3.5 and Eq. 3.12, a 3% systematic uncertainty on the R factor was estimated. This last uncertainty is assigned to each p_{T} and y bins as correlated between the bins as well as the previously quoted 1.9%.

3.5.6 J/ψ polarization

As explained in Sec. 3.3.3, the acceptance and efficiency corrections, A$\times\varepsilon$, strongly depend on the degree of the J/ψ polarization assumed in Monte Carlo simulations. They were calculated in three extreme J/ψ polarization scenarios: completely unpolarized (λ_θ = 0) and in the two cases of fully transverse (λ_θ = +1) or fully longitudinal (λ_θ = -1) polarization. The calculation was performed in the Collins-Soper (CS) and helicity (HE) reference frames.

The unknown degree of polarization of the J/ψ introduces therefore a systematic uncertainty on the J/ψ production cross section which has been calculated assuming, as reference choice, the J/ψ unpolarized. The systematic uncertainties related to the polarization are then calculated for both Collins-Soper and helicity reference frames. For the integrated case, we obtain +32% (λ_θ = -1) and -16% (λ_θ = +1) in the CS frame while in the HE frame +24% (λ_θ = -1) and -12% (λ_θ = +1).

[17] For more details see Chapter 2 and [80].

3.5.7 Total systematic uncertainty

Summary of the systematic uncertainties

Source	(%)
Signal extraction	4
Acceptance input	4
Trigger efficiency	2
Reconstruction efficiency	4
R factor	3
Luminosity	1.9
B.R.	1
Total	8.1

Polarization	λ = -1	λ = +1
Collins-Soper (CS)	+32	-16
Helicity (HE)	+24	-12

Table 3.6. *Systematic uncertainties (in percent) contributing to the measurement of the integrated J/ψ production cross section.*

The systematic uncertainties on the integrated J/ψ production cross section are summarized in Table 3.6 where each contribution is quoted. The total systematic uncertainty, excluding those related to the unknown degree of polarization of the J/ψ, is equal to 8.1%. This value is obtained by quadratically combining the errors from the sources described above. An additional contribution is considered taking into account that the branching ratio B.R. of the J/ψ decay into a muon pair ($\mu^+ \mu^-$) is known with a 1% accuracy.

For the differential cross sections, measured as a function of the transverse momentum and rapidity, the same sources of systematic uncertainties, quoted in Table 3.6, are assigned to each p_T and y bin, as explained above.

3.6 Results

The analysis, described in the previous Sections, allows to measure the integrated and the differential, p_T and y, cross sections for inclusive J/ψ production in proton-proton collisions at $\sqrt{s}$ = 2.76 TeV. The final results are presented in the following two Subsections.

3.6.1 Integrated J/ψ cross section

The integrated inclusive J/ψ production cross section has been obtained at forward rapidities (2.5 < y < 4) for the transverse momentum range $p_T > 0$ GeV/c. It is calculated using Eq. 3.13

$$\sigma_{J/\psi}(2.5 < y < 4) = \frac{N_{J/\psi}/_{<A\cdot\varepsilon>}}{BR(J/\psi \to \mu^+\mu^-)} \cdot \frac{\sigma_{MB}}{N_{MB}^{pile-up}} \cdot \frac{N_{\mu}^{MB}}{N_{\mu}^{\mu-MB}} \tag{3.13}$$

which can be derived by combining the relations shown in Eq. 3.3 3.5 3.6. In Table 3.7, all the ingredients required to calculate $\sigma_{J/\psi}(2.5 < y < 4)$ are summarized. Finally, the following result for the integrated inclusive J/ψ cross section has been achieved:

$$\sigma_{J/\psi}(2.5 < y < 4) = 3.38 \pm 0.14(stat.) \pm 0.27(syst.) + 0.54(\lambda_{CS} = +1) - 1.08(\lambda_{CS} = -1)\mu b \tag{3.14}$$

The polarization-related systematic uncertainties, estimated in the Collins-Soper (CS) and helicity (HE) reference frames, are quoted separately for the reference frame (CS) where they are larger. ALICE has recently measured the J/ψ polarization for $\sqrt{s}$ = 7 TeV at forward rapidity [71] and the results obtained exclude a significant degree of polarization for the J/ψ. However, due to the difficulties to predict the $\sqrt{s}$-dependence of the polarization effect, we have decided to quote the systematic uncertainties relative to two extreme scenarios of fully longitudinal (λ = -1) and fully transverse (λ = +1) degree of polarization.

The ALICE experiment has also studied [81] the J/ψ production at forward rapidity in pp collisions at $\sqrt{s}$ = 7 TeV. The measured production cross section, corresponding to an integrated luminosity L_{INT} = 15.6 nb^{-1}, is $\sigma_{J/\psi}(2.5 < y < 4) = 6.31 \pm 0.25(stat.) \pm 0.76(syst.) + 0.95(\lambda_{CS} = +1) - 1.96(\lambda_{CS} = -1)\mu b$. With respect to the $\sqrt{s}$ = 7 TeV measurement, the $\sqrt{s}$ = 2.76 TeV cross section is smaller by a factor 1.86 ± 0.29. The quoted uncertainty on the ratio is calculated by propagating the quadratic sum of statistical and systematic uncertainties (excluding the polarization-related contribution) of the cross section values.

Integrated J/ψ cross section

Element	Value
$N_{J/\psi}$	1319 $\pm$ 51 (stat.)
<A·ε>	0.3461 $\pm$ 0.0007 (stat.)
B.R.	(5.94 $\pm$ 0.06) % (syst.)
σ_{MB}	55.4 $\pm$ 1.0 (total) mb
$N_{MB}^{pile-up}$	(3.5410 $\pm$ 0.0006) $\cdot$ 10^7 (stat.)
N_{μ}^{MB}	23136 $\pm$ 152 (stat.)
$N_{\mu}^{\mu-MB}$	686132 $\pm$ 828 (stat.)
L_{INT}	18.96 $\pm$ 0.13 (stat.) nb^{-1}

Table 3.7. *Ingredients required to measure the integrated J/ψ production cross section.*

3.6.2 Differential, p_T and y, J/ψ cross sections

A differential study of the J/ψ production has been performed in two kinematical variables: the transverse momentum p_T and the rapidity y. The p_T-dependence has been studied in 7 bins {0-1, 1-2,

2-3, 3-4, 4-5, 5-6, 6-8 GeV/c} while, for the $y-$dependence, 6 bins ($2.5 < y < 4$, $\Delta y = 0.25$) have been considered. Figure 3.16 and 3.17 show the invariant mass spectra for OS muon pairs corresponding to the various p_T and y bins together with the results of the fits performed to extract the J/ψ signal.

The differential cross sections are then calculated with the same approach used for the integrated cross section which is shown in Eq. 3.13. The A$\times\varepsilon$ corrected spectra, $dN^{corr}_{J/\psi}/dp_T$ and $dN^{corr}_{J/\psi}/dy$ shown in Fig. 3.26 in blue, are normalized to the collected integrated luminosity L_{int}.

For what concerns the systematic uncertainties, the differential cross sections are affected by the same error sources as discussed above for the integrated case. The same systematic uncertainty values quoted in Table 3.6 apply to each p_T and y bin. Table 3.8 gives a summary of results on the J/ψ differential cross sections, showing the final numerical values including the various sources of systematic uncertainties. They are presented by quoting, separately, the correlated, uncorrelated and the polarization-related components.

Figure 3.41 presents the differential cross section $d^2\sigma_{J/\psi}/dp_T dy$, averaged over the rapidity interval $2.5 < y < 4$, for the transverse momentum range $0 < p_T < 8$ GeV/c. The vertical error bars represents the statistical errors while the boxes correspond to the systematic uncertainties. The systematic uncertainties relative to the luminosity are not included.

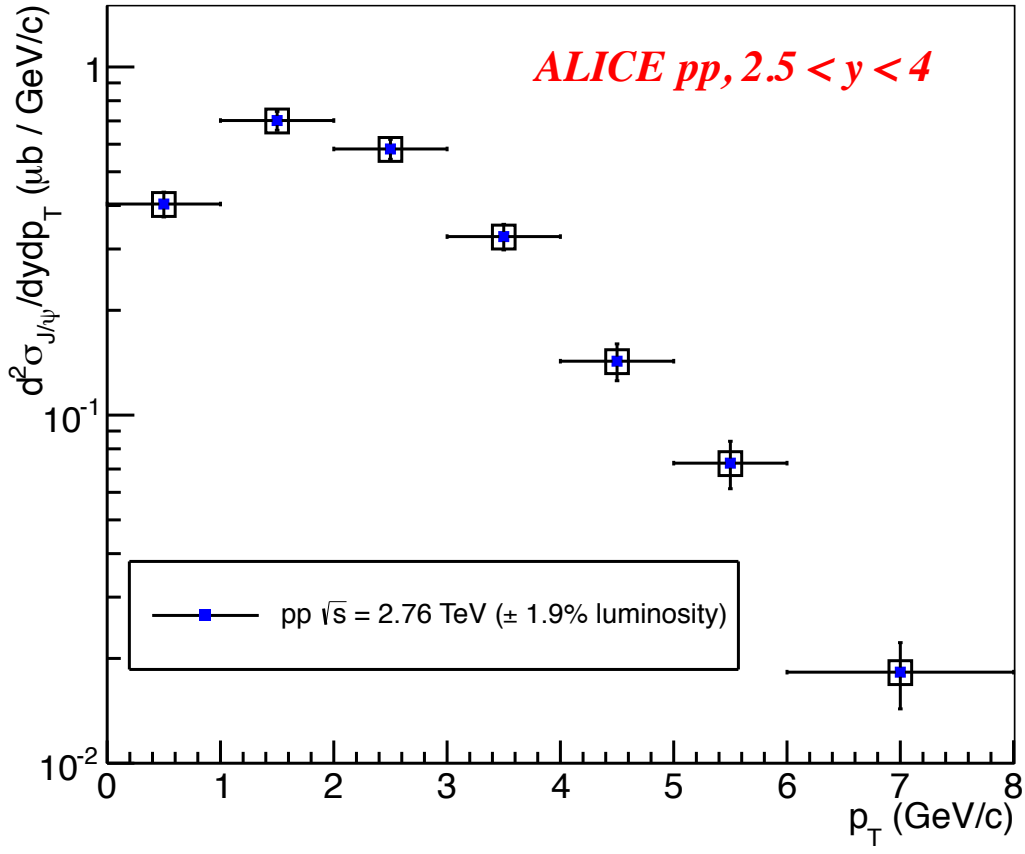

Figure 3.41. *Differential J/ψ production cross section $d^2\sigma_{J/\psi}/dp_T dy$ for pp collisions at $\sqrt{s}$ = 2.76 TeV in the forward rapidity range $2.5 < y < 4$. The symbols are plotted at the center of each p_T bin.*

p_T	$N_{J/\psi}$	A×ε	$d^2\sigma_{J/\psi}/dp_T dy$	*Systematic uncertainties*			
(GeV/c)			(μb / (GeV/c))	Correlated (μb / (GeV/c))	Non-correlated (μb / (GeV/c))	Polarization (CS) (μb / (GeV/c))	Polarization (HE) (μb / (GeV/c))
2.5 < y < 4							
[0;1]	225 ± 18	0.330	0.404 ± 0.033 (stat.)	0.023	0.023	+0.076, −0.155	+0.071, −0.145
[1 ; 2]	387 ± 24	0.326	0.702 ± 0.044 (stat.)	0.041	0.040	+0.123, −0.266	+0.100, −0.207
[2 ; 3]	326 ± 21	0.332	0.581 ± 0.038 (stat.)	0.034	0.033	+0.099, −0.203	+0.068, −0.128
[3 ; 4]	195 ± 16	0.354	0.326 ± 0.027 (stat.)	0.019	0.018	+0.047, −0.096	+0.026, −0.053
[4 ; 5]	96 ± 12	0.397	0.143 ± 0.017 (stat.)	0.008	0.008	+0.014, −0.030	+0.009, −0.020
[5 ; 6]	55 ± 9	0.449	0.073 ± 0.011 (stat.)	0.004	0.004	+0.005, −0.012	+0.006, −0.009
[6 ; 8]	31 ± 7	0.507	0.018 ± 0.004 (stat.)	0.001	0.001	+0.001, −0.001	+0.001, −0.002
y			$d^2\sigma_{J/\psi}/dy$ (μb)	(μb)	(μb)	(μb)	(μb)
[2.5 ; 2.75]	120 ± 14	0.134	3.17 ± 0.38 (stat.)	0.18	0.18	+0.70, −1.47	+0.54, −1.08
[2.75 ; 3]	242 ± 20	0.361	2.38 ± 0.20 (stat.)	0.14	0.13	+0.42, −0.84	+0.39, −0.78
[3 ; 3.25]	325 ± 22	0.489	2.37 ± 0.16 (stat.)	0.14	0.13	+0.30, −0.68	+0.32, −0.64
[3.25 ; 3.5]	292 ± 20	0.503	2.07 ± 0.14 (stat.)	0.12	0.12	+0.28, −0.56	+0.22, −0.39
[3.5 ; 3.75]	238 ± 18	0.416	2.04 ± 0.16 (stat.)	0.12	0.12	+0.34, −0.68	+0.15, −0.31
[3.75 ; 4]	108 ± 12	0.214	1.79 ± 0.20 (stat.)	0.10	0.10	+0.38, −0.73	+0.17, −0.28

Table 3.8. *Summary of the final results concerning the J/ψ differential cross sections for proton-proton collisions at $\sqrt{s}$ = 2.76 TeV.*

In Figure 3.42, we present the results for $d\sigma_{J/\psi}/dy$ for proton-proton collisions at $\sqrt{s}$ = 2.76 TeV in the forward rapidity range 2.5 < y < 4 ($p_{\mathrm{T}} > 0$ GeV/c). The values obtained in the forward rapidity region (blue solid points) were also reflected with respect to $y = 0$ (blue open points) since in proton-proton collisions the physics is symmetric with respect to zero rapidity. As the case of the p_{T} dependence, the vertical error bars represents the statistical errors while the boxes correspond to the total systematic uncertainties where those related to the luminosity are excluded.

For both Figure 3.41 and 3.42, the symbols are plotted at the center of each bin. It should also be remarked that the two differential cross sections assume unpolarized the J/ψ production and the systematic uncertainties due to the unknown degree of J/ψ polarization are not shown.

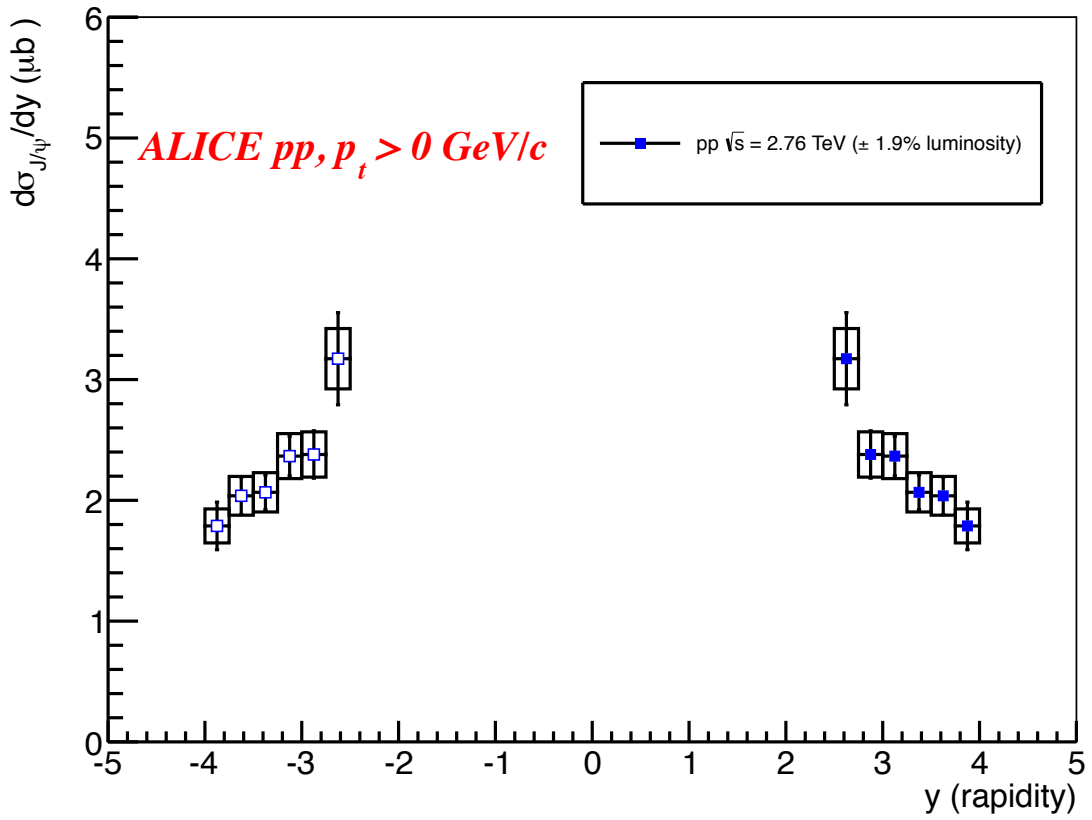

Figure 3.42. *Differential J/ψ production cross section $d\sigma_{J/\psi}/dy$ for pp collisions at $\sqrt{s}$ = 2.76 TeV in the forward rapidity range 2.5 < y < 4 ($p_T > 0$ GeV/c). The symbols are plotted at the center of each y bin.*

Chapter 4

Data analysis: $J/\psi \to \mu^+\mu^-$ in proton-proton collisions at $\sqrt{s} = 7$ TeV

In the first full year of operation of the LHC at CERN, 2010, the hadron accelerator delivered proton-proton collisions at a center-of-mass energy $\sqrt{s}$ = 7 TeV. During this first period of data taking, the LHC machine reached the goal of delivering to the experiments more than 10^{32} cm^{-2} s^{-1} (100 Hz/μb) instantaneous luminosity (peak luminosity) as shown in Fig. 4.1.

The ALICE experiment has studied the inclusive J/ψ production at central and forward rapidities in proton-proton collisions at $\sqrt{s}$ = 7 TeV [81] by analyzing a part of the proton-proton data sample collected in 2010. In order to have a collision pile-up rate in the same bunch crossing below 5%, the instantaneous luminosity delivered to ALICE was kept, for most of the 2010 run, in the range 0.06 - 0.12 Hz/μb. This low pile-up rate condition, required by several analysis performed in the ALICE central barrel, is clearly strongly penalized for a low cross section process like the J/ψ meson production.

In order to increase the statistics for such a process, ALICE has run, for a short period at the end of 2010, at instantaneous luminosities about 10 times higher than the ones previously delivered. Figure 4.1 shows the peak luminosity in the LHC 2010 run for the four LHC experiments (ALICE, ATLAS, CMS and LHCb) as a function of the proton fill number. Actually, starting from fill 1418, the ALICE peak luminosity exceeds 1 Hz/μb. These data, collected with a much larger pile-up rate in the same bunch crossing, allow therefore to increase the J/ψ statistics with respect to the one analyzed in [81].

In this chapter, we present the analysis on inclusive J/ψ production performed with the above-mentioned data collected at the end of 2010 (14 - 31 October 2010) at higher instantaneous luminosities. J/ψ mesons, studied through their decay channel into $\mu^+\mu^-$ pairs, are measured down to zero transverse momentum $p_{\rm T}$ at forward rapidity (2.5 < y < 4). The aim of the analysis is the measurement of the integrated and differential cross section for inclusive J/ψ production, the latter one as a function of the J/ψ transverse momentum $p_{\rm T}$ and rapidity y.

The analysis techniques required to study the J/ψ production have been already fully discussed in Chapter 3 for proton-proton collisions at $\sqrt{s}$ = 2.76 TeV. Since the analysis procedure is exactly the same in the case of proton-proton collisions at $\sqrt{s}$ = 7 TeV, we refer to Chapter 3 for any details. In the following, we therefore present directly the main results pointing out the differences with respect to the analysis described in Chapter 3.

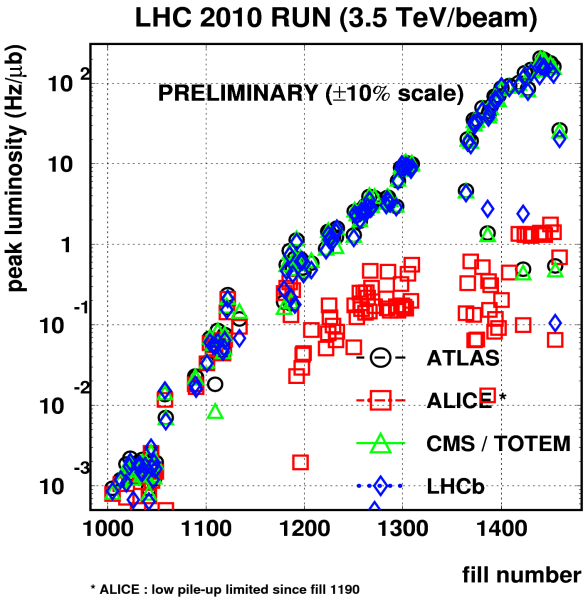

Figure 4.1. *Peak luminosity in the LHC 2010 run for the four LHC experiments (ALICE, ATLAS, CMS and LHCb) as a function of the proton fill number.*

4.1 Data Sample

The event sample used in the analysis of proton-proton collisions at $\sqrt{s} = 7$ TeV consists of Minimum Bias events (MB trigger) and so-called muon events (μ-MB trigger) where the detection of at least one muon in the pseudorapidity acceptance ($-4 < \eta < -2.5$) of the Muon Spectrometer is additionally required in coincidence with a MB trigger [1]. In particular, the μ-MB trigger allows the selection of events where at least one particle, having a transverse momentum larger than a predefined value p_{T}^{trig}, is detected in the trigger chamber of the Muon Spectrometer. Such a p_{T}^{trig} cut permits the rejection of soft muons, dominated by π and K decay, and is also able to limit the muon trigger rate when it is too high the luminosity delivered by the LHC machine.

The collected data were divided in two sub-periods called, according to the ALICE standard rules, *LHC10f* and *LHC10g*. Each one is characterized by a pretty stable tracking and trigger detector configuration and performance. However, for what concerns the p_{T}^{trig} cut value, two different choices have been made for the two sub-periods: the lowest p_{T}^{trig} threshold of 0.5 GeV/c, and 1 GeV/c, respectively. This leads to a difference, between the *LHC10f* and *LHC10g* sub-periods, regarding the mean value of the measured μ-MB trigger rate. In fact, we obtain, respectively, about 700 Hz and 200 Hz. As a consequence of the different p_{T}^{trig} cut choice, the data samples are dissimilar in particular concerning the kinematic distribution of single muon candidate tracks (see Fig. 4.2 and 4.3) .

[1] The details on the detectors used for this analysis and on the trigger definitions can be found in Chapter 2.

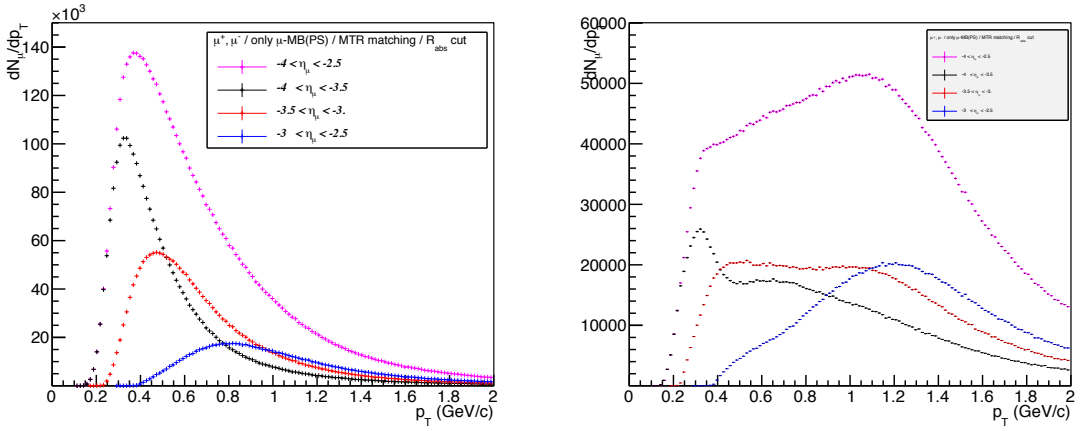

(a) *LHC10f.* (b) *LHC10g.*

Figure 4.2. *p_T distribution for single matched tracks. Only μ-MB trigger event, passing the physics selection, are retained in the analysis and the 17.6 < R_{abs} < 89.5 cm cut is applied (see Section 3.1.2 and 3.1.3 for more details). The p_T distribution is shown for several η ranges.*

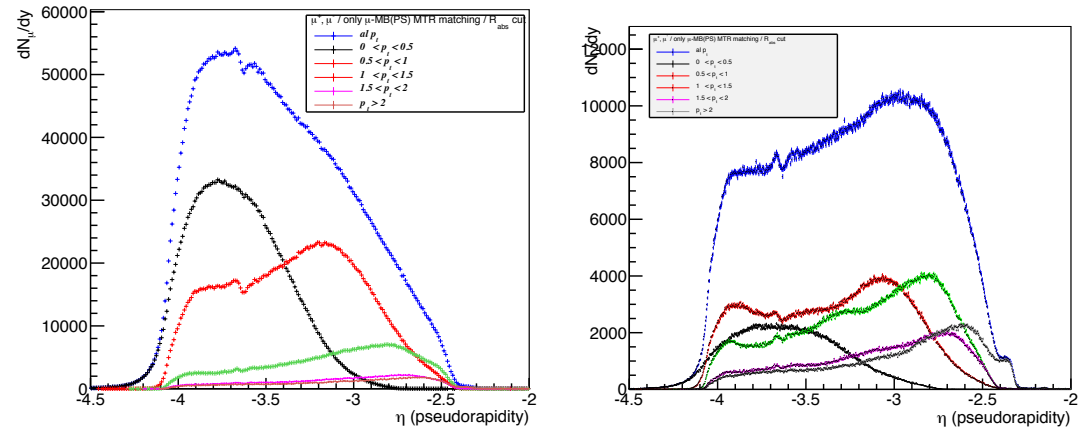

(a) *LHC10f.* (b) *LHC10g.*

Figure 4.3. *η distribution for single matched tracks. Only μ-MB trigger event, passing the physics selection, are retained in the analysis and the 17.6 < R_{abs} < 89.5 cm cut is applied (see Section 3.1.2 and 3.1.3 for more details). The η distribution is shown for several p_T ranges.*

In addition to this, three different proton beam filling schemes have beam adopted: 2 trains of 8 colliding bunches for *LHC10f* and 15 colliding bunches in different trains (and also 1 train of 12 coll. bunches) for *LHC10g*.

Such differences between the two sub-periods prevent us from merely merging them together and performing a global analysis. In the following, the analysis of the *LHC10f* period will be presented.

With the use of quality checks on the detector performances and on the beam status, the run list suitable for the analysis can be built up. Applying the several checks of the data Quality Assurance (QA) presented in Subsection 3.1.1, 4 runs are finally qualified as good runs for analysis relative to

the *LHC10f* sub-period summing up a total of $1.15 \cdot 10^6$ MB events and $29.7 \cdot 10^6$ μ-MB events.

As explained in Section 3.1.2 and 3.1.3, further selections, at event and track level, are mandatory to improve the purity of the data sample under analysis. The event selection, called physics selection, allows to remove from the data sample electromagnetic interactions (beam halo) and beam-gas events. Table 4.1 shows the effect of such a cut on the data sample after having performed, via the ALICE Environment Alien [67], the analysis of all the available ESD files corresponding to the good run list. In Table 4.2, we finally show the summary of all the selection cuts applied on the data sample under analysis pointing out, for each cut, the effect on the numbers of opposite-sign (OS) muon pairs in the invariant mass range $1 < M_{\mu\mu} < 5$ GeV/c^2. Following the choice adopted in the $\sqrt{s}$ = 2.76 TeV analysis, only muon trigger events (μ-MB) are retained in the $\sqrt{s}$ = 7 TeV analysis.

Effect of the physics selection (event cut)

Sub-period	***# MB (w/o PS)***	***# MB (w/ PS)***	***MB reduction (%)***
LHC10f	$1.1435 \cdot 10^6$	$1.0858 \cdot 10^6$	- 5
	# μ-MB (w/o PS)	***# μ-MB (w/ PS)***	***μ-MB reduction (%)***
LHC10f	$2.9650 \cdot 10^7$	$2.55476 \cdot 10^7$	- 14

Table 4.1. *Summary of the effect of the physics selection PS (event cut) introduced in the analysis of the sub-period LHC10f ..*

Summary of the selection cuts

Selection cuts	Number of OS muon pairs
only μ-MB events	291375
+ event selection	230783
+ 1 muon matching MTR	215587
+ $17.6 < R_{abs} < 89.5$ cm	190483
+ $2.5 < y_{Dimuon} < 4$	186323

Table 4.2. *Summary of the selection cuts introduced in the analysis. The second column shows the number of OS muon pairs in the mass region $1 < M_{\mu\mu} < 5$ GeV/c^2, after the application of the different selection cuts.*

4.2 Signal extraction

The red points in Figure 4.4 represent the invariant mass distribution for opposite-sign muon pairs in the mass region $1 < M_{\mu\mu} < 5$ GeV/c^2 after the application of the event and muon track selections. On top of a large continuum, a peak corresponding to the $J/\psi \to \mu^+\mu^-$ decay is clearly visible in the spectrum while the signal corresponding to the ψ(2S) decay is too weak to be detected.The integrated J/ψ yield (total number of signal events, $N_{J/\psi}$, under the conditions $2.5 < y_{J/\psi} < 4$ and $p_T{}^{J/\psi} > 0$) has been extracted by fitting that invariant mass spectrum (red distribution in Figure 4.4) in the mass

region $1.5 < M_{\mu\mu} < 5$ GeV/c^2. The fitting procedure is exactly the same as the one followed in the $\sqrt{s} = 2.76$ TeV analysis.

The fitting function therefore consists of two components: the underlying continuum (background), described by the sum of two exponentials function as shown in Eq. 3.1, and the J/ψ signal. Different fit functions have been tested to describe the resonance line shape, following the approach discussed in Section 3.5.1, in order to study the systematic uncertainty on the signal extraction.

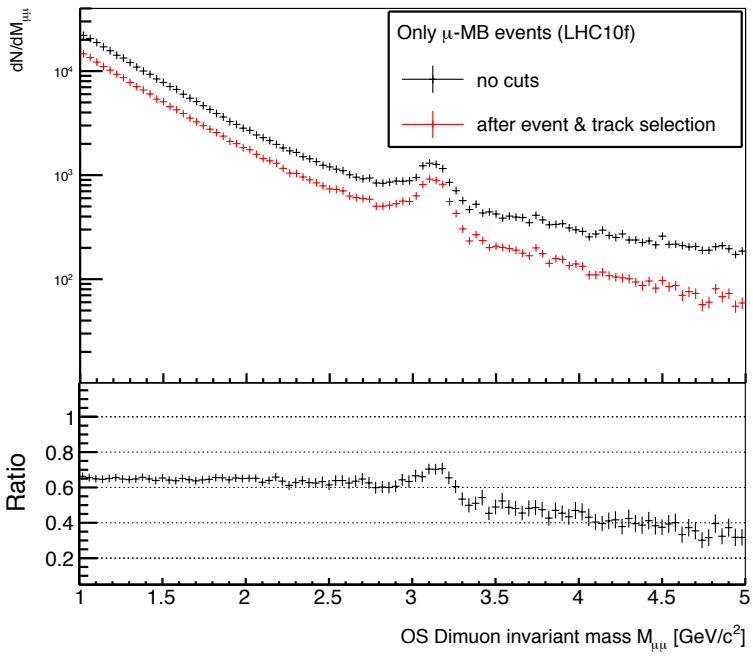

Figure 4.4. *(Top) Invariant mass distribution for opposite-sign muon pairs in the mass region $1 < M_{\mu\mu} < 5$ GeV/c^2. The black and red points correspond, respectively, to the distributions before and after the selections (event and track). Only μ-MB trigger events are retained in the analysis. (Bottom) Ratio of the two distributions.*

The integrated J/ψ yield, $N_{J/\psi}$, is finally obtained using, as reference fitting technique, the one shown in Figure 4.6: J/ψ line shape is reproduced by a CB function with tail fixed to MC simulation and ψ(2S) contribution is considered as negligible.

The CB low-end tail's parameters are then extracted by fitting the invariant mass distribution of a pure Monte Carlo J/ψ signal sample, as shown in Fig. 4.5. The fit, performed using a Crystal Ball function, gives the following values: $\alpha = 0.818 \pm 0.006$ and $n = 5.3 \pm 0.1$. Finally, in order to account for small uncertainties in the Monte Carlo description of the experimental set-up, the position of the J/ψ mass pole $m_{J/\psi}$, as well as the width of the Crystal Ball function $\sigma_{J/\psi}$, is kept as free parameters in the final fit.

The result of the fit ($\chi^2/nDoF = 0.76$) gives a J/ψ line shape described by a Crystal Ball function peaked at $m_{J/\psi} = 3.125 \pm 0.003$ GeV/c^2 (about 1% larger with respect to the PDG mass value [10]) and having a width equal to $\sigma_{J/\psi} = 78 \pm 3$ MeV/c^2. The total number of J/ψ signal events, obtained by integrating the Crystal Ball function over the mass range $1.5 < M_{\mu\mu} < 5$ GeV/c^2, is $N_{J/\psi} = 3697 \pm 118$ (stat.). The signal to background ratio, at three standard deviations, $S/B_{(\pm 3\sigma)}$ is equal to 0.9 while, for the signal significance, one gets $S/\sqrt{S+B}_{(\pm 3\sigma)} = 39.4$.

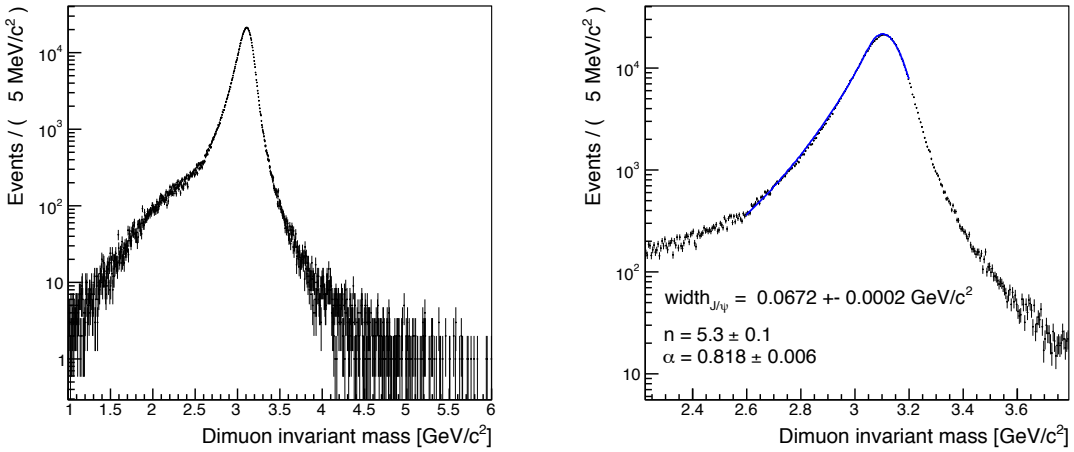

(a) *Invariant mass distribution in the mass range* $1 < M_{\mu\mu} < 6$ *GeV/c*^{2}.

(b) *Fit performed with a CB function in the mass range* $2.6 < M_{\mu\mu} < 3.2$ *GeV/c*^{2}. *The result of the fit is shown in blue line.*

Figure 4.5. *Invariant mass distribution for opposite-sign muon pairs of a pure Monte Carlo J/ψ signal sample (~* $9 \cdot 10^5$ *J/ψ). The production of simulated J/ψ, performed according to a specific* p_T *and y distribution (see details in Section 4.3), is performed taking into account the realistic conditions of the Forward Muon Spectrometer.*

With the present collected J/ψ statistics, it is also possible to study the resonance production as a function, separately, of two kinematic variables: the transverse momentum p_{T} and the rapidity y. Following the choice adopted for the $\sqrt{s} = 2.76$ TeV analysis, the p_{T}-dependance has been studied in seven bins {0-1, 1-2, 2-3, 3-4, 4-5, 5-6, 6-8 GeV/c} while six bins ($2.5 < y < 4$, $\Delta y = 0.25$) have been considered for the y-dependence.

For what concerns the J/ψ line shape, the choice made for the integrated invariant mass spectrum (Fig. 4.6) has been followed in the differential case as well. The J/ψ is described by a standard Crystal Ball function whose low-end tail is fixed, bin by bin, to its Monte Carlo value. The α and n values, used to fix the CB's tails in each p_{T} and y bin, are listed in Appendix B. Unlike the integrated case, the value of the CB width has been fixed for each bin i to the value ${\sigma_{J/\psi}}^{i} = \sigma_{J/\psi} \cdot ({\sigma_{J/\psi}}^{i,MC} / {\sigma_{J/\psi}}^{MC})$, i. e. the measured width for the integrated spectrum ($\sigma_{J/\psi}$) is scaled with the MC ratio between the widths for the bin i and for the integrated spectrum. This conservative approach takes into account the fact that having a limited J/ψ statistics prevents us to be confident in the extraction of the resonance's width directly from the measured distributions. The position of the J/ψ mass pole $\mathrm{m}_{J/\psi}$ is instead kept as free parameter in the final fit.

Concerning the underlying continuum, it can be described, as usual, with the sum of two exponential functions (Eq. 3.1) only for the invariant mass spectra in y bins. While, for the spectra in p_{T} bins, it is not possible anymore for every bin. As it can be verified in Fig. 4.7, the background clearly presets a very different shape as a function of p_{T}. As a consequence, we decided to use the standard sum of two exponential functions for the first three p_{T} bins and a gaussian function for the last four bins. A polynomial function of degree 2 has also been considered and tested in order to study the systematic uncertainties on the signal extraction bin by bin.

The sum of the J/ψ signal events for both p_{T} and y bins agrees well (within 1% and 3% respectively) with the result of the fit to the integrated mass spectrum (Fig. 3.15).

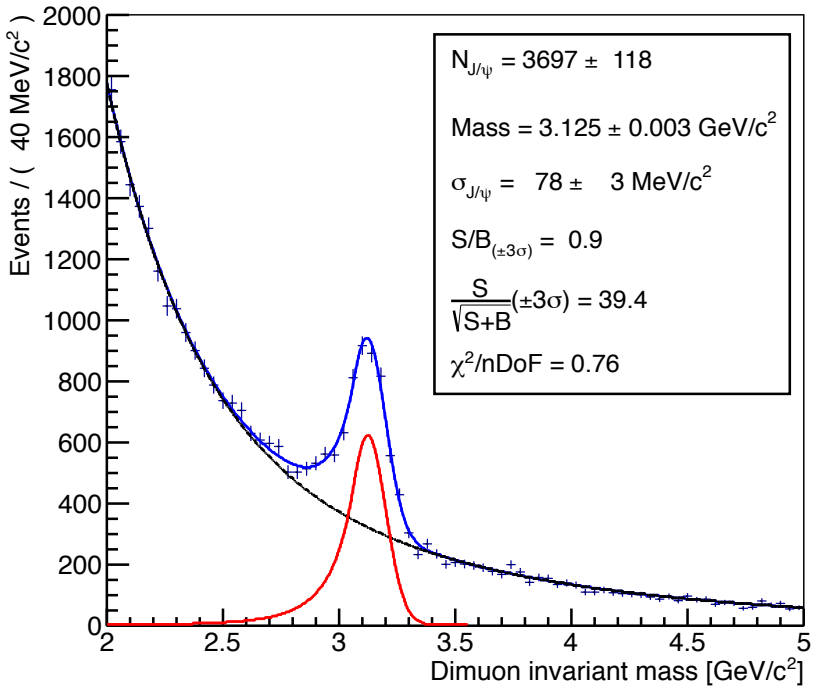

Figure 4.6. *Invariant mass distribution for opposite-sign muon pairs ($2.5 < y_{J/\psi} < 4$, $p_T^{J/\psi} > 0$ GeV/c) in the mass region $2 < M_{\mu\mu} < 5$ GeV/c^2 with the result of the fit performed in the mass range $1.5 < M_{\mu\mu} < 5$ GeV/c^2. Three different functions are plotted. The blue line represents the global fit. The J/ψ signal contribution is shown in red line. The dashed black line shows the background contribution.*

4.3 Acceptance and efficiency corrections

In order to calculate the integrated and the differential (p_T and y) J/ψ production cross sections, the J/ψ yields extracted from the previous fits must be corrected. The corrections allow to properly account for the acceptance of the apparatus and the realistic conditions of the detectors during the data taking, in term of reconstruction and triggering efficiencies.

The numerical values of the acceptance and efficiency corrections, $A \times \varepsilon$, are obtained via Monte Carlo simulation of a large sample of signal events (~$5{\cdot}10^6$ J/ψ generated in total). The J/ψ resonances are generated using realistic p_T and y distributions tuned for proton-proton collisions at $\sqrt{s}$ = 7 TeV. More in details, the input distributions for the two kinematical variables are chosen as a parametrization of the differential cross-sections measured by ALICE at forward rapidity in previous analysis, with data collected at the same center-of-mass energy [81]. The experimental data are interpolated using the functional functions [2] shown in Eq. 4.1

$$f(p_T) = \frac{p_T}{\left[1 + a \cdot (\frac{p_T}{b})^2\right]^n}, \quad g(y) = e^{-\frac{(y/y_0)^2}{2 \cdot \sigma^2}} \tag{4.1}$$

where $a = 0.36$, $b = 2.44$, $n = 3.9$, and $y_0 = 7.72$ $\sigma = 0.383$.

[2] See [70] for a discussion on phenomenological procedures to evaluate the energy dependence of the inclusive J/ψ integrated and differential cross sections in proton-proton collisions.

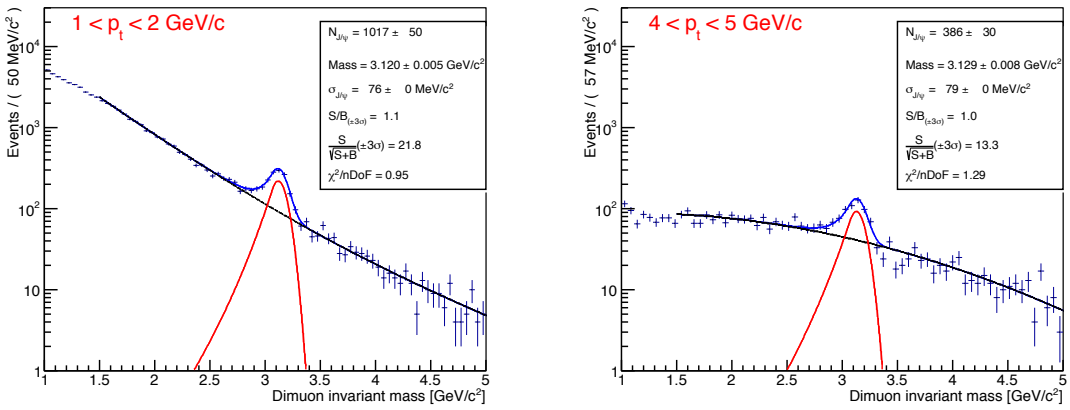

(a) $1 < p_T < 2$ GeV/c bin.

(b) $4 < p_T < 5$ GeV/c bin.

Figure 4.7. *Invariant mass spectra for OS muon pairs ($2.5 < y < 4$) in 2 p_T bins. The results of the fits are also shown. Three different functions are plotted for each y bin. The blue line represents the global fit. The J/ψ signal contribution is shown in red line. The dashed black line shows the background contribution.*

In order to simulate the realistic conditions of the different detectors, the simulation framework[3], as already explained in Section 3.3, makes use of the so-called Offline Condition DataBase (OCDB) which contains informations on the status of each detector during each run. Some of the OCDB files are automatically created during the data taking and keep track of the general conditions of the apparatus on a run-by-run basis; others are built specifically for the MC simulation and contain informations extracted from real data.

The most important OCDB files, specifically built for the present Monte Carlo simulation, are: the trigger chamber efficiency evaluated for each local boards using real data (see Chapter 2), the residual misalignments for each detection element of the muon chamber system (see Chapter 2) and the list of all the dead channels in the muon tracking stations, called *Reject list* [4].

Unlike the procedure adopted in the $\sqrt{s} = 2.76$ TeV analysis (see Section 3.3), only one Monte Carlo simulation was performed for the whole period due to the rather stable detector conditions all over the *LHC10f* period of data taking. Of course, dead channels can change from run to run and therefore this effect should be properly taken into account. This can be achieved using the *Reject list* which contains the probability of having one particular channel in a dead status. It is calculated by considering, for the collected statistics, for how long that channel was off.

4.3.1 Integrated and differential acceptance and efficiency corrections

With the above explained MC simulation, it is finally possible to extract the integrated and differential acceptance and efficiency corrections. Considering the ratio between the total number of reconstructed J/ψ events, satisfying the analysis cuts presented in Section 4.2, and the generated events in the kinematical ranges $p_T > 0$ GeV/c and $2.5 < y < 4$, we obtain the integrated correction for acceptance and efficiency which is equal to $A \times \varepsilon = 0.3092 \pm 0.0004$ (stat.).

[3] The software framework used for the Monte Carlo simulations is AliROOT, the official ALICE software.

[4] Unlike the simulation performed in the $\sqrt{s} = 2.76$ TeV analysis, a realistic primary vertex distribution has been taken

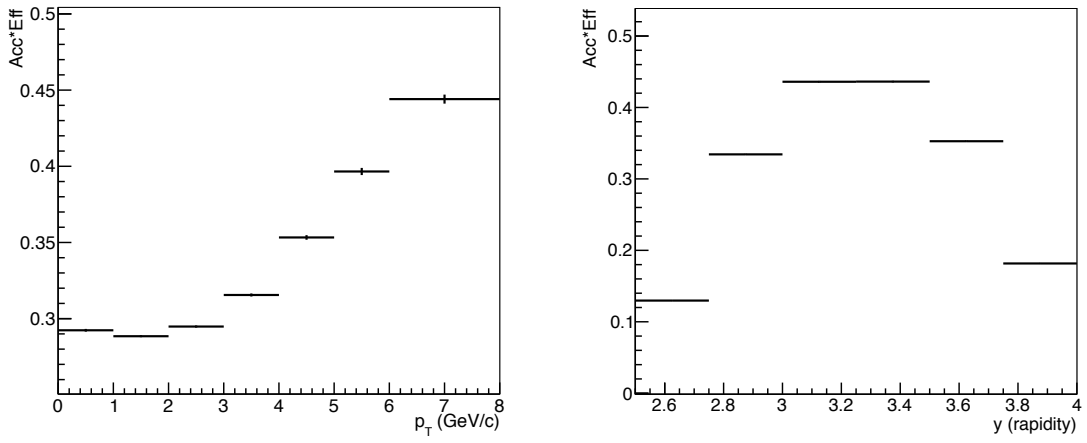

(a) p_T *dependance.* (b) *y dependance.*

Figure 4.8. *Acceptance and efficiency corrections as a function of the kinematical variables, p_T (a) and y (b).*

The study of the J/ψ meson production as a function of the transverse momentum and the rapidity requires the evaluation of the p_{T} and y dependence of the A$\times\varepsilon$ corrections which is presented in Fig. 4.8.

Finally, the differential A$\times\varepsilon$ corrections can be applied to raw J/ψ yields extracted from the fits performed bin by bin. The effect of the correction is shown, in Fig. 4.9, for the p_{T} (a) and y (b) dependence. The two data series, red and blue points, correspond respectively to the distributions before and after the A$\times\varepsilon$ correction. Instead, for what concern the p_{T}- and y-integrated J/ψ yield, we have $\mathrm{N}^{corr}_{J/\psi} = {}^{N_{J/\psi}}\!/_{<A\times\varepsilon>}$ = 11956 $\pm$ 382 (stat.) in the kinematical region 2.5 < y < 4 and p_{T} > 0 GeV/c.

The present A$\times\varepsilon$ corrections are evaluated using a Monte Carlo simulation which assumes the J/ψ meson production to be unpolarized. However, since the J/ψ polarization is unknown, it is important to study and quantify the effect of J/ψ non-zero polarization on the corrections. They were therefore calculated in other two extreme J/ψ polarization scenarios: fully transverse (λ_θ = +1) or fully longitudinal (λ_θ = -1) polarization. The calculation, performed in the Collins-Soper (CS) and helicity (HE) reference frame, gives A$\times\varepsilon$ corrections strongly dependent on the degree of the J/ψ polarization assumed in Monte Carlo simulations as we can see, for the $\sqrt{s}$ = 2.76 TeV analysis, in Fig. 3.25.

The unknown degree of polarization of the J/ψ gives a systematic uncertainty on the J/ψ production cross section which has been calculated assuming, as reference choice, the J/ψ unpolarized. The systematic uncertainties related to the polarization are calculated for both Collins-Soper and helicity reference frames. For the integrated case, we obtain +31% (λ_θ = -1) and -15% (λ_θ = +1) in the CS frame while in the HE frame +22% (λ_θ = -1) and -10% (λ_θ = +1).

into account

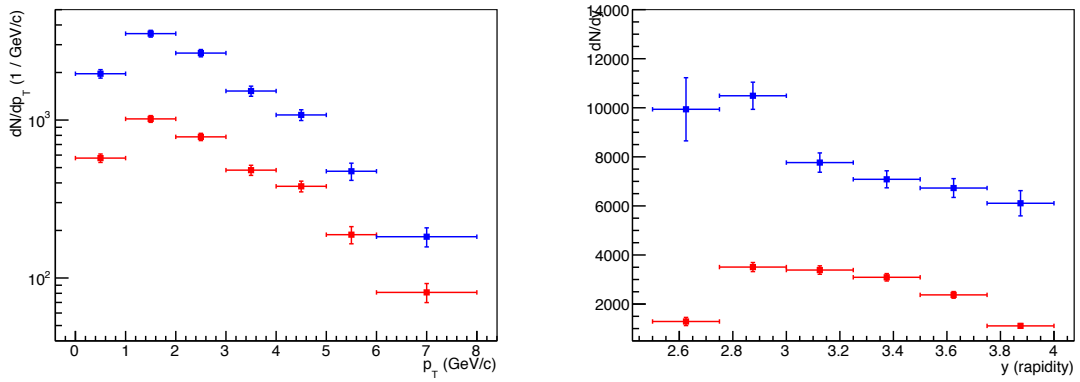

(a) p_T *dependance.* (b) y *dependance.*

Figure 4.9. *Transverse momentum and rapidity dependence of the J/ψ yield. The red and blue points correspond, respectively, to the distributions before and after the A×ε correction.*

4.4 Luminosity normalization

The J/ψ production cross sections (integrated and differential) can be calculated by normalizing the A×ε corrected J/ψ yields, $N^{corr}_{J/\psi}$, to the integrated luminosity L_{INT} corresponding to the analyzed data sample ($L_{INT} = \int L(t)\,dt$ with $L(t)$ instantaneous luminosity). The following relation is used

$$\sigma_{J/\psi}(2.5 < y < 4) = \frac{N_{J/\psi}}{A \times \varepsilon \cdot BR(J/\psi \to \mu^+\mu^-)} \cdot \frac{1}{L_{INT}} \tag{4.2}$$

where BR ($J/\psi \to \mu^+\mu^-$) = (5.94 ± 0.06) % is the branching ratio for the J/ψ decay into a muon pair [10]. As explained in Section 3.4, the integrated luminosity L_{INT} can be calculated choosing a general reference process p as $L_{INT} = {}^{N_p}/_{\sigma_p}$ where σ_p is the absolute cross section for the occurrence of the p trigger condition and N_p is the total number of p-triggered events. In the $\sqrt{s}$ = 2.76 TeV analysis, the minimum bias (MB) trigger condition has been chosen as reference process.

Actually, alternative methods can be used to estimate the integrated luminosity L_{INT}, as already mentioned in Section 3.5.5. L_{INT} can also be expressed as

$$L_{INT} = \int L(t)\,dt \;=\; \frac{N_{\mu-MB} \cdot f_\mu}{\Delta\varepsilon_{triggering} \cdot \sigma_{\mu-MB}} \tag{4.3}$$

where $N_{\mu-MB}$ is the total number of events of the type $\mu - MB$ (muon trigger) and $\sigma_{\mu-MB}$ is the corresponding cross section. $\sigma_{\mu-MB}$ is provided by van der Meer scans performed by ALICE in dedicated runs during the proton-proton data taking at $\sqrt{s}$ = 7 TeV. One of the most attractive features of this method is that there is a negligible response to pile-up (i. e. $f_\mu \sim 1$) compared to the method that uses σ_{MB}[5]. On the contrary, one limitation of this method is related to the fact that the triggering efficiency for detecting muons (which is crucial for the $\mu - MB$ trigger definition) may change over time. Under the hypothesis of a stable triggering efficiency, which is pretty reasonable since the period under analysis is short (few days) and rather stable, $\Delta\varepsilon$ can be neglected (i. e. $\Delta\varepsilon_{triggering} \sim 1$).

[5]This property is important especially for the *LHC10f* period under analysis. As mentioned in Section 4.1, due to a peak luminosity which exceeds 1 Hz/μb and the adopted proton filling scheme, the pile-up play an important role for the minimum bias (MB) trigger in the *LHC10f* period.

We have now all the ingredients to calculate, according to Eq. 4.3 , the integrated luminosity L_{INT} knowing that the absolute cross section for the occurrence of the $\mu-$MB condition (p_{T}^{trig} = 0.5 GeV/c), $\sigma_{\mu-MB}$, is equal to 810 (5% total) μb and $\mathrm{N}_{\mu-MB} = (2.5548 \pm 0.0005) \cdot 10^7$ (stat.). Finally, we obtain L_{INT} = 31.54 $\pm$ 0.01 (stat.) nb^{-1} (systematic uncertainties on luminosity are discussed in Section 4.5).

4.5 Systematics uncertainties

The sources of systematic uncertainties are exactly the same as for the corresponding $\sqrt{s}$ = 2.76 TeV analysis and have been estimated in a similar way (see Section 3.5). Table 4.3 shows their values for the integrated cross section.

For what concerns the systematic uncertainties related to the acceptance input, trigger efficiency and the reconstruction efficiency, we have kept the same values estimated in the analysis released by the ALICE collaboration [81] which analyzes a smaller pp data sample collected at the same center-of-mass energy $\sqrt{s}$ = 7 TeV .

The uncertainty on signal extraction (7.6 %) has been estimated by testing alternative shape for the J/ψ signal as explained in Section 3.5.1.

Finally, for what concerns the integrated luminosity L_{INT}, calculated as $L_{INT} = {}^{N_{\mu-MB}}/_{\sigma_{\mu-MB}}$, the total uncertainty on $\sigma_{\mu-MB}$ equal to 5% is assumed as systematic uncertainty. The 5% value is estimated during the van der Meer scans performed by ALICE to evaluate the $\sigma_{\mu-MB}$ cross section.

Summary of the systematic uncertainties

Source	(%)
Signal extraction	6.2
Acceptance input	5
Trigger efficiency	4
Reconstruction efficiency	3
Luminosity	5
B.R.	1
Total	10.7

Polarization	λ = -1	λ = +1
Collins-Soper (CS)	+31	-15
Helicity (HE)	+22	-10

Table 4.3. *Systematic uncertainties (in percent) contributing to the measurement of the integrated J/ψ production cross section.*

The total systematics uncertainty, excluding those related to the unknown degree of J/ψ polarization, is equal to 12.2 %. This value is obtained by quadratically summing the uncertainty values described above, except the polarization which is quoted separately.

4.6 Results

The analysis, described in the previous Sections, allows to measure the integrated and the differential, p_{T} and y, cross sections for the inclusive J/ψ production in pp collisions at $\sqrt{s}$ = 7 TeV. The final results are presented in the following.

4.6.1 Integrated J/ψ cross section

The integrated cross section for inclusive J/ψ production has been obtained at forward rapidities (2.5 < y < 4) for the transverse momentum range p_{T} > 0 GeV/c. It is calculated using the following Eq. 4.4

$$\sigma_{J/\psi}(2.5 < y < 4) = \frac{N_{J/\psi}/<A\cdot\varepsilon>}{BR(J/\psi \to \mu^+\mu^-)} \cdot \frac{\sigma_{\mu-MB}}{N_{\mu-MB}} \tag{4.4}$$

which can be derived by combining the relations shown in Eq. 4.2 and 4.3. In Table 4.4, all the ingredients required to calculate the integrated cross section are quoted. Finally, the measured integrated cross section is

$$\sigma_{J/\psi}(2.5 < y < 4) = 6.38 \pm 0.21(stat.) \pm 0.78(syst.) + 0.96(\lambda_{CS} = +1) - 1.98(\lambda_{CS} = -1)\mu b \tag{4.5}$$

The systematic uncertainties related to the unknown degree of J/ψ polarization, which have been estimated in both Collins-Soper (CS) and helicity (HE) reference frames, are quoted, in Eq. 4.5, separately for the reference frame (CS) where they are larger. Two extreme scenarios of fully longitudinal (λ = -1) and fully transverse (λ = +1) degree of J/ψ polarization are taken into account to quote the systematic uncertainties .

The ALICE experiment has recently studied [81] the J/ψ production at forward rapidity in pp collisions at $\sqrt{s}$ = 7 TeV. The measured production cross section, corresponding to an integrated luminosity L_{INT} = 15.6 nb^{-1}, is $\sigma_{J/\psi}(2.5 < y < 4) = 6.31 \pm 0.25(stat.) \pm 0.76(syst.) + 0.95(\lambda_{CS} = +1) - 1.96(\lambda_{CS} = -1)\mu b$. The cross section value quoted in Eq 4.5 and obtained analyzing a larger data sample of pp collisions at $\sqrt{s}$ = 7 TeV (L_{INT} = 31.54 nb^{-1}) is well compatible with the corresponding result that have been realized by ALICE.

Integrated J/ψ cross section

Element	Value
$N_{J/\psi}$	3697 $\pm$ 118 (stat.)
<A·ε>	0.3092 $\pm$ 0.0004 (stat.)
B.R.	(5.94 $\pm$ 0.06) % (syst.)
$\sigma_{\mu-MB}$	810 (5% total) μb
$N_{\mu-MB}$	(2.5548 $\pm$ 0.0005) $\cdot$ 10^7 (stat.)
L_{INT}	31.54 $\pm$ 0.01 (stat.) nb^{-1}

Table 4.4. *Ingredients required to measure the integrated J/ψ production cross section (LHC10f sample).*

4.6.2 Differential, p_T and y, J/ψ cross sections

The inclusive J/ψ production has been also studied as a function of two kinematical variables: the transverse momentum p_T and the rapidity y. The p_T-dependence has been analyzed in 7 bins {0-1, 1-2, 2-3, 3-4, 4-5, 5-6, 6-8 GeV/c} while the y-dependence, in the region $2.5 < y < 4$, was investigated in 6 bins ($\Delta y = 0.25$).

The differential cross sections are calculated with the same approach used for the integrated cross section which is shown in Eq. 4.4. The A$\times\varepsilon$ corrected spectra, $dN^{corr}_{J/\psi}/dp_T$ and $dN^{corr}_{J/\psi}/dy$ shown in Fig. 4.9 in blue, are normalized to the collected integrated luminosity L_{INT}.

Concerning the systematic uncertainties, the differential cross sections are affected by the same error sources introduced for the integrated case. The same systematic uncertainties quoted in Table 4.4 apply to each p_T and y bin. Table 4.5 gives a summary of the results obtained for the differential cross sections, showing the final numerical values including the various sources of systematic uncertainties. They are presented by quoting, separately, the correlated, uncorrelated and the polarization-related components.

Figure 4.10 presents the differential cross section $d^2\sigma_{J/\psi}/dp_T dy$, averaged over the rapidity interval $2.5 < y < 4$, for the transverse momentum range $0 < p_T < 8$ GeV/c. The vertical error bars represents the statistical errors while the boxes correspond to the systematic uncertainties. The systematic uncertainties relative to the luminosity (5%) are not included.

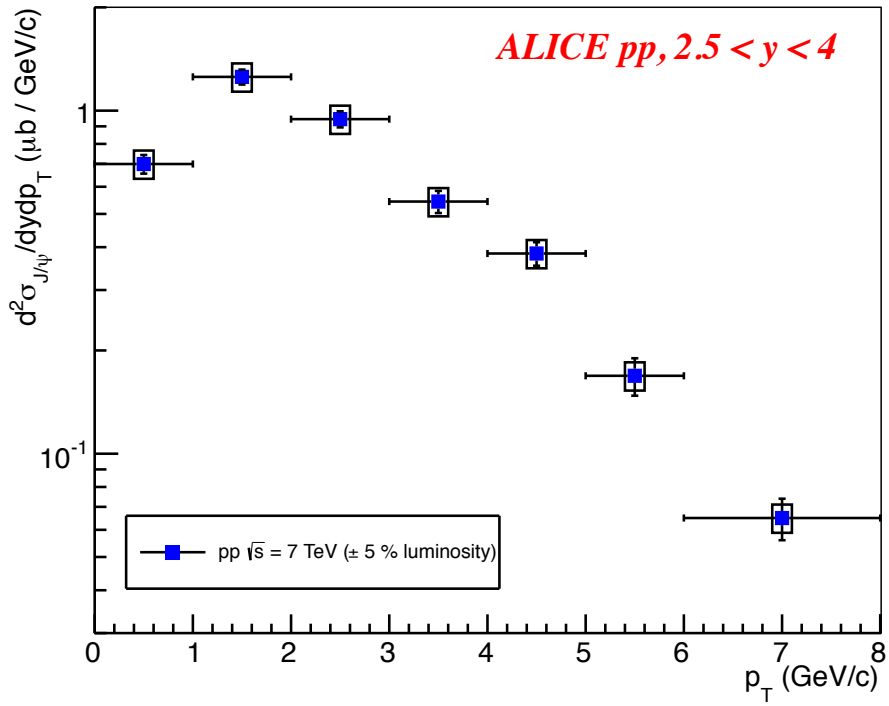

Figure 4.10. *Differential cross section $d^2\sigma_{J/\psi}/dp_T dy$ as a function of p_T for inclusive J/ψ production in pp collisions at $\sqrt{s}$ = 7 TeV at forward rapidity 2.5 < y < 4. The symbols are plotted at the center of each p_T bin.*

In Figure 4.11, we present the differential cross section $d\sigma_{J/\psi}/dy$ as a function of rapidity for inclusive J/ψ production in the forward rapidity range 2.5 < y < 4 ($p_T > 0$ GeV/c). The values

obtained in the forward rapidity region (blue solid points) were also reflected with respect to $y = 0$ (blue open points) since physics is symmetric with respect to zero rapidity in pp collisions. As for the p_T dependence, the vertical error bars represents the statistical errors while the boxes correspond to the total systematic uncertainties where those related to the luminosity are excluded.

For both Figure 4.10 and 4.11, the symbols are plotted at the center of each bin. It should also be remarked that the two differential cross sections assume an unpolarized J/ψ production and the systematic uncertainties due to the unknown degree of J/ψ polarization are not shown.

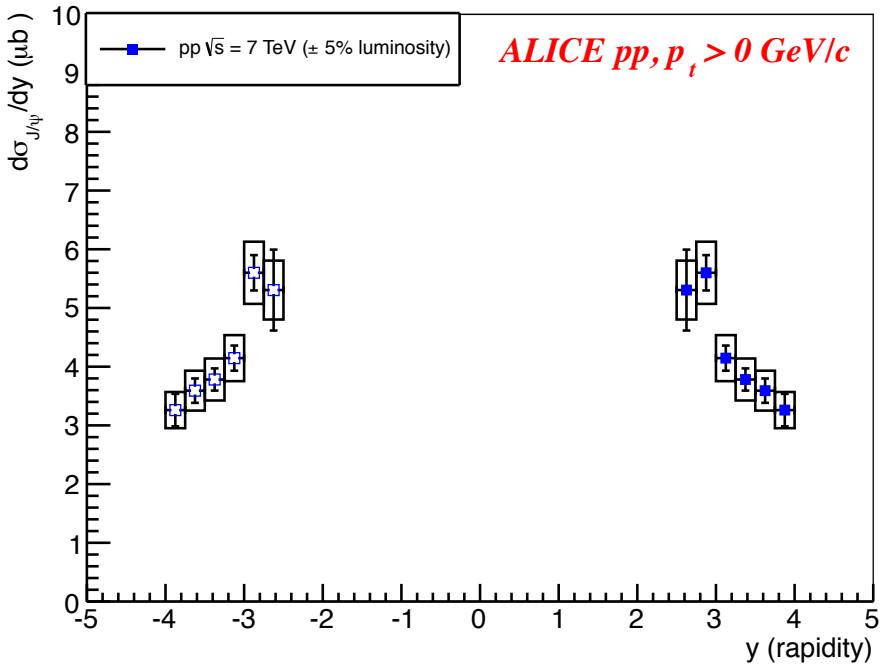

Figure 4.11. *Differential cross section $d\sigma_{J/\psi}/dy$ as a function of rapidity for inclusive J/ψ production in pp collisions at $\sqrt{s}$ = 7 TeV in the forward rapidity range 2.5 < y < 4 (p_T > 0 GeV/c). The symbols are plotted at the center of each y bin..*

Finally, in Fig. 4.12 (a) and (b), the differential cross sections shown, respectively, in Fig. 4.10 and 4.11 are compared to the corresponding results published by the ALICE collaboration [81] analyzing a smaller data sample of pp collisions at $\sqrt{s}$ = 7 TeV .

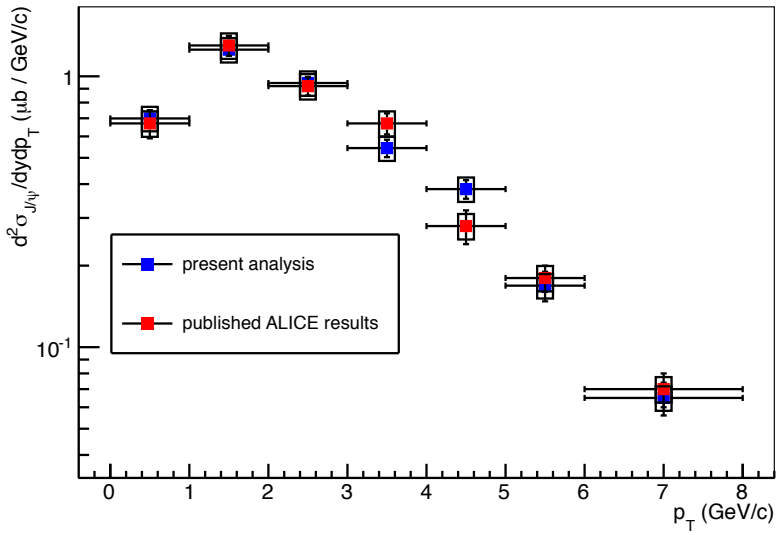

(a) *Differential cross section $d^2\sigma_{J/\psi}/dp_T dy$ as a function of p_T. The points shown in Fig. 4.10 (blue points) are compared to the results previously published by the ALICE collaboration [81](red points).*

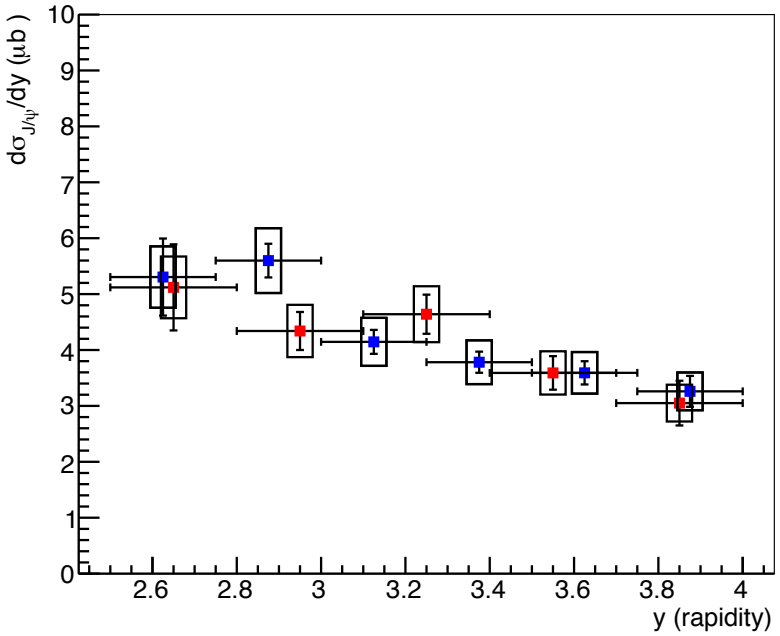

(b) *Differential cross section $d\sigma_{J/\psi}/dy$ as a function of rapidity. The points shown in Fig. 4.11 (blue points) are compared to the results previously published by the ALICE collaboration [81] (red points).*

Figure 4.12. .

p_T	$N_{J/\psi}$	$A\times\varepsilon$	$d^2\sigma_{J/\psi}/dp_T dy$	*Systematic*	*uncertainties*		
(GeV/c)			(μb / (GeV/c))	Correlated (μb / (GeV/c))	Non-correlated (μb / (GeV/c))	Polarization (CS) (μb / (GeV/c))	Polarization (HE) (μb / (GeV/c))
2.5 < y < 4							
[0;1]	574 ± 35	0.292	0.699 ± 0.044 (stat.)	0.050	0.056	+0.146, −0.219	+0.136, −0.198
[1;2]	1017 ± 50	0.288	1.254 ± 0.063 (stat.)	0.090	0.100	+0.299, −0.338	+0.183, −0.280
[2;3]	783 ± 41	0.295	0.945 ± 0.051 (stat.)	0.067	0.075	+0.175, −0.267	+0.092, −0.195
[3;4]	482 ± 35	0.316	0.543 ± 0.040 (stat.)	0.039	0.043	+0.097, −0.146	+0.057, −0.089
[4;5]	381 ± 30	0.353	0.383 ± 0.030 (stat.)	0.027	0.031	+0.055, −0.068	+0.027, −0.041
[5;6]	188 ± 23	0.397	0.169 ± 0.021 (stat.)	0.012	0.013	+0.009, −0.028	+0.009, −0.019
[6;8]	162 ± 22	0.444	0.065 ± 0.009 (stat.)	0.005	0.005	+0.006, −0.003	+0.006, −0.007
y			$d^2\sigma_{J/\psi}/dy$ (μb)	(μb)	(μb)	(μb)	(μb)
[2.5 ; 2.75]	322 ± 42	0.130	5.30 ± 0.69 (stat.)	0.38	0.42	+1.34, −1.68	+0.97, −1.33
[2.75 ; 3]	877 ± 46	0.334	5.60 ± 0.30 (stat.)	0.40	0.45	+1.25, −1.37	+1.10, −1.28
[3 ; 3.25]	847 ± 43	0.436	4.15 ± 0.21 (stat.)	0.30	0.33	+0.47, −0.82	+0.41, −0.78
[3.25 ; 3.5]	773 ± 38	0.436	3.78 ± 0.19 (stat.)	0.27	0.30	+0.43, −0.75	+0.37, −0.71
[3.5 ; 3.75]	593 ± 34	0.353	3.59 ± 0.21 (stat.)	0.26	0.29	+0.58, −0.79	+0.23, −0.54
[3.75 ; 4]	277 ± 23	0.182	3.26 ± 0.28 (stat.)	0.23	0.26	+0.72, −1.08	+0.10, −0.49

Table 4.5. *Summary of the final results on the differential cross sections for inclusive J/ψ production in pp collisions at $\sqrt{s}$ = 7 TeV.*

Chapter 5

Experimental data *versus* model predictions

In Chapter 3 and 4, the inclusive J/ψ production has been studied in the kinematic region $2.5 < y < 4$ and $p_{\mathrm{T}} > 0$, analyzing proton-proton (pp) collisions at center-of-mass energies of $\sqrt{s}$ = 2.76 and 7 TeV, respectively. Fig. 3.41 and 4.10 show the double differential cross sections $d^2\sigma_{J/\psi}/dp_{\mathrm{T}}dy$ as a function of the J/ψ transverse momentum p_{T} while the differential cross sections $d\sigma/dy$ as a function of the rapidity y are plotted in Fig. 3.42 and 4.11.

This chapter, after a short review of experimental results on quarkonium production at hadron colliders (Tevatron, RHIC and LHC), is devoted to compare the above mentioned J/ψ results, presented in Chapter 3 and 4, with the available model predictions.

5.1 Review of recent experimental results on quarkonium production

Quarkonium production has been extensively studied since November 1974 when the discovery of the first quarkonium state ($Q\bar{Q}$), the J/ψ resonance, was announced in the particle physics community. For almost 40 years, many results have been published concerning the quarkonium production in lepton-lepton, lepton-hadron and hadron-hadron collisions. In this section, a review of the main experimental results as obtained by the most recent hadron colliders (Tevatron, RHIC and LHC) is presented [34].

Results from Tevatron. The Tevatron at Fermilab, as stated by its name, delivered proton-antiproton[1] collisions at TeV energies. Two different runs have been performed: for Run I (1993 - 1996) the center-of-mass energy was equal to $\sqrt{s}$ = 1.8 TeV, while a larger value, $\sqrt{s}$ = 1.96 TeV, was reached in Run II.

The Collider Detector at Fermilab (CDF) collaboration measured, in Run I and II , the production cross sections for several charmonium and bottomonium states. Fig. 5.1 shows the differential cross section for prompt production of J/$\psi \to \mu^+\mu^-$, i. e. J/ψ not coming from the decay of B mesons, as a function of p_{T} measured with Run I data sample. The three fractions of prompt J/ψ[2] are plotted as

[1] It is worth observing that high-energy pp and $p\bar{p}$ collisions give similar results for the same kinematics, due to the small contribution of valence quarks in the initial hard processes.

[2] In the CDF analysis, prompt J/ψ's that do not come from $\psi(2S)$ or χ_c decays are assumed to be produced directly.

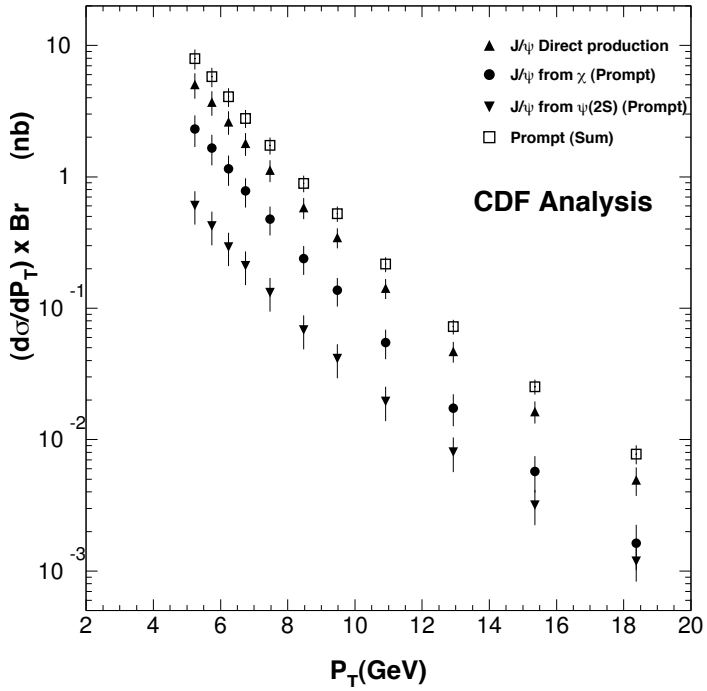

Figure 5.1. *Differential cross section for prompt production of J/ψ→$\mu^+\mu^-$ as a function of p_T for $|\eta| < 0.6$ (Run I data sample) [34].*

well. In Fig. 5.2, experimental results on charmonia, as measured by CDF with Run I data sample, are compared to several theoretical predictions (CSM, CEM and NRQCD factorization approach).

As shown in Fig. 5.2 (a), the observed direct J/ψ and prompt $\psi(2S)$[3] production cross sections were found in disagreement with the predictions of the LO CSM (dotted curves). Actually, prompt cross sections were orders of magnitude above the LO CSM predictions. This problem, known as ψ' anomaly, was confirmed, at LO, even when the gluon fragmentation processes[4] were included within the CSM [34].

The crisis of CSM motivated various theoretical developments which led new interpretations of the quarkonium hadroproduction mechanisms, especially within the NRQCD factorization approach. In particular, NRQCD calculations at LO, including gluon fragmentation processes at high p_T, were able to fit[5] the CDF's charmonium production results showing a pretty good agreement (see Fig. 5.2(a)) [6].

[3]It is worth noting that for $\psi(2S)$, the prompt production identifies with the direct one.

[4]Gluon fragmentation processes, even though of higher order in α_s, are supposed to prevail over the LO CSM for S-wave mesons (J/ψ, ψ', ...) at large p_T [82].

[5]The fit to CDF experimental data allows to extract the non-perturbative matrix elements, the so-called Long Distance Matrix Elements (LDMEs) (see Section 1.2.3.5). Once they are known, NRQCD can be used to obtain other theoretical predictions (e. g. quarkonium polarization).

[6]The application of the LO NRQCD approach to the $\Upsilon(1S)$ differential p_T cross section is satisfactory only for $p_T > 8$ GeV/c, while for lower p_T the theoretical prediction diverges [83].

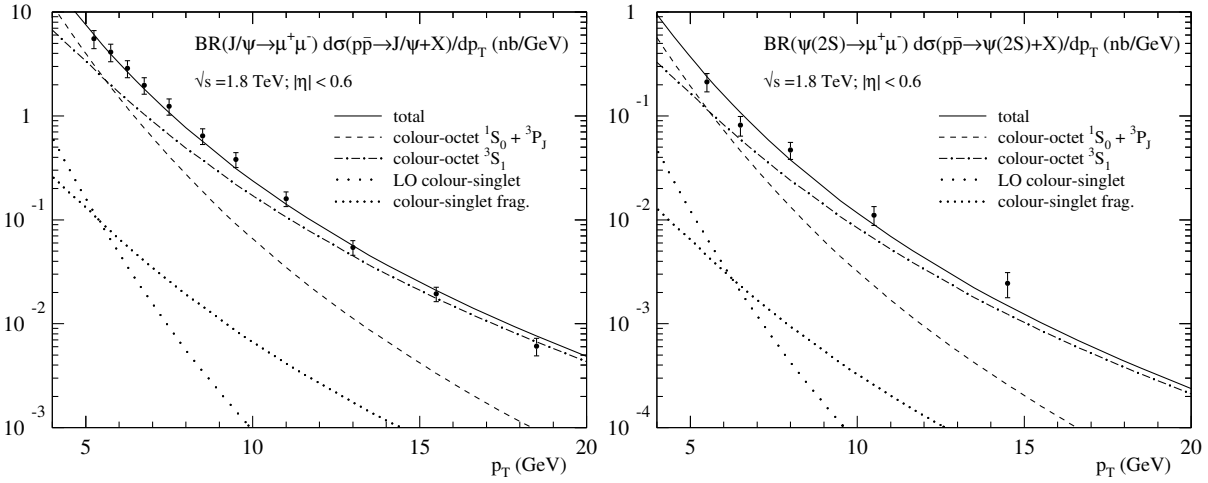

(a) *Direct J/ψ (left) and prompt ψ(2S) (right) production. The dotted curves are the LO CSM contributions. The solid curves are the LO NRQCD factorization fits and the other curves are individual color-octet contribution to the fits.*

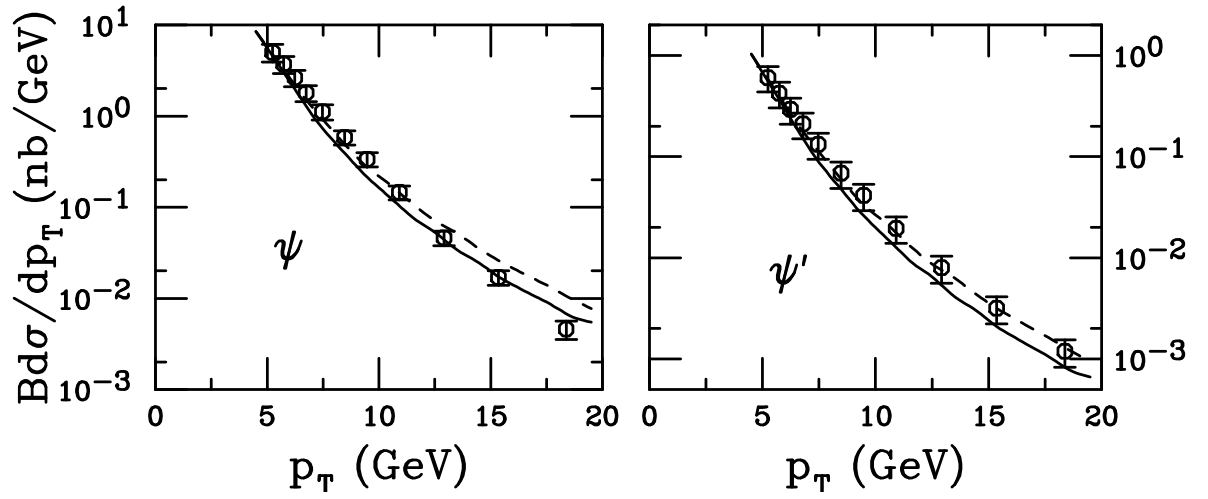

(b) *Direct J/ψ (left) and prompt J/ψ from decays of ψ(2S) (right) production. The dotted and solid solid curves are two CEM predictions at NLO obtained using two different set of parameters.*

Figure 5.2. *Differential cross sections for charmonia production at the Tevatron as a function of p_T. The data points, CDF measurements (Run I, $p\bar{p}$ at $\sqrt{s}$ = 1.8 TeV), are compared to CSM, CEM and NRQCD factorization predictions. From Ref. [84].*

Fig. 5.2 (b) show that direct J/ψ (left) and prompt J/ψ from $\psi(2S)$ decays (right) differential $p_{\rm T}$ cross sections can also be well described by NLO CEM calculations within $k_{\rm T}$-factorization approach[7].

Afterwards, many theoretical efforts from the CSM side have been made in order to recover the above mentioned failure at LO, motivated also by the difficulties of LO NRQCD in describing quarko-

[7] In $k_{\rm T}$-factorization approaches parton are not collinear but have a proper transverse momentum distribution. Within this approach, processes, that appear only at higher order in the standard collinear approach, contribute at low orders in α_s too.

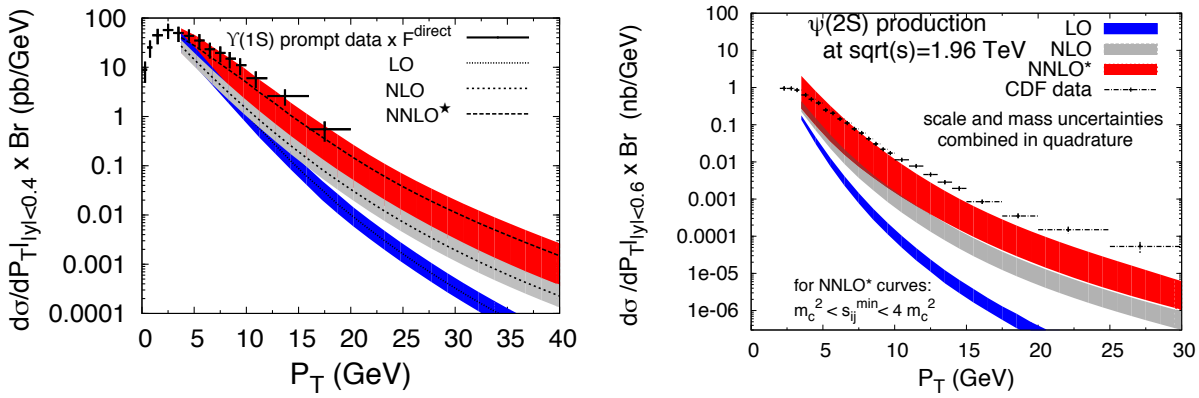

Figure 5.3. *Differential p_T cross sections for prompt $\Upsilon(1S)$ (left) and prompt $\psi(2S)$ (right) production as measured by the CDF experiment in Run I and II, respectively (prompt $\Upsilon(1S)$ yield is multiplied by F^{direct} to obtain the direct yield). Experimental data are compared to CSM predictions (direct production) at various orders. Blue bands represent LO (α_s^3). Grey bands represent full NLO ($\alpha_s^3 + \alpha_s^4$). Red bands represent NNLO* (up to α_s^5).*

nia polarization [85]. Calculations at higher orders in α_s, including NLO and NNLO* [8] contributions [86, 87, 88], have therefore allowed to obtain new predictions for prompt $\Upsilon(1S)$ and $\psi(2S)$ production at Tevatron in Run I and Run II, respectively.

NLO and NNLO* corrections, shown with the CDF experimental data in Fig. 5.3, appeared to be quite important, especially in the high-p_T region leading to predictions which tend to agree much better with the experimental p_T differential cross sections. Therefore, CSM started to play again a key role in the description of quarkonium hadroproduction. New NLO calculations were also computed for the NRQCD fits giving small differences with respect to the LO ones.

Results from RHIC. RHIC collider at BNL run at $\sqrt{s} = 200$ GeV with pp collision. PHENIX and STAR collaboration released several results on J/ψ production for whom new theoretical calculations were available.

In Fig. 5.4 (a), the differential p_T prompt J/ψ cross sections, $d\sigma/dP_T dy \times$ Br, as measured by STAR [89] and PHENIX [90] in pp collisions at $\sqrt{s} = 200$ GeV at mid-rapidity rapidity ($|y| < 0.35$), are compared to CSM predictions for direct J/ψ production [91]. The light blue band represents the NLO$^+$yield, which is namely the yield at NLO accuracy (gg and gq fusion) added to the yield from cg fusion at LO.

The red band instead represents the NNLO* yield (gg and qg fusion) with cg fusion at LO added. The NLO$^+$ prediction agrees with the PHENIX J/ψ data in the low-p_T range ($p_T \lesssim 2$ GeV/c) while, for larger p_T values, it is substantially below the STAR and PHENIX points. The cg LO + NNLO* CSM contribution, which can be computed reliably for $p_T > 5$ GeV/c, is compatible, within the theoretical uncertainty band, with the data points, although the band is quite large.

In Fig. 5.4 (b), the differential p_T prompt J/ψ cross section, as measured by PHENIX [93] in pp collisions at $\sqrt{s} = 200$ GeV at mid-rapidity rapidity ($|y| < 0.35$), is compared to the LO NRQCD and the LO CSM predictions [92] in the region $p_T > 1.5$ GeV. The band surrounded by solid red curve displays the direct J/ψ CSM contribution at LO in α_s which underestimates the data over the whole

[8] The NNLO* is a not complete NNLO (leading-p_T NNLO contributions).

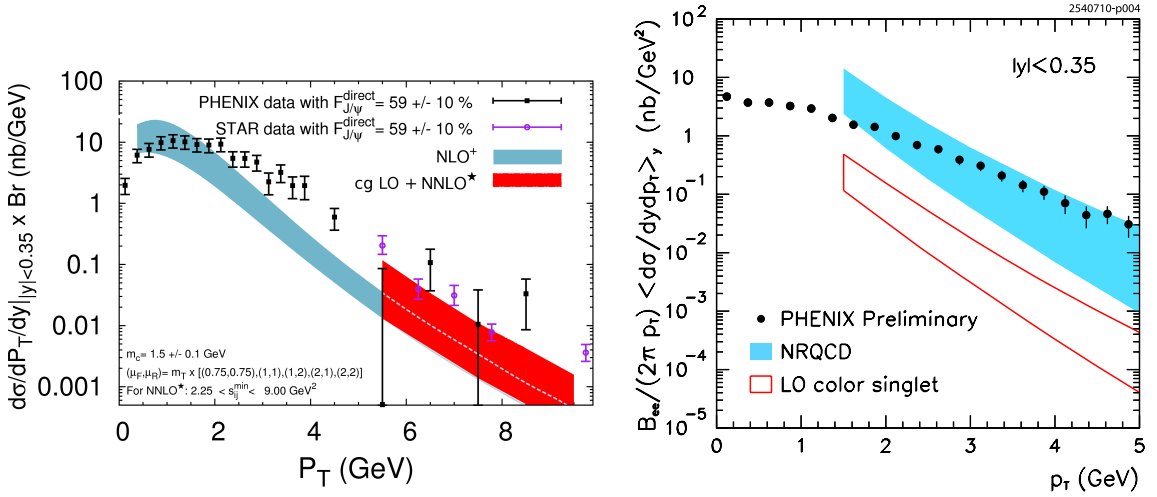

(a) *Direct J/ψ CSM predictions [91]. Light blue band corresponds to NLO$^+$. Red band corresponds to cg LO + NNLO* . Data points are multiplied by $F^{direct}_{J/\psi}$.*

(b) *The shaded band represents the LO NRQCD prediction and the band surrounded by a solid curve is the CSM contribution at LO [92].*

Figure 5.4. *Differential p_T prompt J/ψ cross sections as measured by PHENIX [90] (a) [93] (b) and STAR [89] (a) in pp collisions at $\sqrt{s}$ = 200 GeV at mid-rapidity rapidity ($|y| < 0.35$). Data points are compared to theoretical predictions.*

p_T range. The light blue shaded band indicates the prompt J/ψ NRQCD prediction at LO (α_s^3) and well reproduced the PHENIX experimental data points.

Fig. 5.5 presents the differential y prompt J/ψ cross section, $d\sigma_{J/\psi}/dy \times$ Br, as measured by PHENIX [90, 93, 94] [9] compared to the direct J/ψ CSM predictions [95]. The band surrounded by the thin dashed line indicates the CSM at LO (α_s^3) by gg fusion only. The one surrounded by the solid line represents the CSM at NLO (up to α_s^4) by gg and qg fusion only. Finally, the light-blue band is the NLO$^+$ (NLO + cg fusion) prediction.

The predictions at LO and NLO accuracy appear to be consistent in size, and the theoretical uncertainty band of the latter one (indicated by the two curves in both cases) is smaller than that of the LO. This can be interpreted as an indication that we are in a proper perturbative regime [95]. PHENIX data are compatible with both LO and NLO predictions. Even though the NLO is pretty close to the data, the additional cg contribution (NLO$^+$) improves the agreement.

Results from LHC. In the first two years of activity (2010 and 2011), the LHC collider has delivered pp collisions at the center-of-mass energies $\sqrt{s}$ = 7 and 2.76 TeV[10]. This has allowed the four LHC experiments (ALICE [2], ATLAS [3], CMS [4] and LHCb [5]) to publish many results on quarkonium cross sections. At the same time, new theoretical predictions became available and were compared to experimental data. The major results, obtained by ATLAS, CMS and LHCb, are here reviewed. The ALICE ones are described in Section 5.2

The **ATLAS collaboration** has measured inclusive, prompt and non-prompt J/ψ production [30]

[9] The differential J/ψ production cross section vs y has been measured by PHENIX in the central ($|y| < 0.35$) as well as in the forward ($1.2 < |y| < 2.2$) regions.

[10] In the 2012 pp run, $\sqrt{s}$ has been increased to 8 TeV.

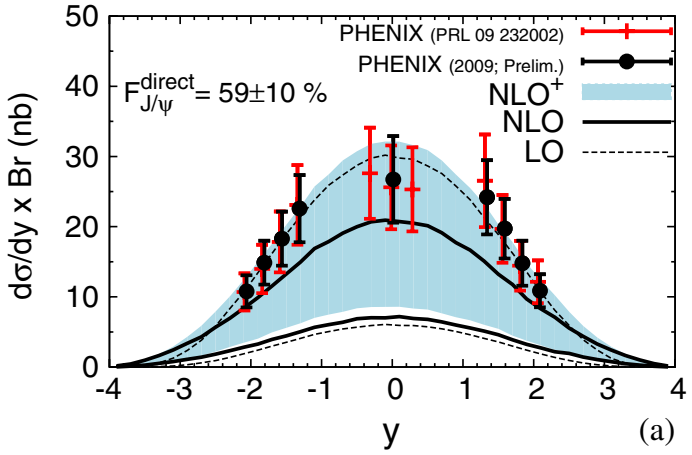

Figure 5.5. *Differential cross section for prompt J/ψ production as a function of rapidity y as measured by PHENIX [90] [93][94] compared to direct J/ψ CSM predictions [95]. LO (thin dashed line). NLO (solid line). NLO$^+$ (light-blue band). Data points are multiplied by* $F^{direct}_{J/\psi}$.

in the decay channel $J/\psi \to \mu^+\mu^-$ in pp collisions at $\sqrt{s} = 7$ TeV. The analysis has been performed as a function of the J/ψ transverse momentum and rapidity in the kinematical range $1 < p_T < 70$ GeV/c and $|y| < 2.4$. The p_T differential prompt J/ψ cross sections, obtained in four rapidity bins, have been compared to different theoretical predictions, namely Color Singlet Model and Color Evaporation Model [96].

In Fig. 5.6 (a), the invariant mass distribution of reconstructed $\mu^+\mu^-$ candidates is shown for the central rapidity bin $|y| < 0.75$. The solid red line indicates the result of the fit used to extract the J/ψ signal. In Fig. 5.6 (b), the prompt J/ψ production as a function of p_T is presented for the same central y bin. The blue solid line (with no uncertainty band defined) is the CEM prediction at NLO, with k_T smearing, for prompt J/ψ production. It includes contributions from $\psi(2S)$ and χ_c feed-down and therefore can be directly compared with the ATLAS points. The normalization predicted by CEM is lower than in data and, in addition, the shape diverges from the measured one.

The shaded grey and red bands are, respectively, the CSM NLO and NNLO* predictions for direct J/ψ production. As the calculation is obtained for direct production, corrections for χ_c and $\psi(2S)$ feed-down must be applied to the calculation in order to directly compare it to data.[11]. The comparison shows that NNLO* predictions significantly improve the description of prompt J/ψ p_T dependence and normalization respect to the NLO predictions. Nevertheless, the agreement, with the upper part of the theoretical band, in only present at low transverse momenta, while for the highest transverse momenta the NNLO* prediction is clearly below the data points. The discrepancy may be attributed to higher order corrections beyond NNLO* that are not included in the present calculation but are expected to be relatively significant for charmonium production.

The fraction of J/ψ coming from the decay of B mesons was studied by ATLAS as a function of p_T (up to p_T = 70 GeV/c) in four rapidity bins. The results, for the most central rapidity bin ($|y| < 0.75$), are shown in Fig. 5.7, together with the results from other experiments.

The **CMS collaboration** has measured inclusive, prompt and non-prompt J/ψ production in the

[11] The correction for feed-down, applied to CSM calculations, assumes a flat 10% factor to account for the contribution of $\psi(2S) \to J/\psi\,\pi\pi$ and a 40% factor is added to account for radiative χ_c decays. A total correction of 50% is therefore applied. The uncertainty on the corrector factor is not included in the CSM theoretical uncertainty.

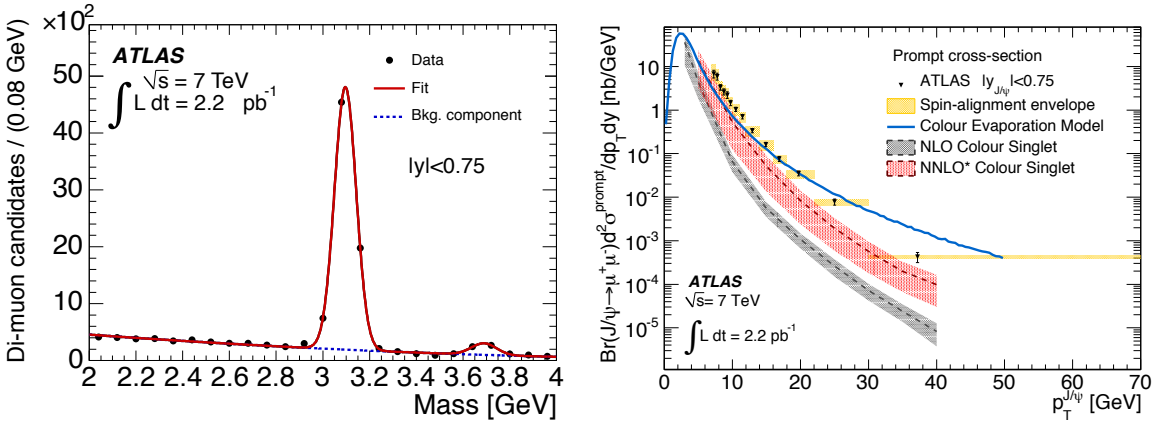

(a) *Invariant mass distribution of reconstructed $\mu^+\mu^-$ candidates. The solid red line is the result of the fit (binned minimum-χ^2 method) where J/ψ and $\psi(2S)$ signals are described by single Gaussians while the background is a straight line.*

(b) *Prompt J/ψ production cross sections as a function of the J/ψ p_T at the mid-rapidity $|y| < 0.75$ compared to different theoretical predictions. The grey and red bands are the CSM predictions at NLO and NNLO* respectively, while the blue solid line is the CEM at NLO prediction.*

Figure 5.6. *J/ψ production as measured by the ATLAS collaboration [30].*

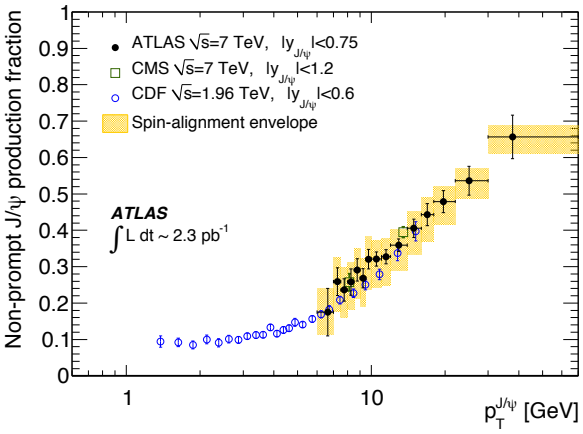

Figure 5.7. *J/ψ non-prompt fractions as a function of J/ψ transverse momentum. Equivalent results from CMS [97] and CDF [77] are plotted (from ref. [30]).*

J/$\psi \to \mu^+\mu^-$ decay channel at $\sqrt{s}$ = 7 TeV [97] [31]. Merging the two analysis ([31] is based on a larger statistics with respect to [97]), allows to study the J/ψ production in a wide $p_{\rm T}$ range, from 0.3 to 70 GeV/c, in five rapidity bins within $|y| < 2.4$. Fig. 5.8 shows the differential cross sections for inclusive J/ψ production as a function of $p_{\rm T}$ for the five rapidity bins. The $p_{\rm T}$ distribution of the prompt J/ψ production is shown, for the five rapidity bins, in Fig. 5.9 (a). The same measurement has also been performed for prompt ψ' production in a smaller $p_{\rm T}$ range, from 6.5 to 30 GeV/c, in three rapidity bins within $|y| < 2.4$. The results are presented in Fig. 5.9 (b).

The results, for both resonances, are compared to NLO NRQCD predictions (light blue bands). The agreements is very good for each rapidity bin and over the full $p_{\rm T}$ range explored.

CMS has measured the fraction of J/ψ and ψ' coming from the decay of B mesons as a function of $p_{\rm T}$ in different rapidity ranges [31]. Fig. 5.7 shows some preliminary CMS results for $|y| < 1.2$.

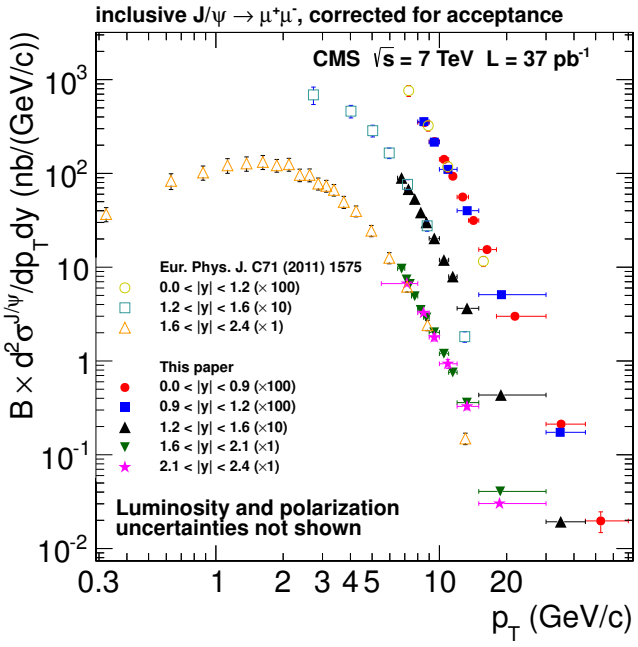

`Figure 5.8.` *Differential cross section for inclusive J/ψ production as a function of p_T for the five rapidity bins as measured by CMS. (from Ref. [31])*

The **LHCb collaboration** has studied the J/ψ production in the J/$\psi \to \mu^+\mu^-$ decay channel at $\sqrt{s}$ = 7 TeV [32]. The differential cross sections for prompt and non-prompt J/ψ production are measured as a function of the J/ψ $p_{\rm T}$ and rapidity y in the kinematical region $0 < p_{\rm T} < 14$ GeV/c and $2.0 < y < 4.5$ (forward rapidity). Fig. 5.10 (a) and (b) present the differential cross sections for prompt J/ψ production as a function of $p_{\rm T}$ and y, respectively. The first distribution is plotted in five y bins while the latter is integrated over the full $p_{\rm T}$ range.

Fig. 5.11 shows the $p_{\rm T}$ differential production cross section for prompt J/ψ in the full rapidity range compared to several theoretical predictions calculated in the LHCb acceptance region. Data points are compared to:

- (top, left) direct J/ψ production as calculated from NRQCD at LO (filled orange band) and at NLO (hatched green band);
- (top, right) direct J/ψ production as calculated from CSM at NLO (hatched grey band) and at NNLO* (filled red band);
- (bottom, left) prompt J/ψ production as calculated from NRQCD at NLO (filled light green band). χ_c and $\psi(2S)$ feed-down is included;
- (bottom, right) prompt J/ψ production as calculated from CEM at NLO (solid blue curve). d). χ_c and $\psi(2S)$ feed-down is included;

The best agreement is found between data and NRQCD prediction. Nevertheless, the CSM prediction tends to approach the data points at high $p_{\rm T}$ once the NNLO* calculation is considered. Finally, CEM prediction presents discrepancies from both normalization and shape point of view.

LHCb has also measured the fraction of J/ψ coming from B hadrons [32]. The results, plotted as a function of the $p_{\rm T}$, are shown in Fig. 1.8 (b).

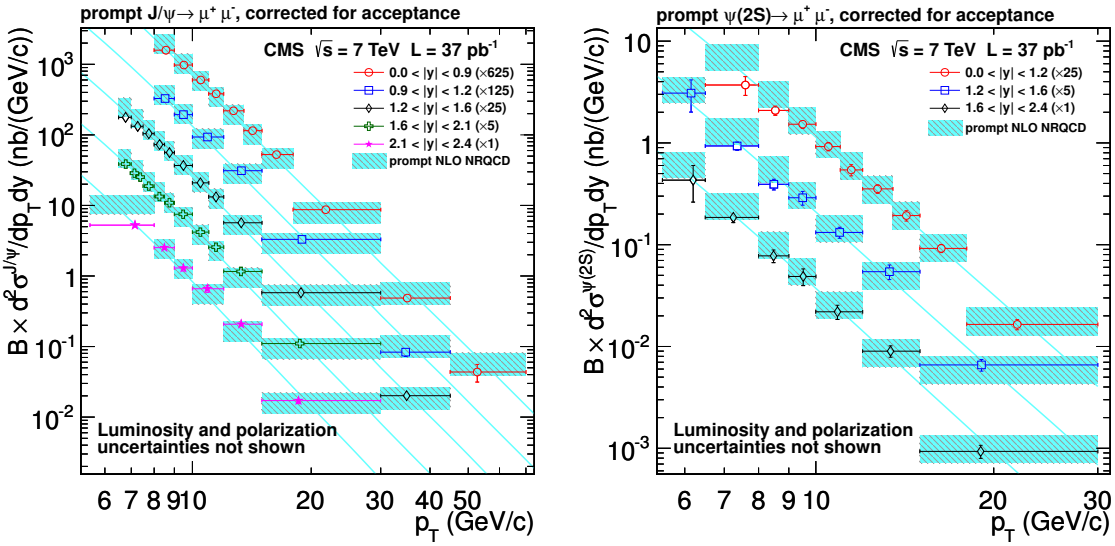

Figure 5.9. *Differential cross section for prompt J/ψ and ψ(2S) production (left and right, respectively) as a function of p_T for different rapidity bins The light blue bands indicate the theoretical prediction corresponding to NLO NRQCD [31].*

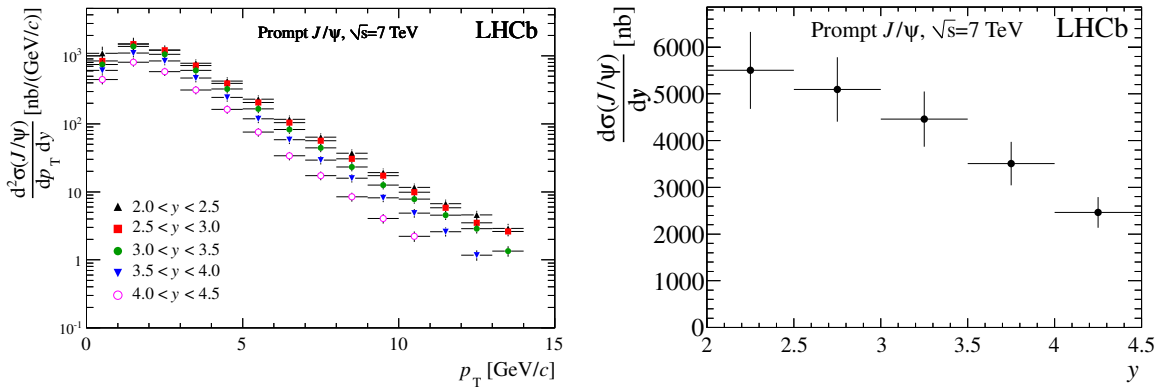

(a) *Differential production cross section for prompt J/ψ as a function of p_T in bins of rapidity.*

(b) *Differential production cross section for prompt J/ψ as a function of y integrated over the full p_T range.*

Figure 5.10. *Prompt J/ψ production as a function of p_T and y as measured by LHCb [32].*

5.2 ALICE results

The ALICE collaboration has measured the inclusive J/ψ production at $\sqrt{s} = 7$ TeV and at 2.76 TeV[12].

In the $\sqrt{s} = 7$ TeV analysis, published in 2011 [81], the inclusive J/ψ production is studied in a wide rapidity range, $|y| < 0.9$ and $2.5 < y < 4$, through the dilepton decay into e^+e^- and $\mu^+\mu^-$, respectively. It is worth remarking that ALICE can explored, at both mid- and forward-rapidity, the zero p_T region where the direct J/ψ production is supposed to be dominant. The analysis in the $\mu^+\mu^-$ channel was carried out on a data sample corresponding to an integrated luminosity $L_{INT} = 15.6$ nb^{-1}

[12]The *pp* run at $\sqrt{s} = 2.76$ TeV was to provide a reference for the Pb-Pb data taken at the same center-of-mass energy per nucleon, $\sqrt{s_{NN}} = 2.76$ TeV.

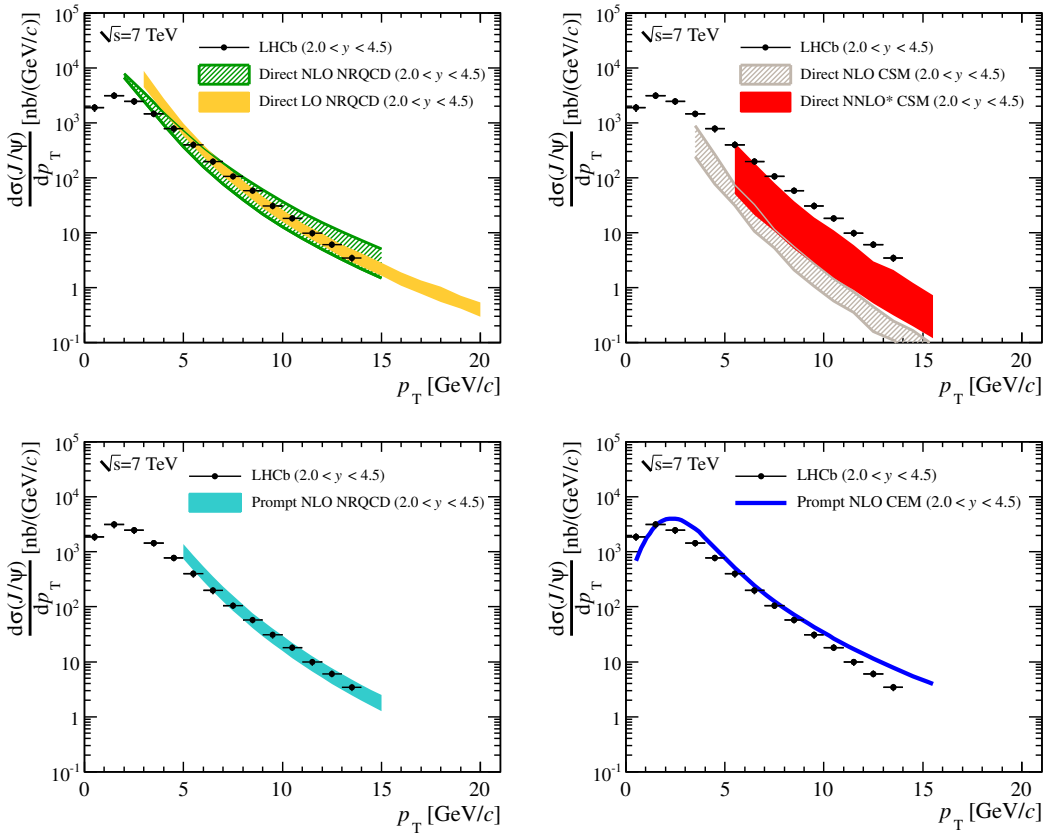

Figure 5.11. *Comparison of the LHCb results for the p_T differential cross section for prompt J/ψ production with several theoretical prediction: (top, left) direct J/ψ NRQCD; (top, right) direct J/ψ CSM; (bottom, left) prompt J/ψ NRQCD; (bottom, right) prompt J/ψ CEM. (from ref. [32])*

and a number of J/ψ signal events $N_{J/\psi}$ = 1924 ± 77 (stat.). The differential cross sections were measured as a function of p_T and y separately. The p_T dependence was studied in seven bins from 0 to 8 GeV/c while the rapidity dependence in five bins from 2.5 to 4. The analysis, presented in Chapter 4, is based on a larger pp data sample at $\sqrt{s}$ = 7 TeV corresponding to an integrated luminosity L_{INT} = 31.54 nb^{-1} and a number of J/ψ signal events $N_{J/\psi}$ = 3697 ± 118 (stat.). The same binning is kept for the p_T distribution while the rapidity dependence is studied in six y bins.

ALICE has presented preliminary results at $\sqrt{s}$ = 2.76 TeV at both mid- and forward-rapidity [98]. In Chapter 3, we give a detailed description of this analysis in the $\mu^+\mu^-$ channel. The differential cross sections are measured, as a function of p_T and y separately, in 7 p_T bins from 0 to 8 GeV/c and 6 rapidity bins from 2.5 to 4, respectively.

Finally, ALICE has also released preliminary results on the fraction of J/ψ coming from B mesons decays at mid-rapidity ($|y| < 0.9$) [29]. The p_T dependence of this fraction (for $p_T > 1.3$ GeV/c) is shown in Fig. 1.8 (a).

5.2.1 Transverse momentum p_T differential cross section

The differential cross sections for inclusive J/ψ production as a function of p_T, shown in Fig. 3.41 and 4.10 for $\sqrt{s}$ = 2.76 and 7 TeV respectively, are here compared to theoretical predictions.

In Fig. 5.12, the experimental points are compared to recent NLO NRQCD predictions [99, 100] calculated in the region $p_T > 3$ GeV/c. Before the LHC era, the normal approach within the factorization theorem of non-relativistic QCD (NRQCD) was to fit Tevatron results ($\sqrt{s}$ =1.8 and 1.96 TeV) to extract the non-perturbative matrix elements (the so-called Long Distance Matrix Elements, LDMEs) involved in the calculation (see Section 1.2.3.5). Once they are estimated, predictions of different observables (p_T dependence, polarization, ...) can be obtained. The high accuracy of the new set of data measured at LHC has recently allowed to perform new kinds of fit. For example, in [99, 100] new NLO NRQCD calculations, based on a new global fit, have been developed. At NLO, the NRQCD framework involve three free parameters, the color-octet LDMEs. Their values are extracted by a global fit to all available high energy data of inclusive J/ψ production from various hadroproduction, photoproduction, two-photon scattering and electron-positron annihilation experiments, including LHC results[13].

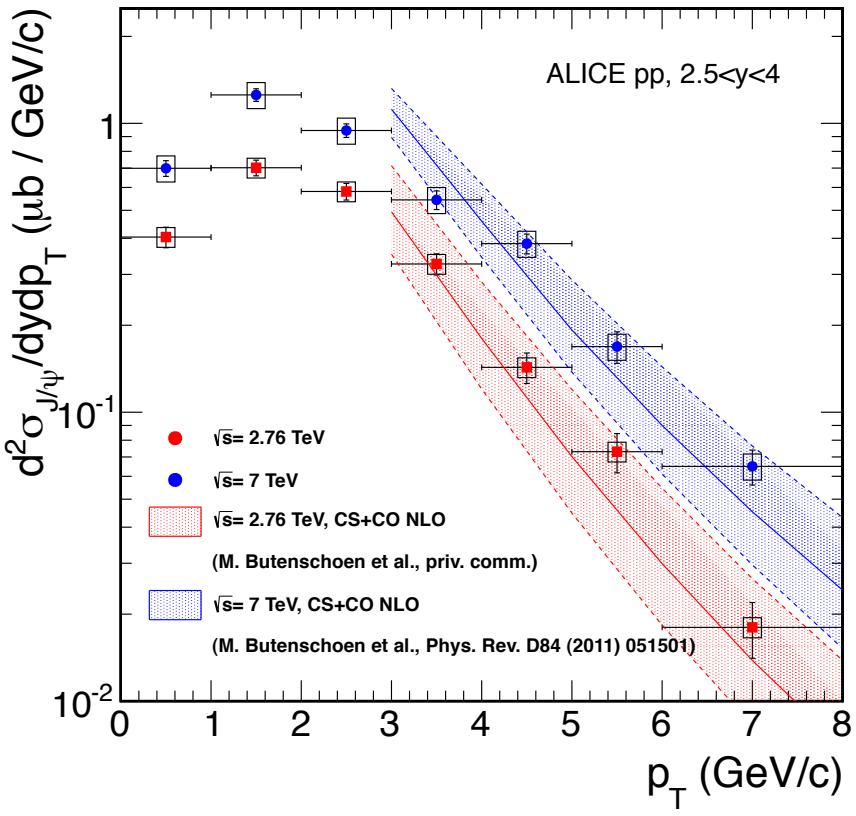

Figure 5.12. *Differential cross section for inclusive J/ψ production at forward rapidity 2.5 < y < 4 as a function of p_T as measured by ALICE at $\sqrt{s}$ = 2.76 (red points) and 7 TeV (blue points). The vertical error bars represent the statistical errors while the boxes correspond to the systematics uncertainties. The systematics on luminosity are not included. The results are compared to NLO NRQCD predictions [99, 100] calculated in the region $p_T > 3$ GeV/c.*

The predictions, shown in Fig. 5.12 for $\sqrt{s}$ = 2.76 and 7 TeV (red and blue band, respectively), are based on this new NLO NRQCD approach. They refer to direct J/ψ production (feed-down is

[13]The global fit, presented in [99, 100], is performed considering a total of 194 data points from 26 data sets.

not considered). Nevertheless the agreement between data and theory is pretty good in the region $p_T > 3$ GeV/c.

5.2.2 Rapidity y dependance

The differential cross sections for inclusive J/ψ production as a function of the rapidity y, shown in Fig. 3.42 and 4.11 for pp collisions at $\sqrt{s}$ = 2.76 and 7 TeV respectively, are here compared to theoretical predictions.

In Fig. 5.13, we show the differential cross section as a function of the rapidity, $d\sigma^{direct}_{J/\psi}/dy \times$ Br, for both gg fusion (dark blue band) and cg fusion (green band) contributions separately and then summed (light blue band) as predicted by LO CSM. The sum of the two contributions is indicated as LO$^+$ CSM prediction.

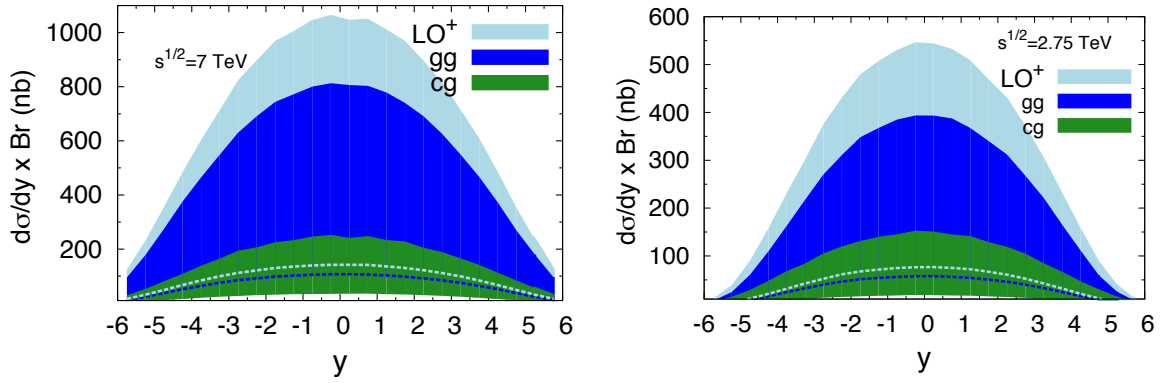

(a) *pp collisions at $\sqrt{s}$ = 7 TeV.* (b) *pp collisions at $\sqrt{s}$ = 2.76 TeV.*

Figure 5.13. *$d\sigma^{direct}_{J/\psi}/dy \times$ Br from gg fusion (dark blue band) and cg fusion (green band) and from all the LO contribution (light blue band) [101].*

The LO$^+$ CSM predictions for the two energies are compared, in Fig. 5.14 and 5.15, to the corresponding ALICE data, as obtained in Chapter 3 and 4. Two series of data points (black and blue points) are plotted and compared to the theoretical predictions They correspond, respectively, to the y differential cross sections for inclusive and direct J/ψ production where the latter one is obtained by applying to the inclusive data a proper correction, as explained in the following. The corrected points should be considered if one wants to properly compare experimental data with LO$^+$ CSM predictions which are obtained for direct J/ψ production.

In Fig. 5.14, which shows results for $\sqrt{s}$ =7 TeV, the black square points (solid and open), at forward rapidities, are the points shown in Fig. 4.11, while the black triangle point (solid) is the value calculated by ALICE at mid-rapidity and published in [81]. The blue points, describing the y differential cross sections for direct J/ψ production, can be obtained using the relation

$$\left(\frac{d\sigma_{J/\psi}}{dy}\right)^{direct} = F^{J/\psi}_{direct} \cdot \left(\frac{d\sigma_{J/\psi}}{dy}\right)^{prompt} = F^{J/\psi}_{direct} \cdot (1 - f_b) \cdot \left(\frac{d\sigma_{J/\psi}}{dy}\right)^{inclusive} \tag{5.1}$$

where $F^{J/\psi}_{direct}$ is the fraction of the prompt J/ψ sample which is directly produced and f_b is the fraction of J/ψ from the decay of b-hadrons. The $F^{J/\psi}_{direct}$ value used in the present calculation is the one measured by CDF (Tevatron) [33] at $\sqrt{s}$ = 1.8 TeV for $|\eta_{J/\psi}| < 0.6$ which was found to be almost constant from 5 to 8 GeV p_T, as shown in Fig. 1.9. We therefore use, as quoted in [34],

$$F_{direct}^{J/\psi} = (64 \pm 6)\% \tag{5.2}$$

which is used for both mid- and forward rapidity [14].

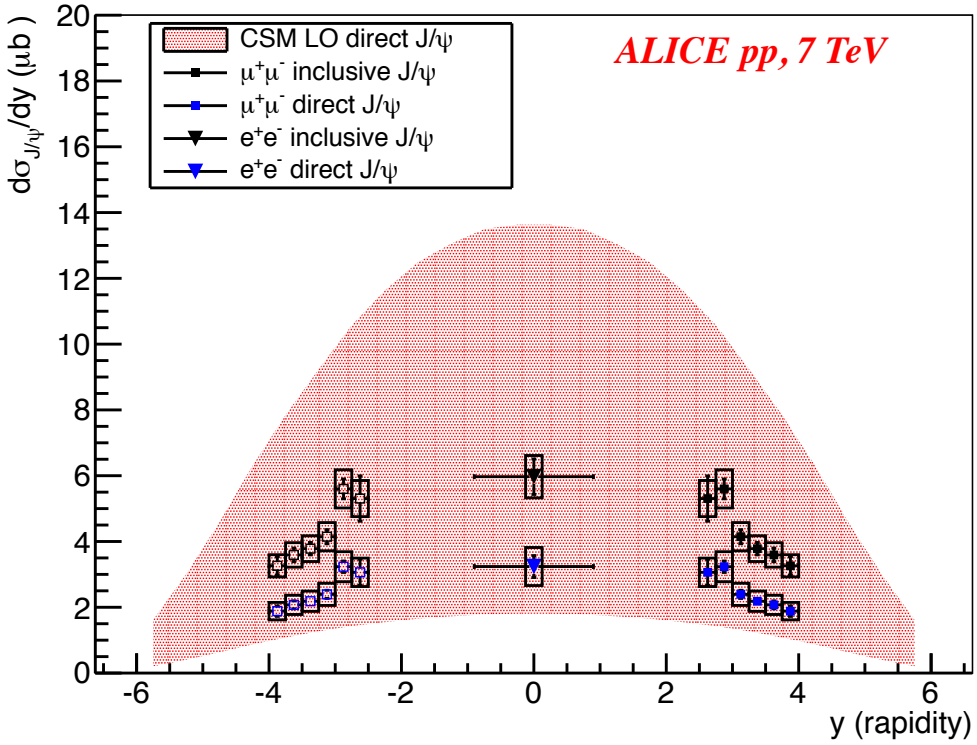

Figure 5.14. *Differential cross sections for inclusive (black points) and direct (blue points) J/ψ production as a function of the rapidity y at $\sqrt{s}$ =7 TeV. The direct points are obtained by applying corrections to the inclusive points as explained in the text. Data are compare to LO CSM prediction for direct J/ψ production (red band).*

For what concerns the correction $(1 - f_b)$, which permits to select only the prompt J/ψ component, a different approach has been followed for the two rapidity domains. At mid-rapidity ($|y| < 0.9$), ALICE has measured [29], for $\sqrt{s}$ = 7 TeV, the fraction f_b in range $p_T > 3$ GeV/c. This measured value was then extrapolated, using a semi-phenomenological function modeled on existing data, to $p_T > 0$ GeV/c obtaining[15]

$$f_b^{extr.}(p_T > 0) = 0.148 \pm 0.037\,(stat.)\,^{+0.018}_{-0.027}\,(syst.)\,^{+0.002}_{-0.005}\,(extr.). \tag{5.3}$$

Using the extrapolated fraction $f_b^{extr.}$, the $(d\sigma_{J/\psi}/dy)$ of prompt J/ψ can be measured and equals[16]

[14] This choice is made under the hypothesis of a negligible $\sqrt{s}$- and rapidity-dependence for $F_{direct}^{J/\psi}$.

[15] The $f_b^{extr.}$ systematic uncertainties related to polarization are not quoted.

[16] The $(d\sigma_{J/\psi}/dy)^{prompt}$ systematic uncertainties related to polarization are not quoted. The extrapolation-related uncertainties are negligible with respect to the other systematic uncertainties.

$$(\frac{d\sigma_{J/\psi}}{dy})^{prompt} = 5.06 \pm 0.52\,(stat.)\,^{+0.76}_{-0.77}\,(syst.)\,^{+0.03}_{-0.01}\,(extr.)\,\mu b. \tag{5.4}$$

Hence, the corrected point at mid-rapidity (blue triangle point in Fig. 5.14) is directly calculated by applying the $F^{J/\psi}_{direct}$ correction to the $(\frac{d\sigma_{J/\psi}}{dy})^{prompt}$ value quoted in Eq. 5.4. On the contrary, at forward rapidity ($2.5 < y < 4$), ALICE cannot measured the fraction f_b and we are forced to use the LHCb results. LHCb has studied [32], at $\sqrt{s}$ = 7 TeV, the prompt and non-prompt J/ψ production in the kinematic region $0 < p_{\rm T} < 14$ GeV/c and $2 < y < 4.5$ (rapidity range larger with respect to the ALICE one). The double-differential cross sections, $\frac{d^2\sigma_{J/\psi}}{dp_T dy}$, for prompt and non-prompt J/ψ are then measured in various ($p_{\rm T}$, y) bins. To obtain the integrated cross sections for prompt and non-prompt J/ψ production in the kinematic range explored by ALICE ($0 < p_{\rm T} < 8$ GeV/c and $2.5 < y < 4$.), we can simply sum the LHCb $\frac{d^2\sigma_{J/\psi}}{dp_T dy}$ results over all the bins within the ALICE kinematic range. The fraction f_b can be therefore calculated as

$$f_b = \frac{\sigma^{non-prompt}_{J/\psi}}{\sigma^{prompt}_{J/\psi} + \sigma^{non-prompt}_{J/\psi}} \tag{5.5}$$

obtaining f_b = 0.098 $\pm$ 0.001 (stat.) $\pm$ 0.018 (syst.). Finally, using this value of f_b, the corrected points at forward-rapidity (blue square points in Fig. 5.14), can be derived.

The analysis presented in Fig. 5.14 for $\sqrt{s}$ = 7 TeV has been repeated for the data taken at $\sqrt{s}$ = 2.76 TeV and the results are shown in Fig. 5.15. The black square points (solid and open), at forward rapidities, are the points shown in Fig. 3.42, while the black triangle point (solid) is the value obtained by ALICE at mid-rapidity and presented as a preliminary in [102]. The same technique, adopted for the $\sqrt{s}$ = 7 TeV case, has been applied to derive the direct points (blue point) by correcting the inclusive ones (black points).

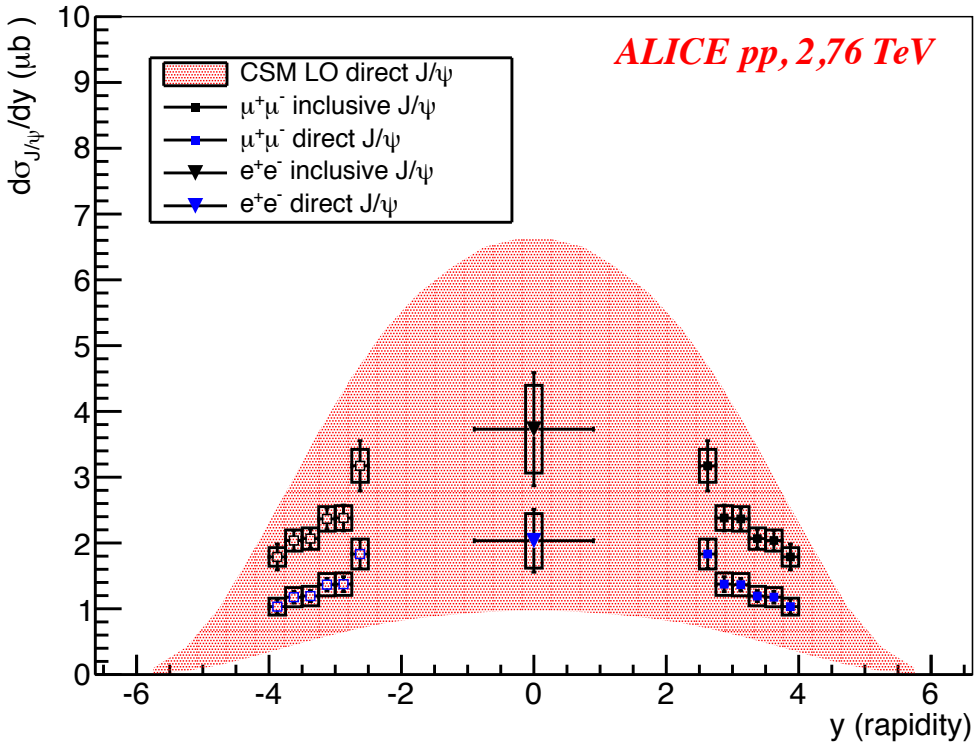

Figure 5.15. *Differential cross sections for inclusive (black points) and direct (blue points) J/ψ production as a function of the rapidity y at $\sqrt{s} = 2.76$ TeV. The direct points are obtained by applying corrections to the inclusive points as explained in the text. Data are compare to LO CSM prediction for direct J/ψ production (red band).*

Chapter 6

Conclusions

The work discussed in this PhD thesis has been carried out at CEA Saclay, Service de Physique Nucléaire (Irfu/SPhN) within the ALICE Collaboration at CERN LHC.

The PhD project focused on the study of inclusive J/ψ production in proton-proton collisions at the center-of-mass energies $\sqrt{s}$ = 2.76 and 7 TeV measured by the ALICE Muon Spectrometer. J/ψ mesons are detected through their dimuon decay channel into $\mu^+\mu^-$ pairs, down to zero transverse momentum $p_{\rm T}$ and at forward rapidity ($2.5 < y < 4$).

On one hand, this activity has required a strong involvement in the LHC proton-proton data taking period in 2010 and 2011 with the contribution to the data taking duties, such as the quality assurance of the acquired data and the evaluation of the performances of the detectors. On the other hand, the physics analysis of the J/ψ production has entailed a detailed learning of the common tools used in high energy physics to perform data processing via computing grid. The study has also required the development of the specific analysis techniques in the framework of the official ALICE software AliROOT.

Several results have been obtained by the end of the PhD project. First, the integrated J/ψ production cross section has been measured in pp collisions at $\sqrt{s}$ = 2.76 TeV and its numerical value is

$$\sigma_{J/\psi}(\sqrt{s} = 2.76 \text{ TeV}) = 3.38 \pm 0.14(stat.) \pm 0.27(syst.) + 0.54(\lambda_{CS} = +1) - 1.08(\lambda_{CS} = -1)\mu b.$$

In addition, the J/ψ production cross section has also been studied, separately, as a function of two kinematic variables: the J/ψ transverse momentum $p_{\rm T}$, in the range $0 < p_{\rm T} < 8$ GeV/c, and the rapidity y. Such pp measurements have a twofold interest.

On one hand, they offer the possibility to study the J/ψ production at an unexplored center-of-mass energy. Actually, $\sqrt{s}$ = 2.76 TeV is an intermediate energy value between the proton-antiproton collisions at $\sqrt{s}$ = 1.8 and 1.96 TeV delivered by Fermilab Tevatron and the LHC top energies reached with pp collisions at $\sqrt{s}$ = 7 and 8 TeV. On the other hand, the pp data provide a crucial baseline for the corresponding J/ψ measurement in Pb-Pb collisions performed by ALICE at the same $\sqrt{s}$ per nucleon pair. The Pb-Pb results released by ALICE have used the pp reference at $\sqrt{s}$ = 2.76 TeV.

The study of the J/ψ production has been also performed at $\sqrt{s}$ = 7 TeV. These results allow to increase, by a factor of ~ 2, the J/ψ statistics with respect to the data sample previously analyzed by ALICE in the first publication on J/ψ production in pp collisions at $\sqrt{s}$ = 7 TeV. The numerical value of the integrated cross section is

$$\sigma_{J/\psi}(\sqrt{s} = 7 \text{ TeV}) = 6.38 \pm 0.21(stat.) \pm 0.78(syst.) + 0.96(\lambda_{CS} = +1) - 1.98(\lambda_{CS} = -1)\mu b.$$

The differential, p_{T} and y, cross sections have been measured as well. The results obtained are compatible with the ALICE published ones.

The measured differential J/ψ cross sections, at both center-of-mass energies, have been compared to recent theoretical predictions. For what concerns the p_{T} dependence, the results at $\sqrt{s}$ = 2.76 and 7 TeV have been compared, in the range 3 < p_{T} < 8 GeV/c, with the predictions of a NRQCD calculation which includes both color singlet and color octet terms at NLO. The model satisfactorily reproduces both data sets of experimental data. The differential cross-section measured as a function of the rapidity y, instead, has been compared to LO CSM predictions. Due to the large theoretical uncertainties, no conclusive statements can be made.

Bibliography

[1] Lyndon Evans and Philip Bryant. LHC machine. *JINST*, 3:S08001, 2008.

[2] ALICE Collaboration. The ALICE experiment at CERN LHC. *JINST*, 3:S08002, 2008.

[3] ATLAS Collaboration. The ATLAS experiment at CERN LHC. *JINST*, 3:S08003, 2008.

[4] CMS Collaboration. The CMS experiment at CERN LHC. *JINST*, 3:S08004, 2008.

[5] LHCb Collaboration. The LHCb experiment at CERN LHC. *JINST*, 3:S08005, 2008.

[6] Helmut Satz. The Quark-Gluon Plasma: A Short Introduction. *Nucl.Phys.*, A862-863:4–12, 2011.

[7] M. E. Peskin and D. V. Schroeder. *An introduction to quantum field theory*. Westview Press, 1995.

[8] W. Greiner and A. Schafer. *Quantum Chromodynamics*. Springer, 1995.

[9] S. Weinberg. *The Quantum Theory of Fields*. Cambridge University Press, 1995.

[10] J. Beringer et al. (Particle Data Group). Review of Particle Physics. *Phys.Rev. D86*, 010001 2012.

[11] Peter Skands. Introduction to QCD. *arXiv:1207.2389*, 2012.

[12] Siegfried Bethke. Experimental tests of asymptotic freedom. *Prog.Part.Nucl.Phys.*, 58:351–386, arXiv:hep-ex/0606035, 2007.

[13] D. J. Gross and F.Wilczek. Ultraviolet behaviour of non-abelian gauge theories. *Phys. Rev. Lett. 30, 1343*, 1973.

[14] D. J. Gross and F.Wilczek. Asymptotically Free Gauge Theories. *Phys. Rev. D 8, 3633*, 1973.

[15] H. D. Politzer. Reliable perturbative results for strong interactions ? *Phys. Rev. Lett. 30, 1346*, 1973.

[16] Rajan Gupta. Introduction to lattice QCD. *arXiv:hep-lat/9807028*, 1997.

[17] J. Greensite. The Confinement problem in lattice gauge theory. *Prog. Part. Nucl. Phys. 51*, 51:1, arXiv:hep-lat/0301023v2, 2003.

[18] S. Necco, R. Sommer. The $N_f = 0$ heavy quark potential from short to intermediate distances. *Nucl. Phys. B622 328*, 2002.

[19] Martin Luscher. Lattice QCD: From quark confinement to asymptotic freedom. *Annales Henri Poincare*, 4:S197–S210, 2003.

[20] Martin Lüscher and Peter Weisz. Quark confinement and the bosonic string. *JHEP07 (2002) 049*.

[21] J. J. Aubert et al. Experimental Observation of a Heavy Particle J. *Phys. Rev. Lett.*, 33:1404–1406, Dec 1974.

[22] J. -E. Augustin et al. Discovery of a Narrow Resonance in e^+e^- Annihilation. *Phys. Rev. Lett.*, 33:1406–1408, Dec 1974.

[23] C. Bacci et al. Preliminary Result of Frascati (ADONE) on the Nature of a New 3.1-GeV Particle Produced in e^+e^- Annihilation. *Phys. Rev. Lett.*, 33:1408–1410, Dec 1974.

[24] S.L. Glashow, J. Iliopoulos, and L. Maiani. Weak Interactions with Lepton-Hadron Symmetry. *Phys.Rev.*, D2:1285–1292, 1970.

[25] G. S. Abrams et al. Discovery of a Second Narrow Resonance in e^+e^- Annihilation. *Phys. Rev. Lett.*, 33:1453–1455, Dec 1974.

[26] J. A. Appel et al. Observation of a Dimuon Resonance at 9.5 GeV in 400-GeV Proton-Nucleus Collisions. *Phys. Rev. Lett.*, 39:252–255, Aug 1977.

[27] J. A. Appel et al. Observation of Structure in the Υ Region. *Phys. Rev. Lett.*, 39:1240–1242, Nov 1977.

[28] M.B. Voloshin. Charmonium. *Prog.Part.Nucl.Phys.*, 61:455–511, 2008.

[29] B. Abelev, et al. (ALICE Collaboration). Measurement of prompt and non-prompt J/ψ production cross sections at mid-rapidity in pp collisions at $\sqrt{s} = 7$ TeV. *arXiv:1205.5880*, 2012.

[30] G. Aad et al. (ATLAS Collaboration). Measurement of the differential cross-sections of inclusive, prompt and non-prompt J/ψ production in proton-proton collisions at $\sqrt{s}$ = 7 TeV. *Nucl.Phys.*, B850:387–444, 2011.

[31] S. Chatrchyan et al. (CMS Collaboration). J/ψ and ψ' production in pp collisions at $\sqrt{s}$ = 7 TeV. *J. High Energy Physics (2) 011 (2012).*

[32] R. Aaij et al. (LHCb Collaboration). Measurement of J/ψ production in pp collisions at $\sqrt{s}$=7 TeV. *Eur.Phys.J.*, C71:1645, 2011.

[33] CDF collaboration. Production of J/ψ from χ_c decays at CDF. *http://www-cdf.fnal.gov/physics/new/bottom/cdf3124/cdf3124.html*.

[34] J.P. Lansberg. J/ψ, ψ ' and Υ production at hadron colliders: A Review. *Int.J.Mod.Phys.*, A21:3857–3916, 2006.

[35] N. Brambilla, S. Eidelman, B.K. Heltsley, R. Vogt, G.T. Bodwin, et al. Heavy quarkonium: progress, puzzles, and opportunities. *Eur.Phys.J.*, C71:1534, 2011.

[36] Geoffrey T. Bodwin. Factorization of the Drell-Yan Cross-Section in Perturbation Theory. *Phys.Rev.*, D31:2616, 1985.

[37] John C. Collins, Davison E. Soper, and George F. Sterman. Factorization of Hard Processes in QCD. *Adv.Ser.Direct.High Energy Phys.*, 5:1–91, 1988.

[38] Jian-wei Qiu and George F. Sterman. Power corrections to hadronic scattering. 2. Factorization. *Nucl.Phys.*, B353:137–164, 1991.

[39] L. V. Gribov, E. M. Levin, and M. G. Ryskin. Semihard processes in QCD. *Phys. Rept.*, 100:1–150, November 1983.

[40] Michelangelo L. Mangano. Two lectures on heavy quark production in hadronic collisions. *arXiv:hep-ph/9711337*, 1997.

[41] C. Lourenco and H.K. Wohri. Heavy flavour hadro-production from fixed-target to collider energies. *Phys.Rept.*, 433:127–180, 2006.

[42] Helmut Satz. The States of Matter in QCD. *arXiv:0903.2778*, 2009.

[43] Frithjof Karsch. Recent lattice results on finite temperature and density QCD. Part I. *PoS*, CPOD07:026, arXiv:0711.0656 2007.

[44] Frithjof Karsch. Recent lattice results on finite temperature and density QCD. Part II. *PoS*, LAT2007:015, arXiv:0711.0661 2007.

[45] Francois Gelis. Some aspects of ultra-relativistic heavy ion collisions. *Acta Phys.Polon.Supp.*, 1:395–402, 2008.

[46] C. Y. Wong. *Introduction to high-energy heavy ion collisions*. World Scientific, 1994.

[47] Helmut Satz. Charm and Beauty in a Hot Environment. *arXiv:hep-ph/0602245*, 2006.

[48] T. Matsui and H. Satz. J/ψ Suppression by Quark-Gluon Plasma Formation. *Phys.Lett.*, B178:416, 1986.

[49] E. Scomparin. J/ψ production in In-In and p-A collisions. *J.Phys.*, G34:S463–470, 2007.

[50] Raphael Granier de Cassagnac. Quarkonia Production in Hot and Cold Matters. *J.Phys.*, G35:104023, 2008.

[51] A. Adare et al. J/ψ Production vs Centrality, Transverse Momentum, and Rapidity in Au+Au Collisions at $\sqrt{s_{NN}}$ = 200 GeV. *Phys.Rev.Lett.*, 98:232301, 2007.

[52] B. Abelev, et al. (ALICE Collaboration). J/ψ Suppression at Forward Rapidity in Pb-Pb Collisions at $\sqrt{s_{NN}}$=2.76 TeV. *Phys. Rev. Lett.*, 109:072301, 2012.

[53] G. Aad et al. (ATLAS Collaboration). Measurement of the centrality dependence of J/ψ yields and observation of Z production in lead-lead collisions with the ATLAS detector at the LHC. *Phys.Lett.*, B697:294–312, 2011.

[54] S. Chatrchyan et al. (CMS Collaboration). Suppression of non-prompt J/ψ, prompt J/ψ, and Υ(1S) in PbPb collisions at $\sqrt{s_{NN}}$ = 2.76 TeV. *JHEP*, 1205:063, 2012.

[55] Christophe Suire (for the ALICE collaboration). Charmonia production in ALICE. *arXiv:1208.5601*, 2012.

[56] Catherine Silvestre (for the CMS collaboration). Quarkonia Measurements by the CMS Experiment in pp and PbPb Collisions. *J.Phys.*, G38:124033, 2011.

[57] Zebo Tang (for the STAR collaboration). J/ψ production and correlation in p+p and Au+Au collisions at STAR. *J.Phys.*, G38:124107, 2011.

[58] K. Adcox et al. (PHENIX Collaboration). Centrality Dependence of Charged Particle Multiplicity in Au-Au Collisions at $\sqrt{s_{NN}}$ = 130 GeV. *Phys. Rev. Lett.*, 86:3500–3505, Apr 2001.

[59] A. Bazilevsky. Charge particle multiplicity and transverse energy measurements in Au - Au collisions in PHENIX at RHIC. *Nucl.Phys.*, A715:486, 2003.

[60] J. Castillo. Alignment of the ALICE MUON spectrometer. *1st LHC Detector Alignment Workshop, CERN, Geneva, Switzerland, 4 - 6 Sep 2006, pp.127-138, http://cdsweb.cern.ch/record/1047110*, 2007.

[61] L. Aphecetche et al. Numerical Simulations and Offline Reconstruction of the Muon Spectrometer of ALICE. *ALICE Internal Note ALICE-INT-2009-044*, https://edms.cern.ch/document/1054937/1.

[62] G.Chabratova et al. Development of the Kalman filter for tracking in the forward muon spectrometer of ALICE. *ALICE Internal Note ALICE-INT-2003-002*, https://edms.cern.ch/document/371480/1.

[63] R. Arnaldi et al. Design and performance of the ALICE muon trigger system. *Nucl.Phys.Proc.Suppl.*, 158:21–24, 2006.

[64] R. Santonico and R. Cardarelli. Development of resistive plate counters. *Nuclear Instruments and Methods in Physics Research*, 187:377 – 380, 1981.

[65] M. Gagliardi. *The ALICE Muon Spectrometer: trigger detectors and quarkonia detection in pp collisions*. PhD thesis, University of Torino, 2008.

[66] R. Arnaldi et al. A dual threshold technique to improve the time resolution of resistive plate chambers in streamer mode. *Nucl. Instrum. Meth. A*, 457:117–125, 2001.

[67] P. Saiz, L. Aphecetche, P. Bunčić, R. Piskač, J. E. Revsbech, and V. Šego. AliEn—ALICE environment on the GRID. *Nuclear Instruments and Methods in Physics Research Section A: Accelerators, Spectrometers, Detectors and Associated Equipment*, 502(2–3):437–440, 4 2003.

[68] J. E. Gaiser. *Appendix F - Charmonium Spectroscopy from Radiative Decays of the J/ψ and ψ'*. PhD thesis, SLAC-R-255, 1982.

[69] Ruben Shahoyan. *J/ψ and ψ' production in 450 GeV pA interactions and its dependence on the rapidity and X_f*. PhD thesis, Universidade Tecnica de Lisboa, 2001.

[70] F. Bossu et al. Phenomenological interpolation of the inclusive J/ψ cross section to proton-proton collisions at 2.76 TeV and 5.5 TeV. *arXiv:1103.2394*, 2011.

[71] B. Abelev, et al. (ALICE Collaboration). J/ψ polarization in pp collisions at $\sqrt{s}$=7 TeV. *Phys.Rev.Lett.*, 108:082001, 2012.

[72] Pietro Faccioli, Carlos Lourenco, Joao Seixas, and Hermine K. Wohri. Towards the experimental clarification of quarkonium polarization. *Eur.Phys.J.*, C69:657–673, 2010.

[73] L. Aphecetche, R. Arnaldi, L. Bianchi, B. Boyer, M. Gagliardi, P. R. Petrov, E. Scomparin, C. Suire, and J. D. Tapia Takaki. Luminosity determination for the J/$\psi \to \mu^+\mu^-$ analysis in p+p interactions at $\sqrt{s}$=7 TeV. *ALICE SCIENTIFIC NOTE-2011-001*, 2011.

[74] S van der Meer. Calibration of the effective beam height in the ISR. oai:cds.cern.ch:296752. Technical Report CERN-ISR-PO-68-31. ISR-PO-68-31, CERN, Geneva, 1968.

[75] Ken Oyama. Analysis of the may 2010 van der Meer scan in ALICE. In *CERN- Proceedings-2011-001*, page 39, 2011.

[76] Martino Gagliardi (for the ALICE collaboration). Measurement of reference cross sections in pp and Pb-Pb collisions at the LHC in van der Meer scans with the ALICE detector. *arXiv:1109.5369*, 2011.

[77] D. Acosta et al. Measurement of the J/ψ meson and $b-$hadron production cross sections in $p\bar{p}$ collisions at $\sqrt{s} = 1960$ GeV. *Phys.Rev.*, D71:032001, 2005.

[78] S. Grigoryan, A. DeFalco. Capabilities of the ALICE Muon Spectrometer to measure quarkonia production in Pb-Pb collisions at 5.5 TeV, ALICE Internal Note ALICE-INT-2008-07-16. *https://edms.cern.ch/document/938944/1*.

[79] A. Alici et al. LHC Bunch Current Normalisation for the October 2010 Luminosity Calibration Measurements. *CERN-ATS-Note-2011-016 PERF*, 2011.

[80] C. W. Fabjan et al. *ALICE trigger data-acquisition high-level trigger and control system: Technical Design Report*. Technical Design Report ALICE. ALICE-TDR-10, CERN-LHCC-2003-062, http://cdsweb.cern.ch/record/684651.

[81] K. Aamodt et al. (ALICE Collaboration). Rapidity and transverse momentum dependence of inclusive J/ψ production in pp collisions at $\sqrt{s} = 7$ TeV. *Physics Letters B*, 704:442 – 455, 05 2011.

[82] Eric Braaten and Tzu Chiang Yuan. Gluon fragmentation into heavy quarkonium. *Phys.Rev.Lett.*, 71:1673–1676, 1993.

[83] Michael Kramer. Quarkonium production at high-energy colliders. *Prog.Part.Nucl.Phys.*, 47:141–201, 2001.

[84] N. Brambilla et al. Heavy quarkonium physics. *CERN Yellow Report, CERN-2005-005, arXiv:hep-ph/0412158*, 2004.

[85] Eric Braaten, Bernd A. Kniehl, and Jungil Lee. Polarization of prompt J/ψ at the Tevatron. *Phys.Rev.*, D62:094005, 2000.

[86] J. Campbell, F. Maltoni, and F. Tramontano. QCD Corrections to J/ψ and Υ Production at Hadron Colliders. *Phys. Rev. Lett.*, 98:252002, Jun 2007.

[87] P. Artoisenet, J.P. Lansberg, and F. Maltoni. Hadroproduction of J/ψ and Υ in association with a heavy-quark pair. *Physics Letters B*, 653(1):60 – 66, 2007.

[88] J. P. Lansberg. On the mechanisms of heavy-quarkonium hadroproduction. *The European Physical Journal C - Particles and Fields*, 61(4):693–703, 2009.

[89] B. Abelev et al. (STAR collaboration). J/ψ production at high transverse momenta in $p+p$ and Cu + Cu collisions at $\sqrt{s_{NN}} = 200$ GeV. *Phys. Rev. C*, 80:041902, Oct 2009.

[90] A. Adare et al. (PHENIX collaboration). J/ψ Production versus Transverse Momentum and Rapidity in $p+p$ Collisions at $\sqrt{s} = 200$ GeV. *Phys. Rev. Lett.*, 98:232002, Jun 2007.

[91] J.P. Lansberg. QCD corrections to J/psi polarisation in pp collisions at RHIC. *Phys.Lett.*, B695:149–156, 2011.

[92] Hee Sok Chung, Chaehyun Yu, Seyong Kim, and Jungil Lee. Polarization of prompt J/psi in proton-proton collisions at RHIC. *Phys.Rev.*, D81:014020, 2010.

[93] Cesar Luiz da Silva. Quarkonia measurement in p+p and d+Au collisions at $\sqrt{s}$ = 200 GeV by PHENIX Detector. *Nucl.Phys.*, A830:227C–230C, 2009.

[94] L.A. Linden Levy. From production to suppression, a critical review of charmonium measurements at RHIC. *Nuclear Physics A*, 830:353c – 360c, 2009.

[95] Stanley J. Brodsky and Jean-Philippe Lansberg. Heavy-quarkonium production in high energy proton-proton collisions at rhic. *Phys. Rev. D*, 81:051502, Mar 2010.

[96] Anthony D. Frawley, T. Ullrich, and R. Vogt. Heavy flavor in heavy-ion collisions at RHIC and RHIC II. *Phys.Rept.*, 462:125–175, 2008.

[97] V. Khachatryan et al. (CMS Collaboration). Prompt and non-prompt J/ψ production in pp collisions at $\sqrt{s}$ = 7 TeV. *Eur.Phys.J.*, C71:1575, 2011.

[98] Claudio Geuna (for the ALICE collaboration). Open heavy flavour and J/psi production in proton-proton collisions measured with the ALICE experiment at LHC. *arXiv:1209.0382*, 2012.

[99] Mathias Butenschoen and Bernd A. Kniehl. J/ψ production in NRQCD: A global analysis of yield and polarization. *Nucl.Phys.Proc.Suppl.*, 222-224:151–161, 2012.

[100] Mathias Butenschoen and Bernd A. Kniehl. World data of J/ψ production consolidate NRQCD factorization at NLO. *Phys.Rev.*, D84:051501, 2011.

[101] J.P. Lansberg. Total J/ψ production cross section at the LHC. 2010.

[102] B. Abelev, et al. (ALICE Collaboration). Inclusive J/ψ production in pp collisions at $\sqrt{s} =$ 2.76 TeV. *arXiv:1203.3641*, 2012.

[103] D. Stocco. Efficiency determination of the MUON Spectrometer trigger chambers from real data, ALICE Internal Note ALICE-INT-2008-004. *https://edms.cern.ch/document/888907/1*.

List of Figures

List of Tables

Appendix A

Data Sample

The run lists, used for the analysis presented in Chapter 3 and 4, are shown in Table A.1 and A.2, respectively. The corresponding numbers of MB and μ-MB trigger events are quoted as well.

	Minimum Bias (MB) trigger	Muon (μ-MB) trigger
RUN number		
146688	627 198	141 407
146689	1 396 431	351 563
146746	508 039	132 218
146747	1 749 890	422 652
146748	678 780	175 925
146801	923 735	238 267
146802	1 869 452	455 520
146803	160 102	40 892
146804	4 075 647	1 074 286
146805	8 644 514	2 198 695
146806	1 529 221	373 559
146807	167 024	40 162
146817	798 243	192 835
146824	4 540 841	1 097 036
146856	1 437 527	366 776
146858	3 614 249	967 200
146859	2 341 516	578 339
146860	845 973	217 205

Table A.1. *Run list of the pp data sample at $\sqrt{s}$ = 2.76 TeV.*

	Minimum Bias (MB) trigger	Muon (μ-MB) trigger
RUN number		
134497	-	15 056 812
134666	166 317	2 630 039
134679	742 930	8 995 873
134685	175 578	2 322 846
134690	66 154	734 698

Table A.2. *Run list of the pp data sample at $\sqrt{s}$ = 7 TeV.*

The numbers quoted in the two Tables indicate the total number of trigger events collected by the ALICE data acquisition system (DAQ) in each run as obtained from the ALICE Electronic Logbook[1].

[1] https://alice-logbook.cern.ch

Appendix B

J/ψ line shape: fit functions

B.1 Crystal Ball function: standard form

The Crystal Ball (CB) function, defined by Eq. B.1, has been introduced for the study of charmonia [68]. It is a probability density function and it consists of a Gaussian core portion and a power-law low-end tail below a certain threshold. Practically, the Gaussian shape is connected to a power-law tail at $x = \bar{x} - \alpha \cdot \sigma$ where $\bar{x}$ and σ are, respectively, the mean and the width of the gaussian function.

$$f(x;\, \bar{x},\, \sigma,\, \alpha,\, n) \;=\; N \cdot \begin{cases} exp(-\frac{(x-\bar{x})^2}{2\sigma^2}), & for\ \frac{x-\bar{x}}{\sigma} > -\alpha \\ A \cdot (B - \frac{x-\bar{x}}{\sigma})^{-n}, & for\ \frac{x-\bar{x}}{\sigma} \leq -\alpha \end{cases} \tag{B.1}$$

$$A = (\frac{n}{|\alpha|})^n \cdot exp\,(-\frac{|\alpha|^2}{2}) \tag{B.2}$$

$$B = \frac{n}{|\alpha|} - |\alpha|\,. \tag{B.3}$$

The sign of α determines if the connection between the gaussian and the power-law function happens on the left or right side (as shown in Fig. B.1, for $\alpha > 0$ the power-law tail is on the left side). The n parameter, which should be positive to correctly define a probability density function, controls the slope of the power-law function. Fig. B.1 shows the shape of the CB function for various sets of parameters of the power-law tail.

The CB function, with its power-law low-end tail, allows to reproduce the non-gaussian fluctuations due to energy loss processes. In the case under consideration, the CB function models the energy loss of the muon tracks inside the front absorber.

B.2 Double Crystal Ball function: extended form

The J/ψ signal shape in Monte Carlo simulations can not be fully reproduced with the CB function described above. As shown in Fig. 3.13 and 4.5, the invariant mass distribution presents deviations from a simple gaussian behavior not only on the left side but also on the right one with a non-gaussian high-end tail. This deviation, attributed to multiple scattering effects experienced by the muon tracks in the forward muon spectrometer, can lead to underestimate the number of J/ψ extracted from a CB fit. Therefore, the standard CB function, shown in Eq. B.1, has been modified to include a second

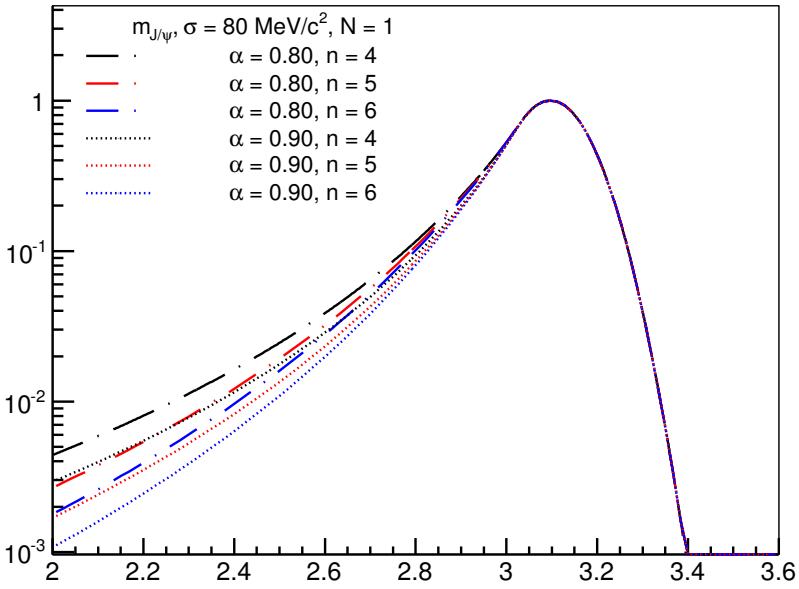

Figure B.1. *Crystal Ball shape for various sets of parameters of the power-law tail.*

power-law tail in the high-end region. The new function, defined in Eq. B.4, is called double Crystal Ball function.

$$f(x;\,\bar{x},\,\sigma,\,\alpha,\,n,\,\alpha',\,n') \;=\; N\cdot\begin{cases} exp(-\frac{(x-\bar{x})^2}{2\sigma^2}), & for\ \frac{x-\bar{x}}{\sigma} > -\alpha \\ A\cdot(B-\frac{x-\bar{x}}{\sigma})^{-n}, & for\ \frac{x-\bar{x}}{\sigma} \leq -\alpha \\ C\cdot(D+\frac{x-\bar{x}}{\sigma})^{-n'}, & for\ \frac{x-\bar{x}}{\sigma} \geq \alpha' \end{cases} \tag{B.4}$$

with

$$A = (\frac{n}{|\alpha|})^n \cdot exp(-\frac{|\alpha|^2}{2}) \tag{B.5}$$

$$B = \frac{n}{|\alpha|} - |\alpha| \tag{B.6}$$

$$C = (\frac{n'}{|\alpha'|})^{n'} \cdot exp(-\frac{|\alpha'|^2}{2}) \tag{B.7}$$

$$D = \frac{n'}{|\alpha'|} - |\alpha'| \tag{B.8}$$

In Fig. B.2, the shape of the double Crystal Ball function for various sets of parameters of the power-law high-end tail is shown.

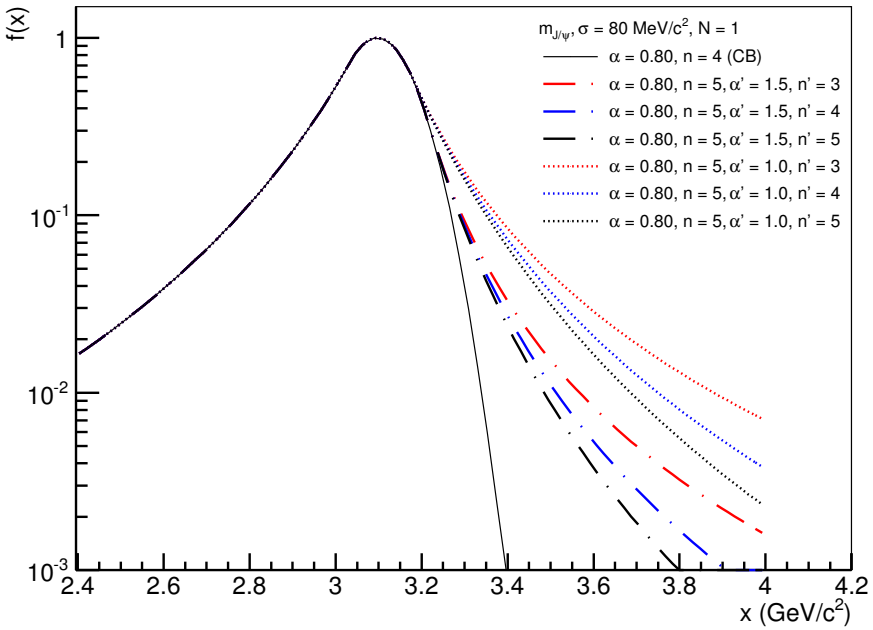

Figure B.2. *Double Crystal Ball shape for various sets of parameters of the power-law high-end tail.*

B.3 NA50 / NA60 function

The NA50 / NA60 function has been introduced and used by the NA50 and NA60 collaboration (CERN) to fit the charmonium signal shapes [69]. It is a gaussian function with a variable (mass dependent) width $\sigma_{J/\psi}(x)$. As explained in [69], the shape of the J/ψ resonance is described by the functional form shown in Eq. B.9

$$f(x) = N \cdot exp[-\frac{1}{2} \cdot (\frac{x-\bar{x}}{\sigma_{J/\psi}(x)})^2] \tag{B.9}$$

where $\sigma_{J/\psi}(x)$ is the variable width which depends on several parameters as defined in Eq. B.10,

$$\sigma_{J/\psi}(x) = \begin{cases} \sigma_1 + b_1(c_1M_0 - x)^{d_1 - g_1\sqrt{c_1M_0 - x}}, & for\ x \leq c_1M_0 \\ \sigma_1, & for\ c_1M_0 < x \leq M_0 \\ \sigma_2, & for\ M_0 \leq x < c_2M_0 \\ \sigma_2 + b_2(c_2M_0 - x)^{d_2 - g_2\sqrt{c_2M_0 - x}}, & for\ x \geq c_2M_0 \end{cases} \tag{B.10}$$

B.4 List of α and n parameters

The reference fitting technique, adopted in the analysis presented in Chapter 3 and 4, describes the J/ψ line shape in term of a CB function with tail fixed to Monte Carlo simulation. The α and n values, used to fix the CB's tails (in each p_T and y bins), are listed in Table B.1.

	α ($\sqrt{s}$ = 2.76 TeV)	n ($\sqrt{s}$ = 2.76 TeV)	α ($\sqrt{s}$ = 7 TeV)	n ($\sqrt{s}$ = 7 TeV)
p_{T}- and y-integrated	0.839161	5.27918	0.818278	5.34032
p_{T}				
[0;1]	0.786302	5.98542	0.794645	6.73516
[1 ; 2]	0.848842	5.45795	0.752234	8.59476
[2 ; 3]	0.805078	5.88443	0.802696	6.83112
[3 ; 4]	0.873239	4.35551	0.79959	5.80543
[4 ; 5]	0.873092	5.29108	0.787013	6.59772
[5 ; 6]	0.814774	7.46599	0.828332	7.04182
[6 ; 8]	0.951794	4.00851	0.992149	4.36053
y				
[2.5 ; 2.75]	0.7753	3.3408	0.650542	6.01612
[2.75 ; 3]	0.798106	5.43817	0.748819	6.63365
[3 ; 3.25]	0.870121	5.17553	0.84185	5.68085
[3.25 ; 3.5]	0.877522	6.12761	0.823661	7.78897
[3.5 ; 3.75]	0.884913	6.99409	0.83396	7.75916
[3.75 ; 4]	0.81126	8.13504	0.857659	4.68817

Table B.1. *Summary of the α and n values used to fix the CB's tails.*

Appendix C

Monte Carlo inputs for the p_{T} and y distributions: functional form

As explained in Section 3.3 and 4.3, the measurement of the integrated and the differential (p_{T} and y) J/ψ production cross sections requires the evaluation of the acceptance and efficiency corrections, $A \times \varepsilon$. They take into account the acceptance of the apparatus and the realistic conditions of the detectors during the data taking, in term of reconstruction and triggering efficiencies. The numerical values of the $A \times \varepsilon$ corrections are obtained via Monte Carlo simulation of large samples of events containing J/ψ signals. These J/ψ samples are generated according to realistic p_{T} and y distributions, tuned for pp collisions at $\sqrt{s}$ = 2.76 or 7 TeV.

In Section C.1, the functional forms of the Monte Carlo p_{T} and y inputs, used as nominal shapes in the $\sqrt{s}$ = 2.76 TeV analysis, are presented. These shapes give the $A \times \varepsilon$ corrections shown in Fig. 3.20, 3.22 and 3.23. Section C.2 presents, instead, several alternative p_{T} and y shapes used, as explained in Section 3.5.2, to estimate the systematic uncertainties relative to the choice of the Monte Carlo inputs.

C.1 Nominal shapes ($\sqrt{s}$ = 2.76 TeV analysis)

In the $\sqrt{s}$ = 2.76 TeV analysis, the nominal p_{T} dependence is described by Eq. C.1

$$f(p_{\mathrm{T}}) = \frac{p_{\mathrm{T}}}{\left[1 + a \cdot (\frac{p_{\mathrm{T}}}{p_0})^2\right]^n} \tag{C.1}$$

with $a = 0.36$, $p_0 = 2.31$ GeV/c and $n = 3.9$. The nominal y dependence is described by the gaussian function shown in Eq. C.2

$$g(y) = e^{-\frac{(y/y_0)^2}{2 \cdot \sigma^2}} \tag{C.2}$$

with $y_0 = 6.79$ and $\sigma = 0.383$.

The values of the parameters, tuned for pp collisions at $\sqrt{s}$ = 2.76 TeV, are obtained performing an universal fit of J/ψ results measured at different center-of-mass energies as explained in [70].

C.2 Other shapes

In Table C.1, there is the list of the functional forms of the alternative p_T and y shapes used to estimate the systematic uncertainties relative to the choice of the Monte Carlo inputs (see Section 3.5.2).

$\sqrt{s}$ (TeV)	p_T **input**	parameters	y **input**	parameters
1.96	fit of CDF data $f(p_T) = \frac{p_T}{\left[1+(\frac{p_T}{p_0})^2\right]^n}$	$p_0 = 4.233$ GeV/c $n = 4.071$	gaussian $g(y) = e^{-\frac{(y/y_0)^2}{2\cdot\sigma^2}}$	$y_0 = 6.42$ $\sigma = 0.383$
2.76	scaled from CDF data $f(p_T) = \frac{p_T}{\left[1+(\frac{p_T}{p_0})^2\right]^n}$	$p_0 = 4.435$ GeV/c $n = 4.071$	gaussian $g(y) = e^{-\frac{(y/y_0)^2}{2\cdot\sigma^2}}$	$y_0 = 6.79$ $\sigma = 0.383$
2.76	universal fit $f(p_T) = \frac{p_T}{\left[1+a\cdot(\frac{p_T}{p_0})^2\right]^n}$	$p_0 = 2.31$ GeV/c $n = 3.9$; $a = 0.36$	polynomial ($n = 4$) $g(y) = A\cdot(\frac{y}{y_0})^n + B$	$A = -6.628$ $B = 0.96$ $y_0 = 6.79$ $n = 4$
3.94	scaled from CDF data $f(p_T) = \frac{p_T}{\left[1+(\frac{p_T}{p_0})^2\right]^n}$	$p_0 = 4.647$ $n = 4.071$	CEM parametrization $g(y) = A\cdot y^n + B$	$A = -2.7454$ $B = 107.389$ $n = 2$

Table C.1. *Summary of the p_T and y Monte Carlo inputs introduced in Section 3.5.2.*

In Fig. C.1 and C.2, the different p_T and y Monte Carlo inputs, used in the $\sqrt{s}$ = 2.76 TeV analysis, are plotted.

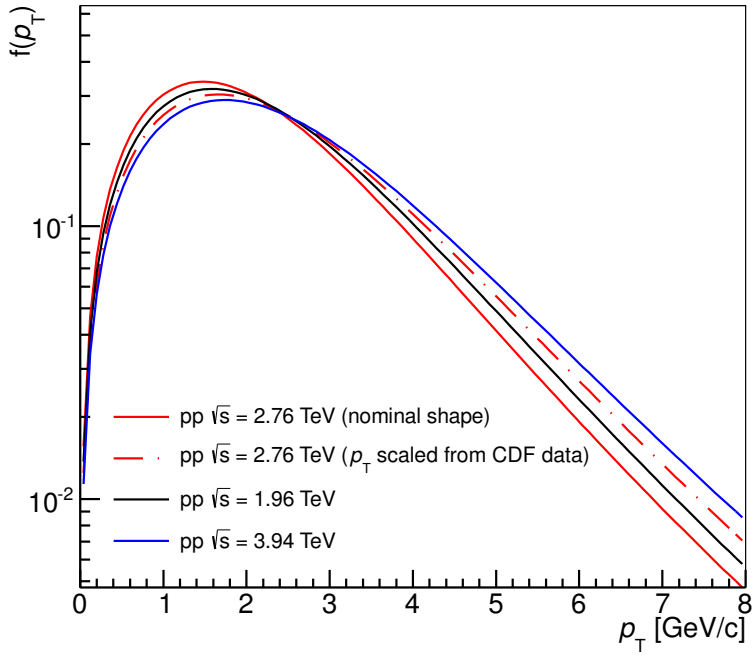

Figure C.1. *Monte Carlo p_T input shapes.*

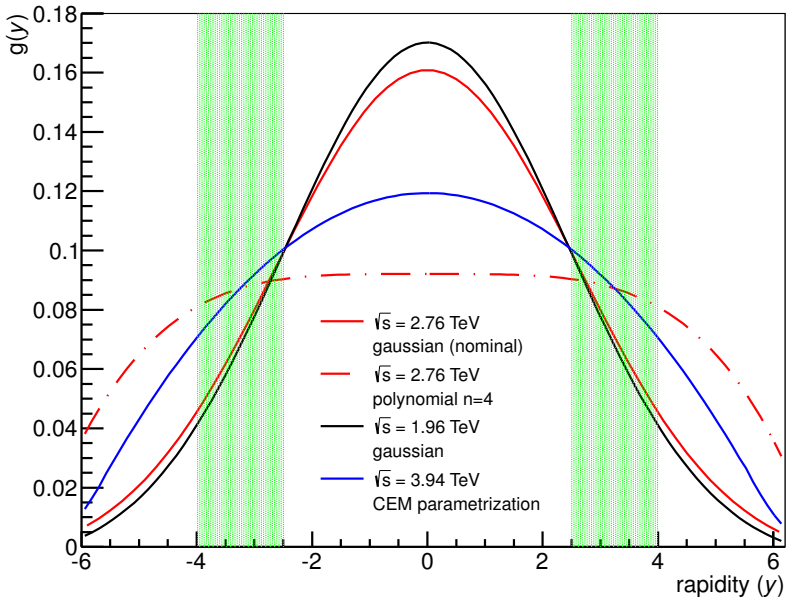

Figure C.2. *Monte Carlo y input shapes. The green bands indicate the rapidity intervals under analysis.*

Appendix D

Muon Tracking and Trigger system: efficiency evaluation

The procedures used to estimate the efficiency of the Muon Tracking and Trigger chambers during the data taking are presented in Section D.1 and D.2, respectively.

D.1 Muon Tracking system

The algorithm developed to measure the efficiencies of the muon tracking chambers is based on the specific design of the Muon Tracking system. As explained in Section 2.3.3, the system is arranged in five stations each made of two planes of Cathode Pad Chambers (CPC). The presence of two planes per station is actually the key feature used to estimate the chamber efficiencies.

As shown in Fig. D.1, a particle crossing Station n can give four possible detector responses in term of clusters associated to the particle track. We can have:

1. a cluster reconstructed in both chamber i and j (1-1);
2. a cluster reconstructed only in chamber i (1-0);
3. a cluster reconstructed only in chamber j (0-1);
4. no clusters reconstructed in chamber i or j (0-0);

The total number of tracks crossing Station n can therefore be expressed as $N_{total} = N_{1-1} + N_{1-0} + N_{0-1} + N_{0-0}$. The latter term, which represents the number of tracks without any attached cluster, is unknown and does not enter the efficiency algorithm[1].

The efficiencies of chamber i and j can be defined as

$$\varepsilon_i = \frac{N_{1-1} + N_{1-0}}{N_{total}}; \qquad \varepsilon_j = \frac{N_{1-1} + N_{0-1}}{N_{total}} \tag{D.1}$$

Bearing in mind that $N_{1-1} = \varepsilon_i \cdot \varepsilon_j \cdot N_{total}$, the efficiencies can be re-expressed as

$$\varepsilon_i = \frac{N_{1-1}}{N_{1-1} + N_{0-1}}; \qquad \varepsilon_j = \frac{N_{1-1}}{N_{1-1} + N_{1-0}}. \tag{D.2}$$

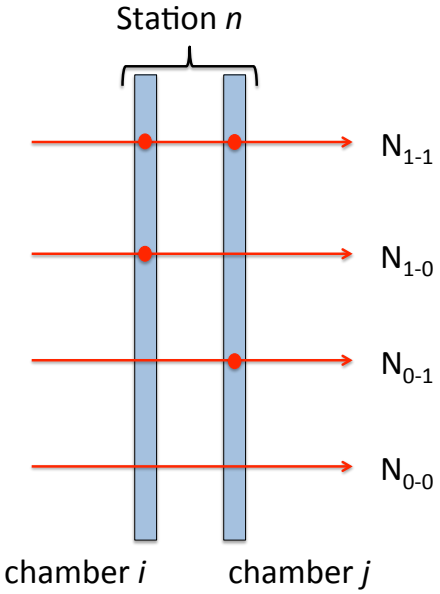

Figure D.1. *Particle crossing a station of the muon tracking system. The four possible responses of the detector are displayed.*

In the Muon Spectrometer, track reconstruction is based on an algorithm[2] which requires the presence of at least one cluster in station 1,2 and 3 and at least 3 clusters among station 4 and 5. Following this requirement, the total tracking efficiency ε_{TOT} can be calculated as

$$\varepsilon_{TOT} = \varepsilon_1 \cdot \varepsilon_2 \cdot \varepsilon_3 \cdot \varepsilon_{45}. \tag{D.3}$$

where the four factors represent the station tracking efficiencies. In particular, for the first three stations, the efficiencies ε_k (with k = 1, 2, 3) can be obtained as

$$\varepsilon_k = 1 - (1 - \varepsilon_m) \cdot (1 - \varepsilon_n) \tag{D.4}$$

where ε_m and ε_n are the efficiencies of the two chambers, m and n, which form station k (m = 1, 3, 5 and n = 2, 4, 6)[3]. For the last two stations (4 and 5), bearing in mind the reconstruction algorithm, the global efficiency can be expressed, in analogy with Eq. D.4, as

$$\varepsilon_{45} = \prod_{i=7}^{i=10} \varepsilon_i + \sum_{j=7}^{j=10} \left[(1 - \varepsilon_j) \cdot \prod_{i=7, i\neq j}^{i=10} \varepsilon_i \right] \tag{D.5}$$

The above mentioned procedure of measuring the total tracking efficiency ε_{TOT} is blind to the correlated inefficiencies of the detection elements, i.e. dead areas located in front of each other within the same station. Their presence leads to an overestimation of the total tracking efficiency. A dedicated method, able to spot such correlated inefficiencies, has therefore been developed and used to estimate the efficiency overestimation.

[1]The tracking reconstruction algorithm does not allow to have access to such tracks (N_{0-0}).

[2]A Kalman filter algorithm is used to perform the track reconstruction in the ALICE muon spectrometer [61, 62].

[3]The ten tracking chambers are conventionally numbered from 1 to 10 starting from the one placed next to the front absorber.

D.2 Muon Trigger system

As explained in Section 2.3.4, the signal produced in the RPCs by a crossing charged particle is picked-up by strips positioned on both sides of the chamber. The strips of the so-called bending plane lie horizontally and provide informations on the position of the crossing particle in the direction along which charged tracks are bent by the dipole magnetic field. Instead, the strips of the non-bending plane lie vertically and provide informations on the particle position along the direction orthogonal to the previous one.

The trigger algorithm searches, separately for the bending and the non-bending plane, for fired strips which lie within a region whose width is defined by the applied p_{T} cut. The trigger condition is satisfied if strips in at least three out of four chambers are found in the bending and in the non-bending plane. Under this condition, the tracks can be reconstructed or, in other words, are triggerable. The method developed to measure the efficiency of the muon trigger chambers [103] is based on this specific trigger algorithm.

Given a sample of N_{tot} particles crossing the four chambers of the muon trigger system, the number of triggerable tracks which fire all the four chambers is

$$N_{4/4} = N_{tot} \prod_{11 \leq i \leq 14} \varepsilon_i \tag{D.6}$$

where ε_i are the efficiencies of the trigger chambers which are conventionally numbered from 11 to 14 (starting from the one placed next to the iron filter) in order to distinguish them from the ten tracking chambers. Instead, the number of tracks that would be triggered independently from the response of a chosen chamber *ch* (while the remaining three chambers are necessarily fired) is

$$N^{ch}_{3/3} = N_{tot} \prod_{11 \leq i \leq 14}^{i \neq ch} \varepsilon_i. \tag{D.7}$$

Hence, the efficiency of the chamber *ch* can be calculated as

$$\varepsilon_{ch} = \frac{N_{4/4}}{N^{ch}_{3/3}}. \tag{D.8}$$

It is worth noting that the efficiency can be calculated separately for the bending and non-bending plane, since the 3/4 trigger condition has to be satisfied by both planes independently. The algorithm develop to measure the trigger chamber efficiencies analyzes the reconstructed tracks searching for the presence of the associated fired strips in all chambers. In this way it is possible to determine $N_{4/4}$ and $N^{ch}_{3/3}$ (as schematically shown in Fig. D.2) and then the chamber efficiency ε_{ch}. This method can be applied to all collected data with no need of dedicated runs. The chamber efficiency can be therefore constantly monitored during the data taking.

The calculated efficiency is an average over the efficiencies of all RPCs belonging to chamber *ch*. However, the projective geometry of the muon spectrometer allows to determine the efficiency for each RPC. It is enough to apply the explained method to a sub-sample of tracks crossing the RPCs placed at the same position in each chamber. The final result is a set of 18 $N_{4/4}$ and $N^{ch}_{3/3}$ values, whose ratio gives the efficiency for each RPC.

The efficiency calculation can also be repeated for the smallest part of the detector entering the trigger algorithm: the trigger local boards. The method adopted is the same used to determine the efficiency for each RPC. Since local boards are disposed in a projective geometry it is possible to calculate the ratio $N_{4/4}/N_{3/3}$ for the sub-sample of tracks crossing the boards placed at the same position

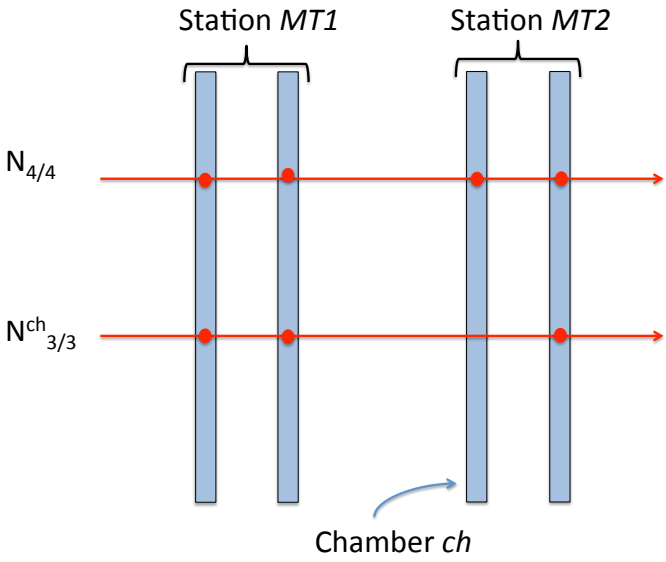

Figure D.2. *Particles crossing the muon trigger system and satisfying the 3/4 trigger algorithm. These tracks are used to measure the efficiency of the chamber ch.*

in all the chambers. It is therefore possible to measure up to 234 efficiency points for both bending and non-bending planes in each chamber.

Typical maps of the trigger chamber efficiency, obtained analyzing the pp data sample at $\sqrt{s}$= 2.76 TeV, are shown in Fig. D.3. They display the efficiency values for each local board.

Finally, the trigger efficiency (i.e. probability to satisfy the trigger 3/4 condition) can be inferred from the efficiencies of the 4 trigger chamber planes. It is calculated as multinomial probability of firing at least 3/4 muon trigger chambers [103].

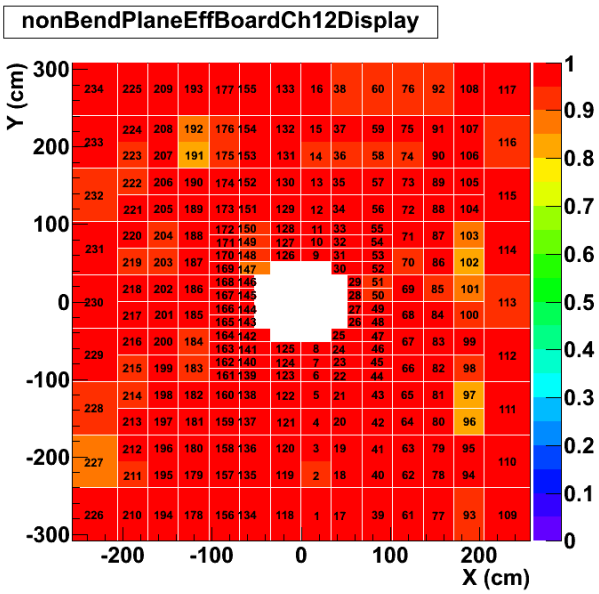

(a) *Chamber 12 (non-bending plane).*

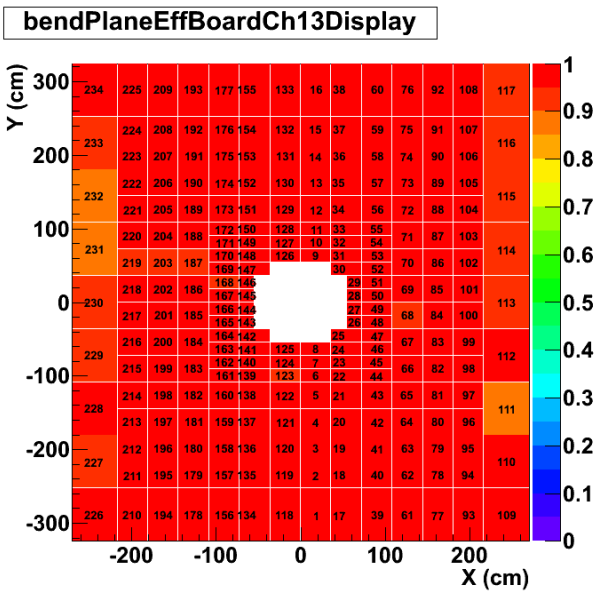

(b) *Chamber 13 (bending plane).*

Figure D.3. *Maps of the trigger chamber efficiency. The efficiency values for each local board are shown.*

Résume

Le plasma de quarks et de gluons (QGP) est un état de la matière nucléaire apparaissant à haute densité d'énergie. En laboratoire, il est possible de reproduire de telles conditions grâce aux collisions d'ions lourds aux énergies ultra-relativistes. ALICE (A Large Ion Collider Experiment) est l'expérience du LHC dédiée à la mise en évidence du QGP.

Différentes signatures ont été proposées et étudiées expérimentalement comme manifestations du QGP. Parmi celles-ci, le méson J/ψ joue un rôle central. Il fait partie de la famille des quarkonia, états mésoniques ($Q\bar{Q}$) formées d'un quark lourd c ou b et de son anti-quark, liés par un potentiel d'interaction forte. En 1986, Matsui et Satz proposèrent la suppression des charmonia (états liés $c\bar{c}$) et notamment du J/ψ comme signature de la formation du plasma de quarks et de gluons.

ALICE peut détecter le J/ψ à grande rapidité ($2.5 < y < 4$) via le canal de désintégration en deux muons. Cette thèse porte sur la mesure de la production du J/ψ, via le canal muonique, dans les collisions pp à une énergie dans le centre de masse de 2.76 et 7 TeV. Elle a exploité les données acquises en 2010 et 2011 auprès du collisionneur LHC.

Tenter d'appréhender le mécanisme de production du J/ψ (et plus généralement du quarkonium) dans les collisions pp est un préalable nécessaire avant d'aborder le degré de complexité suivant que constitue le cas des collisions noyau-noyau. Il est également un test important pour la Quantum Chromo Dynamics (QCD), la théorie de l'interaction forte, aux énergies très élevées du LHC.

Mots-clefs: collisions proton-proton, plasma de quarks et de gluons, J/ψ, ALICE

Abstract

Quarkonia are meson states whose constituents are a *charm* or *bottom* quark and its corresponding antiquark ($Q\bar{Q}$). The study of the production of such bound states in high-energy hadron collisions represents an important test for the Quantum Chromo-Dynamics. Despite the fact that the quarkonium saga has already a 40-year history, the quarkonium production mechanism is still an open issue. Therefore, measurements at the new CERN Large Hadron Collider (LHC) energy regimes are extremely interesting.

In this thesis, the study of inclusive J/ψ production in proton-proton (pp) collisions at $\sqrt{s} = 2.76$ and 7 TeV, obtained with the ALICE experiment, is presented. J/ψ mesons are measured at forward rapidity ($2.5 < y < 4$), down to zero p_{T}, via their decay into muon pairs ($\mu^+\mu^-$).

Quarkonium resonances also play an important role in probing the properties of the strongly interacting hadronic matter created, at high energy densities, in heavy-ion collisions. Under such extreme conditions, the created system, according to QCD, undergoes a phase transition from ordinary hadronic matter to a new state of deconfined quarks and gluons, called *Quark Gluon Plasma* (QGP). The ALICE experiment at CERN LHC has been specifically designed to study this state of matter. Quarkonia, among other probes, represents one of the most promising tools to prove the QGP formation. In order to correctly interpret the measurements of quarkonium production in heavy-ion collisions, a solid baseline is provided by the analogous results obtained in pp collisions.

Hence, the work discussed in this thesis, concerning the inclusive J/ψ production in pp collisions, also provides the necessary reference for the corresponding measurements performed in Pb-Pb collisions which were collected, by the ALICE experiment, at the very same center-of-mass energy per nucleon pair ($\sqrt{s_{NN}} = 2.76$ TeV).

Keywords: proton-proton collisions, quark gluon plasma, J/ψ, ALICE